East Asian Monsoon variability on orbital- and millennial-to-sub-decadal time scales.

Kumulative Dissertation
zur Erlangung des Doktorgrades
der Mathematisch-Naturwissenschaftlichen Fakultät
der Christian-Albrechts-Universität
zu Kiel

vorgelegt von
Christian Bühring

Kiel, 2001

Referent/in: Prof. Dr. Michael Sarnthein.....

Korreferent/in: Prof. Dr. Wolfgang Kuhnt.....

Tag der mündlichen Prüfung: 13. November 2001.....

Zum Druck genehmigt: Kiel, 14. November 2001.....

Der Dekan

Abstract

Sedimentological, geochemical and paleomagnetic records were employed to reconstruct the history of East Asian Monsoon variability in the South China Sea (SCS) on orbital- and millennial-to-sub-decadal time scales.

A detailed magnetostratigraphy for the southern central SCS was established as well as a stable isotope stratigraphy for ODP Site 1144 for the last 1.2 million years in the northern South China Sea. Furthermore a volcanic tephra layer from the southern central SCS could be identified as the Youngest Toba Ash, which thus represents an important age marker and was used to reconstruct paleo wind directions during the eruption 74 ka. Special attention was paid to the high- and ultrahigh-frequency variability in the last glacial-interglacial cycle and the Holocene, and to a precise age control of climate changes in general.

The magnetostratigraphical framework for the Pleistocene Monsoon variability in the area of SONNE-95 core 17957-2 from the central SCS was established on the basis of continuous high-resolution (Susceptibility, NRM and ARM) magnetic records. The Brunhes/Matuyama magnetic polarity reversal (0.78 Ma) here is apparent as a change to negative inclination and a 180° swing of the declination. Similarly, the Jaramillo normal polarity interval (0.99-1.07 Ma) is defined by distinct changes in declination and inclination. A third magnetic event might correspond to the Cobb Mountain event (1.201-1.211 Ma). This magnetostratigraphy is corroborated by several biostratigraphic datums.

Ocean Drilling Program Site 1144 in the northern South China Sea provides, with high sedimentation rates, a climatic record of East Asian Monsoon variations on centennial to orbital time scales over **M**arine **I**sotope **S**tage (MIS) 2-5 and MIS 6-12. Stable oxygen and carbon isotope records of the planktonic foraminifer *G. ruber* (white) extend as almost continuous records from the Holocene back to MIS 12 and with low resolution to the early Pleistocene MIS 29. Major hiatuses occur at peak warm stages 5.5 and 11.3, possibly as a result of strong

contour current erosion. Another hiatus occurs between MIS 29 and MIS 73(?). The variations in the isotope record of the last 110 k.y. closely parallel the $\delta^{18}O$ record of the GISP2 ice core record.

Geochemical analyses of volcanic ash particles prove, for the first time, the occurrence of the Youngest Toba Ash (74 ka) in sediments of the South China Sea and expand the previously known ash-fall zone over more than 1800 km to the east. The dispersal of ashes from Sumatra in both eastern and western directions indicates two contrasting wind directions and suggests that (1) the Toba eruption probably happened during the Southeast Asian summer monsoon season, and (2) the volume of erupted magma was twice as large as previously interpreted.

Sediment colors from the northern South China Sea off Hong Kong (core 17940) provide a unique time series of monsoon-controlled sediment deposition spanning the last 11,000 years. Both the sampling resolution of < 0.3 mm and sedimentation rates of 40-90 cm/k.y. lead to a theoretical time resolution of 0.3-0.7 years, permitting the detection of centennial-to-sub-decadal-scale climate cycles in the non-laminated sediment section despite bioturbational mixing. The the blue-color intensity records the portion of clay enriched in TOC and thus the strength of the wet summer monsoon. The intensity of the red color documents the portion of reddish stained loess dust and thus the strength of the dry winter monsoon. Suborbital climate periodicities (of both the color codes and the bi-decadal-scale resolution $\delta^{18}O$ curve) are dominated by a 950-year cycle which lags an analog GISP2 temperature signal by 250-400 years and documents the global linkages of monsoon variability to a northern high-latitude solar forcing (documented in ^{10}Be GISP2 ice records of solar irradiance; Finkel 1977; Sarnthein et al., in prep.). Multi- to semicentennial periodicities comprise the 200-year de-Vries/Suess and the 85-105-year Gleissberg cycles of solar irradiance. 20/24-year (Hale) and close-to-11-year (Schwabe or NAO) periodicities, and ENSO cycles of 3-8 years reveal prominent, probably internal climate forcings in the high-frequency range of the color records.

Kurzfassung

Um die Geschichte der Variabilität des Ostasiatischen Monsuns im Südchinesischen Meer im Bereich von orbitalen, tausendjährigen bis sub-dekadischen Zeitskalen zu rekonstruieren wurden sedimentologische, isotopische, geochemische und paleomagnetische Zeitserien erstellt.

Es wurde eine detaillierte Magnetostratigraphie für das südliche Südchinesische Meer erstellt sowie eine stabile Isotopen Stratigraphie der letzten 1.2 Millionen Jahre für ODP Site 1144 im nördlichen Südchinesischen Meer. Weiterhin konnte eine vulkanische Aschenlage aus dem Südteil des zentralen Südchinesischen Meeres als jüngste Toba-Asche identifiziert werden, die somit einen wichtigen Leithorizont darstellt und zur Rekonstruktion der Paläo-Windrichtungen während der Eruption herangezogen werden konnte. Besondere Aufmerksamkeit galt der Variabilität im hohen und sehr hohen Frequenzbereich während des letzten glazial-interglazial Zyklus und während des Holozäns sowie der präzisen Alterskontrolle der Klimaschwankungen im Allgemeinen.

Der magnetostratigraphische Rahmen für die pleistozäne Monsunaktivität in Gebiet von SONNE-95 Kern 17957-2 aus dem zemtralen Südchinesischen Meer wurde auf der Grundlage eines durchgehenden, hochauflösenden magnetischen Datensatzes (Suszeptibilität, NRM und ARM) erstellt. Die magnetische Brunhes/Matuyama Polaritätsumkehr (0.78 MJ) ist hier deutlich als Wechsel zu negativen Inklinationswerten und als 180° Drehung der Deklination erkennbar. Analog dazu ist das Jaramillo-Interval mit normaler Polarität (0.99-1.07 MJ) durch deutliche Wechsel in der Deklination und Inklination definiert. Ein drittes magnetisches Ereignis entspricht vermutlich dem Cobb Mountain Event (1.201-1.211 MJ). Diese Magnetostratigraphie wird von einigen biostratigraphischen Alterskontrollpunkten bestätigt.

Ocean Drilling Program Site 1144 im nördlichen Südchinesischen Meer lieferte aufgrund der hohen Sedimentationsraten einen Klimadatensatz der Monsunvariabilität im Bereich von

orbitalen Zeiträumen bis wenigen Jahrhunderten ($\delta^{13}C$ und $\delta^{18}O$ der planktischen Foraminifere *G. ruber* (white)). Hohe zeitliche Auflösung reicht vom Holozän zurück bis zum Marinen Isotopenstadium 12, niedrige Auflösung bis zum frühpleistozänen Isotopenstadium 29. Größere Hiaten befinden sich in den Zeitabschnitten der extrem warmen Stadien 5.5 und 11.3, möglicherweise erzeugt durch die erosive Wirkung von Konturströmungen. Die Isotopenkurve von Site 1144 der letzten 110 kJ verläuft eng parallel zur $\delta^{18}O$-Kurve des GISP2 Eiskerns.

Geochemische Analysen vulkanischer Aschenpartikel bewiesen erstmalig das Vorkommen der jüngsten Toba Asche (74 kJ v. h.) in Sedimenten des Südchinesischen Meeres, wodurch das bekannte Verbreitungsgebiet der Aschenlage um mehr als 1.800 km nach Osten verdoppelt wurde. Die Verbreitung der Asche aus Sumatra sowohl in westliche als auch in östliche Richtung zeigt gegensätzliche Windrichtungen an. Daraus kann gefolgert werden, daß (1) die Toba Eruption wahrscheinlich während des Südostasiatischen Sommermonsuns stattgefunden hat und (2), daß das Volumen des eruptierten Magmas doppelt so groß war als bislang angenommen.

Die Farben der Sedimente des nördlichen Südchinesischen Meeres vor Hong Kong (Kern 17940) bilden die Grundlage für eine einzigartige Zeitserie monsungesteuerter Sedimentation, welche die vergangenen 11.000 Jahre erfasst. Eine Datenauflösung von weniger als 0.3 mm zusammen mit Sedimentationsraten von 40-90 cm/kJ führt zu einer theroretischen zeitlichen Auflösung von 0.3-0.7 Jahren. Dies erlaubt es, -trotz Bioturbation-, Klimazyklen im Bereich von Jahrhunderten, Jahrzenten und wenigen Jahren in dieser nicht-laminierten Sedimentabfolge zu erfassen.

Die Intensität des Blauanteils der Sedimentfarbe gibt den Anteil des mit organischem Kohlenstoff angereicherten Tongehaltes wider und reflektiert somit die Stärke des regenreichen Sommermonsuns. Die Intensität des Rotanteils dokumentiert den Gehalt an rötlichem Löß-Staub und steht somit für die Stärke des trockenen Wintermonsuns.

Die suborbitalen Klimazyklizitäten (sowohl nach den Farbwerten als auch der dekadisch aufgelösten Sauerstoff-Isotopenkurve) werden dominiert von einem 950-Jahr-Zyklus. Dieser Zyklus eilt einem analogen GISP2 Temperatursignal um 250-400 Jahre nach und zeigt deutlich die globalen Verbindungen der Monsunvariabilität mit einem solaren Klimaantrieb der nördlichen hohen Breiten auf (dokumentiert auch in ^{10}Be-Zeitreihen von GISP2; Finkel, 1997; Sarnthein et al., in prep.). Weitere Periodizitäten im Bereich von mehreren Jahrhunderten bis wenigen Jahrzehnten umfassen den solaren 200-jährigen deVries/Suess-und den 85-105 jährigen Gleissberg Zyklus. Weitere Periodizitäten von 20/24 Jahren (Hale) und nahe 11 Jahren (Schwabe oder NAO), sowie ENSO Zyklen von 3-8 Jahren Dauer offenbaren bedeutende, wahrscheinlich interne Klimasteuerprozesse im Hochfrequenzbereich der Farbdatensätze.

Table of Contents

1. Introduction

Background and Objectives

The main objective of this study is to reveal the past variability of the East Asian Monsoon system through an investigation of sediment records from the South China Sea **(SCS)** using different methods at high- and ultra-high resolution (decimeter to sub-millimeter scale).

The East Asian Monsoon is an integral part of the tropical global climate system and represents the dominating climatic factor for Southeast and East Asia. As such its variability and evolution are of great interest not only to paleoclimatologists and climate modelers, but also to scientists from other disciplines ranging from sedimentology to agriculture. To reconstruct this climate variability we rely on proxy indices preserved in the geological record. In this study, deep-sea sediment records from the South China Sea were used to examine the history of the last 1.1 million years of East Asian Monsoon with special emphasis on its high-frequency oscillations during the Holocene and the Last Glacial-to-Interglacial cycle. These reconstructions may, in turn, provide more insight into the forcings of the variability in Monsoon and their implications for predicting past and future global climate change.

Climatic and volcanic events leave their traces in sedimentary sequences either as variations in the isotopic signatures of marine organisms, as variations in the sediment color indicating changes in sediment composition, or as distinct layers which represent unique age markers. To thoroughly understand the evolution of the paleomonsoon it is essential to document these variations and to analyse their nature and periodicities. With this in mind major emphasis was given to the following research questions:

- Little is known about atmospheric circulation patterns of the tropical and subtropical atmosphere at the end of the last Interglacial. Once the source of a volcanic ash layer in deep-sea sediments is determined by geochemical methods, this volcanic tephra could serve as a tracer for the reconstruction of past wind directions and atmospheric circulation patterns.
- The time resolution of sediment records, which is necessary to resolve ultra-high climate variability in deep-sea sediments, is limited by simple physical constraints such as sedi-

mentation rate and the size of the sampling tools. Nevertheless, to obtain the needed information, non-destructive methods like digital sediment color analysis with a theoretically unlimited sampling resolution offer an answer to this problem. However, digital sediment color records need to be defined as an indicator for climate variability. Furthermore, these color records need to be studied for persistent periodicities that bear relation to other climate records such as ice cores and thus to uncover potential climate forcing mechanisms.

- Any study of the long-term variability of monsoon in the South China Sea needs to be based on a complete and detailed stable isotope stratigraphy. As anticipated, Site 1144 yielded the highest sedimentation rates and is therefore ideal to establish a high-resolution stable isotope record for the last 1.1 million years, including a potential centennial-to- millennial-scale variability. Open questions are, whether the high-frequency oscillations occur equally in all the isotope stages. Moreover, whether and in which way the events in the isotope record are correlated to other high-resolution climate records. Finally, any features in the sediment profile, which might reflect profound climate-driven changes in the sedimentation regime and thus in current activity, such as hiatuses, need to be identified.
- The southern South China Sea is part of the Western Pacific Warm Pool (WPWP), and therefore of special interest to paleoceanographers. Because of the low sedimentation rate, cores from this region provide continuous and long Pleistocene deep-sea sediment records necessary to reconstruct the long-term history of the South China Sea in the context of the WPWP. The main research objective of this part of the thesis, as part of an interdisciplinary approach, was to establish a detailed magnetostratigraphc framework in core 17957-2 to better constrain the age control of stable isotopic, biostratigraphic, and coarse-fraction stratigraphic records. The underlying basic question of this study was to assess the long- and short-term, possibly monsoon-driven, planktonic and benthic foraminiferal response to paleoceanographic changes in a key region near to the WPWP.

- To answer these questions six different sediment profiles from a transect across the South China Sea were examined and the results reported this thesis. Four sites are located in the southern central part near the Dangerous Grounds and Nansha Islands (cores 17957, 17961, 17962 and ODP Site 1143) and two lie on the northern continental slope (core 17940 and ODP Site 1144) (Figure 1).

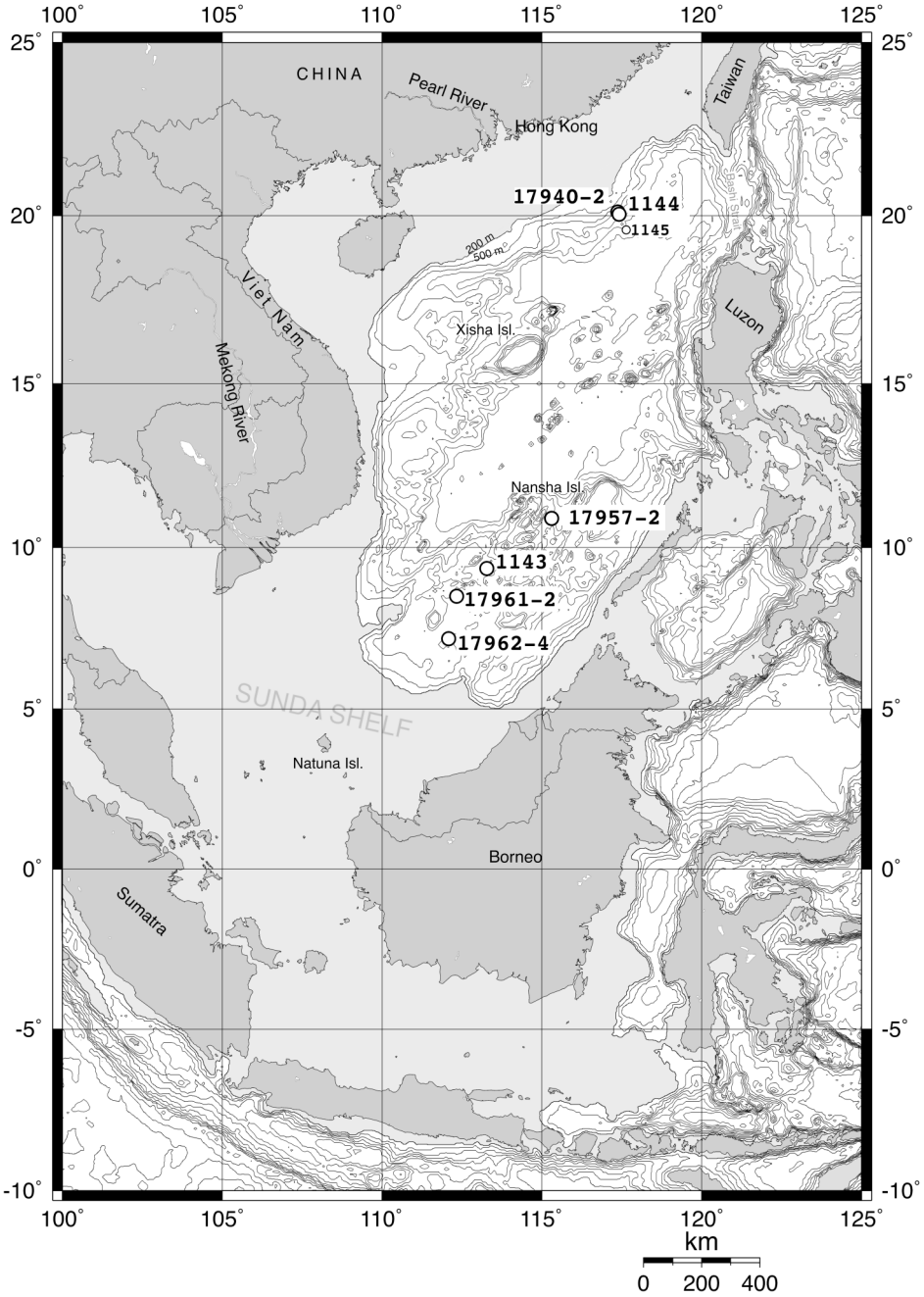

Figure 1: Map of the South China Sea region with locations of sites studied.

Strategy

This thesis is set up as a quasi-cumulative dissertation since a substantial part was already submitted to or was published in international reviewed journals. The samples and methods used or developed for this study are summarized in chapter 2 (Material and Analytical Methods). The Results chapter 4 consists of four main sections, each representing an article either published (chapters 4.1 and 4.4) or submitted (chapters 4.2, 4.3).

The questions concerning the use of volcanic ash layers in deep-sea sediments for the reconstruction of past atmospheric circulation patterns are treated in chapter 4.1. The Results chapter 4.2 presents a case study of modern digital sediment color analysis which has been applied to high sedimentation rate sediment profiles to produce ultra-high resolution data records that contain detailed information about Holocene climate variability on millennial-to-sub-decadal time scales. The oxygen isotope stratigraphy of ODP Site 1144 is documented in chapter 4.3 with special emphasis on the last five glacial-interglacial cycles. Furthermore, this part of the thesis is aimed at providing a detailed stable isotope record for the last 1.1 million years which is the stratigraphic basis for several other research projects within the Ocean Drilling Program.

The Results chapter 4.4 consist of two parts, the first one is a published article about foraminiferal responses to major Pleistocene paleoceanographic changes in the southern South China Sea (chapter 4.4) as part of the WPWP. Supplementary information on the magnetostratigraphy of this SONNE-95 core 17957-2, which was generated within the scope of this thesis, is presented in the second part of chapter 4.4.

Tectonic framework

The South China Sea is the largest marginal sea basin of the western Pacific. It is bordered by the passive continental margins of southeastern China, Vietnam, and the Malaysian Peninsula. The active margins of the Philippine Archipelago with the Manila Trench and Palawan Trench off eastern Borneo, form the eastern and southeastern boundaries (Figure 2). The South China Sea basin was formed coincident with the large-scale deformation of the Asian

continent following the Eocene collision with India. Different models relate the opening of the South China Sea basin either to left-lateral displacment along the Red River fault zone (Briais et al., 1993) during the Oligocene and Miocene and/or to a back-arc type of extension in connection with subduction under the Philippines (Taylor and Hayes, 1980, 1983). The central deep-water basin is underlain by oceanic crust (Ludwig et al., 1979; Hékinian et al., 1989), which contains a sequence of sea-floor spreading magnetic anomalies ranging from 31 to 16 Ma (Briais et al., 1993) and reaches a maximum water depth of over 4000 m. In summary, the present-day shape of the South China Sea is a result of the continued counter-clockwise rotation of the Philippine Sea Plate to the east and the collision of Asia with the Australian Plate to the south (Packham, 1996). The collison of the Philippine Arc with the underthrusting oceanic crust of the SCS led to the rapid uplift of Taiwan and the Bashi Strait since 6.5 Ma (Huang et al., 1997) and further isolation of the South China Sea basin from the West Pacific. The southern and central South China Sea contains numerous terranes (Lüdmann et al., 2001), which probably have rifted southwards during the early opening of the South China Sea (Jin, 1992). Several of them are capped by coral reefs such as the Dangerous Grounds (Nansha Islands) or the Paracel Islands (Xisha Islands) (Figure 1).

The shelf areas of the South China Sea constitute about half of its present-day size. The largest shelf area is the Sunda Shelf in the south, which covers together with the Gulf of Thailand and the Java Sea shelf, a total area of 1,800,000 km^2. In the north of the South China Sea another large shelf area reaches more than 200 km off China and extends from Taiwan to Vietnam. During glacial sea-level lowstands vast portions of these shelf areas were subaerially exposed (P. Wang, 1999; Hanebuth, 2000). This led to an even stronger enclosure of the South China Sea with profound influences on the local oceanic circulation patterns.

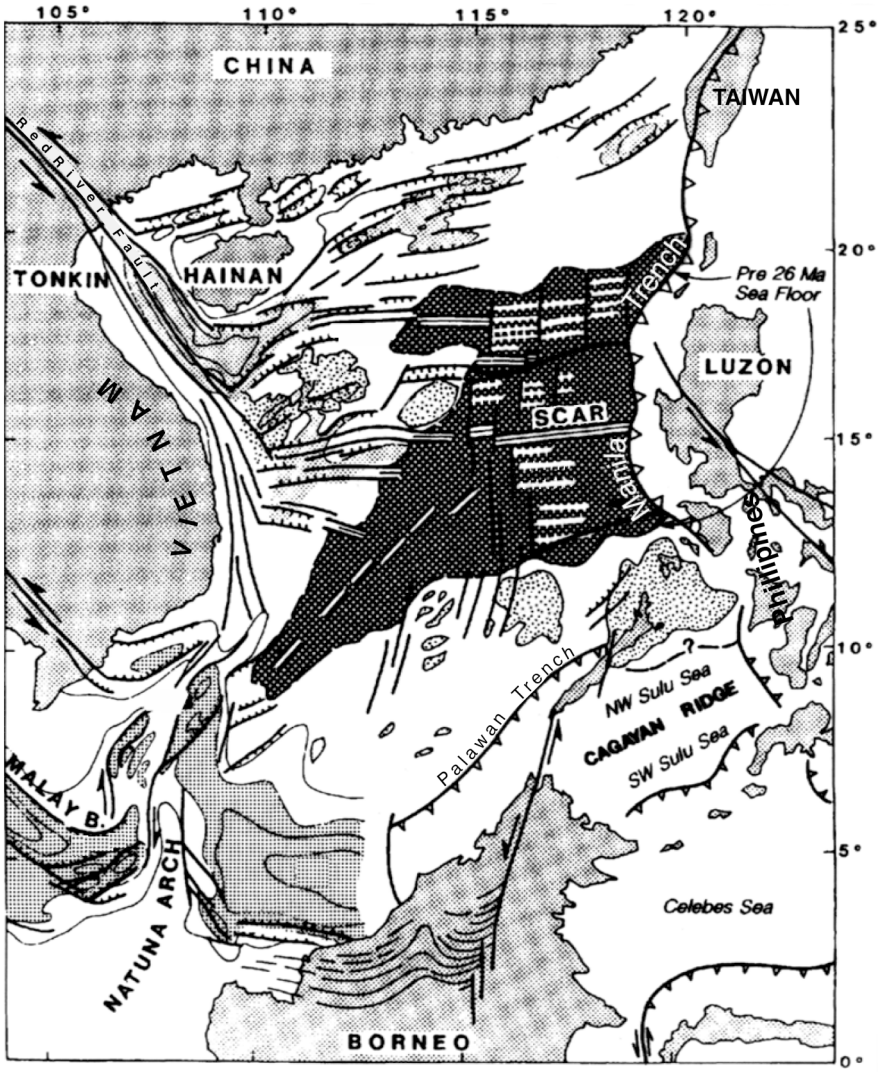

Figure 2: Tectonic structure of the South China Sea (Packham, 1996, modified). Oceanic crust = dark dotted, shallow areas of continental crust = light dotted. SCAR = Scarborough Seamounts.

Monsoon Climate of the South China Sea region

The Asian Monsoon is a primary component of the tropical and global climate system (Clemens et al., 1996). It consists of three subsystems, the Indian Monsoon, the East Asian Monsoon and the Plateau Monsoon. (An, 2000b). Of these the East Asian Monsoon is the dominating climate factor for the area east of the Bay of Bengal and the Tibetan Plateau, and especially for the region of the South China Sea and the Chinese mainland.

As generally known, two fundamental mechanisms are driving the East Asian Monsoon, (1) the thermal differences between the highly elevated Asian landmass and the Pacific, which are responsible for the primary atmospheric pressure gradient and, (2) the subsequent release

of latent heat over the Asian plateau (Webster, 1987; Hastenrath, 1991). In the northern winter season, cold air from high-latitudes is driven by the continental high-pressure system over Asia southward along the eastern margin of the Tibetan Plateau, forming a strong northerly flow of cold and dry air. This winter monsoon influences China, the South China Sea and even propagates across the Equator into the southern Hemisphere where it enhances the southern summer monsoon.

During the northern Hemispere summer, warm and humid air originating from low latitude oceans, especially the Indian Ocean, moves northward across the South China Sea onto the East Asian landmass as far as Mongolia (An, 2000a). The summer monsoon is the main source of precipitation in East Asia with far reaching implications on vegetation, erosion and sedimentation. In conclusion, the East Asian Monsoon climate is characterized by extreme seasonal variations in wind direction, precipitation and temperature between winter (cold and dry) and summer (hot and humid).

Modern sea surface circulation and water mass properties

The surface water circulation pattern within the South China Sea is mainly controlled by the reversal of the seasonal East Asian Monsoon winds, and to a smaller degree, by the warm Kuroshio current, a perennial western boundary current of the Pacific Ocean that flows northwards along the east coasts of the Philippines and Taiwan towards Japan (Stommel and Yoshida, 1972; Kawai, 1998). Along its way, a branch of the Kuroshio current enters the South China Sea through the Bashi Strait between Luzon and Taiwan (Shaw, 1991) and advects warm and salty surface water westward along the continental slope south of China (Metzger and Hurlburt, 1996; Pflaumann and Jian, 1999). The narrow and shallow water ways within the Indonesian archipelago in the south, limit the exchange of water between the South China Sea and the tropical Pacific or the Indian Ocean, however, these water ways still influence the sedimentationary environment during times of high sea-level stands.

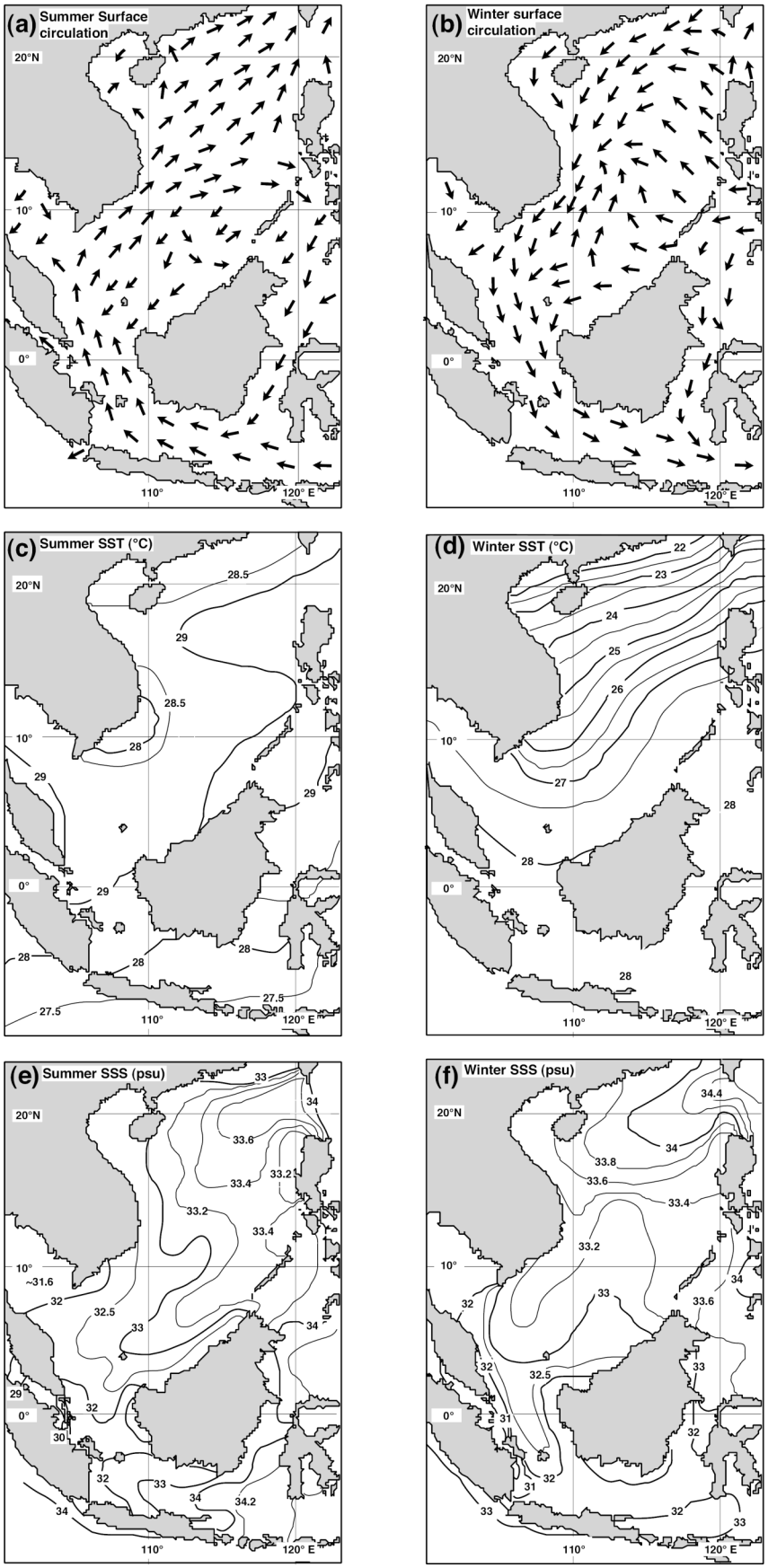

Figure 3: Modern hydrography in the SCS during summer and winter: (a-b) sea surface circulation; (c-d) sea surface temperatures; (e-f) sea surface salinity. Temperatures after Levitus and Boyer (1994), surface circulation and salinities redrawn from Wyrtki (1961). (psu= practical salinity units)

The flow of surface water masses (Figure 3a-b) during the winter season (November to April) is generally directed to the southwest, owing to the strong northeasterly winds. During summer monsoon (May to September) the surface flow pattern is reversed, generally directed to the northeast, driven by the southwesterly summer monsoon winds (Wyrtki, 1961; Liu and Xie, 1999). In response to the differential wind stress and resulting current direction, eddies form in different parts of the SCS at different times of the year. In Spring a counterclockwise eddy exists in the central SCS (Wyrtki, 1961), while in Winter two cyclonic gyres develop, one west of Luzon and the other off the southern tip of Vietnam (Liu and Xie, 1999). According to modeling studies (Chao et al., 1996) and inferred from wind stress observations (Liu and Xie, 1999), deep-water upwelling occurs in two regions of the SCS; during the winter monsoon off the northwestern edge of Luzon (Udarbe-Walker and Villanoy, 2001) and during the summer monsoon northeast of South Vietnam (Wiesner et al., 1996; Jian et al., 2001). Shallow upwelling may occur along the edge of the Sunda shelf from October to December.

Similar to the sea surface current directions **S**ea **S**urface **T**emperatures (SST) and **S**ea **S**urface **S**alinities (SSS) are also subjected to strong seasonal change (Figure 3c-f). While in Summer, SST's almost uniformly range from 27-29° C across the South China Sea, during the winter monsoon season SST's display a steep north-south gradient with temperatures near 22°C in the north and close to 29 °C in the very southern part (Levitus and Boyer, 1994).

Sea surface salinities are slightly higher in Winter than in Summer and range from 32.8 to 34.6 ‰ (Levitus and Boyer, 1994). Summer salinities in the SCS range from 31.6 in the Gulf of Thailand to 34 ‰ near the Bashi Strait, as a result of the inflow of high-salinity surface waters from the Western Pacific (Metzger and Hurlburt, 1996). The input of riverine freshwater into the SCS can be traced in front of the major river mouths, with especially low salinities below 33 ‰ in the Gulf of Tonkin (Red River) and in front of the Mekong River delta (Wyrtki, 1961). A low-salinity plume also marks the shelf southeast of Hong Kong (Pearl River; P. Wang et al., 1999).

The annual average depth of the thermocline ranges from approximately 25 m on the inner shelf off Hong Kong to ~200-250 m towards the Bashi Strait, with temperatures gradually decreasing from 20°C to 11°C (Miao and Thunell, 1996; Jian et al., 2000). Mixed intermediate water masses in the SCS reach from ~250 to 1000 m water depth, and homogenous deep water extends from 1000 m to the sea floor. Temperature decreases from 11°C at 250 m to 4°C near 1000 m water depth while salinity increases slightly from 34.4 ‰ to 34.6‰. The oxygen minimum zone with lowest O_2-values of 1.25 ml/L extends between 500 m and 1500 m water depth. The deep water masses of the SCS below 1000 m are derived from Pacific deep water and have fairly uniform properties with a salinity of 34.6 ‰ (Miao et al., 1994). The lowest temperature of 2.3 °C is reached at a water depth of 2500 m (Sarnthein et al., 1994). The inflow of cold (~2°C) western Pacific bottom water through the Bashi Strait (P. Wang, 1999) positively influences the ventilation of the SCS by increasing the deep water oxygen content to 2.0 ml/L (Miao et al., 1994).

Modern sea surface productivity

Sea surface primary productivity in the SCS is relatively high on the continental margins of Vietnam and China and off the Borneo coastal area (400 g C m^{-2} yr^{-1}), but decreases in the deeper and more central parts to values between 90 and 160 g C m^{-2} yr^{-1} (Platt et al., 1995; Kuhnt et al., 1999). High productivity also characterizes the upwelling cell east of South Vietnam.

Sedimentation rate patterns

Sedimentation rates in the South China Sea are the result of a complex system of biogenic, volcanogenic and, above all, of terrigenous sediment sources and input mechanisms. The fluvial contribution is the dominating factor in the SCS, especially in front of the large rivers (i. e. Mekong River, Pearl River, Red River) draining the Asian continent and, to a lesser degree, in front of minor rivers draining the islands bordering the SCS (Schönfeld and Kudrass, 1993; P. Wang, 1999). Wind transported sediments such as loess from the desert areas of Inner Asia

play a lesser, but nonetheless considerable role (Wiesner et al. 1996), which was probably of greater importance during colder and dryer periods (L. Wang et al., 1999a, b).

Volcanic particles such as glass shards and pumice are common constituents of the SCS sediments and originate mostly from the Philippine archipelago (Wiesner et al., 1994). The importance of volcanic sediments for the gross sedimentation rates is low (Chen and Zhou, 1992), however single events can constitute important accumulation events with rates of up to several cm/year (Wiesner et al., 1995; Wiesner and Wang, 1996; Lee et al., 1999).

According to P. Wang (1999) average sedimentation rates vary significantly between the Holocene and the Last Glacial. At some sites higher rates occur during the cold stage (Last Glacial) and lower rates in the warm stage (Holocene), while at other sites the reversed pattern is observed. Peak sedimentation rates in the southern SCS reach 13 to 15 cm/k.y., in the northern part, maximum values reach 20 to 66 cm/k.y.: At Site 1144 more than 1 m/k.y. were observed (Sarnthein et al., 1994; P. Wang, 1999; Bühring et al., subm.). The exceptionally high sedimentation rates in the area of core 17940-2 and Site 1144 may be either the result of a lateral sediment advection from the Strait of Taiwan and the Yellow Sea (P. Wang, 1999), but only during times of high sea level, or the result of a complex interaction of sea-level changes and sediment discharge from the Pearl River mouth (L. Wang et al., 1999; Lüdmann et al., 2001).

2. Material and Analytical Methods

Selection of core sites

The sediments sampled and analysed for the present study are mainly from cores collected during the RV SONNE Cruise 95 (cores 17957-2, 17961-2, 17962-4, 17940-2; Sarnthein et al., 1994) and were taken at the Kiel University core repository. The cores from Site 1144 were retrieved during ODP Leg 184 (P. Wang et al., 2000). The samples were taken at the ODP Gulf Coast Core Repository in College Station. Specific details regarding site locations and sample preparation are given in Chapters 1 through 3.

The position of core 17957-2 was chosen because it is situated at the northern slope of the Nansha Islands area (Dangerous Grounds) which is distinguished by low sedimentation rates because of the limited input of terrigenous material. This area provides continuous and long Pleistocene deep-sea profiles and is thus ideal to record the long-term paleoceanographic variations in the region as part of the West Pacific Warm Pool (WPWP).

SONNE 95 sites 17961-2 and 17962-4 are located at the southern end of the Dangerous Grounds area and are characterized by much higher sedimentation rates. This position monitors the changes in the sediment input for the Mekong River and the Sunda Shelf, with low-to-medium high sedimentation rates.

Site 17940-2 and ODP Site 1144 on the northern continental slope of the South China Sea are characterized by the highest sedimentation rates of the SCS and are therefore ideal for high- and ultrahigh resolution studies.

Magnetic susceptibility and paleomagnetic measurements

The chronostratigraphic framework for gravity core 17957-2 from the southern center of the South China Sea is largely based on the magnetostratigraphy presented here (Chapter 4.4).

Low field volume magnetic susceptibility (k_{lf}) of core 17957-2 was measured in high-resolution on u-channels using the special susceptibility track at the LSCE in Gif-sur Yvette,

France (Kissel et al., 1998). **N**atural **R**emanent **M**agnetization (NRM) and subsequent **A**nhysteretic **R**emanent **M**agnetization (ARM) were also measured on u-channels with a pass-through DC-SQUID cryogenic magnetometer in the shielded room of the LSCE. Alternating field demagnetization was applied in 6 to 8 steps from 0 to 60 mT. More details are given in the supplement to Chapter 4.4.

Stable isotope analysis of planktonic foraminifera

The stratigraphy for the cores used in this study is based largely on the oxygen isotope record of planktonic foraminifera. For cores 17961-1 and 17940-2 the isotope records are from L. Wang et al. (1999). The stratigraphy for ODP Site 1144 relies on the oxygen isotope record generated in the context of this study for ODP Scientific Results Volume 184 and is documented in Chapter 4.3.

Stable oxygen and carbon isotope ratios of planktonic foraminifers constitute one of the most important stratigraphic tools in marine geology. The isotopic composition of the carbonatic tests of planktonic foraminifers largely reflects the relative abundance of the ^{18}O and ^{16}O isotopes (and additionally that of the carbon isotopes $^{13}C/^{12}C$) of the ambient water mass in which the foraminifers lived. The isotopic signal is a complex proxy which depends on specific chemo-physical, (salinity, Urey, 1947) and biological fractionation processes (vital effect; Urey et al., 1951). The ratios of $^{18}O/^{16}O$ of the calcitic tests are reported as relative deviations from a laboratory standard, here with reference to the PeeDee Belemnite (PDB) standard (Epstein et al., 1953). Since this specific standard has been completely used up, the calibration to the PDB standard is calculated via the **N**ational **B**ureau of **S**tandards NBS 19 and NBS 20 standards and, in Kiel, via an internal laboratory standard of Solnhofen Limestone (Erlenkeuser, pers. comm.)

Radiocarbon dating

Radiocarbon (^{14}C) datings (Chapter 4.3) were performed at the Leibniz Laboratory at Kiel University with a Tandetron **A**ccelerator **M**ass **S**pectrometer (AMS) following standard pro-

cedures (Nadeau et al., 1997; Schleicher et al., 1998). All AMS-^{14}C were corrected with a standard mean ocean reservoir age of -400 years (Stuiver and Braziunas, 1993; Stuiver et al., 1998). This general correction for -400 years represents a conservative mean estimate, and lies within the range of the modern reservoir ages of 300-550 years for the SCS (Southon et al., in press). AMS-^{14}C ages of less than 20,000 reservoir-corrected years were converted to calibrated calendar (cal) years using the CALIB 4.3 software (Stuiver and Reimer, 1993), which includes the most recent calibration data sets (Stuiver et al., 1998). Radiocarbon ages older than 20,000 reservoir-corrected ^{14}C years were converted to calendar years in analogy to Voelker (1999) and Bard et al. (1998). To limit the effects of bioturbation and to avoid mixing of different reservoir ages resulting from different water masses, only near-surface dwelling planktonic foraminifers *Globigerionides ruber* white (D`ORBIGNY) following the *sensu strictu* morphotype classification of L. Wang (2000), and *Globigerionides sacculifer* (BRADY) were utilized for the AMS ^{14}C datings. To reduce the effects of bioturbational mixing, the radiocarbon datings were performed on samples where the planktonic foraminifers reach abundance maxima.

Sub-mm-scale color analysis of climate signals in hemipelagic sediments

Fine scale variations in sediment composition and their potential climatic controls were investigated with high-resolution sediment color analysis. This technique measures the relative intensity of light reflected from the sediment in three different color bands. It further develops on previous techniques for generating non-destructive, high-resolution color records of sediment properties (Mix et al., 1992, 1995; Merrill et al., 1995). In contrast to spectrophotometer single-point measurements (Balsam et al., 1998; Ortiz et al., 1999a; Chapman and Shackleton, 1998, 2000) the digital color video camera images used for this study provide quasi-continuous data sets with a resolution only limited by the numbers of pixels per square unit (here a camera with 370,000 pxels was employed).

Our digital sediment color analysis was performed on SONNE 95 cores 17961-2 and 17940-2. The color of the sediment surface of the archive halves in cores 17961-2 (0-992 cm)

and 17940-2 (top 720 cm) was measured and analysed from the digital images with an off-the-shelf image processing software. Color values for red, green and blue (R, G, B) of each pixel were determined simultaneously within a selected area in the center of each image, and digitally saved separately for each color channel. One pixel represents approximately 0.3 mm of sediment. A detailed description of the experimental array and methodology is given in Chapter 4.2.

2.6 Microprobe analysis of volcanic glass shards

Samples of two volcanic ash layers from SONNE-95 cores 17961-2 and 17962-4, respectively, were analysed for major oxides composition at the Institut für Geowissenschaften der Universität Kiel with a Cameca CAMEBAX electron-beam microprobe.

The ash layers were first detected in the magnetic susceptibility records (Sarnthein et al., 1994). The layers are 2-3 cm-thick, light grey colored and consist almost entirely of medium-to-fine grained glass particles. No large-scale bioturbation was observed.

In total 38 glass shards were analyzed, 20 from core 17961-2 and 18 from core 17962-4. Each individual grain was analyzed at least twice, but most grains were analyzed three times for calculating the means. Analytical totals ranged between 94 and 98 wt%; further details are given in Chapter 4.1.

3. References for Chapters 1 and 2

An, Z., 2000a. The history and variability of the East Asian paleomonsoon climate. *Quaternary Science Reviews*, **19**: 171-187.

An, Z., Kutzbach, J.E., Prell, W.L., and Porter, S.C., 2001. Evolution of Asian monsoons and phased uplift of the Himalaya-Tibetan plateau since Late Miocene times. *Nature*, **411**: 62-66.

An, Z., Porter, S.C., Kutzbach, J.E., Wu, X., Wang, S., Liu, X., and Zhou, W., 2000b. Asynchronous Holocene optimum of the East Asian monsoon. *Quaternary Science Reviews*, **19**: 743-762.

Balsam, W.L., Deaton, B.C., and Damuth, J.E., 1998. The effects of water content on diffuse reflectance spectrophotometry studies of deep-sea sediment cores. *Marine Geology*, **149**(1-4): 177-189.

Bard, E., Arnold, M., Hamelin, B., Tisnerat-Laborde, N., and Cabioch, G., 1998. Radiocarbon calibration by means of mass spectrometric 230Th/234U and 14C ages of corals. An updated base including samples from Barbados, Mururoa and Tahiti. *Radiocarbon*, **40**: 1085-1092.

Briais, A., Patriat, P., and Tapponnier, P., 1993. Updated interpretation of magnetic anomalies and seafloor spreading stages in the South China Sea: implications for the Tertiary tectonics of Southeast Asia. *Journal of Geophysical Research*, **98**: 6299-6328.

Bühring, C., Sarnthein, M., and Erlenkeuser, H., subm. Toward a high-resolution stable isotope stratigraphy of the last 1.1 million years: Site 1144, South China Sea. *Proceedings of the Ocean Drilling Program, Scientific Results*, **184**.

Bühring, C., Sarnthein, M., and Leg 184 Shipboard Scientific Party, 2000. Toba ash layers in the South China Sea: Evidence of contrasting wind directions during eruption ca. 74 ka. *Geology*, **28**(3): 275-278.

Chao, S.-Y., Shaw, P.-T., and Wu, S.Y., 1996. Deep water ventilation in the South China Sea. *Deep-Sea Research I*, **43**(4): 445-466.

Chapman, M.R., and Shackleton, N.J., 1998. What level of resolution is attainable in a deep-sea core? Results of a spectrophotometer study. *Paleoceanography*, **13**(4): 311-315.

Chapman, M.R., and Shackleton, N.J., 2000. Evidence of 550-year and 1000-year cyclicities in North Atlantic circulation patterns during the Holocene. *The Holocene*, **10**(3): 287-291.

Chen, W., and Zhou, F., 1992. A study of volcanic glass in northern South China Sea during the last 100ka. *in* Jin, X., Kudrass, H.R., and Pautot, G., eds., Marine Geology and Geophysics of the South China Sea: Beijing, China Ocean Press, p. 174-178.

Clemens, S.C., Murray, D.W., and Prell, W.L., 1996. Nonstationary Phase of the Plio-Pleistocene Asian Monsoon. *Science*, **274**: 943-948.

Epstein, S., Buchsbaum, R., Lowenstamm, H.A., and Urey, H.C., 1953. Revised carbonate-water isotopic temperature scale. *Geological Society of America Bulletin*, **64**: 1315-1325.

Finkel, R.C., and Nishiizumi, N., 1997. Beryllium 10 concentrations in the Greenland Ice Sheet Project 2 ice core from 3-40 ka. *Journal of Geophysical Research*, **102**(C12): 26,699-26,706.

Hanebuth, T., Stattegger, K., and Grootes, P.M., 2000. Rapid flooding of the Sunda Shelf: A late-glacial sea-level record. *Science*, **288**(5468): 1033-1035.

Hastenrath, S., 1991. Climate dynamics of the tropics. *in* Berger, A., Crutzen, P.J., Georgii, H.-W., Hobbs, P.V., and Hollingsworth, A., eds., Climate Dynamics of the Tropics, Volume 8: Dordrecht, Netherlands, Kluwer Academic Publishers, p. 182-197.

Hékinian, R., Bonté, P., Pautot, G., Jacques, D., Labeyrie, L.D., Mikkelsen, N., and Reyss, J.-L., 1989. Volcanics from the South China Sea ridge system. *Oceanologica Acta*, **12**(2): 101-115.

Huang, C.-Y., Wu, W.-Y., Chang, C.-P., Tsao, S., Yuan, P.B., Lin, C.-W., and Xia, K.-Y., 1997. Tectonic evolution of accretionary prism in the arc-continent collision terrane of Taiwan. *Tectonophysics*, **281**: 31-51.

Jian, Z., Huang, B., Kuhnt, W., and Lin, H.-L., 2001. Late Quaternary upwelling intensity and East Asian Monsoon Forcing in the South China Sea. *Quaternary Research*, **55**: 363-370.

Jian, Z., Wang, P., Chen, M.-P., Li, B., Zhao, Q., Bühring, C., Laj, C., Lin, H.-L., Pflaumann, U., Bian, Y., Wang, R., and Cheng, X., 2000. Foraminiferal responses to major Pleistocene paleoceanographic changes in the southern South China Sea. *Paleoceanography*, **15**(2): 229-243.

Jin, X., 1992. Tectogenesis and origin of northern South China Sea. *in* Jin, X., Kudrass, H.R., and Pautot, G., eds., Marine Geology and Geophysics of the South China Sea: Proceedings of the Symposium on the Recent Contributions to the Geological History of the South China Sea: Beijing, China Ocean Press, p. 1-9.

Kawai, H., 1998. A brief history of the recognition of the Kuroshio. *Progress in Oceanography*, **41**: 578.

Kissel, C., Laj, C., Mazaud, A., and Dokken, T., 1998. Magnetic anisotropy and environmental changes in two sedimentary cores from the Norwegian Sea and the North Atlantic. *Earth and Planetary Science Letters*, **164**: 617-626.

Kuhnt, W., Hess, S., and Jian, Z., 1999. Quantitative composition of benthic foraminiferal assemblages as a proxy indicator for organic carbon flux rates in the South China Sea. *Marine Geology*, **156**: 123-157.

Lee, M.-Y., Wei, K.-Y., and Chen, Y.-G., 1999. High resolution oxygen isotope stratigraphy for the last 150,000 years in the southern South China Sea:Core MD972151. *Terrestrial, Atmospheric and Oceanic Sciences*, **10**(1): 239-254.

Levitus, S., and Boyer, T.P., 1994. World Ocean Atlas 1994, 4.Temperature. Washington, D. C., U. S. Dept. of Commerce, 117 p.

Liu, W.T., and Xie, X., 1999. Spacebased observations of the seasonal changes of South Asian monsoons and oceanic responses. *Geophysical Research Letters*, **26**(10): 1473-1476.

Lüdmann, T., Wong, H.K., and Wang, P., 2001. Plio-Quaternary sedimentation processes and neotectonics of the northern continental margin of the South China Sea. *Marine Geology*, **172**: 331-358.

Ludwig, W.J., Kumar, N., and Houtz, R.E., 1979. Profiler-sonobuoy measurements in the South China Sea basin. *Journal of Geophysical Research*, **84**(B7): 3505-3518.

Merrill, R.B., and Beck, J.W., 1995. The ODP color digital imaging system; color logs of Quaternary sediments from the Santa Barbara Basin, Site 893. *in* Kennett, J.P., Baldauf, J.G., and Lyle, M., eds., Proceedings of the Ocean Drilling Program, Scientific Results, Volume 146 (Pt. 2): College Station, Ocean Drilling Program, p. 45-59.

Metzger, E.J., and Hurlburt, H.E., 1996. Coupled dynamics of the South China Sea, the Sulu Sea and the Pacific Ocean. *Journal of Geophysical Research*, **101**(C5): 12331-12352.

Miao, Q., and Thunell, R.C., 1996. Late Pleistocene-Holocene distribution of deep-sea benthic foraminifera in the South China Sea and Sulu Sea: paleoceanographic implications. *Journal of Foraminiferal Research*, **26**(1): 9-23.

Miao, Q., Thunell, R.C., and Anderson, D.M., 1994. Glacial-Holocene carbonate dissolution and sea surface temperatures in the South China Sea and Sulu seas. *Paleoceanography*, **9**: 269-290.

Mix, A.C., Harris, S.E., and Janecek, T.R., 1995. Estimating lithology from nonintrusive reflectance spectra; Leg 138. *in* Pisias, N.G., Mayer, L.A., Janecek, T.R., Baldauf, J.G., et al., eds., Proceedings of the Ocean Drilling Program, Scientific Results, Volume 138: College Station, TX, United States, Texas A & M University, Ocean Drilling Program, p. 413-427.

Mix, A.C., Rugh, W., Pisias, N.G., Veirs, S., Leg 138 Shipboard Sedimentologists, and Leg 138 Scientific Party, 1992. Color Reflectance Spectroscopy: A tool for rapid characterization of deep-sea sediments. *in* Mayer, L., Pisias, N., and Janecek, T., eds., Proceedings of the Ocean Drilling Program, Initial Reports, Volume 138: College Station, Ocean Drilling Program, p. 67-77.

Nadeau, M.-J., Schleicher, M., Grootes, P.M., Erlenkeuser, H., Gottang, A., Mous, D.J.W., Sarnthein, M., and Willkomm, H., 1997. The Leibniz-Labor AMS facility at the Christian-Albrechts-University, Kiel, Germany. *Nuclear Instruments and Methods in Physics Research*, **B123**: 22-30.

Ortiz, J., Mix, A., Harris, S., and O'Connell, S., 1999. Diffuse spectral reflectance as a proxy for percent carbonate content in North Atlantic sediments. *Paleoceanography*, **14**(2): 171-186.

Packham, G., 1996. Cenozoic SE Asia: reconstructing its aggregation and reorganization. *in* Hall, R., and Blundell, D., eds., Tectonic Evolution of Southeast Asia, Volume 106: Geological Society Special Publication: London, p. 123-152.

Pflaumann, U., and Jian, Z., 1999. Modern distribution patterns of planktonic foraminifera in the South China Sea and western Pacific: a new transfer technique to estimate regional sea-surface temperatures. *Marine Geology*, **156**(1-4): 41-83.

Platt, T., Sathyendranath, S., and Longhurst, A., 1995. Remote sensing of primary production in the ocean: promise and fulfilment. *Philos. Trans. R. Soc. London*, **B 348**: 191-202.

Sarnthein, M., Pflaumann, U., Wang, P.X., and Wong, H.K., 1994. Preliminary Report on Sonne-95 Cruise "Monitor Monsoon" to the South China Sea. *Berichte-Reports, Geologisch-Paläontologisches Institut der Universität Kiel*, **68**: 0-225.

Schleicher, M., Grootes, P.M., Nadeau, M.-J., and Schoon, A., 1998. The carbonate 14C background and its component at the Leibniz AMS facility. *Radiocarbon*, **40**: 85-94.

Schönfeld, J., and Kudrass, H.-R., 1993. Hemipelagic sediment accumulation rates in the South China Sea related to Late Quaternary sea-level changes. *Quaternary Research*, **40**: 368-379.

Schönfeld, J., and Kudrass, H.-R., 1993. Hemipelagic Sediment Accumulation Rates in the South China Sea Related to Late Quaternary Sea-Level Changes. *Quaternary Research*, **40**: 368-379.

Shaw, P.-T., 1991. The seasonal variation of the intrusion of Philippine Sea water into the South China Sea. *Journal of Geophysical research*, **96**: 821-827.

Southon, J., Kashgarian, M., Fontugne, M., Metivier, B., and Yim, W.W.-S., in press. Marine reservoir corrections for the Indian Ocean and Southeast Asia. *Radiocarbon*.

Stommel, H., and Yoshida, K., 1972. Kuroshio, Physical Aspects of the Japan Current., Univ. of Washington Press.

Stuiver, M., and Braziunas, T.F., 1993. Sun, ocean, climate and atmospheric $^{14}CO_2$: an evaluation of causal and spectral relationships. *The Holocene*, **3**(4): 289-305.

Stuiver, M., and Reimer, P.J., 1993. Extended 14C database and revised CALIB radiocarbon calibration program. *Radiocarbon*, **35**: 215-230.

Stuiver, M., Reimer, P.J., Bard, E., Beck, J.W., Burr, G.S., Hughen, K.A., Kromer, B., McCormack, G., Van Der Plicht, J., and Spurk, M., 1998. INTCAL98 radiocarbon age calibration, 24,000-0 cal BP. *Radiocarbon*, **40**(3): 1041-1083.

Taylor, B., and Hayes, D.E., 1980. The tectonic evolution of the South China Sea Basin. *in* Hayes, E.D., ed., Tectonic and Geologic Evolution of Southeast Asian Sea and Islands, Volume 23: Geophysical Monograph, AGU, p. 89-104.

Taylor, B., and Hayes, D.E., 1983. Origin and history of the South China Sea Basin. *in* Hayes, E.D., ed., Tectonic and Geologic Evolution of Southeast Asian Sea and Islands (Pt. 2), Volume 27: Geophysical Monograph, AGU, p. 23-56.

Udarbe-Walker, M.J.B., and Villanoy, C.L., 2001. Structure of potential upwelling areas in the Philippines. *Deep Sea Research I*, **48**: 1499-1518.

Urey, H.C., 1947. The thermodynamic properties of isotopic substances. *Journal of the Chemical Society*: 562-581.

Urey, H.C., Lowenstamm, H.A., Epstein, S., and McKinney, C.R., 1951. Measurements of paleotemperatures and temperatures of the Upper Cretaceous of England, Denmark, and the Southeastern United States. *Geological Society of America Bulletin*, **62**: 399-416.

Voelker, A.H.L., 1999. Zur Deutung der Dansgaard-Oeschger Ereignisse in ultra-hochauflöesnden Sedimentprofilen aus dem Europäischen Nordmeer. *Berichte-Reports, Inst. für Geowiss., Universität Kiel*, **9**: 278.

Wang, P., Prell, W.L., Blum, P., and Leg 184 Shipboard Scientific Party, 2000. Proceedings of the Ocean Drilling Program, Initial Reports. College Station , TX, Ocean Drilling Program, 1-77 p.

Wang, L., 2000. Isotopic signals in two morphotypes of *Globigerinoides ruber* (white) from the South China Sea: implications for monsoon climate change during th last glacial cycle. *Palaeogeography, Palaeoclimatology, Palaeoecology*, **161**: 381-394.

Wang, L., Sarnthein, M., Erlenkeuser, H., Grimalt, J., Grootes, P., Heilig, S., Ivanova, E., Kienast, M., Pelejero, C., and Pflaumann, U., 1999a. East Asian monsoon climate during the Late Pleistocene: high-resolution sediment records from the South China Sea. *Marine Geology*, **156**: 245-284.

Wang, L., Sarnthein, M., Erlenkeuser, H., Grootes, P.M., Grimalt, J.O., Pelejero, C., and Linck, G., 1999b. Holocene variations in asian monsoon moisture: A bidecadal sediment record from the South China Sea. *Geophysical Research Letters*, **26**(18): 2889-2892.

Wang, P., 1999. Response of western Pacific marginal seas to glacial cycles: paleoceanographic and sedimentological features. *Marine Geology*, **156**: 5-39.

Webster, P.J., 1987. The elementary monsoon. *in* Fein, J.S., and Stephens, P.L., eds., Monsoons: New York, John Wiley & Sons, p. 3-32.

Wiesner, M., Wang, Y., and Wong, H.-K., 1994. Ash layers in the South China Sea (Sonne-95 Cruise). *Preliminary Report on Sonne-95 Cruise "Monitor Monsoon" to the South China Sea*, **68**: 195-196.

Wiesner, M.G., and Wang, Y., 1996. Dispersal of the 1991 Pinatubo Tephra in the South China Sea. *in* Newhall, C.G., and Punongbayan, R.S., eds., Fire and mud: eruptions and lahars of Mount Pinatubo, Philippines: Quezon City, Philippine Institute of Volcanology and Seismology, p. 537-543.

Wiesner, M.G., Wang, Y., and Zheng, L., 1995. Fallout of volcanic ash to the deep South China Sea induced by the 1991 eruption of Mount Pinatubo (Phillipines). *Geology*, **23**(10): 885-888.

Wiesner, M.G., Zheng, L., Wong, H.K., Wang, Y., Chen, W., Schäfer, P., Honjo, S., and Depetris, P.J., 1996. Fluxes of Particulate Matter in the South China Sea. *in* Ittekott, V., ed., Particle Fluxes in the Ocean, John Wiley & Sons Ltd, p. 293-312.

Wyrtki, K., 1961. Physical oceanography of the southeast Asian waters. La Jolla, California, Neyenesch Printers, San Diego, 195 p.

4. Results (articles published, in press and submitted)

4.1: Toba ash layers in the South China Sea: Evidence of contrasting wind directions during eruption ca. 74 ka (C. Bühring, M. Sarnthein, Leg 184 Shipboard Scientific Party)

Toba ash layers in the South China Sea: Evidence of contrasting wind directions during eruption ca. 74 ka

Christian Bühring
Michael Sarnthein
Institut für Geowissenschaften, Universität Kiel, Germany
Leg 184 Shipboard Scientific Party

ABSTRACT

Two cores from the southern South China Sea contain discrete ash layers that mainly consist of rhyolithic glass shards. On the basis of the SPECMAP time scale, the ash layers were dated to ca. 74 ka, the age of the youngest Toba eruption in northern Sumatra. This link is supported by the chemical composition of the glass, which is distinct from volcanic glass supplied from the Philippines and the northern South China Sea, but is almost identical with the chemistry of the Toba ash. The youngest Toba ash layers in the South China Sea expand the previously known ash-fall zone over more than 1800 km to the east. The dispersal of ashes from Sumatra in both western and eastern directions indicates two contrasting wind directions and suggests that (1) the Toba eruption probably happened during the Southeast Asian summer monsoon season, and (2) the volume of erupted magma was larger than previously interpreted.

Keywords: Toba, South China Sea, deep-sea sediments, monsoon.

INTRODUCTION

The youngest Toba eruption, ca. 74 ka, is considered to be the largest eruption of the late Pleistocene (Chesner et al., 1991), the impact of which on global climate has been discussed (Rampino, 1993; Rampino and Self, 1992; Kerr, 1996). Until now, silicic ash layers and dispersed glass shards from the eruption of the Toba caldera in northern Sumatra have been reported from Malaysia, the northeastern Indian Ocean (Ninkovich, 1979; Ninkovich et al., 1978; Dehn et al., 1991; Pattan et al., 1999), the Indian subcontinent (Shane et al., 1995; Westgate et al., 1998), and the Arabian Sea (Schulz et al., 1998), i.e., only from areas west of the Toba caldera on Sumatra, except for one occurrence in Malaysia (Fig. 1). Here we report newly discovered ash layers in sediment cores 17961-2 and 17962-4 in the southern South China Sea; these ash layers are identified as youngest Toba ash by stratigraphic and geochemical analyses. These new Toba ash falls occur more than 1800 km east of the eruption caldera and may imply contrasting wind directions during the time of eruption.

REGIONAL SETTING

Sediment samples for this study are from gravity core 17961-2 (08°30.4′N, 112°19.9′E, 1968 m water depth) and piston core 17962-4 (07°10.9′N, 112°04.9′E, 1969 m water depth; Fig. 1), both retrieved from elevated sites in the southern part of the Dangerous Grounds during the RV *Sonne-95* cruise (Sarnthein et al., 1994). In harmony with the geomorphology, the parasound profiles across these sites (Sarnthein et al., 1994) reveal a clear hemipelagic sediment drape, devoid of any traces of turbidite injections. In this region, the hemipelagic terrigenous sediment is mainly derived from the Mekong discharge during sea-level highstands and from the Sunda Shelf during sea-level lowstands (Wang et al., 1999). Sedimentation rates for core 17961-2 range from 7 cm/k.y. during the Holocene to 11 cm/k.y. during glacial and semiglacial times (oxygen isotope stages 2–4) (Wang et al., 1999).

SAMPLES AND METHODS

In both sediment cores the ash layers were first recorded as outstanding magnetic-susceptibility spikes (Sarnthein et al., 1994). Their similar sequence and amplitudes allowed a clear stratigraphic correlation of the ash layers between the two cores.

In core 17961-2, the 2.5-cm-thick, light grayish ash layer occurs at 781–783.5 cm depth, with a sharp lower and a slightly undulating upper boundary; there is no further impact of bioturbational mixing. A similar, 3.5-cm-thick, light grayish ash layer is found in core 17962-4 at 1075.5–1079 cm. Its basal contact on the host sediment is sharp, and its top is slightly undulating. On the basis of (1) this visual inspection, (2) almost identical magnetic susceptibility curves, and (3) the spatial proximity of the two sites, the ash layers in the two cores most probably have the same age and origin.

Ash samples from both cores were wet sieved over a 63 μm mesh sieve and dry sieved over a 150 μm mesh sieve. Both grain-size fractions consist almost entirely of glass shards. The ash particles were cast in epoxy resin, cut, and polished to expose their interior.

Analyses of major oxides were made at the Institut für Geowissenschaften, Kiel University, with a Cameca CAMEBAX electron-beam microprobe, using an accelerating voltage of 14–15 kV and an electron-beam current of 15 nA, with the beam defocused to 6 μm width.

Microprobe analyses were focused on the center of individual, fresh, glass shards with well-exposed interiors. We analyzed 20 glass shards from the ash layer in core 17961-2 and 18 glass shards from the ash in core 17962-4.

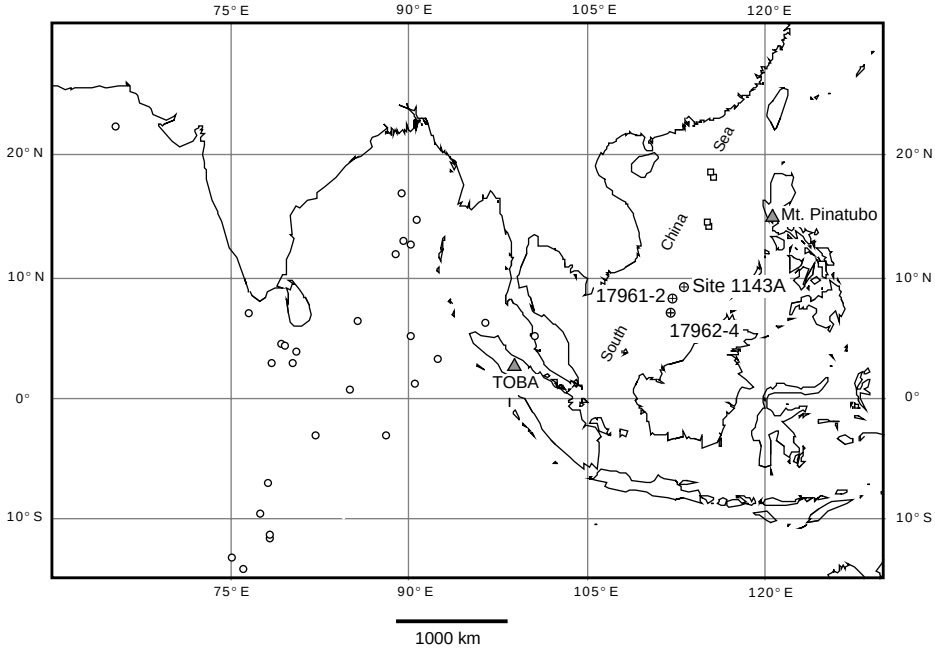

Figure 1. Occurrences of Toba ash in deep-sea cores and on Malaysian Peninsula (open circles), and in South China Sea (crossed circles). Squares show cores with other ash layers, and position of sediment trap with Pinatubo ash.

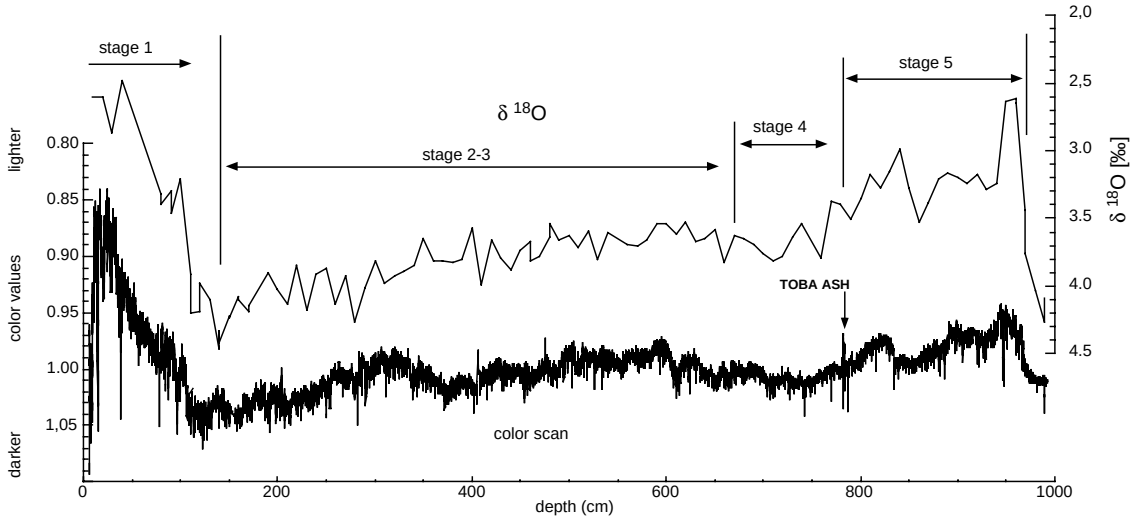

Figure 2. Benthic oxygen isotope curve (*C. wuellerstorfi*) marine isotope stages from Wang et al. (1999) and ultrahigh-resolution color-scan curve of core 17961-2. Ash layer appears as distinct spike toward lighter values at stage 4-5 transition.

Each individual grain was analyzed at least twice, but most grains were analyzed three times for calculating the means. Analytical totals range between 94 and 98 wt%; the balance consists of elements not analyzed and H_2O from secondary hydration.

AGE CONTROL

In core 17961-2, the age control is based on the 10-cm-spaced benthic and planktonic $\delta^{18}O$ records of Wang et al. (1999), which closely parallel our ultrahigh-resolution (0.35 mm) color-scan curve (Fig. 2). Here the ash layer forms a well-defined light color excursion at 781–783.5 cm depth, right at the oxygen isotope stage 4-5 boundary. According to the SPECMAP-based age model of Wang et al. (1999), the ash was dated to ca. 74 ka. This age matches previous age estimates for the Toba eruption, deduced from various dating methods such as $^{40}K/^{40}Ar$ dating (73 500 ± 3000 yr B.P.; Ninkovich et al., 1978), $^{39}Ar/^{40}Ar$ dating (73 000 ± 4000 yr B.P.; Chesner et al., 1991), SPECMAP orbital dating of other core records (73 910 ± 2590 yr B.P.; Rampino and Self, 1992) and especially from geomagnetic polarity records (75 000 yr B.P.; Westgate et al., 1998) and fission-track dating of glass shards (79 000 ± 8000 yr B.P.; Westgate et al., 1998).

In core 17962-4, the age control is solely based on the intercore stratigraphic correlation of the magnetic susceptibility records.

A similar ash layer has also been identified slightly farther east, in Ocean Drilling Program Site 1143, Hole A (Leg 184 Shipboard Scientific Party); according to a correlation based on magnetic susceptibility and color-reflectance records, it occurs at the same stratigraphic position as the Toba ash in our cores.

MICROSCOPIC DESCRIPTION OF ASH COMPOSITION

Under the microscope, the composition of the ash layers in cores 17961-2 and 17962-4 is almost identical. The grains consist almost entirely of colorless glass shards and only minute amounts of mineral grains such as biotite and feldspar. The glass shards are optically isotropic and thin walled; they have a platy shape (Fig. 3). Bubble-wall-shard forms dominate; blocky forms are rare. Colored (i.e., brown) volcanic glass shards are absent. The glass appears fresh and without any alteration. Maximum grain sizes of the shards reach 500 μm; average grain sizes are about 100 μm.

GEOCHEMISTRY OF THE GLASS SHARDS

The glass shards have the composition of high-silica rhyolites; their SiO_2 contents are 75–78 wt%, and they have high alkali averages of 7.4–7.6 wt%. They show very little variation both within and between samples. The chemical composition of the shards from the ash layers in both cores is nearly identical (Table 1) and supports the assumption of an identical origin.

DISCUSSION

Two different volcanic regions qualify as potential source areas for the ash layers in the southern South China Sea, the Philippine Archipelago, more than 1000 km to the east, and the western Indonesian islands, about 1600–1800 km to the west.

Modern volcanic glass from Mount Pinatubo on the Philippines (Wiesner et al., 1995; Luhr and Melson, 1996; Pallister et al., 1992) and from Pleistocene ash layers (oxygen isotope stages 2 and 4, 26–42 ka, 61–64 ka, respectively; Chen and Zhou, 1992) in deep-sea cores from the northern South China Sea of unknown, but probably also Philippine or Taiwanese (Zhou et al., 1992) origin, were analyzed by microprobe. Their chemistry clearly differs from that of the ash layers in cores 17961-2 and 17962-4 (Fig. 4). The Pinatubo glass shards have distinctively

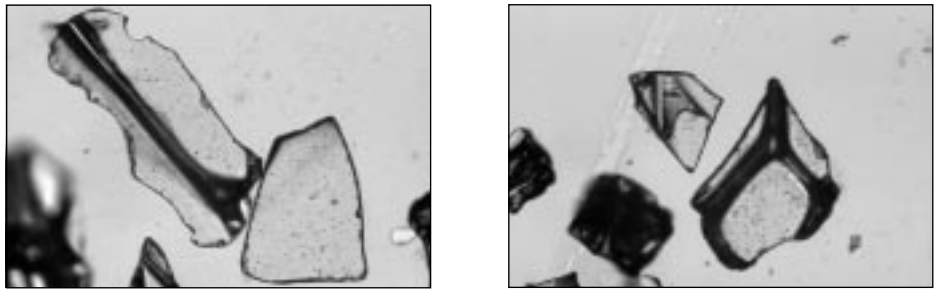

Figure 3. Digital images (A, B) of platy and bubble-wall volcanic glass shards from ash layer in core 17962-4.

TABLE 1. CHEMICAL COMPOSITIONS OF SHARDS

Core	SiO_2	Al_2O_3	TiO_2	FeO	MnO	MgO	CaO	Na_2O	K_2O	Sum	n
17961-2	78.04 ± 0.24	12.49 ± 0.06	0.08 ± 0.02	0.85 ± 0.05	0.07 ± 0.02	0.06 ± 0.01	0.78 ± 0.01	2.66 ± 0.08	4.86 ± 0.05	100	20
17962-4	78.05 ± 0.29	12.52 ± 0.05	0.05 ± 0.01	0.84 ± 0.04	0.07 ± 0.02	0.06 ± 0.01	0.77 ± 0.02	2.73 ± 0.07	4.85 ± 0.05	100	18

higher CaO and lower SiO_2 contents (Fig. 4A) than the ashes from our cores.

Furthermore, the glass particles from cores 17961-2 and 17962-4 display much higher K_2O contents (Fig. 4B). The other ashes from the northern South China Sea show even greater differences in the CaO content (Fig. 4A) as well as in K_2O concentrations (Fig. 4B) and decidedly lower SiO_2 values. Because of these differences, the ashes in cores 17961-2 and 17962-4 can not be assigned a Philippine origin.

The ash layers in cores 17961-2 and 17962-4 are coeval with the Toba eruption on northern Sumatra, Indonesia, at the oxygen isotope stage 4-5 boundary. Likewise, the chemical composition of the glass shards from the South China Sea (Fig. 5) closely matches the published data for volcanic glass from the latest Toba eruption, sampled from the Toba caldera (Westgate et al., 1998), the coeval Toba ash layer A at Ocean Drilling Program Site 758 (Westgate et al., 1998; Dehn et al., 1991), and at various sites in the eastern and central Indian Ocean (Rose and Chesner, 1990; Pattan et al., 1999) and the Arabian Sea off Pakistan (Schulz et al., 1998). This striking similarity applies to the Na, K, Fe, and (high) SiO_2 contents (Fig. 5). Minor deficits in Na_2O and K_2O are insignificant, because they are probably linked to differences in the analytical procedures and instrumental facilities used. For example, Na_2O values that are slightly lower than other published data may result from Na volatilization under the electron beam, a depletion that in turn produces a minor enrichment in SiO_2 and FeO.

In summary, both the age and chemistry confirm the youngest Toba eruption as the most likely origin of the ash layers in our two South China Sea cores.

Rose and Chesner (1990) calculated a magma volume of more than 2800 km^3 for the Toba eruption, including a volume of 800 km^3 of massive ash falls covering 1% of the Earth's surface. The Toba caldera does not provide any evidence of the corresponding high-reaching (+45 km) Plinian eruption column during that time (Rose and Chesner, 1987; Chesner, 1998). However, the Toba eruption cloud may still have reached heights well above the tropical troposphere (Rampino and Self, 1992) and even higher stratospheric levels of 32–40 km through extreme temperature-induced buoyancy (Woods and Wohletz, 1991).

For this youngest Toba eruption, Ledbetter and Sparks (1979) estimated a total duration of 9–14 days. This interval may have occurred either during winter or during summer. Today the climate of the tropics in Southeast Asia is governed by a semiannual circulation change. In the lower troposphere, we encounter a circulation change from a northeasterly flow in winter to westerly to southwesterly winds over the Indian Ocean (Krishnamurti, 1987) and the South China Sea during summer monsoon (Kalnay et al., 1996; Shaw and Chao, 1994). At the time of its onset, the westerly jet stream in the upper troposphere abruptly retreats to a location north of the Himalayas while an easterly jet stream is established over the Indian Ocean (Dümenil and Bauer, 1998). This so-called tropical easterly jet has its strongest wind velocities between 200 and 100 hPa in the region of 5 to 20°N (Dümenil and Bauer, 1998).

Most Toba ash deposits hitherto known occur to the west and northwest of Sumatra. Here they

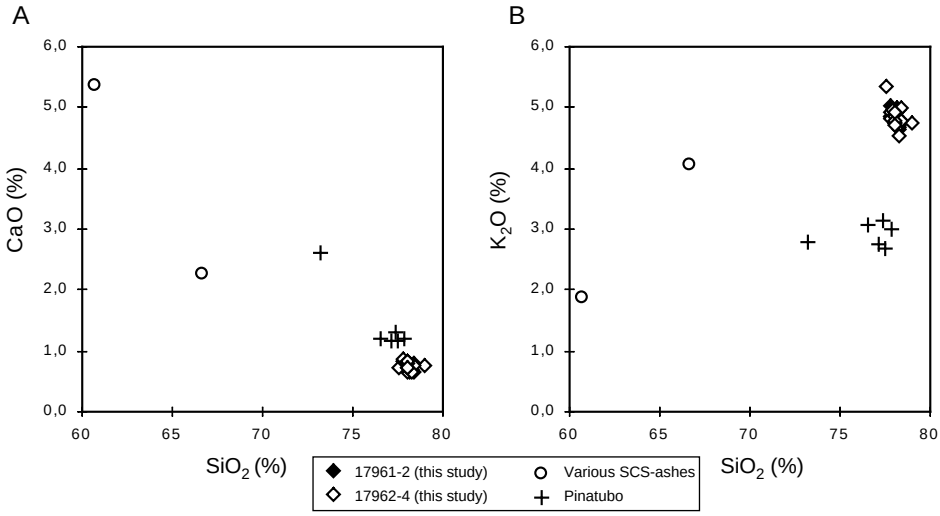

Figure 4. Microprobe data of glass shards in cores 17961 and 17962, compared to published data for Mount Pinatubo ashes (Wiesner et al., 1995; Pallister et al., 1992; Luhr and Melson, 1996) and other volcanic glasses in deep-sea cores from South China Sea (SCS) (Chen and Zhou., 1992). A: SiO_2 vs. CaO. B: SiO_2 vs. K_2O. All analyses recalculated to 100% on volatile-free basis.

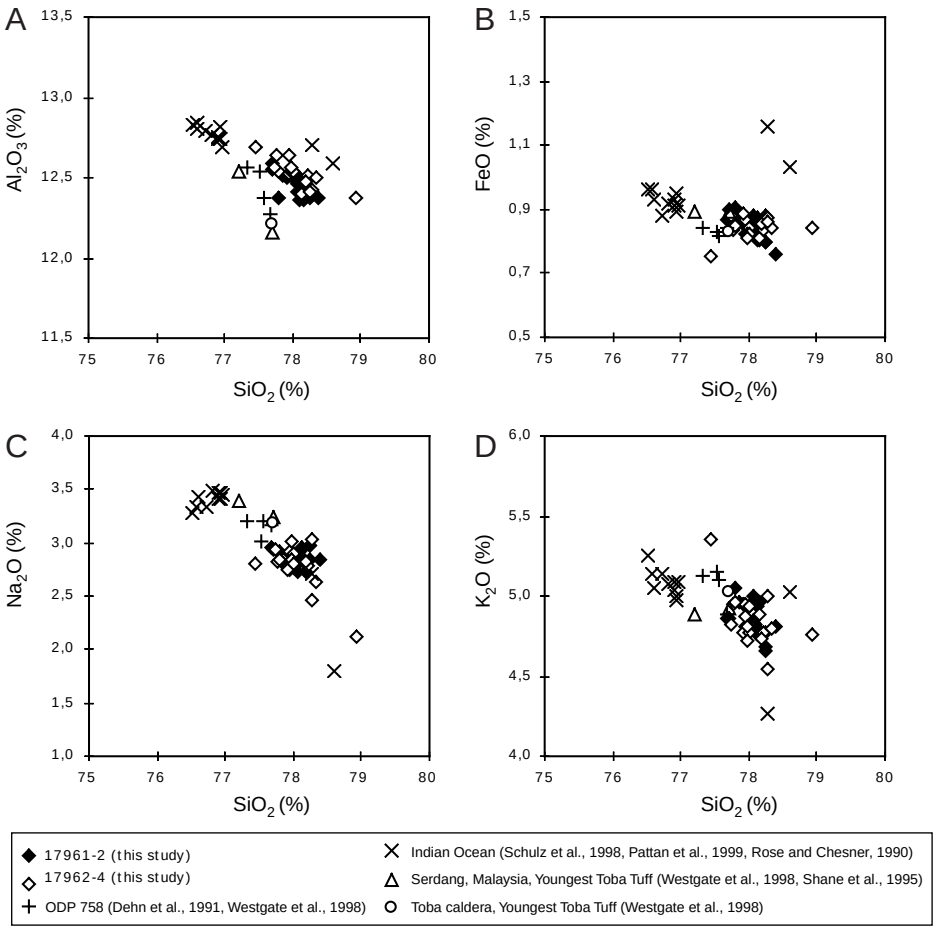

Figure 5. Percentage of major elements (on volatile-free basis) determined by microprobe analyses. Glass shards from cores 17961 and 17962 are compared to published data for Toba ashes in deep-sea cores. A: SiO_2 vs. Al_2O_3. B: SiO_2 vs. FeO. C: SiO_2 vs. Na_2O. D: SiO_2 vs. K_2O. Note strong similarity between FeO (B) and K_2O (D) values of our ash particles and values for Toba caldera.

are linked to the prevailing jet stream over the region (Schulz et al., 1998) during summer, but not to the winter-monsoon wind, which blows in the opposite direction.

This scenario is now enlarged and supplemented twice by our findings about the abundant Toba ash that has also been spread far east, into the South China Sea. On the one hand, the previous estimates of the erupted ash volume must be enlarged significantly, perhaps doubled. On the other hand, the eastward spreading of the ash cloud into the South China Sea requires westerly and/or southwesterly winds that only occur during the summer monsoon. Hence, a major eruption with ash production must have occurred during the Northern Hemisphere summer, in support of the outlined jet-stream regime inferred from the Toba ash sites in the Gulf of Bengal and off Pakistan (Fig. 1).

In summary, we suggest that at the oxygen isotope stage 4-5 boundary upper tropospheric easterly winds spread Toba ash particles from a high-reaching eruption cloud across the Indian Ocean. At the same time mid- to low-level tropospheric southwesterly summer monsoon winds transported ash from both the lower parts of the eruption column and coignimbrite clouds eastward over the Sunda Shelf into the South China Sea.

On the basis of the correlation of Zielinsky et al. (1996), the youngest Toba eruption may have been within the onset of the 1000 yr cold spell prior to Dansgaard-Oeschger event 19. An approximate doubling of the volume of the Toba eruption as suggested by our new findings may be in support of its potential catastrophic influence on climate change at the onset of the oxygen isotope stage 4 glacial. However, in line with Kerr (1996), this conclusion is not mandatory, because a similar cold spell also preceded Dansgaard-Oeschger event 20, here without a Toba-style eruption, and because the subsequent Dansgaard-Oeschger interstadial 19 was as warm as Dangaard-Oeschger interstadial 20 (Zielinsky et al., 1996).

CONCLUSIONS

Rhyolithic ash layers as much as 3.5 cm thick in two cores from the southern South China Sea were first identified as ash falls from the youngest Toba eruption. The ash layers were deposited at the oxygen isotope stage 4-5 boundary ca. 74 ka, on the basis of benthic and planktonic $\delta^{18}O$ stratigraphy and the SPECMAP orbital time scale, supplemented by magnetic susceptibility and ultrahigh-resolution color-scan curves for intercore stratigraphic correlation. The age estimated precisely matches the date of the great Toba eruption on Sumatra. Likewise, the chemical composition of dominating high-silica glass shards (78 wt% SiO_2 and alkali averages of 7.6–7.7 wt%) closely resembles the composition of youngest Toba ash layers, but differs significantly from any ash falls originating from the Philippine volcanoes in the east.

The new findings about the dispersal of abundant Toba ash to the east require significantly increased volume estimates of erupted Toba ash and perhaps imply a more extended eruption during summer.

ACKNOWLEDGMENTS

We appreciate the careful supervision of microprobe analyses by D. Ackermann, B. Mader, and S. Fretzdorff, and the generous initial funding of our "Monitor Monsoon" project by the German Federal Minister of Education and Research and later by the German Science Foundation in Bonn.

REFERENCES CITED

Chen, W., and Zhou, F., 1992, A study of volcanic glass in northern South China Sea during the last 100 ka, *in* Jin, X., et al., eds., Marine geology and geophysics of the South China Sea: Beijing, China Ocean Press, p. 174–178.

Chesner, C. A., 1998, Petrogenesis of the Toba Tuffs, Sumatra, Indonesia: Journal of Petrology, v. 39, p. 397–438.

Chesner, C. A., Rose, W. I., Deino, A., Drake, R., and Westgate, J. A., 1991, Eruptive history of Earth's largest Quaternary caldera (Toba, Indonesia) clarified: Geology, v. 19, p. 200–203.

Dehn, J., Farrell, J. W., and Schmincke, H.-U., 1991, Neogene tephrochronology from Site 758 on northern Ninetyeast Ridge: Indonesian arc volcanism of the Past 5 Ma, *in* Weissel, J., Peirce, J., Taylor, E., Alt, J., et al., Proceedings of the Ocean Drilling Program, Scientific results, Volume 121: College Station, Texas, Ocean Drilling Program, p. 273–295.

Dümenil, L., and Bauer, H.-S., 1998, The tropical easterly jet in a hierarchy of GCMs and in reanalysis: Reports of the Max-Planck-Institute for Meteorology, v. 247 (http://www.mpimet.mpg.de/deutsch/Sonst/Reports/HTMLReports/247/).

Kalnay, E., Kanamitsu, M., Kistler, R., Collins, W., Deaven, D., Gandin, L., Iredell, M., Saha, S., White, G., Woollen, J., Zhu, Y., Chelliah, M., Ebisuzaki, W., Higgins, W., Janowiak, J., Mo, K. C., Ropelewski, C., Wang, J., Leetmaa, A., Reynolds, R., Jenne, R., and Joseph, D., 1996, The NCEP/NCAR 40-Year Reanalysis Project: American Meteorological Society Bulletin, v. 77, p. 437–471.

Kerr, R. A., 1996, Volcano-ice age link discounted: Science, v. 272, p. 817.

Krishnamurti, T. N., 1987, Monsoon models, *in* Fein, J. S., and Stephens, P. L., eds., Monsoons: New York, John Wiley & Sons, p. 467–522.

Ledbetter, M., and Sparks, R. S. J., 1979, Duration of large-magnitude explosive eruptions deduced from graded bedding in deep-sea ash layers: Geology, v. 7, p. 240–244.

Luhr, J. F., and Melson, W. G., 1996, Mineral and glass compositions in June 15, 1991, pumices: Evidence for dynamic disequilibrium in the dacite of Mount Pinatubo, *in* Newhall, C. G., and Punongbayan, R. S., eds., Fire and mud: Eruptions and lahars of Mount Pinatubo, Philippines: Quezon City, Philippine Institute of Volcanology and Seismology, p. 733–749.

Ninkovich, D., 1979, Distribution, age and chemical composition of tephra layers in deep-sea sediments off western Indonesia: Journal of Volcanology and Geothermal Research, v. 5, p. 67–86.

Ninkovich, D., Shackleton, N. J., Abdel-Monem, A. A., Obradovich, J. D., and Izett, G., 1978, K-Ar age of the late Pleistocene eruption of Toba, north Sumatra: Nature, v. 276, p. 574–577.

Pallister, J. S., Hoblitt, R. P., and Reyes, A. G., 1992, A basalt trigger for the 1991 eruptions of Pinatubo volcano?: Nature, v. 356, p. 426–428.

Pattan, J. N., Shane, P., and Banakar, V. K., 1999, New occurrence of youngest Toba tuff in abyssal sediments of the central Indian Basin: Marine Geology, v. 155, p. 243–248.

Rampino, M. R., 1993, Climate-volcanism feedback and the Toba eruption of ≈74,000 years ago: Quaternary Research, v. 40, p. 269–280.

Rampino, M. R., and Self, S., 1992, Volcanic winter and accelerated glaciation following the Toba super-eruption: Nature, v. 359, p. 50–52.

Rose, W. I., and Chesner, C. A., 1987, Dispersal of ash in the great Toba eruption, 75 ka: Geology, v. 15, p. 913–917.

Rose, W. I., and Chesner, C. A., 1990, Worldwide dispersal of ash and gases from Earth's largest known eruption: Toba, Sumatra, 75 ka: Palaeogeography, Palaeoclimatology, Palaeoecology, v. 89, p. 269–275.

Sarnthein, M., Pflaumann, U., Wang, P. X., and Wong, H. K., 1994, Preliminary report on *SONNE-95* cruise "Monitor Monsoon" to the South China Sea: Geologisch-Paläontologisches Institut Universität Kiel, Berichte-Reports, v. 68, p. 225.

Schulz, H., Rad, U. V., and Erlenkeuser, H., 1998, Correlation between Arabian Sea and Greenland climate oscillations of the past 110,000 years: Nature, v. 393, p. 54–57.

Shane, P., Westgate, J., Williams, M., and Korisettar, R., 1995, New geochemical evidence for the youngest Toba Tuff in India: Quaternary Research, v. 44, p. 200–204.

Shaw, P.-T., and Chao, S.-Y., 1994, Surface circulation in the south China Sea: Deep-Sea Research, v. 41, p. 1663–1683.

Wang, L., Sarnthein, M., Erlenkeuser, H., Grimalt, J., Grootes, P., Heilig, S., Ivanova, E., Kienast, M., Pelejero, C., and Pflaumann, U., 1999, East Asian monsoon climate during the late Pleistocene: High-resolution sediment records from the South China Sea: Marine Geology, v. 156, p. 245–284.

Westgate, J. A., Shane, P. A. R., Pearce, N. J. G., Perkins, W. T., and Korisettar, R., 1998, All Toba tephra occurrences across Peninsular India belong to the 75,000 yr B.P. eruption: Quaternary Research, v. 50, p. 107–112.

Wiesner, M. G., Wang, Y., and Zheng, L., 1995, Fallout of volcanic ash to the deep South China Sea induced by the 1991 eruption of Mount Pinatubo (Phillipines): Geology, v. 23, p. 885–888.

Woods, A. W., and Wohletz, K., 1991, Dimensions and dynamics of co-ignimbrite eruption columns: Nature, v. 350, p. 225–227.

Zielinsky, G. A., Mayewski, P. A., Meeker, L. D., Whitlow, S., and Twickler, M. S., 1996, Potential atmospheric impact of the Toba mega-eruption ~71 000 years ago: Geophysical Research Letters, v. 23, p. 837–840.

Zhou, F., Yun, Z., Feng, C., and Guo, L., 1992, Deposition process and character of the deep-water sediment in the northern South China Sea, in Jin, X., et al., eds., Marine geology and geophysics of the South China Sea: Beijing, China Ocean Press, p. 190–196.

Manuscript received September 8, 1999
Revised manuscript received December 3, 1999
Manuscript accepted December 14, 1999

4.2: Holocene ultrahigh-resolution color records of monsoon in hemipelagic sediments of the northern South China Sea (C. Bühring and M. Sarnthein)

Holocene ultrahigh-resolution color records of monsoon in hemipelagic sediments of the northern South China Sea

Christian Bühring, Michael Sarnthein

Institut für Geowissenschaften, Universität Kiel, 24118 Kiel, Germany

17.01.2002 Draft

Submitted to Paleoceanography

Contents

Abstract

Sediment colors from the northern South China Sea off Hong Kong (core 17940) provide a unique time series of monsoon-controlled sediment deposition spanning the last 11,000 years. Both a sampling resolution of < 0.3 mm and sedimentation rates of 40-90 cm/kyr lead to a theoretical time resolution of 0.3-0.7 years, enabling us to detect centennial and sub-decadal-scale climate cycles in the non-laminated sediment section despite of bioturbational mixing. The intensity of the blue color records the portion of clay enriched in TOC, and thus the strength of the wet / summer monsoon. The intensity of red documents the portion of reddish stained loess dust and thus the strength of the dry / winter monsoon. Suborbital climate periodicities (of both the color codes and the decadal-scale resolution $\delta^{18}O$ curve) are dominated by a 950-year cycle which lags the GISP2 temperature signal by 250-400 years and clearly documents the global linkages of monsoon variability to northern high-latitude climate components. Multi- to semicentennial periodicities comprise the 200-year deVries/Suess and the 90-105-year Gleissberg cycles of solar irradiance. 20/24-year (Hale) and close-to-11-year (Schwabe or NAO) periodicities, and ENSO cycles of 3-8 years reveal prominent, probably internal climate forcings in the high-frequency range of the color records.

Introduction

The monsoon system which primarily controls the climate in South East Asia is characterized by the strong seasonal alteration of summer and winter monsoon winds (Zhang and Liu, 1992). During summer the heating of the Asian land surface relative to the ocean generates low air-pressure over land, leading to an inflow of moist monsoonal air inland. The resulting rainfalls during summer form the main source of precipitation in southern Asia and China (Wei and Gasse, 1999). Dry phases with markedly reduced summer rain and enhanced dust (loess) deposition in the past were mainly linked to glacial (cold) stages and cold spells in the northern hemisphere such as short-term Heinrich events (Porter and An, 1995; L. Wang et al., 1999a) and the Younger Dryas (Kudrass et al., 1991). During interglacial (warm) stages and

interstadials an increased summer monsoon circulation provided more moisture onto the continent, leading to soil formation and increased fluvial runoff (L. Wang et al., 1999a, b). Accordingly, high-frequency changes in dust flux recorded in loess profiles of central China during marine isotope stage (MIS) 3 were probably linked to the rapid succession of cold and warm events (An and Porter,1997).

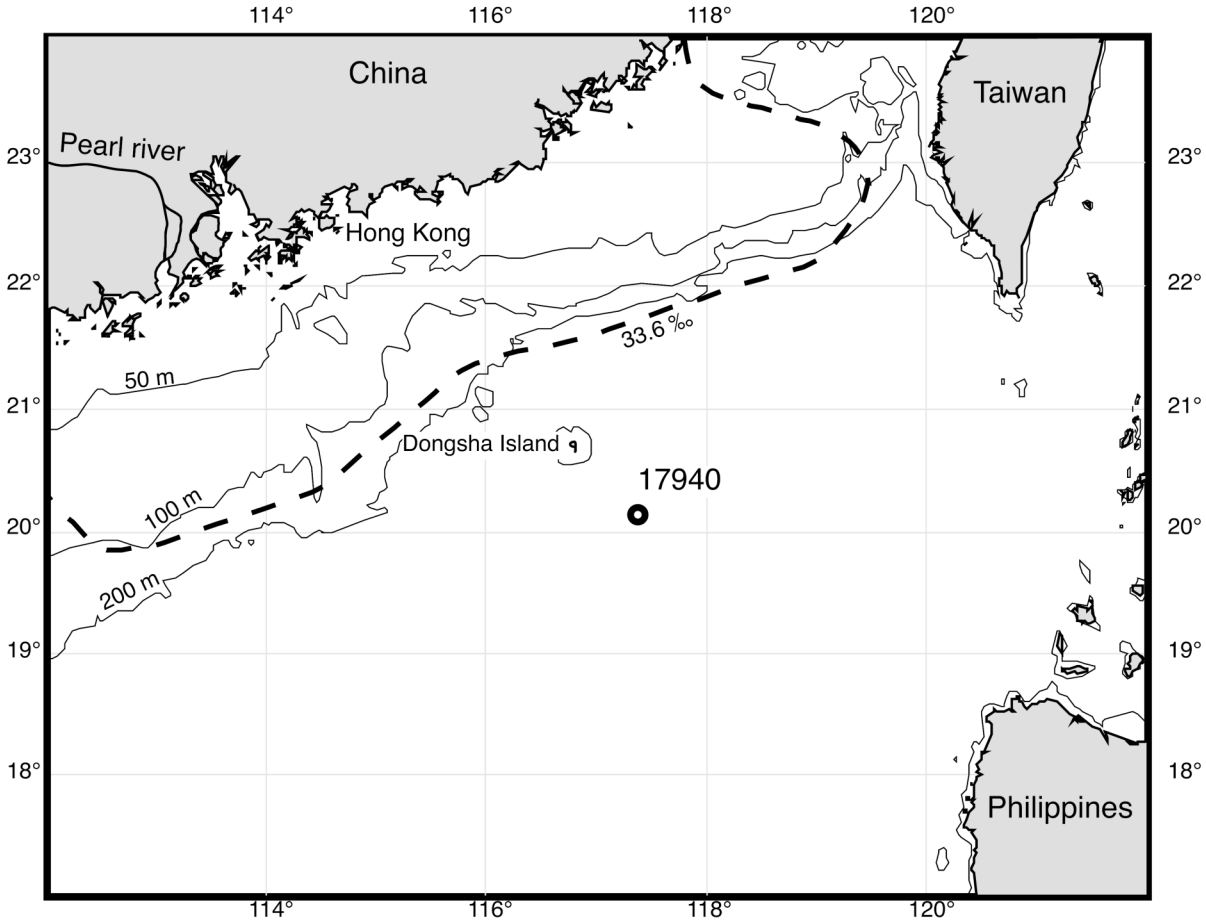

Figure 1. Northern South China Sea with core position of 17940-2. 50-m isobath corresponds to a coast line at 11500 yr BP (Hanebuth et al., 2000). At 10,000 yr BP the shoreline had approximately reached the modern position (L. Wang et al., 1999). The freshwater plume of the Pearl River mouth west of Hong Kong, the most important source of fluvial sediment, is shown by a stippled line (Japan Hydrographic Association, 1978; modified).

Few published paleoceanographic records from this region provide a time resolution sufficient to resolve sub-millennial-scale to decadal variations in local ocean circulation and in the evolution of the East Asian Monsoon System. In this context, gravity core 17940-2 (20°07´ N, 117°23´ E, 1727 m water depth), retrieved from a thick, hemipelagic sediment drape (Sarnthein et al., 1994) on the northern continental slope of the South China Sea (Figure 1), offers

an unprecedented opportunity to reconstruct Holocene monsoonal variations on decadal to centennial scales.

This core already served for various paleoclimate studies of the past 40 kyr (L. Wang et al., 1999a, b, c; Jian et al, 1999; Pflaumann and Jian, 1999; Sun and Li, 1999), based on the faunal composition of benthic and planktonic foraminifera, carbon and oxygen isotope ratios, pollen, charcoal, clay content and siliciclastic grain sizes. These proxies indicate that the Holocene monsoon climate was highly variable, possibly forced by variations in ocean thermohaline circulation and solar activity (L. Wang, 1999a, b).

It is the main objective of the present study (1) to uncover the whole spectrum of high-frequency climate oscillations, (2) to establish whether, and to what degree, these high-frequency fluctuations in atmospheric and oceanic circulation persist over the Holocene, and (3) to better constrain their possible forcings.

Methods and samples

Methods

To investigate variations in sediment deposition and its potential climatic controls, we employed high-resolution sediment color analysis on digital images, measuring the relative intensity of light reflected from the sediment in three different color bands. This method further develops on previous techniques for generating non-destructive high-resolution color records of sediment properties (Cortijo et al., 1995; Hughen et al., 1996). In contrast to common single-point measurements (Chapman and Shackleton, 2000; Ortiz et al., 1999a) performed by spectrophotometers (e.g. by Minolta CM2002) our digital color video camera images provide quasi-continuous data sets with theoretically unlimited resolution.

We compared these color records of the Holocene section in core 17940-2 with various conventional sediment records (% $CaCO_3$, % C_{org}, siliciclastic grain sizes). Special attention

was given to cyclicities which may serve as potential tracers of high-frequency changes in East Asian Monsoon intensity.

Data base

Of the fresh and smoothed sediment surface of the archive half in core 17940-2 (top 720 cm) we took digital images of 21.5 cm length (5 cm overlap at both the top and bottom) with a Hitachi color video camera. Our illumination system (Figure 2) follows the system described by Cortijo et al. (1995). However, we employed 4 neon glow lamps and, additionally, polarizing filters for the lamps and for the camera lens to eliminate direct reflections produced by a thin water film on the sediment surface. In this way distorting artifacts of a light cone were reduced to a neglectible minimum. Light conditions were kept constant during image acquisition, although minor gradual changes of light intensity are inevitable due to ageing of the lamps. Images of Kodak color control patches were used as calibration standards at the beginning and end of each core section.

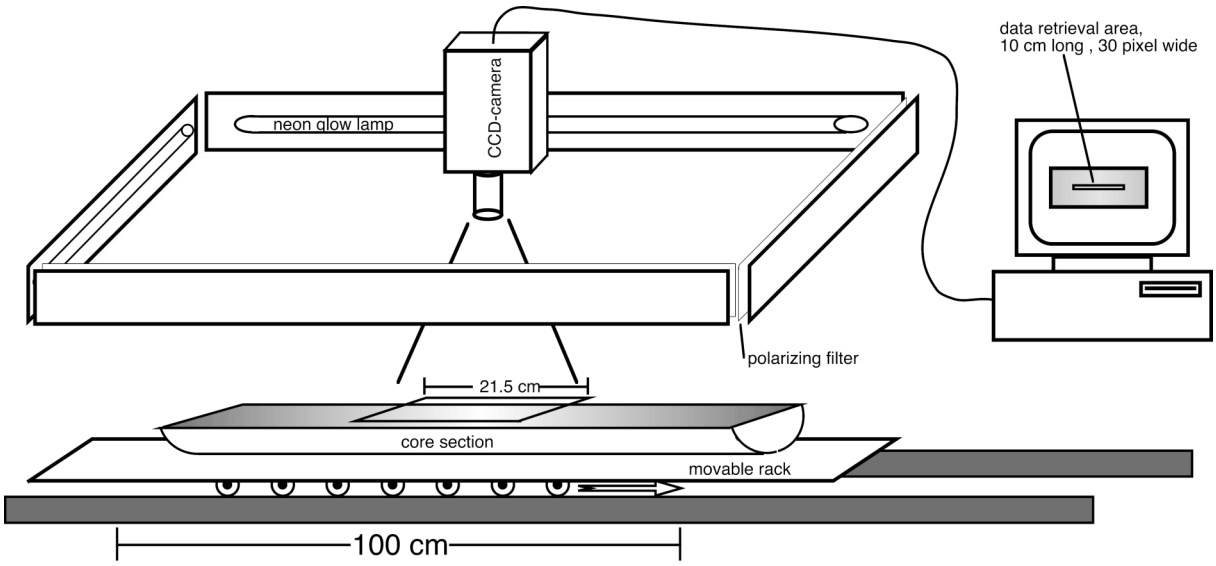

Figure 2. Camera and illumination setup. A Hitachi CCD color video camera rests on an adjustable camera stand in a dark room. Four neon glow lamps are mounted rectangularly above the split core section resting on a movable rack. Video images are digitized using a high-end video grabber card and saved as transportable image file format (TIFF)-files for further processing.

The sediment color reflectance was measured from the digital images using off-the-shelf image processing software (NIH-Image 1.6: Rasband, 1996). To avoid coring artifacts and marginal biasing by the light cone, color values for red, green and blue (R, G, B) of each pixel

were determined over an area 30 pixel (~≈0.8 cm) wide and 10 cm long in the center of each image. To reduce noise 30 pixels in width were averaged and the mean stored separately for each color channel. Color values are expressed on a conventional intensity scale ranging from 0 (white) to 255 (red, green or blue). This approach proved sufficient to minimize inevitable artefacts caused by lighting and lens distortions.

The scale of core depth is defined by a millimeter-ruler in the original image, with an absolute error of less than 0.5 mm. One pixel represents approximately 0.28 mm of sediment.

We applied to core 17940-2 the composite-depth (c.d.) scale as defined by L. Wang et al. (1999a), which is based on the match of $\delta^{18}O$ and $\delta^{13}C$ records in the giant spade-box core 17940-1 and gravity core 17940-2. Accordingly, the depth of 2.5 cm in core 17940-1 equals 0 cm in core 17940-2.

The 10-cm long R-G-B-data sets were manually trend corrected for remaining small illumination offsets by comparison to Kodak color standards (Kodak, 1997). The long-term trend in color intensity, a general tilt in the record induced by the gradual illumination change, was removed by slightly rotating each 10-cm data set until it fitted to the following set. After this careful correction the primary data for each color channel were concatenated into complete records for the core interval 0-722.5 cm (c.d.) (Figure 4), comprising ca. 24,000 data points for each color.

Origin of other proxy data records

The stable isotope ratios, $\delta^{18}O$ and $\delta^{13}C$, (Figure 4), were measured on tests of planktonic foraminifera *Globigerinoides ruber s.s. (white)* with a sampling resolution of 1-2 cm (L. Wang et al., 1999a). Silt modal grain sizes and clay contents are from L. Wang et al. (1999a and c). The magnetic susceptibility record (Figure 5) was measured on whole-core sections on board *RV Sonne* with a sampling resolution of 1 cm (Sarnthein et al., 1994). Low resolution (5 cm) carbonate (% $CaCO_3$) and total organic carbon (TOC) records (Figure 4) of core 17940-2 were described in Jian et al. (1999). In addition, a 1-cm resolution carbonate curve was gene-

rated for the interval 465-510 cm (c.d.) with a Micromeritics Coulomat at the Institut für Geowissenschaften, Universität Kiel, for detailed comparison (Figure 6) with our color reflectance records.

Techniques of Frequency Analysis

To facilitate spectral analysis, low-frequency trends in the reflectance record were initially removed by applying a 2.0-kyr high-pass filter on the data set to ensure that the residual higher-frequency variability was relatively undisturbed by non-climatic influences such as sea level rise in the earliest Holocene. A similar trend removal was previously employed to data from varved lake sediments (Rittenour et al., 2000) and dendrochronological time series (Cook et al., 1995).

Phase relationships between the GISP2 ice core $\delta^{18}O$-record and the records of core 17940 were determined with the ENVELOPE program (Schulz, 1996) which estimates the envelope of periodic signal components by a harmonic filtering algorithm, comparable to a band-pass filter.

Spectral analysis for the whole interval 2,200-11,600 yr BP was performed using Blackman/Tuckey method (BT, Blackman and Tukey, 1958) with the AnalySeries 1.2 program (Paillard et al., 1996) (Figure 8, Table 1).

To analyse the frequency spectra in this unevenly spaced time series we also used the a Lomb-Scargle Fourier transform (LSFT, Lomb 1976; Scargle, 1989; Schulz and Stattegger, 1997) approach in combination with a Welch-Overlapped-Segment-Averaging procedure (WOSA, Welch, 1967; Schulz and Stattegger, 1997). Red-noise background spectra of the time series were estimated by fitting a first-order autoregressive (AR1) process directly to the unevenly spaced time series (REDFIT 3.4, Schulz and Mudelsee, in press). The statistical significance of the spectral peaks was assessed from calculated significance levels based on Chi^2 –distribution and percentiles of the Monte Carlo ensembles (Schulz and Mudelsee, in press)

To assess and avoid influences from core intervals with a high trend potential even after high-pass filtering, and also to facilitate and accelerate computations, the complete record was cut into three segments (0-2,100, 2,100-5,500 and 6,000-11,600 years BP) for further spectral analyses (Figure 4).

To investigate the temporal modulation and evolution of periodicity signals in the record, a wavelet analysis (Torrence and Compo, 1998) was carried out on overlapping segments of the 2.0-kyr high-pass filtered record. The wavelet transform is a tool well suited to the study of multiscale, nonstationary processes occurring over finite spatial and temporal domains (Lau and Weng, 1995), such as in the color reflectance records. A non-orthogonal Morlet-wavelet function was employed for analysis of the data sets. The significance of the wavelet power spectra was tested against the red-noise background (Torrence and Compo, 1998) and shown as percent confidence level (Figure 9).

Age control and sedimentation rates

Core 17940-2 was dated by 40 AMS-^{14}C ages (L. Wang et al., 1999a) on monospecific samples of planktonic foraminifera *Globigerinoides ruber* (white) and/or *Globigerinoides sacculifer*. The ^{14}C-ages for the last 11,000 years were converted into calendar (cal.) years BP using the CALIB 4.1–program (Stuiver et al., 1998), tentatively employing a correction for a general reservoir age of 402 years in the South China Sea. The local large input of fluvial freshwater with an increased ^{14}C-age (Raymond and Bauer, 2001, and references therein) and various features of ocean circulation may possibly enlarge this ^{14}C reservoir age of planktonic foraminifera to an unknown value.

The color reflectance record of core 17940-2 spans the late deglaciation (13-11.6 ka), the Early Holocene (11.6-6.0 ka) and Late Holocene (6.0-0 ka).

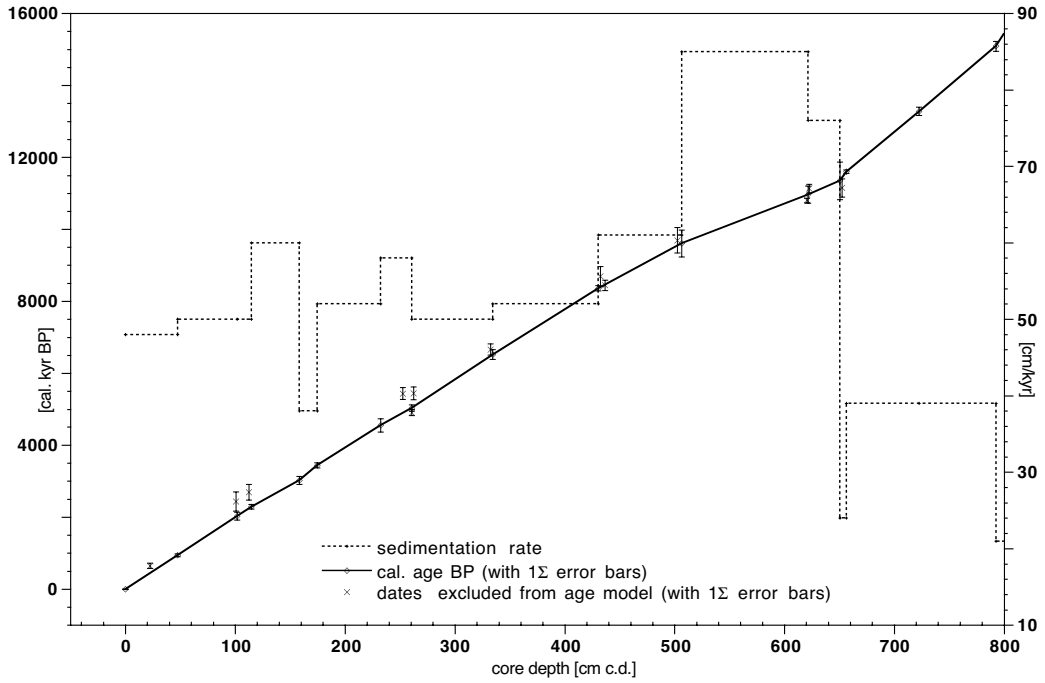

Figure 3. Age model and sedimentation rates and for the Holocene section in core 17940-2. ^{14}C dates of L. Wang et al. (1999a) were recalibrated to calendar years, using the CALIB 4.1 program with an assumed general reservoir age of 402 years (Stuiver et al., 1998). Different from L. Wang et al. (1999a) the new age model ignores the averages of multiple AMS-^{14}C datings but it only considers the younger ages of multiple AMS-^{14}C datings each since marine AMS-^{14}C ages are mainly biased toward higher values either because of locally increased ^{14}C reservoir ages and/or a lateral supply of reworked foraminifera. In some cases the age model relies on the ages with a minimum Σ1 error.

Hemipelagic sedimentation rates in core 17940-2 are among the highest ever recorded in the South China Sea, reaching 40-85 cm per kyr in the Holocene (Figure 3). In the earliest Holocene changes in sedimentation rate of core 17940-2 may partly be linked to changing sediment supply due to the postglacial sea level rise and lateral shifts of the shoreline across the shelf. However, over the last 9,000 years, subsequent to the Preboreal, the sea level had almost reached modern values (9,000 yr BP: -20 m, Bard et al., 1996; 8,000 yr BP: -12 m, Hesp et al., 1998) precluding any further lateral shift of the coastline which presently follows a steep rock cliff (L. Wang et al., 1999a). During this time interval the large fluctuations in sedimentation rates are ascribed to changes in precipitation and riverine runoff from the continent, driven by changes in the strength of the East Asian summer monsoon.

Results

Comparison of color variability to other sediment properties:

The reflectance curves of the three color channels (R G B) in part show different trends (Figure 4). The blue channel curve displays a variability which is lowest in the lower part and highest near the top section, whereas the red reflectance record, probably a tracer of reddish dust (loess) input, shows an inverse pattern. As expected, the curve of the green channel follows an intermediate trend. The color reflectance records start at 722.5 cm (c.d.), near the top of the Bølling-Allerød time interval (13.280 ± 100 cal. yr BP, L. Wang et al.,1999a) which is identified by pronounced negative $\delta^{18}O$ values. Here the color curves of all three channels exhibit generally high intensities ("dark colors"), with maximum values for blue. During the Younger Dryas (YD) interval, which spans the core interval from 714.5 to 656.5 cm (c.d.) according to the oxygen isotope curve, the color reflectance remains almost stable. After the YD the red reflectance, but not the blue, rapidly decreases towards lower intensities from 565-570 cm (c.d.). This decrease parallels a marked and abrupt increase in clay content, and a drastic drop in % $CaCO_3$ and magnetic susceptibility (Figures 4 and 5).

Near 460-390 cm (c.d.) the blue (and necessarily the green) reflectance record show a distinct decrease, corresponding to an increase in $\delta^{13}C$, a feature hardly revealed in the red record (Figure 4). This color shift introduces a long-term minimum in both TOC and clay content and a weak maximum in % carbonate at 400-105 cm (c.d.) (Figures 4 and 5). Here the color values display a high variability.

Figure 4 (next page). Records of sediment color reflectance (red, green, blue, on an intensity scale from 0=low to 255= high) vs. core depth, at Site 17940 in ultrahigh resolution of 03.-0.7 yr. To highlight the (bi-)decadal trends in color variability, the original records (grey lines, 0.028 cm/pixel) were smoothed by a 36-point running average (bold lines), equal to a sample spacing of 1 cm. Stratigraphic intervals (B/A = Bølling/Allerød, YD = Younger Dryas, EHO = Early Holocene Climatic Optimum) are derived from the planktonic $\delta^{18}O$-record and marked by vertical lines. Bold bracket at the bottom figure indicates an interval of potential core alteration during transport. Arrows mark major trend in planktonic $\delta^{13}C$, % TOC and % $CaCO_3$ records, which correspond to changes in color reflectance.

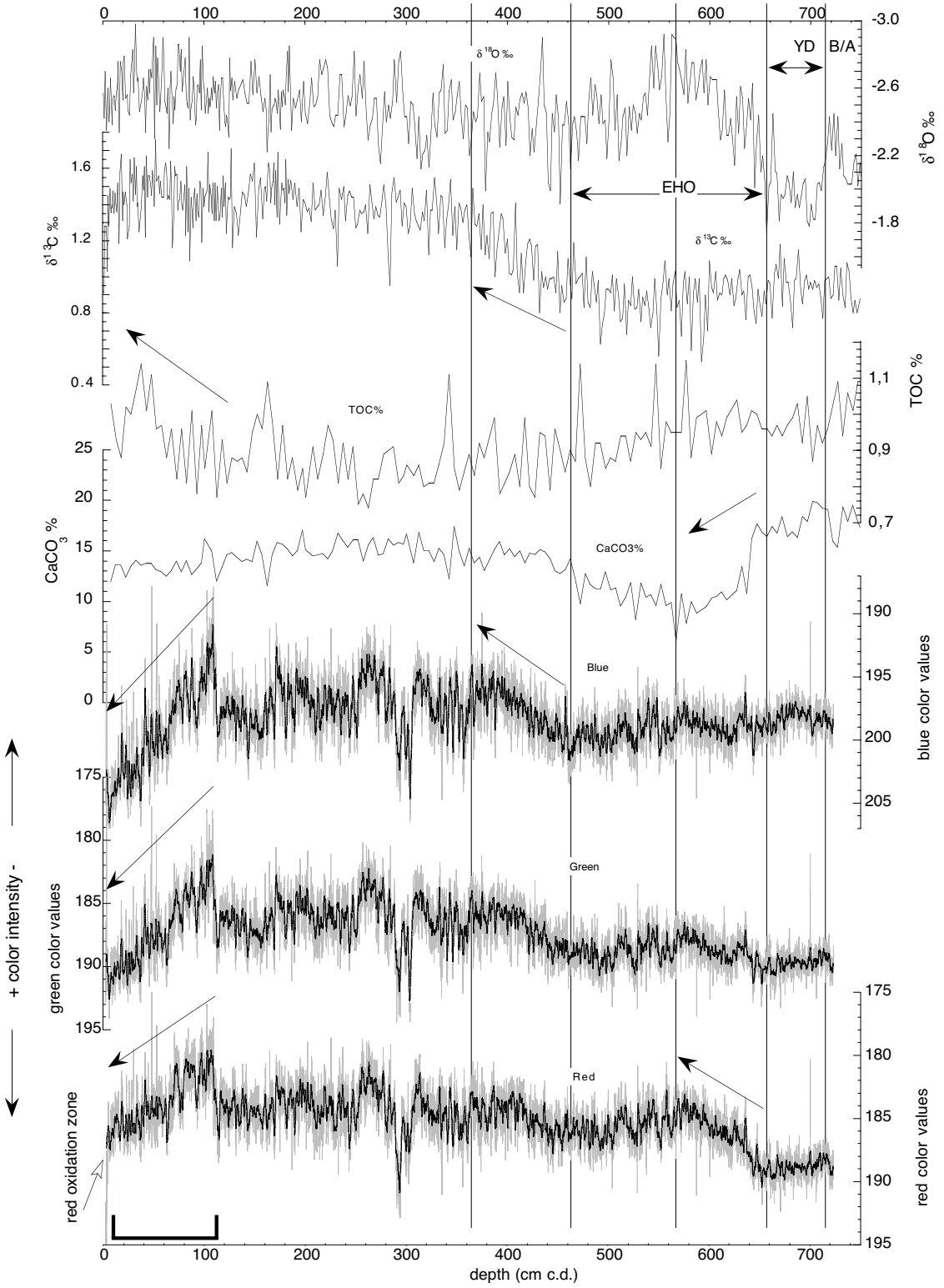
δ 18O ‰
δ 13C ‰
YD
B/A
EHO
δ 18O ‰
δ 13C ‰
TOC%
TOC %
CaCO3%
CaCO3 %
Blue
blue color values
Green
green color values
Red
red color values
+ color intensity -
red oxidation zone
depth (cm c.d.)

Figure 4

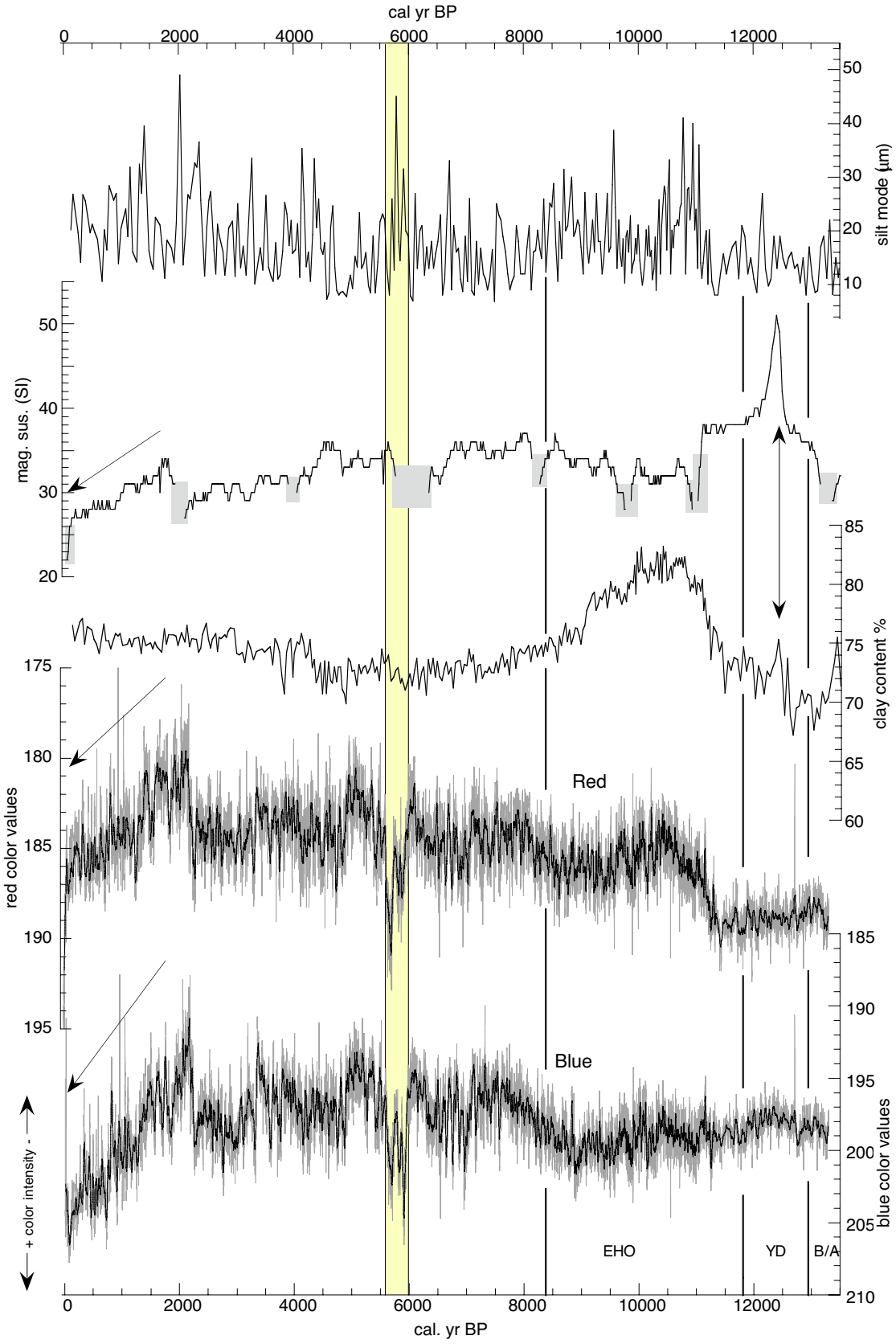
cal yr BP
0
2000
4000
6000
8000
10000
12000
silt mode (µm)
mag. sus. (SI)
clay content %
red color values
blue color values
Red
Blue
+ color intensity -
EHO
YD
B/A
cal. yr BP

Figure 5

Figure 5 (previous page). Comparison of red and blue color reflectance with siliciclastic grain sizes and magnetic susceptibility vs. time. Clay content was measured on the $CaCO_3$ free siliciclastic fraction <63 μm. The silt mode curve was measured on the siliciclastic grain size fraction 63-6.3 μm. In the magnetic susceptibility curve (mag.-sus., in SI units) areas near to partly void ends of core sections are shaded. No mag.-sus. record exists between 5,700 and 6,400 yr BP, because the section (300-321 cm) was too short. Color records of red and blue (grey line) were smoothed by a 36-point moving average for better visibility of trends (bold line). Bold vertical lines mark major stratigraphic time intervals, identified in Figure 4. Shaded vertical bar shows decline in red color intensity, possibly a result of coarse silt grain sizes (near 5,800 yr BP). Arrows mark major trends in mag.-sus. and color.

A joint marked color maximum from 305-275 cm (c.d.) (Figure 4) matches a pronounced maximum in silt modal grain size (Figure 5) either resulting from diagenetic oxidation or representing a maximum input of hematite linked to loess discharge.

The interval of high variability ends at 105 cm (c.d.) with an abrupt jump to a general short-lasting color minimum. Further upcore, color curves of all three channels show a rapid, gradual increase towards darker colors up to 10 cm (c.d.), with the steepest gradient in the blue channel. The topmost 6 cm in this core are reddish-brown because of common oxidation of the sediment surface, homogenized by bioturbation (long arrows in Figures 4 and 5)

High color intensity spikes, especially in blue, generally match high total organic carbon (TOC) excursions and vice versa. Particularly obvious is this trend in the topmost 1-m core section, where a rise in TOC content parallels a long-term increase in color reflectance from 105-10 cm (c.d.) (Figure 4). On the other hand, this may be partly an artifact of core transport and storage, where this section was shortened (≈16%). In addition, Holocene TOC variations may play a minor role, because of their insignificant range, amounting to only ~ 0.2-0.3 %.

Magnetic susceptibility (artificial susceptibility minima near core breaks removed; Figure 5) increases with high red reflectance, that is, with lower clay content, equal to high silt, probably hematite coated, and high carbonate content. On the other hand, a prominent peak in susceptibility at 11.800 yr BP [690 cm (c.d.)] goes along with a small increase in clay, but no color signal.

We surmise that the blue intensity may serve as a proxy of % clay and TOC, whereas the intensity of red may reflect silt-borne hematite. Based on this reasoning, more blue stands for stronger summer (wet) monsoon and more red for stronger winter (dry) monsoon, providing the input of red-yellowish loess.

Different from Atlantic sediment records (Cortijo et al., 1995; Ortiz et al., 1999b) core 17940-2 does not display any correlation between short-term color changes and carbonate content (Figure 6). In part, this may result from the large difference in sampling resolution (0.028 cm versus 1 cm sampling intervals). A more important factor may be the low magnitude of variations in the % $CaCO_3$ between 10 and 12 %, equal to relative changes of 1-2 %. Balsam et al. (1999) observed similar poor correlations in Atlantic cores with comparably low carbonate contents.

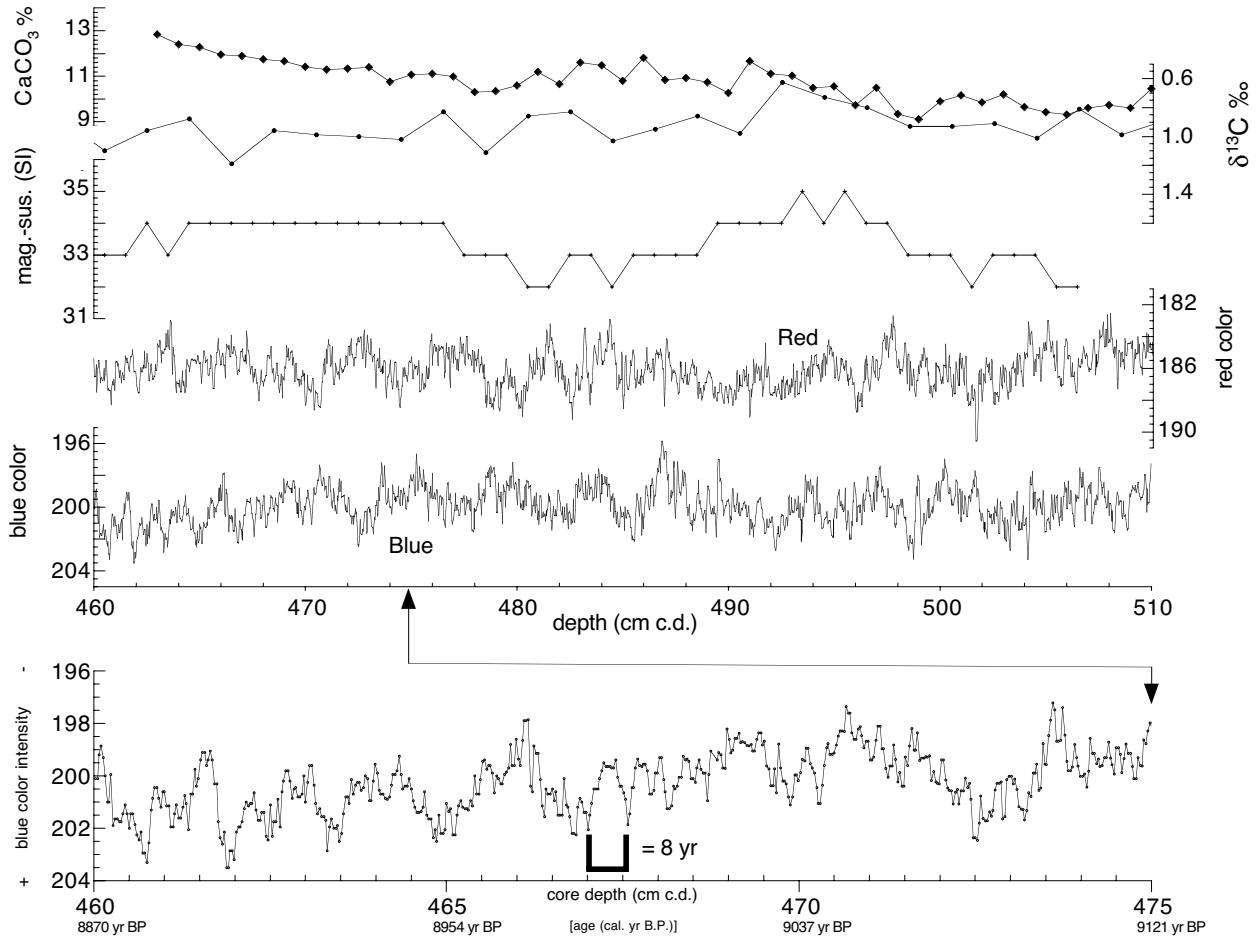

Figure 6. Close-up of core section 460-510 cm (c.d.) with 1-cm spaced $CaCO_3$ record and ultra-high resolution color intensity records (red and blue channel, 0.028 cm sampling resolution, equal to 0.5 years). High-frequency quasi-cyclic variations in color reflectance show little or no correlation with the $CaCO_3$ record. Low-resolution mag.- sus. and planktonic $\delta^{13}C$ records do not reflect any high- or low-frequency trends of the color records. Lowermost panel: Close-up of blue-color intensity record with discrete data points (460-475 cm c.d.).

The chromaticity ratio R/B (Figure 7), also serves as a tracer of major changes in sediment composition (Adkins et al., 1997; P. Wang et al., 2000), possibly linked to differing sediment source areas. Pronounced jumps in R/B near 8,800 and 11,100 yr BP (Figure 7) are hardly recognized in the blue and weak in the red reflectance record. In general, the warmish and more humid B/A and Preboreal intervals (L.Wang et al., 1999a), that are more TOC and enriched in clay, show a lower R/B ratio than the YD cold spell, especially the lower YD, and to a lesser degree the middle Holocene, 9,000-2,000 yr BP, where silt and hematite increase. Accordingly the marked R/B decrease over the last 2000 yr may indicate a general increase in runoff and/or fluvial sediment discharge.

The role of bioturbation in destructing short term sedimentation changes

The thickness of the homogenously bioturbated layer in core 17940-2 was deduced from the carbon flux rate (Jian et al., 1999), using the approach of Trauth et al. (1997). Today it amounts to 6-8 cm, a value that matches the thickness of 6 cm measured for the reddish core top layer.

Non-laminated oceanic sediment records to date were generally considered to be as too smoothed and altered by bioturbation for preserving any signals of high-frequency climatic change lasting as short as a few decades to centuries and less. Accordingly most studies of past ultrahigh-resolution climate signals hitherto concentrated on laminated sediment records hardly affected by bioturbation (Hughen et al., 1996; Zolitschka, 1996, Zolitschka et al., 2000; Schaaf and Thurow, 1995). In fact, the homogenous mixing of the sediment surface layers by bioturbation tends to smooth, probably also slightly shift the signals of rapid climatic events in core depth, but it does not necessarily remove them completely from the marine record (Cortijo et al., 1995; Trauth, 1995) nor generates “new“ artificial signals. Hence it is no surprise that recent studies clearly demonstrate that paleoceanographic records from non-laminated sediments with a spatial resolution of 1 cm and less are suitable to provide relevant records of past short-term changes (Chapman and Shackleton, 1998, 2000). On

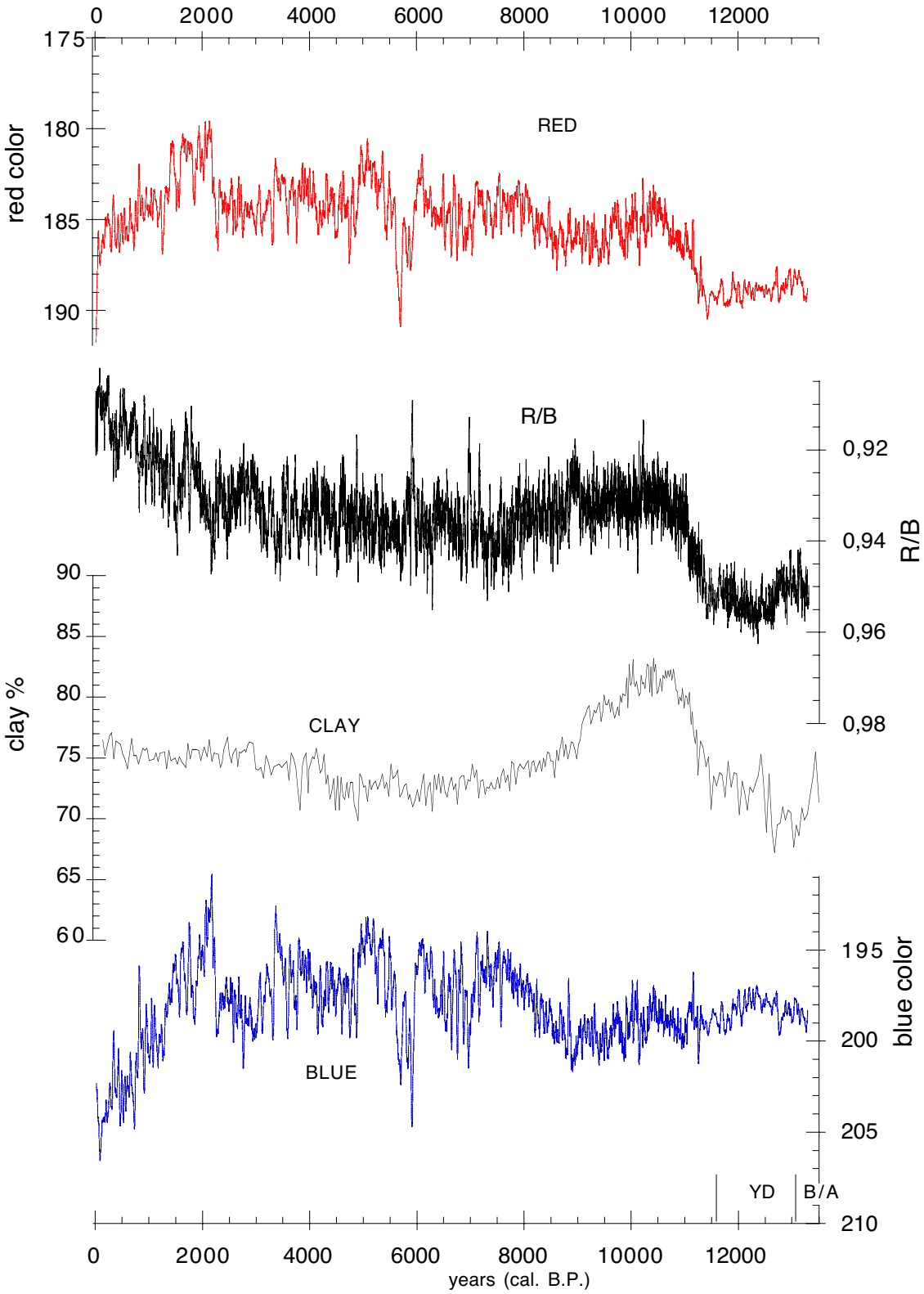

Figure 7. Red-blue (R/B) color ratio as indicator of major changes in sediment composition. Color records for red and blue are smoothed by 36-point moving average, R/B record is unsmoothed. Note jumps in R/B at 11,000 and 8,800 years, possibly marking substantial changes in sedimentation and/or sediment source areas. At 13,300-12,400 yr BP, near the start of the Younger Dryas, a minor maximum marks in the R/B ratio, neither observed in the red nor in the blue reflectance curves.

the basis of this reasoning we tend to regard the short-term, cm-wise color changes (Figure 6) as real signals, all the more since these fairly periodic color oscillations are substantiated by gradual color shifts based on tens of pixel data in each "flank" without relation to any features of bioturbation.

Color variations in the frequency domain

Periodicities derived from Fourier analysis

Frequency analyses of the reflectance and R/B-ratio records of core 17940-2 resulted in a number of periodicities exceeding the red noise level summarized in Table 2 and Figures 8 and 11.

In the interval 0-2,100 years BP the periodicities in red and blue are most significant in the high-frequency band near 5 years, and moreover, near 350 and 1,220 years. In contrast, the R/B ratio is dominated by periods of 12 and 20-24 years. Possibly the periodicities in this core section have suffered from core transport.

For the interval of 2,100-5,500 yr BP numerous significant periodicities for red and blue occur near 960, 140, around 5.9-5.3, 4.2 and 3.8-3.3 years. Further significant periods near 175 and 9 years characterize the red and R/B records, whereas periodicities near 11 years are significant in the blue and the R/B records. Significant periodicities near 17 and 7 years appear in the R/B record only.

frequency range	number of lags	window type	confidence level	bandwidth
0.0-0.2	2820 (30 % of time series)	Bartlett	95%	0.000027

Table 1. Boundary conditions used for Blackman-Tuckey Fourier frequency analysis (AnalySerie 1.2; Paillard et al., 1996) of spectra shown in Figure 8.

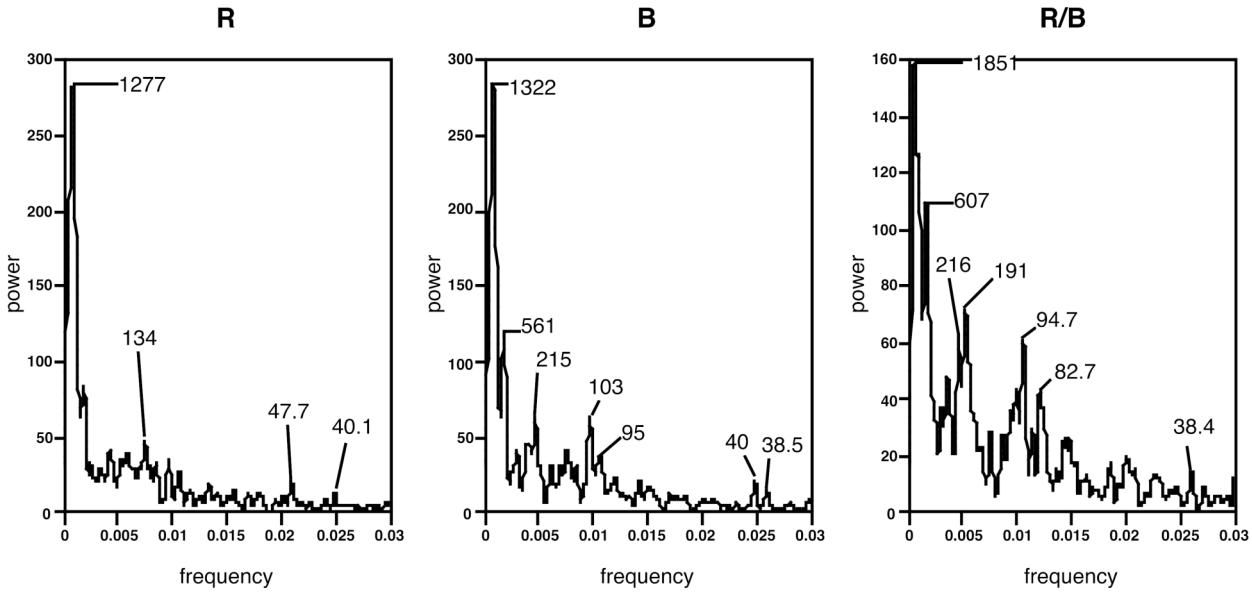

Figure 8. Blackman-Tukey spectral analyses of red (R) and blue (B) color reflectance records and the red/blue (R/B) ratio for the time interval 2,200-11,600 yr BP (Analyserie 1.2 software of Paillard et al., 1996). Longer periods were removed using a 2.5- kyr high-pass filter.

The earliest and largest segment, spanning from 6,000-11,600 years BP, contains the most pronounced cyclicities, several times exceeding the Thomson (1990) significance level, that is definitively beyond the level of noise. Periodicities of 105-101 and 12-10.4 years occur within all three color records. The red record also contains highly significant periodicities of 492, 177, near 15 and 6 years, as compared to marked periodicities of 400, 206, 103, and 8.7 years in blue and of 200, 101, and 11.7-11.3 years in the R/B.

In summary, the Fourier analysis yields a broad spectrum of high- and ultrahigh-frequency periodicities for the various colors and Holocene time intervals. Ever recurring and most significant are the periodic signals of 206-170, 105-93, 12.0-10.7, 9.2-8.7 and 6.6-5.4 years. Periodicities in the Early Holocene appear more pronounced than after 6,000 yr BP. R/B cyclicities concentrate particularly to the high-frequency bands of 20-24, 9-12 and near 7 years, but less to long periods.

Table 2.

Time interval (ka)	Red	Blue	R/B	Range of periods
0-2.1 ka	**350** 163 **5.6, 4.8**	**1220** 152 55.6 4.8	 128 **24/20.4**, 14.8, **12.2**	1500-400 yr 200-100 yr 100-10 yr < 10 yr
2.1-5.5	**957 (!)** 174, 141 8.8, 5,9-5.3, 4.2-3.3	**957 (!)** **136** 93, **11.0** **5.9-5.4, 4.2-3.2**	 201 **17.2/16.2,11.5/10.7** **9.2, 7.0/6.6**	1500-400 yr 200-100 yr 100-10 yr < 10 yr
6.0-11.6	**492 (!)** 177, 105 15.4, 12/11.6/10.4, 6.2-6.0 (!)	**400 (!)** 206, 103 (!), 71 8.7, 6.2	 200, 101 67, 11.7-11.3	1500-400 yr 200-100 yr 100-10 yr < 10 yr
2.2-11.6	1280 134 48	1320 (561) 215, 103/95	1850, 600 215/190 95/83, 38	1500-400 yr 200-100 yr 100-10 yr < 10 yr

Table 2. Summary of periodicities resulting from spectral analyses of red and blue reflectance and the R/B-ratio for three time intervals in core 17940-2. Periods with significance > 99% are in **bold,** periodicities reaching the Thomson (1990) level are marked by (**!**). The periodicities are grouped into millennial-to-multicentennial, bicentennial-to-centennial, multidecadal-to decadal, and subdecadal cycle lengths.

Periodicities based on wavelet analysis

Wavelet analyses employed to up to 1,000-yr long overlapping segments (Figure 9) of the red and blue records and the results are summarized in Figures 10 a, b. The significance of any periods longer than 260 years is partially low because zero-padding at the ends of each time series segment (Figure 9) leads to edge-effects (Torrence and Compo, 1998).

In general the short lasting periodicites resulting from wavelet analysis do not simply match those established as an average for several 1,000 years by Fourier-Analysis. *In the red record* periodicities of 170-210 years dominate during the intervals 2,500-3,200, 5,300-6,100, and most pronounced, between 7,000-10,500 yr BP. Shorter periodicities of 85-125 years occur throughout almost the entire record, being most persistent from 6,500-8,700 and from 10,000-11,300 yr BP such as in the Fourier spectrum.

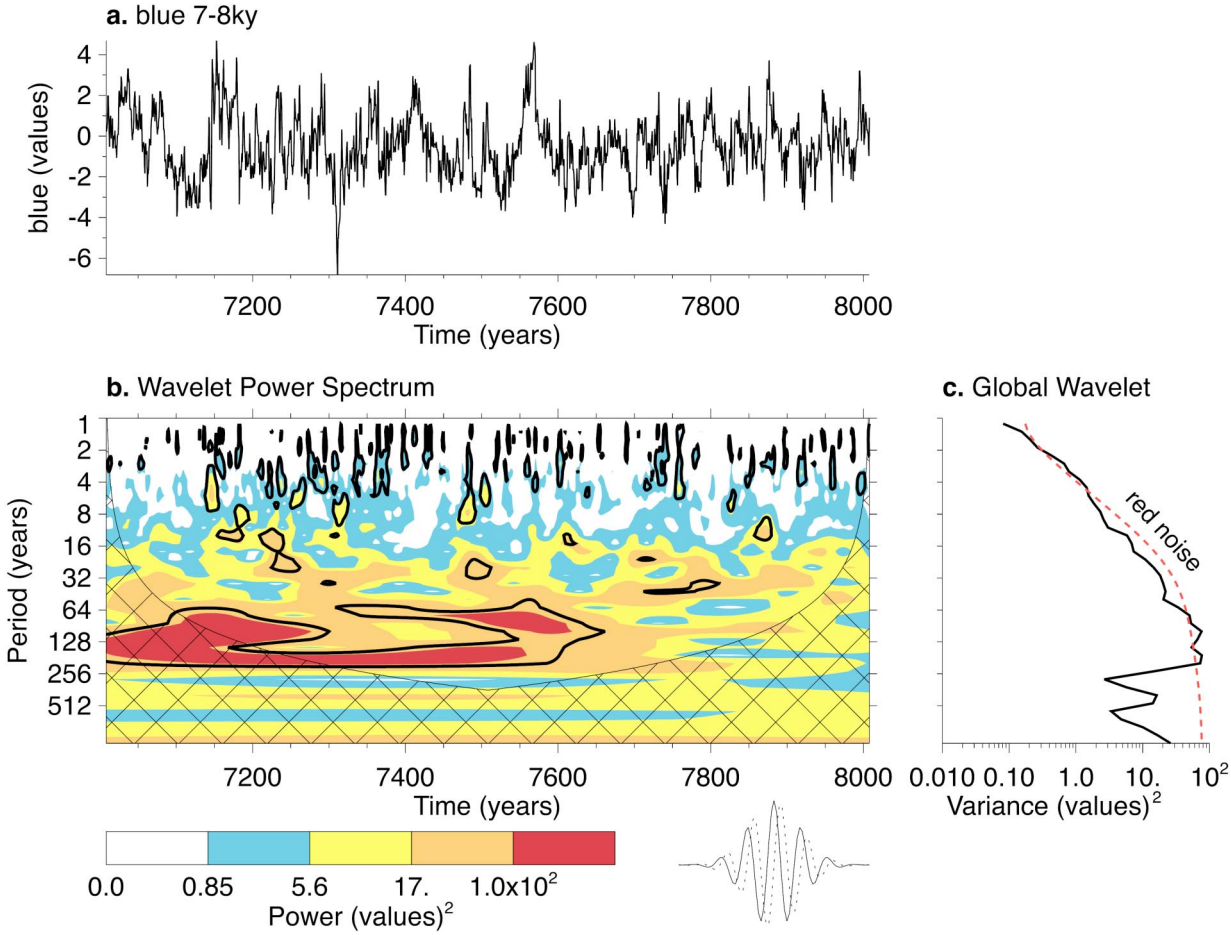

Figure 9. Wavelet analysis plot of red reflectance values 7,500-8,500 years BP, using a Morlet k=6.0 wavelet function (right lower corner; solid = real, dashed=imaginary), calculated with software of Torrence and Compo (1998). For better performance wavelets were analysed for overlapping time windows representing up to 1000 years. To remove long-term oscillations the datasets were initially treated with a 2.0-kyr high-pass filter. Bold lines mark prominent areas of spectral density above 95% significance, also depicted in c) by the "global wavelet" as spectral peaks above the red noise level (stippled line). Zero-padding at the ends of the time series segments leads to reduced confidence in the cross-hatched region (details in Torrence and Compo, 1998).

Periodicities of 70-80 years and 30-50 years are most frequent between 6,500 and 11,500 yrs BP. Short periods around 20 years are particularly obvious in the time range 9,800-11,000 yrs BP (Figure 11 a-c). Accordingly, wavelet analysis basically confirms the results of Fourier analysis that Early Holocene periodicities are more strongly developed than later during the late Holocene.

The same applies to the the *blue color reflectance record*. Here wavelet analyses reveal periodicities in the range of 170-210 years in the mid-Holocene intervals 2,700-3,800, 5,300-

6,000 and 6,700-7,800 years BP. Strong periodic signals of 80-125 years occur between 3,000-5,500, 5,800-6,000 and 6,500-12,000 years BP. Periodicities of 70-80 years are most obvious between 7,500 and 12,000 years BP, those of 30-50 years at 7,500-12,200 years BP. Near-to-22 year periods occur in particular between 4,300-4,700, 9,800-9,900 and 10,500-10,700 years BP, periodicities of around 10-16 years from 10,500-11,000 years BP (Figure 11 a-c)

In summary, the short lived periodicities from Wavelet analysis somewhat differ from the long-term average periodicities obtained by Fourier spectral analysis. However, with this technique we can observe the long-term changes in frequency and amplitude of oscillations and also their mergence or disappearance during certain time intervals (Figure 10a, b). Note that oscillations of intermediate periods (80-200) years are common throughout the Holocene time series in both R and B reflectance records. Shorter periods of less than 70 years do not appear in either record between 0-7,500 years BP. Perhaps they are smoothed by low sedimentation rates, because high frequency periods are found in the early Holocene record where sedimentation rates are higher.

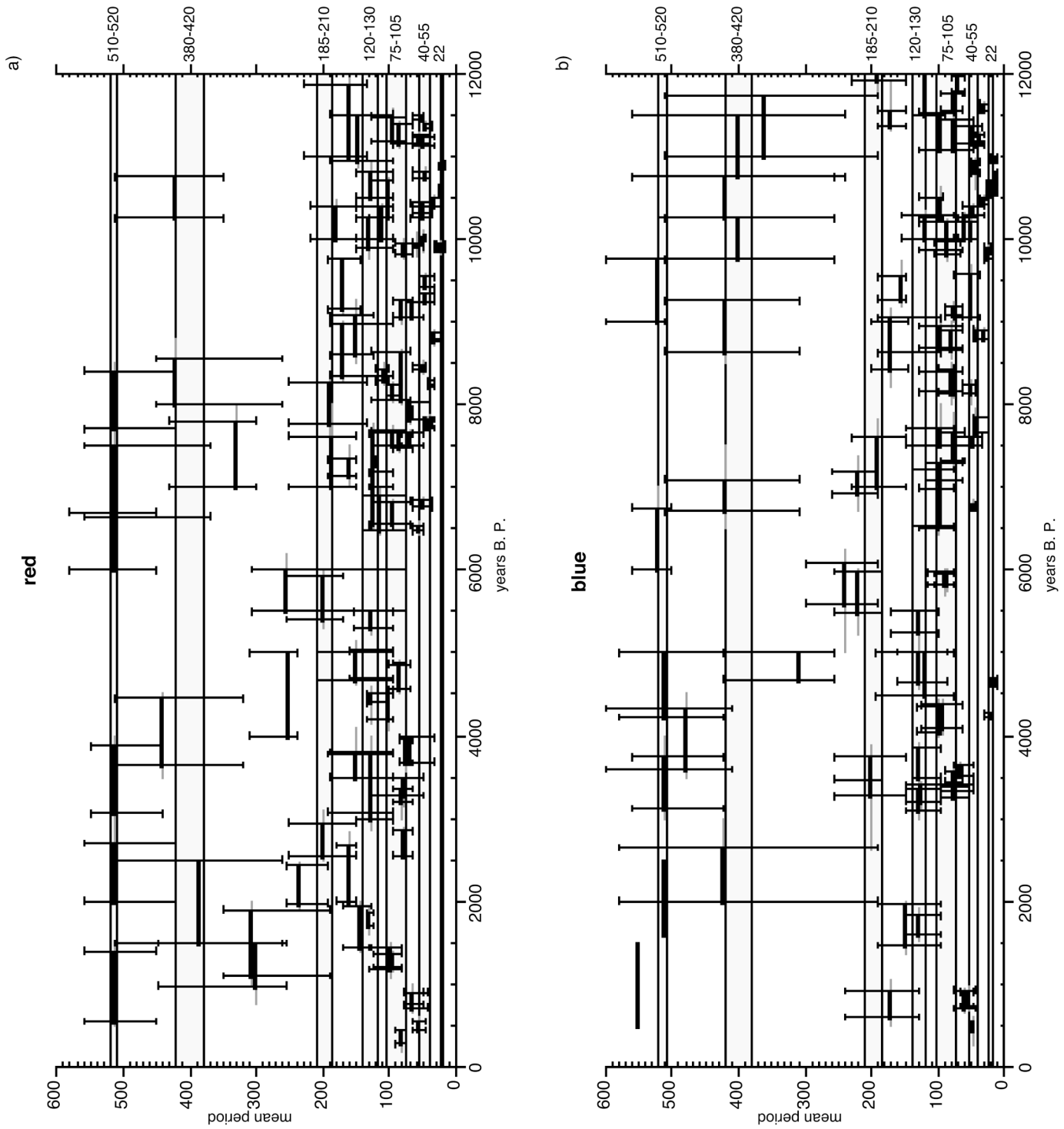

Figure 10 . Integrated results of wavelet analyses for the time interval 0-12,000 yr BP. Bold lines show significant periodicities (with error bars deduced from signal width in original wavelet plots; Fig. 9) during the Holocene. Dotted bars mark bandwidth of climatic/solar periodicities (200-yr de Vries (or Suess) cycle, 90-80 yr Gleissberg solar cycle, 22 yr Hale solar magnetic cycle) as listed in Table 3. (A) Red color reflectance, (B) Blue color reflectance.

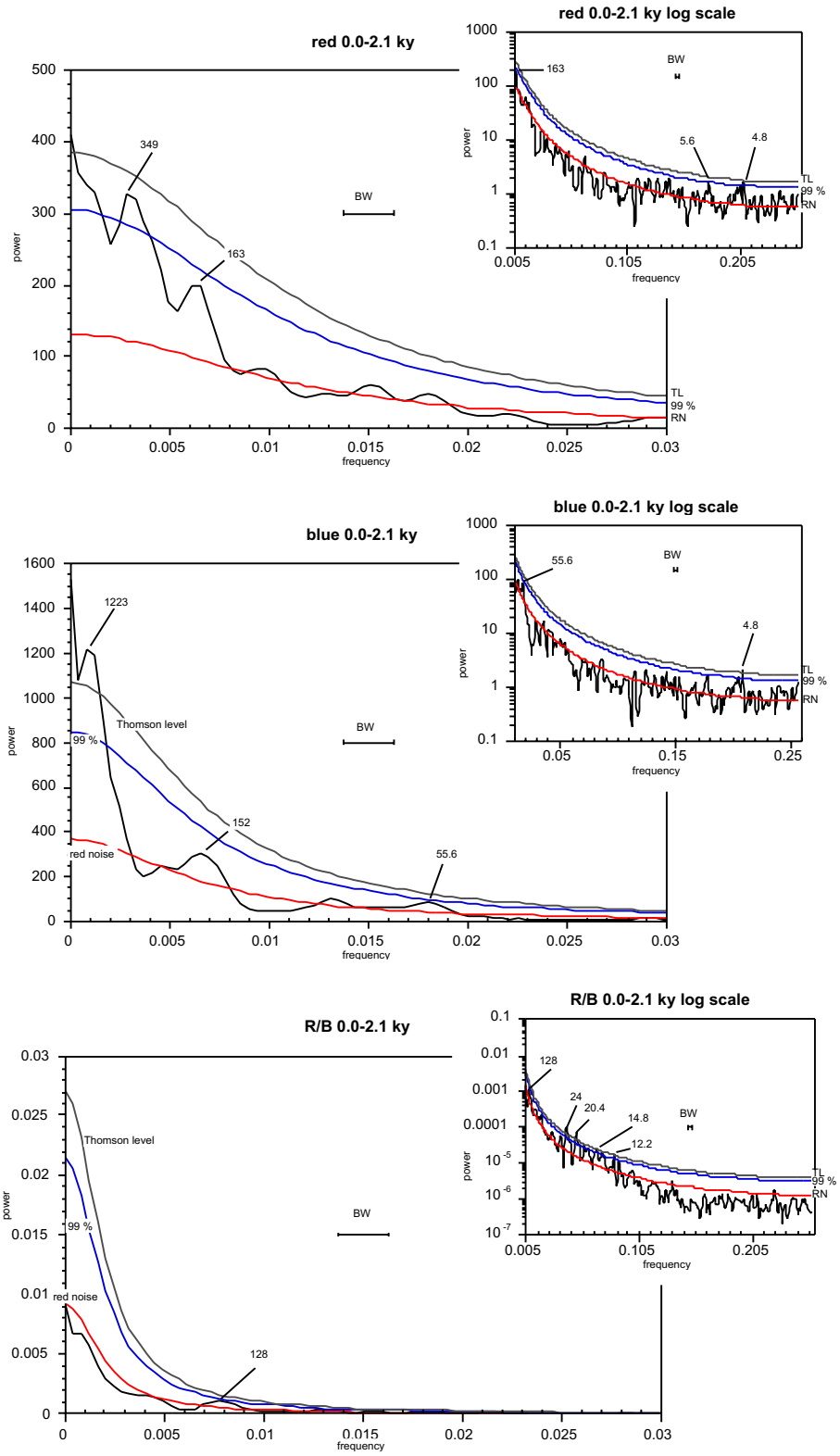

Figure 11a. Spectral analyses of red and blue color reflectance records and the R/B ratio for the time intervals 0-2100yr. Resulting periodicities are summarized in Table 2. Periods longer than 2000 yr were removed using a highpass filter. High-frequency ends of spectra are enlarged (REDFIT 3.4 software ; Schulz and Mudelsee, in press). Dotted thin lines represent the levels of red-noise (RN), 99 % significance, and Thomson (1990) significance level (TL) at which a spectral peak is considered to be statistically above the noise level.

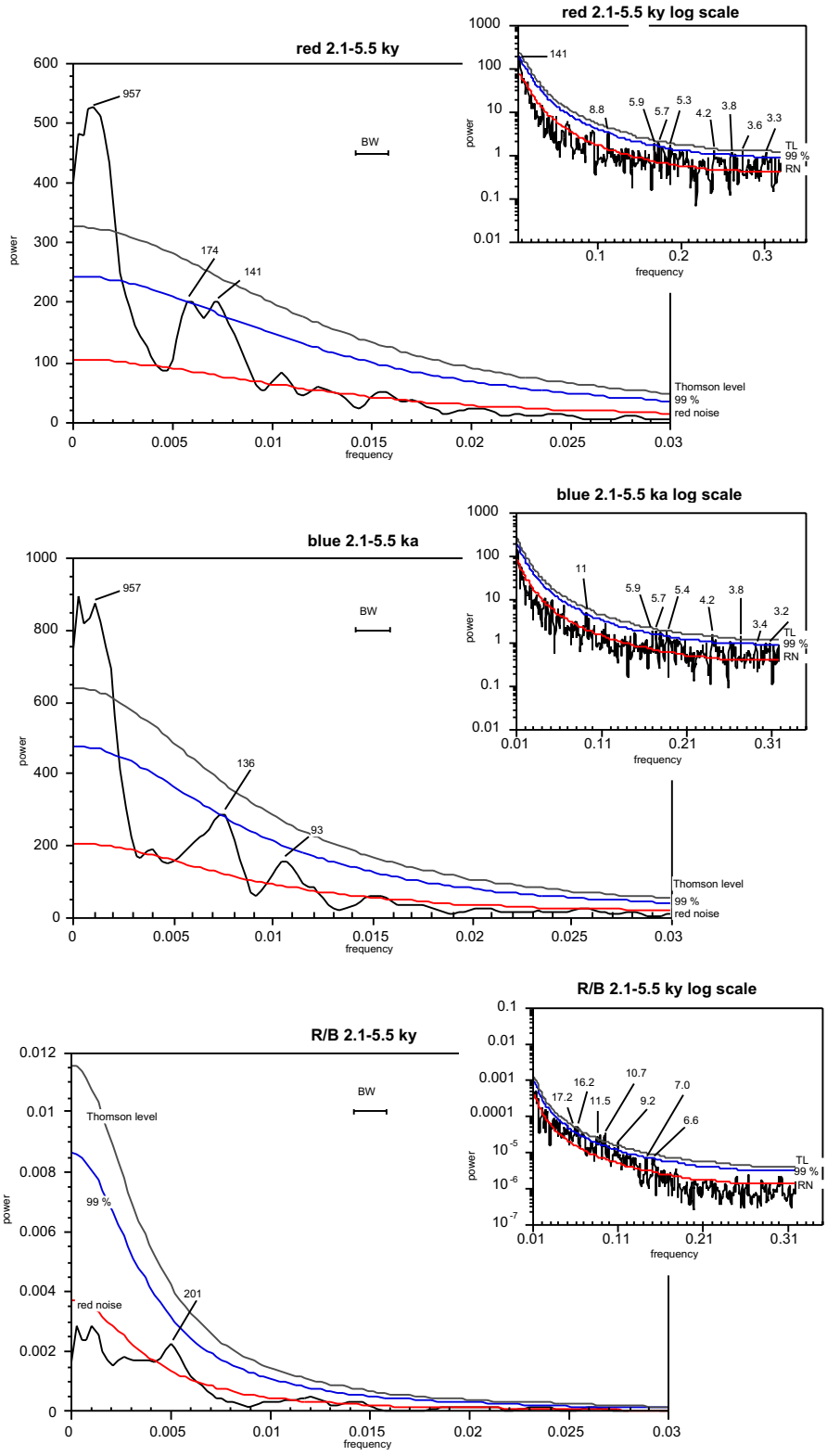

Figure 11b. Spectral analyses of red and blue color reflectance records and the R/B ratio for the time interval 2,100-5,500yr. Resulting periodicities are summarized in Table 2. Periods longer than 2000 yr were removed using a highpass filter. High-frequency ends of spectra are enlarged (REDFIT 3.4 software ; Schulz and Mudelsee, in press). Dotted thin lines represent the levels of red-noise (RN), 99 % significance, and Thomson (1990) significance level (TL) at which a spectral peak is considered to be statistically above the noise level.

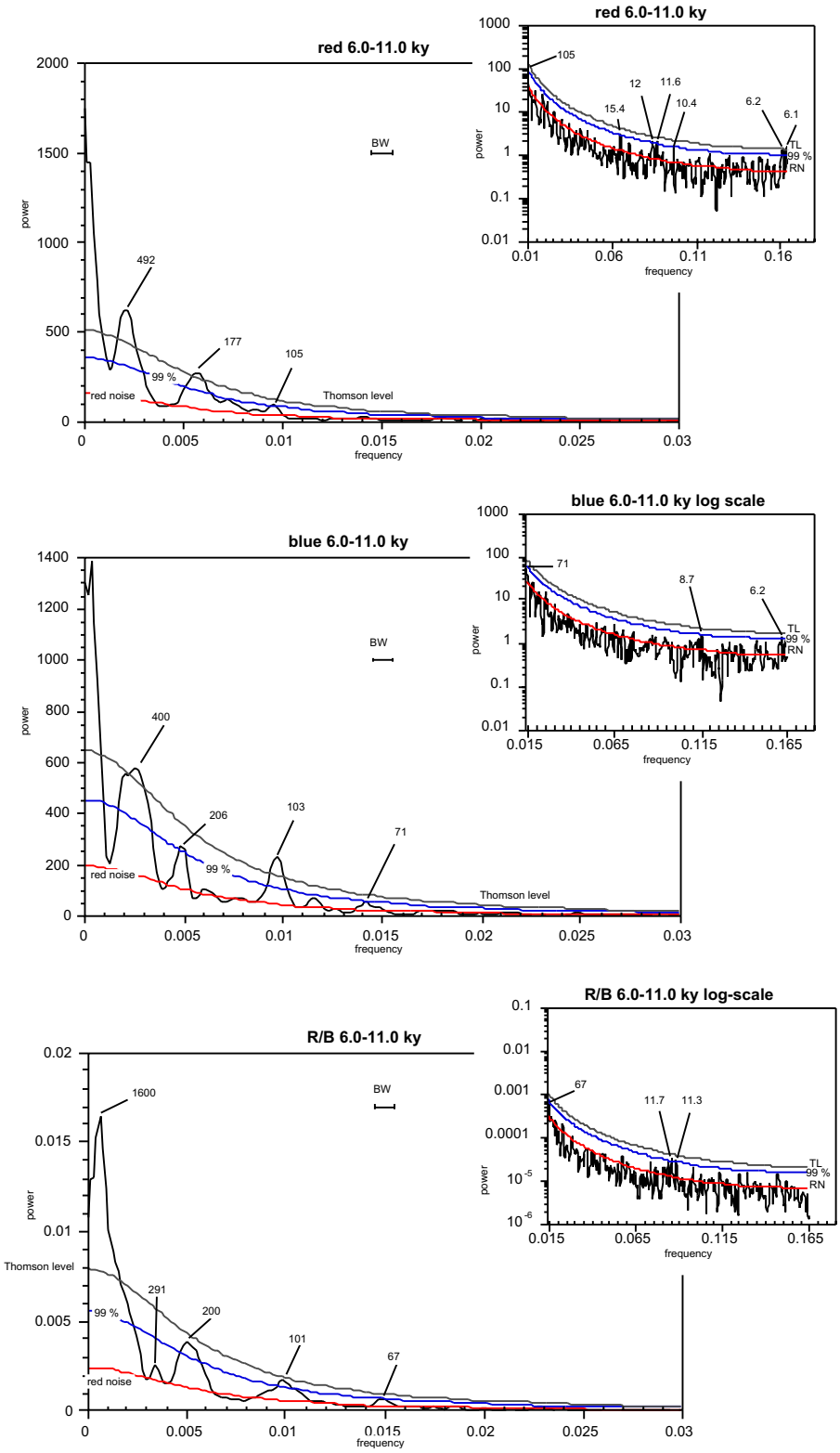

Figure 11 c. Spectral analyses of red and blue color reflectance records and the R/B ratio for the time interval 0- 6,000-11,600 yr BP. Resulting periodicities are summarized in Table 2. Periods longer than 2000 yr were removed using a highpass filter. High-frequency ends of spectra are enlarged (REDFIT 3.4 software ; Schulz and Mudelsee, in press). Dotted thin lines represent the levels of red-noise (RN), 99 % significance, and Thomson (1990) significance level (TL) at which a spectral peak is considered to be statistically above the noise level.

Discussion

1. Origin of changes in color reflectance

In recent years various techniques (Merrill and Beck, 1995; Balsam and Deaton, 1996; Nagao and Nakashima, 1992) employed sediment reflectance as proxy for deducing paleoceanographic and paleoclimatic time series in high time resolution. Reflectance data were measured on a variety of sediment facies from different environments and regions (Keigwin et al., 1994; Cortijo et al., 1995; Adkins et al., 1997; Porter, 2000;). It turned out that even minor environmental changes may leave precise traces in the color record (Rack and Merrill, 1995; Chapman and Shackleton, 1998, 2000;).The changes in sediment color are mainly caused by changes in the mineral- and organic-matter contents (Schaaf and Thurow, 1994; Merrill and Beck, 1995; Balsam et al., 1997, 1999; Bauch and Helmke, 1999;).

In theory, changes in the sediment color of core 17940-2 mainly reflect the balance between fluvial and eolian derived sediment input from China, apart from a whitish pelagic component, where the red color probably stems from reddish minerals and/or red colored clastic particles. Likewise, hematite coated loess particles and iron oxides including goethite were identified as the origin for the stain in North Atlantic sediments and as the tracer of red colored eolian dust from Africa (Ehrenberg, 1847; Sarnthein and Koopmann, 1980; Barranco et al., 1989; Balsam et al., 1995, 1997).

Indeed, the increased red color intensity (Figure 4) parallels the enhanced eolian sediment input during the YD (L. Wang et al., 1999a), and vice versa, the steep decline in red color at the end of the YD reflects a massive reduction in loess concentration. Additionally, the high portion of mountain conifers in the YD pollen spectrum (Sun and Li, 1999, Sun et al., 2000) indicates a rather cool and more arid environment instead of low-latitude rain forest, thus supporting the concept of red loess as the main coloring agent.

The blue intensity seems to reflect a joint signal of TOC and clay content, since high portions of clay promote the adsorption and preservation of organic carbon on mineral particles

(Hedges and Keil, 1995). TOC was identified as an important stain in North Atlantic sediments by Balsam et al. (1996) and Nakajima et al. (1998). In core 17940-2 this relationship is supported by a strong decline in blue color intensity from 460-400 cm (c.d.) (~ 8,900-7,700 yr BP), which parallels a weak decrease in TOC. Moreover, increased concentrations and mass accumulation rates of organic carbon (Jian et al., 1999) are probably responsible for higher blue color intensities ending near 410 cm (c.d.)

Basically, we may suppose that the R/B ratio is summarizing the variability in red and blue, that is the ratio between the dominance of sedimentation from either dry or wet monsoon. As expected, the red/blue ratio R/B in core 17940 closely correlates with the clay record (Figure 7), corroborating the results of Adkins et al. (1997), and showing that the chromaticity ratio of certain color ranges (e.g. red/yellow, red/blue) can also be used as indicator for variations in clay content.

2. Suborbital climate periodicities in sediment color

Suborbital quasi-cyclic periodicities have been documented in a great number of oceanographic, geological and biological records (Table 3a,b,c). For some of these periodicities, such as the El Niño Southern Oscillation (ENSO), the forcing mechanisms are fairly well established (bold numbers in Table 3 a). For the majority of periodicities however, the postulated forcings and mechanisms are still controversial. In principle, two groups of forcings, external and internal factors, are distinguished in the literature, as listed in Table 3.

Both groups of frequencies are represented in the Holocene reflectance records of core 17940-2 (Table 2). Many of them have already been reported from other monsoon-controlled hemipelagic sediments records ("**M**" in Table 3).

Table 3: Forcings of sub-orbital climate cyclicities

Cycle (years) / Forcings	**Evidence / Observations**	**reference**
11yr sunspot (*Schwabe*) cycle	sunspot cycles measured over the last century (**13.3-9.9** yr)	Mursula & Ulich, 1998
	swedish lake varve counts	De Geer, 1912
	^{10}Be oscillations in ice cores	Steig et al. 1998
	dust variations in GISP2 ice core: **11 yr**	Ram et al., 1997; Ram & Stolz, 1999
	δ^{18}O record of Greenland ice cores: **11-12**, 17 yr	Fischer et al., 1998
	atmospheric oscillation record	Shindell et al., 1999
	satellite solar irradiance record	Beer et al., 2000
	digital-color data St. Barbara basin	Merrill & Beck, 1995
	Gulf of California, laminated sediments: **11**, 22-24, 50 yr	Pike & Kemp, 1997
	solar activity in Holzmaar varves: **11**, 88, 208 yr	Vos et al. 1997
18-yr lunar tidal (*Zagros*) cycle	variations in drought intensity of North America	Cook et al., 1997; Laird et al., 1996
22-yr solar magnetic (*Hale*) cycle	varve record North America	Hale, 1924; Rittenour et al., 2000
	11, 22 yr oscillations in δ^{18}O of Galapagos corals	Dunbar et al., 1994
	Arabian Sea varve record: 23, 20 yr	von Rad et al., 1999 **M**
	circum North Atlantic tree ring records	Cook et al., 1997
	Gulf of California, laminated sediments: 22-24, 50 yr	Pike & Kemp, 1997
	variations in drought intensity of North America	Laird et al., 1996
88-yr solar (*Gleissberg*) cycle	variations in ^{14}C record, sun spot numbers	Stuiver & Braziunas, 1993; Friis-Christensen & Lassen, 1991; Gleissberg,1958
190-208 solar cycle (*de Vries or Suess*) cycle	variations in ^{14}C record, laminated marine sediment records	Stuiver & Braziunas, 1993; Sonett & Suess, 1984; Schaaf & Thurow, 1995
	200- yr variations in δ^{18}O Tibetan ice core	Thompson et al., 1997 **M**
420-yr (solar?)	drought record of North America: 420, 218, 143 yr	Yu & Ito, 1999, 2000

Table 3 a. External forcings as solar/lunar cycles. Potential forcings of sub-Milankovitch climate cycles based on published evidence. Most prominent periods are in **bold**. **M** indicates periodicities linked to monsoon controlled regions.

Cycle (years) / Forcings	**Evidence / Observations**	**reference**
ENSO-type and less than 10-yr long cycles		
2.75-6 yr	coral record, (MIS 5 Sulawesi paleo-ENSO)	Hughen et al., 1999 **M**
4-2 yr	Pacific SST and Southern Oscillation index	Neelin & Latif, 1998
5.0-5.5, 3.5-4.0, 1.7-2 yr	coral records (Seychelles, ENSO)	Charles et al., 1997 **M**
5-6 yr	oscillations in African precipitation	Nicholson et al, 1996
3-5 yr (ENSO) + 12 yr (Asian Monsoon)	coral records Indian Ocean/ Red Sea	Pätzold & Dullo, 2000 **M**
8.3, 7, 4.7, 3.9 yr	Holocene records of laminated Arabian Sea sediments	von Rad et al., 1999 **M**
8.4, 7.6, 3.5, 3.1	laminated sediments from Santa Barbara Basin, marine production and coastal runoff	Bull et al, 2000
6-7 yr	stalagmite records of NE Atlantic climate	Baker et al., 2000
> 15 yr	Greenland ice cores	Appenzeller et al., 1998
10-15 yr	modern time series of global temperature, atmospheric CO_2	Keeling & Whorf, 1995
17-15, 8.5-6.5, 6-4.5, 4-3 yr	Holocene periodicities of lake laminae in Ecuador	Rodbell et al.,1999
NAO-style cyclicity	climate variations associated with the North Atlantic Oscillation (NAO)	Hurrell & Van Loon, 1997
50, 60, 70 yr	modeling, surface temperature, ice cores	Broecker 1999, 1997, 1975; Delworth & Mann, 2000; Cook et al., 1998; Stuiver et al., 1995, 1997
55-88 yr	modeling	Schlesinger & Ramankutty, 1994
80-90 yr	North Atlantic Oscillation (NAO) in ice cores and stalagmite records	Appenzeller et al., 1998; Baker, 2000,

Table 3 b. Internal climatic/oceanic oscillations. Potential forcings of sub-Milankovitch climate cycles based on published evidence. Most prominent periods are in **bold**. **M** indicates periodicities linked to monsoon controlled regions.

Cycle (years) / Forcings	**Evidence / Observations**	**reference**
420, 218, 143 yr	drought record North America	Yu & Ito, 1999; Dean, 1997
512 yr	early Holocene tree ring record of ^{14}C variations	Stuiver & Braziunas, 1993
750, 500, 250 yr	Arabian Sea varve thickness record	von Rad et al., 1999 **M**
950 yr	Holocene cyclicity in North Atlantic sediment grain sizes	Bianchi & McCave, 1999
550 + 1000-yr	Holocene cyclicities in North Atlantic circulation patterns	Chapman & Shackleton, 2000
890/1000	GISP2 & North GRIP Holocene temperature record	Schulz & Paul, 2001
1450-1470 1120-1150	D/O cycles in Arabian Sea sediment records	Sirocko et al., 1996 **M**
1100 + 1470 yr	D/O cycles in North Atlantic and sediment records	Grootes & Stuiver, 1997; Bond et al., 1997; van Kreveld et al., 2000
1450 + 1800+ 2300 yr	$\Delta^{14}C$ residual (GISP2)	Mayewski et al., 1997

Table 3 c. Further internal low-frequency oscillations of climate and ocean. Potential forcings of sub-Milankovitch climate cycles based on published evidence. Most prominent periods are in **bold**. **M** indicates periodicities linked to monsoon controlled regions.

Millennial-to -semimillennial-scale periodicities:

In the multicentennial range, the planktonic $\delta^{18}O$-record of core 17940-2 had shown a significant periodicity around 750-770 years (L. Wang, 1999a, c) over the last 10,000 years. This periodicity would be an overtone of a 1,500-year Dansgaard-Oeschger-style (DO) cyclicity in the Holocene, which has also been claimed for the North Atlantic region (Bond et al., 1999), the Indian Ocean (Sirocko et al., 1996) and in North America (Campbell et al., 1998).

However, on the basis of our revised stratigraphy (Figure 3), the 770-year periodicity has now shifted to *940 years* (narrow bandwidth) *and 900/1170* years (broad bandwidth), respectively (Figure 12). Further significant periodicities occur in the 1850-, 1220/1320-, and 520 to 400-year bands of red and blue. The latter frequency band is confined to 11,600-6,000 years BP. The 940 years match a mid-Holocene frequency of red and blue, which occurs at 1/960

(Figure 11). More interestingly, it also matches a dominant early-to-mid Holocene temperature periodicity of ~ 900 years (Table 3c), found in the GISP2 and North-GRIP ice cores (Schulz and Paul, 2001), and thus reveals a global signal.

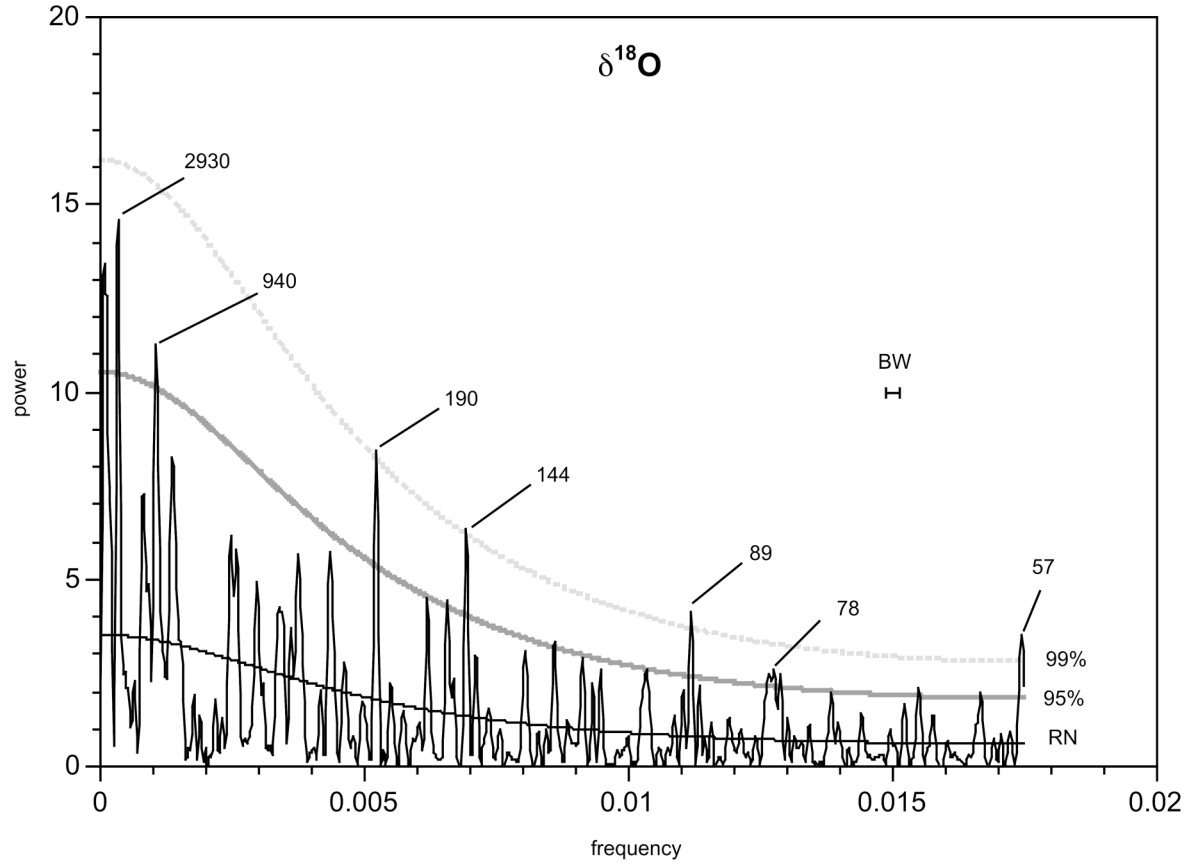

Figure 12. Power spectrum of planktonic $\delta^{18}O$ variability in core 17940 for the Holocene 0-11,600 yr BP (REDFIT 3.4 software ; Schulz and Mudelsee, in press). Dotted line represents the 99% significance level, solid lines that of 95 % and of "red-noise" (average continous decrease of spectral amplitude with increasing frequency). Most significant (>99%) are major spectral peaks at periods of 57, 90, 145, and 190 yr. Spectral peaks of 78, 940 and 2930 are well above the 95% level.

When extracting the 950-year component from the $\delta^{18}O$ records of GISP2 and core 17940 with a band-pass filter envelope (Figure 13) the two records run approximately parallel for most of the Holocene, with the GISP2 $\delta^{18}O$ warming signal leading the (inverted!) $\delta^{18}O$ signal of wet monsoon at Site 17940 by 100 to 350 years between 7.5 ka and 2.5 ka. Prior to 7,750 yr BP, when the precession-driven insolation had reached its maximum, the two signals almost run in antiphase, with the lead of GISP2 reaching 420-485 years. By applying the same filter to the red and blue-color records, the $\delta^{18}O$-maxima (equal to SSS minima), are lar-

gely in phase with or lead by up to 200 yr the minima in the blue-color record between 7 and 1.5 ka (Figure 14). This further corroborates our initial assumption that blue may be a good proxy for river-born sediment and increased precipitation over China. However, the two records vary in antiphase at 9-7ka, a relationship yet unexplained.

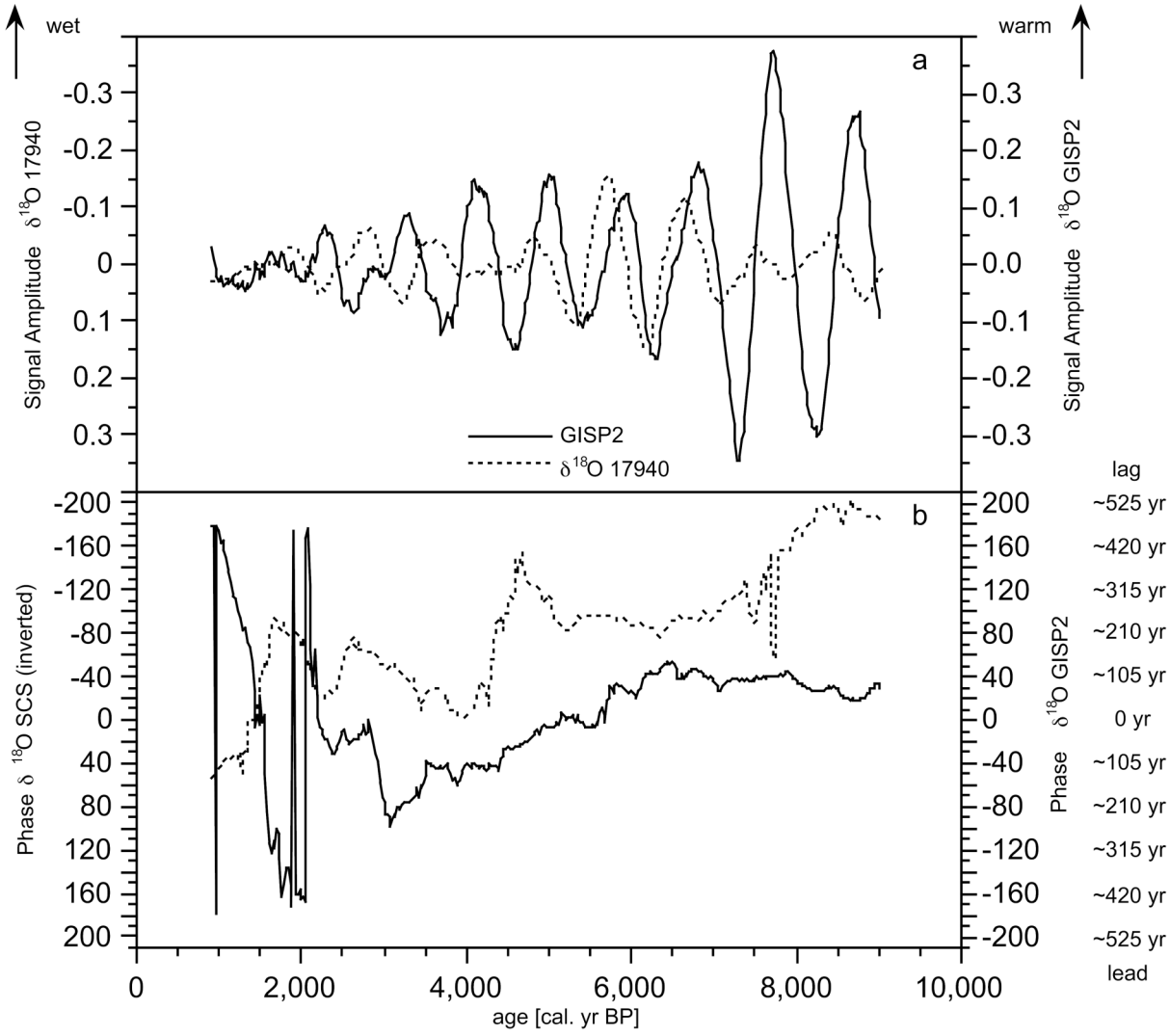

Figure 13. Phase relationships in the 950-year frequency band.

(a) 950-year components (estimated by the harmonic-filtering algorithm after Schulz, 1996) of the GISP2 $\delta^{18}O$ temperature record and the inverted planktonic $\delta^{18}O$-record of monsoon wetness at Site 17940.

(b) Phases of the filtered 950-year-signal components in the GISP2 and core 17940 $\delta^{18}O$ records. The GISP2 signal (small or negative phase angles) precedes the 17940-signal of monsoon wetness (positive angles) in the middle Holocene by 100-350 yr, over the last 2000 yr hard to define. We draw the important conclusion that monsoon variations in the 950-yr cycle generally respond to temperature changes in Greenland and northern high latitudes. In the earliest Holocene when the precessional insolation reached a maximum, the lead of GISP2 increases to up to 450 years.

We conclude that the Holocene variations in wet monsoon, as depicted by the 950-yr components of the blue and $\delta^{18}O$-records (Figure 13b and 14c), generally lag the atmospheric temperature cycles on the Greenland ice summit 100-350 years, in the earliest Holocene by up mto 450 yr. This implies that North Atlantic climate variations may largely control the variability of monsoon rather than vice versa, if we assume that the variable with the phase lead by less than 475 yr is driving the variable with the phase lag. This reasoning, however, is not stringent, as possibly indicated by the Early Holocene antiphase relationsihp.

Different to our expectations, Holocene 950-yr components of the blue and red records, extracted by a band-pass filter, are generally in phase between 9000 and 3000 years BP, which is possibly a result of fluvial sediment reworking. Only from 7500 to 6800 years BP and for the last 3000 years red and blue are in antiphase, as actually anticipated from the opposed mechanisms of eolian (red) and fluvial (blue) discharge.

The ~1000- and 550-year cyclicities are also found in North Atlantic Deep Water circulation (Chapman and Shackleton, 2000). Periodicities of 900 ± 200 yr and 450 ± 100 yr mark the Holocene records of North American drought intensity (Yu and Ito, 1999) and have been tentatively assigned to long ENSO-style oscillations and/or solar activity cycles, respectively. On the other hand, Stuiver and Braziunas (1993) ascribe similar periods in Holocene tree-ring based $\Delta^{14}C$ records to internal oscillations of the Atlantic thermohaline circulation.

In conclusion, the periodicities around 900-1170 years and their potential harmonics of 400-520 years find many obvious analogues in Holocene climate records from tree rings and various marine sediment and ice cores. However, these cycles still lack a clear, process-based explanation. Their periods significantly differ from the 1500-yr span characteristic of DO-cycles and the monsoon variability during glacial stages 2-4 (L. Wang et al., 1999a). Accordingly, DO-cycles do not control the Holocene monsoon variations at Site 17940.

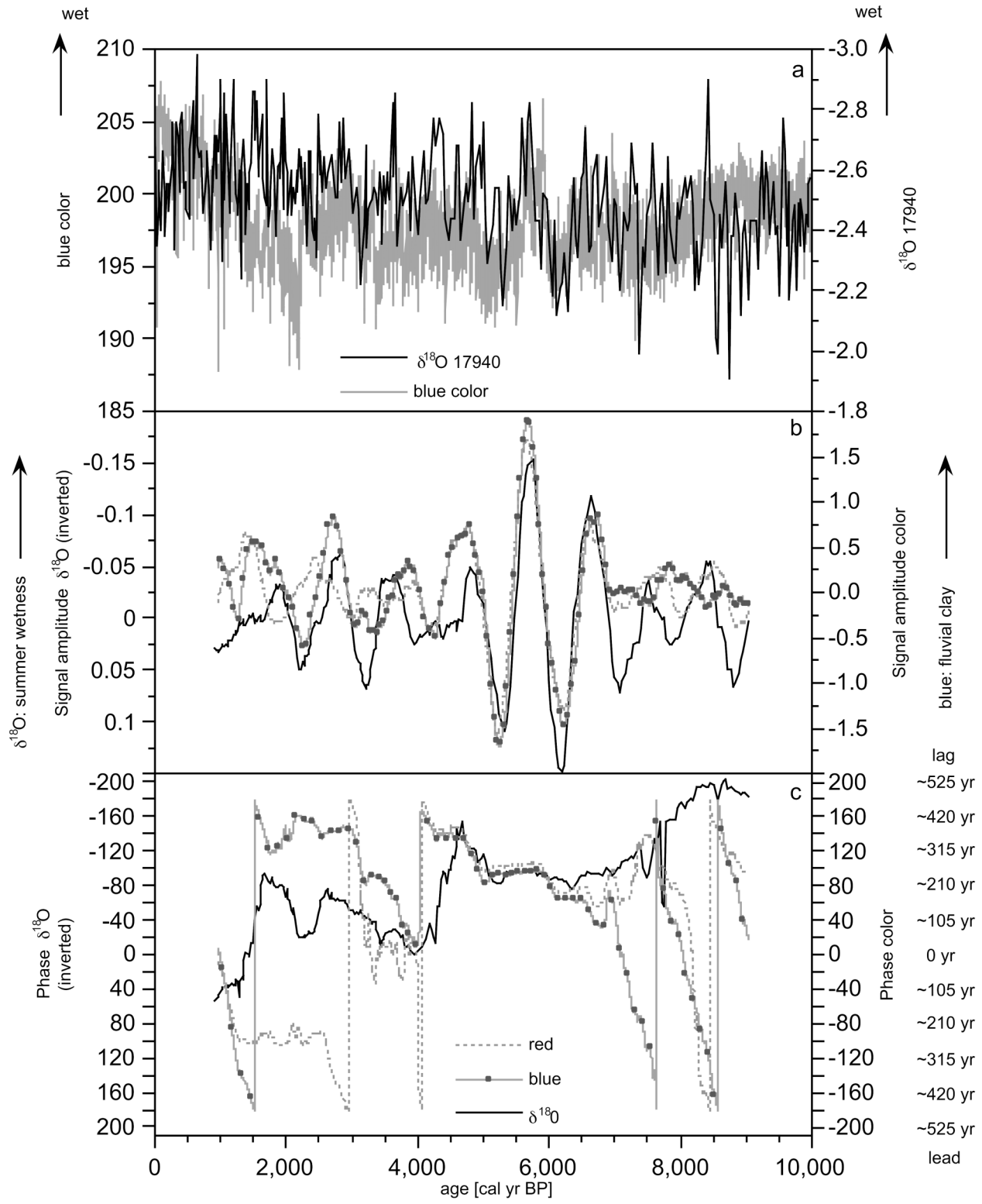

Figure 14. Phase relationships between the inverted $\delta^{18}O$ record of monsoon wetness and the color record of differential siliciclastic sediment composition and supply. (a) $\delta^{18}O$ and blue-color records in the time domain. (b) 950-year-signal components (estimated by the harmonic-filtering algorithm after Schulz, 1996) of the planktonic $\delta^{18}O$-record of monsoon wetness and the red and blue-color records at Site 17940. (c) Phases of the filtered 950-year-signal components of $\delta^{18}O$, red, and blue-color records in core 17940. From 7000-1500 yr BP the $\delta^{18}O$ record of wetness and the blue-color record of TOC enriched clay run parallel, until 4000 yr BP almost in phase. Later the blue signal is lagging by 100-200 years, after 1500 yr BP by ~300 years. Note that the red-color record runs largely in phase with blue between 9000 and 3000 yr BP.

Bi- to semicentennial-scale periodicities:

The periodicities of 206-170 years in our color records from 11,600-2,100 years BP (Figures 9 and 11), resemble cyclicities near 200 years found in several paleoclimate records, often referred to as "deVries" or "Suess" cycle. It was detected in variations of ^{14}C-radioactivity deduced from tree ring counts (Sonett and Suess, 1984) and in ^{10}Be-variations of Antarctic and Arctic ice cores (Beer et al., 1994a, b; Friedrich et al., 2001). Both records suggest that solar forcing probably plays a major role in generating this cycle, possibly enhanced by oceanic feedback mechanisms (Stuiver and Braziunas, 1993).

The 80-105 year periodicities in core 17940-2 reflect the influence of the globally recognized (Table 3) Gleissberg sunspot cycle (near 88 years; Gleissberg, 1944, 1958; Hoyt and Schatten, 1997) on the monsoon-driven sediment flux. Similarly, the Gleissberg frequency band was reported from varved Arabian Sea sediments (95-year frequency-peak, von Rad et al.,1999), and from the Santa Barbara Basin (90-years, Schaaf and Thurow, 1997; a cycle of "near 100 years", Biondi et al.,1997). The transmission mechanism of the Gleissberg sunspot and irradiance cycle into the differential intensity of wet and dry monsoon is yet unclear, apparently acting through differential sea surface temperatures near the equator (Findlater, 1969; Hastenrath and Lamb, 1980).

Periodicities in the range of 63-70 years in core 17940-2 (Figures 10, 11c) may be related to multidecadal surface temperature oscillations first identified by Delworth and (2000) and ascribed to internal ocean instability. This range is similar to a 65-70-year oscillation identified in global-temperature records, which is ascribed to the North Atlantic Oscillation (Schlesinger and Ramankutty, 1994).

Multidecadal-scale periodicities:

Significant spectral peaks near 24-20 years (Figure 10, 11a) between 9,500 and 11,000 yr BP may reflect the 22-year solar magnetic Hale cycle. Frequent peaks near 40-55 years may represent a multiple of this cycle (Figure 8, 10: 6,000-12,000 yr BP).

Further significant spectral peaks *close to 11 years* occur in the red and blue color reflectance records and also in the R/B ratio (Figures 11 b, c). In the tropics and in the monsoon regions the 11- and 22-year solar cycles were also reported from several other records (Table 3a), in particular from gauge readings of the Yangtze River over the last 150 years (Feng et al, 1993). These periodicities possibly reflect influences of the Schwabe sunspot cycle (Schwabe, 1843) on the sedimentation of core 17940-2. Ultimately, the solar origin of the 11- and 22-year periodicities, which were also observed in many climate time series from ice cores (Stocker and Mysak, 1992; Steig et al., 1998) was deduced from tree-ring based $\Delta^{14}C$ variations (Stuiver and Braziunas, 1993). Labitzke and van Loon (1988) verified influences of solar irradiance variations on the upper and lower atmosphere, supported by model results of Haigh (1996), which specified the possible influences of the 11-year solar cycle on atmospheric temperature and circulation patterns. On the other hand, Ghil and Vautard (1991) questioned the solar origin of decadal- to bidecadal oscillations, but attributed them to North Atlantic Oscillation (NAO)-style internal oscillations of the climate system. A final explanation of the 20 to 24-yr cyclicities is yet unclear.

On the basis of a rough estimate of peak height and number of the $\delta^{18}O$ frequency spectrum (Figure 12), the spectral peaks of longer than 50 yr periods which exceed the 95% significance level, explain approximately 20-25% of the total variance of SSS and thus monsoon wetness.

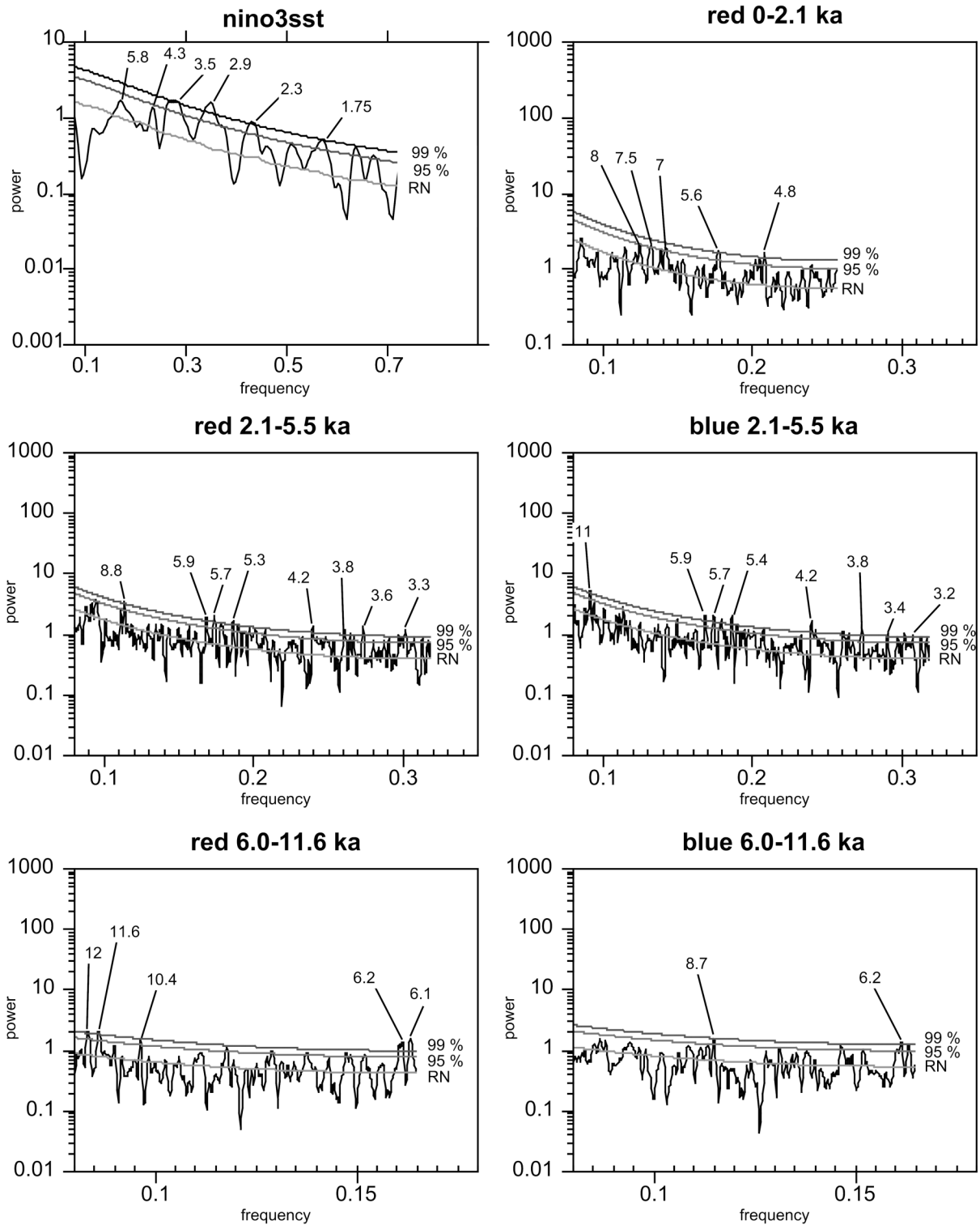

Figure 15. Power spectrum of a modern El Niño SST time series (Meteorological Office, 1992; NINO3 Sea Surface Temperature GISST 2.3 dataset [5S-5N, 150W-90W]) and of the subdecadal-scale variability in the red and blue-color records in core 17940 for the time intervals 0-2.1 kyr, 2.1-5.5 kyr and 6.0-11.6 kyr ago. El Niño-style spectral peaks are significant at >99% over the last 6000 years, in the Early Holocene El Niño-style frequencies are rare except for a significant peak close to 6 years.

Subdecadal cyclicities

A significant portion of spectral energy in core 17940 (Figure 11) occurs in the subdecadal range and largely resembles the modern ENSO spectral signature (Mann and Park, 1994, and references therein) with a broad spectrum of *periodicities between 3 and 8 years* (Figure 15). These high-frequency oscillations already clearly emerge in the time domain (Figures 6 a, b)

Potential teleconnections between the Pacific ENSO and the South Asian monsoon were first discussed for the last 5,000 years by von Rad et al. (1999). However their laminated sediment record from the Arabian Sea does not show a significant response to the ENSO cycle. Further in the geological past, during the last glaciation and the Holocene, Heusser and Sirocko (1997) first related cyclic variations in the Asian monsoon to the Pacific El Niño system (Sirocko et al., 1999), suggesting oscillations of the ENSO-system as the main forcing mechanism. Climate model results of Clement et al. (1999) also suggest that changes in the ENSO generate a mean climate response in the tropics, a concept which is supported by variations of the seasonal SST anomaly as measured in banded corals of the Indian Ocean over the last 150 years (Charles et al., 1997).

In contrast to the laminated sediment records from the Pakistan continental margin, our non-laminated sediment record off Hong Kong shows -despite bioturbational mixing- an ENSO signal of high significance, which is in harmony with both the coral and the modelled records (Figure 15). The typical ENSO frequency in the (blue and red) color records of core 17940 is less well developed between 11,600 and 5,500 years BP and more obvious later (Table 2, Figure 15). This corroborates paleoclimate records from Ecuador lakes and coral-based SST (Rodbell et al., 1999; Gagan et al., 1998, 2000) and modeling results of Liu et al. (1999). They show that an intensified Asian Monsoon may have induced a reduction in El Niño variability in the Early Holocene.

Conclusions

Sonne-95 core 17940 has been retrieved from a "watchdog site " monitoring the monsoon variability southeast off Hong Kong (Sarnthein et al., 1994). Here the fluvial runoff of the Pearl River is documented both as a δ^{18}O-freshwater signal and by variations in the color records of siliciclastic sediment discharge, with the following results:

The intensity of the blue (B) sediment color stands for the portion of fluvial clay, enriched in total organic carbon (TOC). The intensity of red (R) stands for the fraction of hematite coated eolian quartz grains, that is the input of loess dust. Accordingly, the chromaticity ratio R/B is used as indicator of a sedimentation regime dominated by dry (winter) or wet (summer) monsoon.

Despite bioturbational mixing the apparently homogenous, non-laminated sediment section of core 17940 contains an unexpected but significant record of subdecadal climate variability, when sampled at a resolution of 0.3mm, equal to 0.3-0.7 years.

On the basis of wavelet analyses the suborbital periodicities are more discontinuous the shorter they are. However, various independent spectral techniques identify a number of significant millennial-to-decadal-scale periodicities which prevail over long time intervals.

Both the δ^{18}O-freshwater signal and the blue record of fluvial clay discharge show that the Holocene millennial-to-semimillennial-scale monsoon variations are dominated by a ~950-year periodicity, especially at 5500-2100 yr BP, and by a (? overtone) 400/500-yr periodicity at 6,000-11,600 yr BP. However, no DO-style cyclicity of ~1500 years was found.

In the 1/950-year frequency band the northern high-latitude climate components, as documented in the GISP2 ice core record, clearly lead, and thus probably control, the low-latitude monsoon variations by several 100 years. This lead increases to ~450 years in the Early Holocene, when orbital precession has reached a maximum. The mechanism of the 950-year periodicity and its global signal transfer are unknown.

A number of "common" solar cyclicities (200-year Suess cycle, 80-105 year Gleissberg cycle, 20/24 year Hale cycle and its multiple near 44 years, 11-yr Schwabe cycle) form a sub-

stantial portion of decadal-to-centennial-scale monsoon variability as documented at Site 17940.

The monsoon clearly responds to the ENSO signal with a broad spectrum of significant subdecadal frequencies over the last 6,000 years, but only with a single near-to-six-year period in the Early Holocene 6.0-11.6 ka.

In summary, the suborbital monsoon variability is controlled by basically 3-4 groups of external and internal forcings including the ENSO and solar cyles which in total roughly explain some 20-25% of the Holocene monsoon climate variability.

Acknowledgements

We are grateful to many people who have given us ideas and provided constructive criticism of this paper. This includes our late colleague Luejiang Wang who devoted great efforts to start this project with his outstanding experience. We are also greatly indebted to Michael Schulz for his assistance in spectral analysis. We thank Michael Schaaf for many valuable comments in an early phase of this project. This study was supported by the "Graduiertenkolleg Dynamik Globaler Kreisläufe im System Erde" and by grants of the Deutsche Forschungsgemeinschaft (DFG) "Monitor Monsun" and "ODP Site 1144 Monsun Südchina See".

References

Adkins, J.F., E.A. Boyle, L. Keigwin, and E. Cortijo, Variability of the North Atlantic thermohaline circulation during the last interglacial period, Nature, 390, 154-156, 1997.

An, Z., and S.C. Porter, Millennial-scale climatic oscillations during the last interglaciation in central China., Geology, 25(7), 603-606, 1997.

Appenzeller, C., T.F. Stocker, and M. Anklin, North Atlantic Oscillation dynamics recorded in Greenland ice cores, *Science*, 282(5388), 446-449, 1998.

Baker, A., C. Proctor, S.-F. Lauritzen, and J. Lundberg, SPEP: High-resolution stalagmite records of NE Atlantic Climate in the Last Millennium, *Pages Newsletter*, 8(2), 14, 2000.

Balsam, W.L., J.E. Damuth, and R.R. Schneider, Comparison of shipboard vs. shore-based spectral data from Amazon Fan cores: Implications for interpreting sediment composition, in *Proceedings of the Ocean Drilling Program, Scientific Results*, edited by Flood, R.D., Piper, D.J.W., Klaus, A., and Peterson, L.C., pp. 193-215, Ocean Drilling Program, 1997.

Balsam, W.L., and B.C. Deaton, Determining the composition of late Quaternary marine sediments from NUV, VIS, and NIR diffuse reflectance spectra, *Marine Geology*, 134(1-2), 31-55, 1996.

Balsam, W.L., B.C. Deaton, and J.E. Damuth, Evaluating optical lightness as a proxy for carbonate content in marine sediment cores, *Marine Geology*, 161(2-4), 141-153, 1999.

Balsam, W.L., B.L. Otto-Bliesner, and B.C. Deaton, Modern and last glacial maximum eolian sedimentation patterns in the Atlantic Ocean interpreted from sediment iron oxide content, *Paleoceanography*, 10, 493-507, 1995.

Barranco, F.T.J., W.L. Balsam, and B.C. Deaton, Quantitative reassessment of brick red lutites: evidence from reflectance spectrophotometry, *Marine Geology*, 89, 299-314, 1989.

Bauch, H.A., and J.P. Helmke, Glacial-Interglacial records of the reflectance of sediments from the Norwegian-Greenland-Iceland Sea (Nordic seas), *International Journal of Earth Sciences*, 88, 325-336, 1999.

Beer, J., S. Baumgartner, B. Hannen-Dittrich, J. Hauenstein, P. Kubik, C. Lukasczyk, W. Mende, R. Stellmacher, and M. Suter, Solar variability traced by cosmogenic isotopes, in *The sun as a variable star: Solar and stellar irradiance variations*, edited by Pap, J.M., Fröhlich, C., Hudson, H.S., and Solanki, S.K., pp. 291-300, Cambridge University Press, Cambridge, 1994a.

Beer, J., C.F. Joos, C. Lukasczyk, W. Mende, U. Siegenthaler, R. Stellmacher, and M. Suter, ^{10}Be as an indicator of solar variability and climate, in *The solar engine and its influence on terrestrial atmosphere and climate*, edited by Nesme-Ribes, E., pp. 221-233, Springer, Berlin, 1994b.

Beer, J., W. Mende, and R. Stellmacher, The role of the sun in climate forcing, *Quaternary Science Reviews*, 19, 403-415, 2000.

Bianchi, G.G., and N. McCave, Holocene periodicity in North Atlantic climate and deep-ocean flow south of Iceland, *Nature*, 397, 515-517, 1999.

Biondi, F., C.B. Lange, M.K. Hughes, and W.H. Berger, Interdecadal signals during the last millennium (AD 1117-1992) in the varve record of Santa Barbara Basin, California, *Geophysical Research Letters*, 24, 193-196, 1997.

Blackman, R.B., and J.W. Tukey, *The measurement of power spectra from the point of view of communication engineering*, 199 pp., Dover Publishing, New York, 1958.

Bond, G., W. Showers, M. Cheseby, R. Lotti, P. Almasi, P. deMenocal, P. Priore, H. Cullen, I. Hajdas, and G. Bonani, A Pervasive Millenial-Scale Cycle in North Atlantic Holocene and Glacial Climates, *Science*, 278, 1257-1266, 1997.

Bond, G.C., W. Showers, M. Elliot, M. Evans, R. Lotti, I. Hajdas, G. Bonani, and S. Johnson, The North Atlantic's 1-2 kyr climate rythm: Relation to Heinrich Events, Dansgaard/Oeschger Cycles and the Little Ice Age, in *Mechanisms of global climate change at millennial time scales*, edited by Clark, P.U., Webb, R.S., and Keigwin, L.D., pp. 35-58, American Geophysical Union, Washington DC, 1999.

Campbell, I.D., C. Campbell, M.J. Apps, N.W. Rutter, and A.B.G. Bush, Late Holocene ~ 1500 yr climatic periodicities and their implications, *Geology*, 26(5), 471-473, 1998.

Chapman, M.R., and N.J. Shackleton, What level of resolution is attainable in a deep-sea core? Results of a spectrophotometer study, *Paleoceanography*, 13(4), 311-315, 1998.

Chapman, M.R., and N.J. Shackleton, Evidence of 550-year and 1000-year cyclicities in North Atlantic circulation patterns during the Holocene, *The Holocene*, 10(3), 287-291, 2000.

Charles, C.D., D.E. Hunter, and R.G. Fairbanks, Interaction between the ENSO and the Asian Monsoon in a coral record of tropical climate, *Science*, 277, 925-928, 1997.

Clement, A., and M.A. Cane, A role for the tropical Pacific coupled ocean-atmosphere system on Milankovitch and millennial time scales. Part I: A modeling study of tropical Pacific variability, in *Mechanisms of global climate change at millennial time scales*, edited by Clark, P.U., Webb, R.S., and Keigwin, L.D., pp. 363-371, American Geophysical Union, Washington DC, 1999.

Cook, E.R., B.M. Buckley, and R.D. D'Arrigo, Interdecadal temperature oscillations in the Southern Hemisphere: Evidence from Tasman tree rings since 300 B.C., in *Natural climate variability on decade-to-century time scales*, edited by National Research Council, pp. 532-532, National Academy Press, Washington D.C., 1995.

Cook, E.R., R.D. D'Arrigo, and K.R. Briffa, A reconstruction of the North Atlantic Oscillation using tree-ring chronologies from North America and Europe, *The Holocene*, 8(1), 9-17, 1998.

Cook, E.R., D.M. Meko, and C.W. Stockton, A new assessment of possible Solar and Lunar forcing of the bidecadal drought rhythm in the western United States, *Journal of Climate*, 10(6), 1343–1356, 1997.

Cortijo, E., P. Yiou, L. Labeyrie, and M. Cremer, Sedimentary record of rapid climatic variability in the North Atlantic Ocean during the last glacial cycle, *Paleoceanography*, 10(5), 911-926, 1995.

De Geer, G., A geochronology of the last 12,00 years, Compte Rendus du XI Congres Geologique International, Stockholm, 1912.

Dean, W.E., Rates, timing, and cyclicity of Holocene eolian activitiy in north-central United States: Evidence from varved lake sediments, *Geology*, 25(4), 331-334, 1997.

Delworth, T.L., and M.E. Mann, Observed and simulated multidecadal variability in the Northern Hemisphere, *Climate Dynamics*, 16(9), 661-676, 2000.

Dunbar, R.B., G.M. Wellington, M.W. Colgan, and P.W. Glynn, Eastern Pacific sea surface temperature since 1600 A.D.: The δ^{18}O record of climate variability in Galápagos corals, *Paleoceanography*, 9(2), 291-315, 1994.

Ehrenberg, C.G., Passatstaub und Blutregen. Ein großes organisches unsichtbares Wirken und Leben in der Atmosphäre, *Abh. Kgl. Akad. Wiss. Berlin 1847*, 269-460, 1849.

Feng, Z., L.G. Thompson, E. Mosley-Thompson, and T. Yao, Temporal and spatial variations of climate in China during the last 10 000 years, *The Holocene*, 3(2), 174-180, 1993.

Findlater, J., A major low level air current near the Indian Ocean during the northern summer, *Quarterly Journal of the Royal Meteorological Society*, 95, 362-380, 1969.

Fischer, H., M. Werner, D. Wagenbach, M. Schwager, T. Thorsteinnson, F. Wilhelms, J. Kipfstuhl, and S. Sommer, Little ice age clearly recorded in northern Greenland ice cores, *Geophysical Research Letters*, 25(10), 1749-1752, 1998.

Friedrich, M., B. Kromer, K.F. Kaiser, M. Spurk, K.A. Hughen, and S.J. Johnsen, High-resolution climate signals in the Boelling/Alleroed Interstadial as reflected in European tree-ring chronologies compared to marine varves and ice-core records, *Quaternary Science Reviews*, 848(in press), 2001.

Friis-Christensen, E., and K. Lassen, Length of the solar cycle; an indicator of solar activity closely associated with climate, *Science*, 254(5032), 698-700, 1991.

Gagan, M.K., L.K. Ayliffe, J.W. Beck, J.E. Cole, E.R.M. Druffel, R.B. Dunbar, and D.P. Schrag, New views of tropical paleoclimates from corals, *Quaternary Science Reviews*, 19, 45-64, 2000.

Gagan, M.K., L.K. Ayliffe, D. Hopley, J.A. Cali, G.E. Mortimer, J. Chappell, M.T. McCulloch, and M.J. Head, Temperature and surface-ocean water balance of the Mid-Holocene tropical western Pacific, *Science*, 279, 1014-1018, 1998.

Gleissberg, W., A table of secular variations of the solar cycle, *Journal of Geophysical Research*, 49, 243-244, 1944.

Gleissberg, W., The Eighty-Year Sunspot Cycle, *J. British Astron. Ass.*, 68, 148-152, 1958.

Grootes, P.M., and M. Stuiver, Oxygen 18/16 variability in Greenland snow and ice with 10^{-3} - to 10^{5}-year resolution, *Journal of Geophysical Research*, 102(C12), 26455-26470, 1997.

Hale, G.E.,The Law of Sun-Spot Polarity, in *Sunspot Cycles* edited by Schove E. J., Hutchinson Ross Publishing Company 1983, Stroudsburg, PA, pp. 221, 1924.

Hastenrath, S., and P.J. Lamb, On the heat budget of hydrosphere and atmosphere in the Indian Ocean, *Physical Oceanography*, 10(5), 649-708, 1980.

Hedges, J.I., and R.G. Keil, Sedimentary organic matter preservation: an assessment and speculative synthesis, *Marine Chemistry*, 49, 81-115, 1995.

Hesp, P.A., C.C. Hung, M. Hilton, C.L. Ming, and I.M. Turner, A first tentative Holocene sea-level curve for Singapore, *Journal of Coastal Research*, 14(1), 308-314, 1998.

Heusser, L.E., and F. Sirocko, Millennial pulsing of environmental change in southern California from the past 24 k.y.: a record of Indo-Pacific ENSO events?, *Geology*, 25(3), 243-246, 1997.

Hoyt, D.V., and K.H. Schatten, *The role of the sun in climate change*, 279 pp., Oxford University Press, New York, 1997.

Hughen, K.A., J.T. Overpeck, L.C. Peterson, and R.F. Anderson, The nature of varved sedimentation in the Cariaco Basin, Venezuela, and its paleoclimatic significance., in *Paleoclimatology and Paleoceanography from laminated sediments*, edited by Kemp, A.E.S., pp. 117-183, Geological Society Special Publication, 1996.

Hughen, K.A., D.P. Schrag, S.B. Jacobsen, and W. Hantoro, El Niño during the last interglacial period recorded by a fossil coral from Indonesia, *Geophysical Research Letters*, 26(20), 3129-3132, 1999.

Hurrell, J.W., and H. van Loon, Decadal variations in climate associated with the North Atlantic Oscillation, *Climatic Change*, 36(3/4), 301-326, 1997.

Jian, Z., L. Wang, M. Kienast, M. Sarnthein, W. Kuhnt, H. Lin, and P. Wang, Benthic foraminiferal paleoceanography of the South China Sea over the last 40,000 years, *Marine Geology*, 156, 159-186, 1999.

Keeling, C.D., and T.P. Whorf, Decadal oscillations in global temperature and atmospheric carbon dioxide, in *Natural climate variability on decade-to-century time scales*, edited by National Research Council, pp. 97-109, National Academy Press, Washington D.C., 1995.

Keigwin, L.D., W.B. Curry, S.J. Lehman, and S. Johnsen, The role of the deep ocean in North Atlantic climate change between 70 and 130 kyr ago, *Nature*, 371, 323-326, 1994.

Kodak Scientific Imaging Systems, *Kodak color separation guide and gray scale (small)*, Eastman Kodak Company, 1997.

Kudrass, H.R., H. Erlenkeuser, R. Vollbrecht, and W. Weiss, Global nature of the Younger Dryas cooling event inferred from oxygen isotope data from Sulu Sea cores, *Nature*, 349, 406-409, 1991.

Labitzke, K., and H. van Loon, Associations between the 11-year solar cycle, the QBO, and the atmosphere. Part I: The troposphere and stratosphere in the northern hemisphere during winter, *J. of Atmos. Terr. Phys*, 50, 197-206, 1988.

Laird, K.R., S.C. Fritz, K.A. Maasch, and B.F. Cumming, Greater drought intensity and frequency before AD 1200 in the Northern Great Plains, USA, *Nature*, 384, 552-554, 1996.

Lau, K.-M., and H. Weng, Climate signal detection using wavelet transform: How to make a time series sing, *Bulletin of the American Meteorological Society*, 76(12), 2391-2402, 1995.

Liu, Z., R. Jacob, J. Kutzbach, S. Harrison, and J. Anderson, Monsoon impact on El Niño in the early Holocene, *PAGES Newsletter*, 7(2), 16-17, 1999.

Lomb, N.R., Least-squares frequency analysis of unequally spaced data, *Astrophysics and Space Science*, 39, 447-462, 1976.

Mann, M.E., and J. Park, Global-scale modes of surface temperature variability on interannual to century timescales, *Journal of Geophysical Research*, 99, 25819-25833, 1994.

Mayewski, P.A., L.D. Meeker, M.S. Twickler, S. Whitlow, Q. Yang, W.B. Lyons, and M. Prentice, Major features and forcing of high-latitude northern hemisphere atmospheric circulation using a 110,000-year-long glaciochemical series, *Journal of Geophysical Research*, 102(C12), 26345-26366, 1997.

Merrill, R.B., and J.W. Beck, The ODP color digital imaging system; color logs of Quaternary sediments from the Santa Barbara Basin, Site 893, in *Proceedings of the Ocean Drilling Program, Scientific Results*, edited by Kennett, J.P., Baldauf, J.G., and Lyle, M., pp. 45-59, Ocean Drilling Program, College Station, 1995.

Mursula, K., and T. Ulich, A new method to determine the solar cycle length, *Geophysical Research Letters*, 25(11), 1837-1840, 1998.

Nagao, S., and S. Nakashima, The factors controlling vertical color variations of North Atlantic Madeira Abyssal Plain sediments, *Marine Geology*, 109, 83-94, 1992.

Nakajima, T., H. Kawahata, and S. Nagao, Estimating organic carbon contents in pelagic calcareous sediments by color measurements, *Journal of the Geological Society of Japan*, 104(1), 64-67, 1998.

Neelin, D., and M. Latif, El Niño Dynamics, *Physics Today*, 51(12), 32-36, 1998.

Nicholson, S.A., A review of climate dynamics and climate variability in Eastern Africa, in *The limnology, climatology and paleoclimatology of the East African Lakes*, edited by Johnson, T.C., and Odada, E., pp. 25-56, Gordon and Breach, Amsterdam, 1996.

Ortiz, J., A. Mix, S. Harris, and S. O'Connell, Diffuse spectral reflectance as a proxy for percent carbonate content in North Atlantic sediments, *Paleoceanography*, 14(2), 171-186, 1999b.

Ortiz, J.D., S. O'Connell, and A. Mix, Data report: Spectral reflectance observations from recovered sediments, in *Proc. ODP, Sci. Results 162*, edited by Raymo, M.E., Jansen, E., Blum, P., and Herbert, T.D., pp. 259-264, (Ocean Drilling Program), College Station, TX, 1999a.

Paillard, D., L. Labeyrie, and P. Yiou, Macintosh program performs time-series analysis, *Eos Trans. AGU*, 77, 379., 1996.

Pätzold, J., and C. Dullo, Reconstruction of sea surface temperatures in Holocene times: coral-based studies in the Red Sea and the Western Indian Ocean, *Pages Newsletter*, 8(2), 16-17, 2000.

Pflaumann, U., and Z. Jian, Modern distribution patterns of planktonic foraminifera in the South China Sea and western Pacific: a new transfer technique to estimate regional sea-surface temperatures, *Marine Geology*, 156(1-4), 41-83, 1999.

Pike, J., and A.E.S. Kemp, Early Holocene decadal-scale ocean variability recorded in Gulf of California laminated sediments, *Paleoceanography*, 12(2), 227-238, 1997.

Porter, S.C., High-resolution paleoclimatic information from Chinese eolian sediments based on grayscale intensity profiles., *Quaternary Research*, 53, 70-77, 2000.

Porter, S.C., and Z. An, Correlation between climate events in the North Atlantic and China during the last glaciation, *Nature*, 375, 305-308, 1995.

Rack, F.R., and R.B. Merrill, Interhole correlations at site 893, Santa Barbara basin : Construction of a 16,000 year composite record using magnetic susceptibility and digital color imaging data, in *Proceedings of the Ocean Drilling Program, Scientific Results*, edited by Kennett, J.P., Baldauf, J.G., and Lyle, M., pp. 169-183, Ocean Drilling Program, College Station, 1995.

Ram, M., M. Stolz, and G. Koenig, Eleven year cycle of dust concentration variability observed in the dust profile of the GISP2 ice core from Central Greenland: Possible solar cycle connection, *Geophysical Research Letters*, 24(19), 2359-2362, 1997.

Ram, M., and M.R. Stolz, Possible solar influences on the dust profile of the GISP2 ice core from Central Greenland, *Geophysical Research Letters*, 26(8), 1043-1046, 1999.

Rasband, W., NIH Image 1.61 PPC, National Institutes for Health, USA, 1996.

Raymond, P.A., and J.E. Bauer, Riverine export of aged terrestrial organic matter to the North Atlantic Ocean, *Nature*, 409, 497-500, 2001.

Rittenour, T.M., J. Brigham-Grette, and M.E. Mann, El Niño-like climate teleconnections in New England during the Late Pleistocene, *Science*, 288(5468), 1039-1042, 2000.

Rodbell, D.T., G.O. Seltzer, D.M. Anderson, M.B. Abbott, D.B. Enfield, and J.H. Newman, An 15,000-year record of El Niño-driven alluviation in southwestern Ecuador, *Science*, 283, 516-520, 1999.

Sarnthein, M., and B. Koopmann, Late Quaternary deep-sea record on Northwest African dust supply and wind circulation, in *Sahara and surrounding seas; sediments and climatic changes; proceedings of an international symposium*, edited by Sarnthein, M., Seibold, E., and Rognon, P., pp. 239-253, A.A. Balkema, Cape Town, South Africa, 1980.

Sarnthein, M., U. Pflaumann, P.X. Wang, and H.K. Wong, Preliminary Report on Sonne-95 Cruise "Monitor Monsoon" to the South China Sea, *Berichte-Reports, Geologisch-Paläontologisches Institut der Universität Kiel*, 68, 0-225, 1994.

Scargle, J.D., Studies in astronomical time series analysis. III. Fourier transforms, autocorrelation functions, and cross-correlation functions of unevenly spaced data., *The Astrophysical Journal*, 263(2), 874-887, 1989.

Schaaf, M., and J. Thurow, A fast and easy method to derive highest-resolution time-series datasets from drillcores and rock samples, *Sedimentary Geology*, 94, 1-10, 1994.

Schaaf, M., and J. Thurow, Late Pleistocene-Holocene climatic cycles recorded in Santa Barbara Basin Sediments: Interpretation of color density logs from Site 893, in *Proceedings of the Ocean Drilling Program, Scientific Results Leg 146*, edited by Kennett, J.P., Baldauf, J.G., and Lyle, M., pp. 31-43, Ocean Drilling Program, College Station, 1995.

Schaaf, M., and J. Thurow, Tracing short cycles in long records-The study of interannual to inter-centennial climate change from long sediment records, examples from the Santa Barbara Basin, *Journal of the Gological Society, London*, 154(4), 613-622, 1997.

Schlesinger, M.E., and N. Ramankutty, An oscillation in the global climate system of period 65-70 years, *Nature*, 367, 723-726, 1994.

Schulz, M., SPECTRUM und ENVELOPE Computerprogramme zur Spektralanalyse nicht äquidistanter paläoklimatischer Zeitreihen, *Ber. Sonderforschungsbereich 313, Univ. Kiel*, 65, 1-131, 1996.

Schulz, M., and M. Mudelsee, REDFIT: estimating red-noise spectra directly from unevenly spaced paleoclimatic time series, *Computers & Geosciences*, in press,

Schulz, M., and A. Paul, Holocene climate variability on centennial-to-milennial timescales: 1. Climate records from the North-Atlantic realm., in *Past climate and its significance for human history in NW Europe, the last 10,000 years*, edited by Berger, W.H., and Wefer, G., Springer Verlag, Berlin, 2001.

Schulz, M., and K. Stattegger, SPECTRUM: Spectral analysis of unevenly spaced paleoclimatic time series, *Computers & Geosciences*, 23(9), 929-945, 1997.

Schwabe, H., Beobachtungen der Sonne im Jahre 1843, *Astronomische Nachrichten*, 20(495), 1843.

Shindell, D., D. Rind, N. Balachandran, J. Lean, and p. Lonergan, Solar cycle variability, ozone, and climate, *Science*, 284, 305-308, 1999.

Sirocko, F., D. Garbe-Schönberg, A. McIntyre, and B. Molfino, Teleconnections between the subtropical monsoons and high-latitude climates during the last deglaciation, *Science*, 272, 526-529, 1996.

Sirocko, F., D. Leuschner, M. Staubwasser, J. Maley, and L. Heusser, High-frequency oscillations of the last 70,000 years in the tropical/subtropical and polar climates, in *Mechanisms of global climate change at millennial time scales*, edited by Clark, P.U., Webb, R.S., and Keigwin, L.D., pp. 113-126, American Geophysical Union, Washington DC, 1999.

Sonett , C.P., and H.E. Suess, Correlation of bristlecone pine ring widths with atmospheric ^{14}C variations : A climate-Sun relation., *Nature*, 307, 141-143, 1984.

Steig, E.J., D.L. Morse, E.D. Waddington, and P.J. Polissar, Using the sunspot cycle to date ice cores, *Geophysical Research Letters*, 25(2), 163-166, 1998.

Stuiver, M., and T.F. Braziunas, Sun, ocean, climate and atmospheric $^{14}CO_2$: an evaluation of causal and spectral relationships, *The Holocene*, 3(4), 289-305, 1993.

Stuiver, M., T.F. Braziunas, P.M. Grootes, and G.A. Zielinski, Is there evidence for solar forcing of climate in the GISP2 oxygen isotope record?, *Quaternary Research*, 48(3), 259-266, 1997.

Stuiver, M., P.M. Grootes, and T.F. Braziunas, The GISP2 $\delta^{18}O$ climate record of the past 16,500 years and the role of the sun, ocean, and volcanoes, *Quaternary Research*, 44, 341-354, 1995.

Stuiver, M., P.J. Reimer, E. Bard, J.W. Beck, G.S. Burr, K.A. Hughen, B. Kromer, G. McCormack, J. Van Der Plicht, and M. Spurk, INTCAL98 radiocarbon age calibration, 24,000-0 cal BP, *Radiocarbon*, 40(3), 1041-1083, 1998.

Sun, X., and X. Li, A pollen record of the last 37 ka in deep sea core 17940 from the northern slope of the South China Sea, *Marine Geology*, 156, 227-244, 1999.

Sun, X., X. Li, Y. Luo, and X. Chen, The vegetation and climate at the last glaciation on the emerged continental shelf of the South China Sea, *Palaeogeography, Palaeoclimatology, Palaeoecology*, 160, 301-316, 2000.

Thompson, L.G., T. Yao, M.E. Davis, K.A. Henderson, E. Mosley-Thompson, P.-N. Lin, J. Beer, H.-A. Synal, J. Cole-Dai, and J.F. Bolzan, Tropical climate instability: The last glacial cycle from a Qinghai-Tibetan ice core, *Science*, 276, 1821-1825, 1997.

Torrence, C., and G.P. Compo, A practical guide to wavelet analysis, *Bulletin of the American Meteorological Society*, 79(1), 61-78, 1998.

Trauth, M., Bioturbate Signalverzerrrung hochauflösender paläozeanographischer Zeitreihen., *Berichte-Reports, Geologisch-Paläontologisches Institut der Universität Kiel*, 74, 0-167, 1995.

Trauth, M.H., M. Sarnthein, and M. Arnold, Bioturbational mixing depth and carbon flux at the seafloor, *Paleoceanography*, 12(3), 517-526, 1997.

UK Meteorological Office, NINO3 Sea Surface Temperature GISST 2.3 dataset [5S-5N, 150W-90W]., *UK Meteorological Office*, 1992.

van Loon, H., and K. Labitzke, Associations between the 11-year solar cycle, the QBO, and the atmosphere. Part II: Surface and 700mb in the northern hemisphere winter, *Journal of Climate*, 1, 905-920, 1988.

von Rad, U., M. Schaaf, K.H. Michels, H. Schulz, W.H. Berger, and F. Sirocko, A 5000-yr Record of Climate Change in Varved Sediments from the Oxygen Minimum Zone off Pakistan, Northeastern Arabian Sea, *Quaternary Research*, 51(1), 39-53, 1999.

Vos, H., A. Sanchez, B. Zolitschka, A. Brauer, and J.F.W. Negendank, Solar activitiy variations recorded in varved sediments from the crater lake of Holzmaar - a maar lake in the Westeifel Volcanic Field, Germany, *Surveys in Geophysics*, 18, 163-182, 1997.

Wang, L., M. Sarnthein, H. Erlenkeuser, J. Grimalt, P. Grootes, S. Heilig, E. Ivanova, M. Kienast, C. Pelejero, and U. Pflaumann, East Asian monsoon climate during the Late Pleistocene: high-resolution sediment records from the South China Sea, *Marine Geology*, 156, 245-284, 1999a.

Wang, L., M. Sarnthein, H. Erlenkeuser, P.M. Grootes, J.O. Grimalt, C. Pelejero, and G. Linck, Holocene variations in asian monsoon moisture: A bidecadal sediment record from the South China Sea, *Geophysical Research Letters*, 26(18), 2889-2892, 1999b.

Wang, L., M. Sarnthein, P.M. Grootes, and H. Erlenkeuser, Millennial reoccurrence of century-scale abrupt events of East Asian monsoon: A possible heat conveyor for the global deglaciation, *Paleoceanography*, 14(6), 725-731, 1999c.

Wang, P., W.L. Prell, P. Blum, and Leg 184 Shipboard Scientific Party, *Proceedings of the Ocean Drilling Program, Initial Reports*, vol. 184, 1-77 pp.,Ocean Drilling Program, College Station , TX, 2000.

Webster, P.J., and T.N. Palmer, The past and the future of El Niño, *Nature*, 390, 562-564, 1997.

Wei, K., and F. Gasse, Oxygen isotopes in lacustrine carbonates of West China revisited: implications for post glacial changes in summer monsoon circulation, *Quaternary Science Reviews*, 18(12), 1315-1334., 1999.

Yu, Z., and E. Ito, Possible solar forcing of century-scale drought frequency in the Northern Great Plains, *Geology*, 27(3), 263-266, 1999.

Yu, Z., and E. Ito, Historical solar variability and mid-continent drought, *Pages Newsletter*, 8(2), 6-7, 2000.

Zhang, J.C., and Z.G. Liu, *Climate of China*, 376 pp., Wiley, New York, 1992.

Zolitschka, B., Image analysis and microscopic investigation of annually laminated lake sediments from Fayetteville Green Lake (NY, USA) lake C2 (NWT, Canada) and Holzmaar (Germany): a compilation, in *Paleoclimatology and Paleoceanography from laminated sediments*, edited by Kemp, A.E.S., pp. 49-55, Geological Society Special Publication, 1996.

Zolitschka, B., A. Brauer, J.F.W. Negendank, and A. Lang, Annually dated late Weichselian continental paleoclimate record from the Eifel, Germany, *Geology*, 28(9), 783-786, 2000.

4.3: Toward a high-resolution stable isotope stratigraphy of the last 1.1 million years: Site 1144, South China Sea (C. Bühring, M. Sarnthein, H. Erlenkeuser)

Toward a high-resolution stable isotope stratigraphy of the last 1.1 million years: Site 1144, South China Sea

Christian Bühring[1], Michael Sarnthein[1], Helmut Erlenkeuser[2]

[1] Institut für Geowissenschaften, Christian-Albrechts-Universität zu Kiel

[2] Leibniz-Labor für Altersbestimmung und Isotopenforschung, Christian-Albrechts-Universität zu Kiel

07.09.2001 Draft

Submitted to

Proceedings of the Ocean Drilling Program,

Scientific Results Volume 184

Table of Contents

Abstract

Ocean Drilling Program Site 1144 in the northern South China Sea provides, with high sedimentation rates, a climatic record of monsoon variations on centennial to orbital time scales. Here we present oxygen and carbon stable isotope records of planktonic foraminifer *G. ruber* (white). They extend, as almost continuous records from the Holocene to Marine Isotope Stage 12 and with low resolution to the early Pleistocene stage 29. Sedimentation rates average 0.74 m/k.y. and vary from 0.13 to 1.8 m/k.y. Major hiatuses occur at peak warm stages 5.5 and 11.3, possibly as a result of strong contour current erosion. Another hiatus extends from isotope stage 29 to 73(?). The short-term variations in the isotope record for the last 110 k.y. closely parallel the $\delta^{18}O$ record of the GISP2 ice core.

Introduction

A principal objective of ODP Leg 184, Site 1144 (Figure 1), was to recover a complete sequence of high-sedimentation-rate, hemipelagic sediments of the middle and late Pleistocene to address fundamental questions regarding the paleoenvironment in the South China Sea (SCS) and to reconstruct the history of the East Asian Monsoon on orbital to sub-Milankovitch time scales over the last 1 million years.

To date only a few published paleoceanographic records from South East Asian marginal seas provide a time resolution sufficient to resolve high-frequency variations in local ocean circulation and paleoclimate. The high accumulation rates at Site 1144 (20.05° N, 117.42°E, 2037 m water depth; Figure 1), retrieved from a thick, hemipelagic sediment drape (Sarnthein et al., 1994; ODP Leg 184 Shipboard Scientific Party, 2000) on the northern continental slope of the South China Sea, offer an unprecedented opportunity to reconstruct Quaternary monsoon variations on millennial to centennial time scales.

Our primary goals are (1) to provide a detailed and reliable high resolution stable isotope stratigraphy for the northern South China Sea over the last 1 million years, (2) to uncover stratigraphic gaps in centennial-to-millennial climate oscillations during the Brunhes Chron,

with special focus on the last three glacial and interglacial periods, and (3) to compare paleoclimatic variability inferred from stable isotopes of planktonic foraminifers during marine isotope stages (MIS) 1-3 with the GISP2 ice core record and thus establish the links between marine and terrestrial records.

Additionally, this stratigraphy forms the paleoclimatic framework and precise age model for a number of paleoceanographic and paleoclimatic studies published in this volume (Tamburini et al., Boulay et al, Higginson et al., chapters XX) and elsewhere.

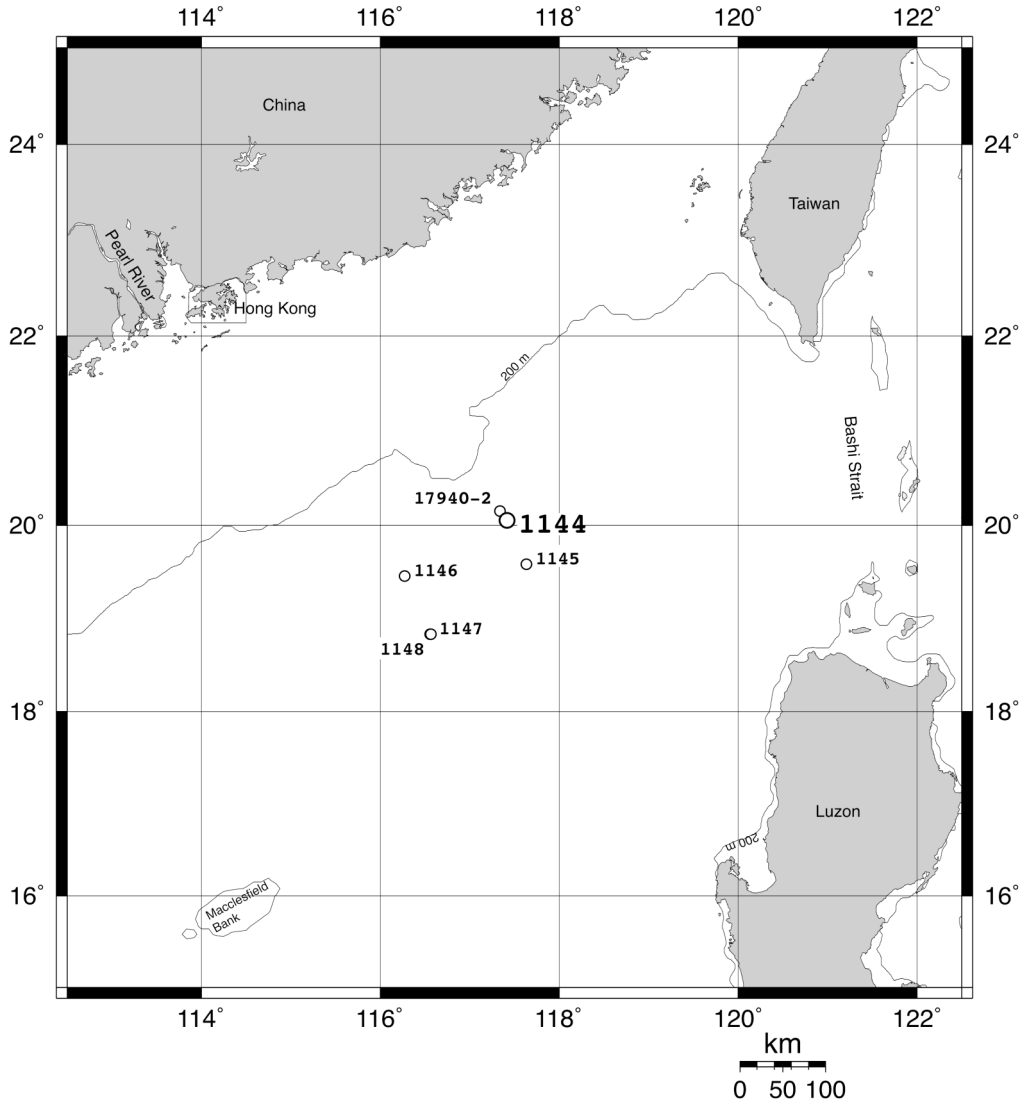

Figure 1. Map showing the locations of ODP Leg 184 Sites 1144 through 1148 and the position of SONNE-95 core 17940-2 in the northern South China Sea. 200 m isobath marks shelf edge.

Methods

Stable isotope analysis

The oxygen isotope record is based on *Globigerinoides ruber*, a surface dwelling planktonic foraminifer (Bé and Tolderlund, 1971) that records changes in surface water $\delta^{18}O$ and $\delta^{13}C$ (Linsley and v. Breymann, 1991). Stable oxygen ($\delta^{18}O$) and carbon ($\delta^{13}C$) isotope analyses at Site 1144 were made at uneven sampling intervals (listed in Table 1), and more than 1285 samples were processed for this study.

Depth interval [mcd]	sample interval [cm]
0-122	0.25
122.0-164.5	0.8
164.8- 235.2	0.24
251.6-422.6	0.27
427.4-517.6	1.15

Table 1. Average sample spacing for stable isotope measurements at Site 1144.

Approximately 15-20 cm^3 of wet bulk sediment were freeze-dried for each sample, weighed, and wet-sieved to remove the fraction <63μm. The sand fraction (>63μm) was oven dried at 40° C for 24 hours, then weighed to determine the percent sand fraction.

Because foraminifer tests are rare in the common size class 315-400 μm we chose to use the 250-315 μm fraction (Linsley and Dunbar, 1993; Lee et al., 1999). For each sample ~ 15-20 tests of the planktonic foraminifer *Globigerinoides ruber,* white variety, were picked out of the 250-315μm fraction, following the morphotype classification of L. Wang (2000).

In a few samples not enough specimens complying with the *sensu strictu* morphotype requirements were found. These samples were supplemented with as many *sensu latu* tests as necessary to reach the amount of carbonate required for reliable measurements. The number of specimens (15-20) and the rather narrow size fraction were chosen to minimize the influ-

ence of vital effects (Berger et al., 1978), and moreover, to average out the signal noise linked to differential bioturbational mixing.

Only tests that were intact and without visible dissolution were selected. A substantial effort was made to avoid pink *G. ruber* which is generally isotopically lighter (Δ 0.17‰ $\delta^{18}O$, Thompson et al., 1979) than *G. ruber* white. At Site 1144 the pink variety of *G. ruber* is either light pink throughout or, more often, the pigmentation is very weak and only the very first chambers are pink coloured, which complicates identification.

Before isotope analysis, the foraminifer tests of each sample were immersed in ultra-pure ethanol, carefully cracked to expose the interior of the chambers and ultrasonified for 20 seconds. Subsequently, the ethanol with possible contaminants still in suspension was siphoned off with a syringe and the remaining foraminifer fragments dried at 40°C. The cleaned samples for isotopic measurements weighed 150-200 μg. For isotope analysis standard techniques were used: the carbonate was reacted with 100% ortophosphoric acid at 70°C and the isotopic ratios were determined using a Finnigan MAT 251 micromass spectrometer with the Carbo Kiel device (Kiel I type) at the Leibniz Laboratory of Kiel University. Samples from the interval 172.16 - 182.17 mcd (meters composite depth) were measured on a Finnigan Delta Plus XL mass spectrometer combined with a Kiel GasBench II continous flow interface. Precision was regularly checked by running (internal) Solnhofen limestone standards. Conversion to the PeeDee Belemnite (PDB) scale was performed using the National Bureau of Standards NBS-20 carbonate standard. At the MAT 251 the external standard errors over one year (2000-2001) were <0.08‰ for $\delta^{18}O$ and < 0.05‰ for $\delta^{13}C$ (both 1-sigma values), at the Delta Plus XL mass spectrometer the errror reached <0.096‰ for $\delta^{18}O$ (NBS 19).

Composite depth model

We used the continuous shipboard-defined (Leg 184 Shipboard Scientific Party, 2000) composite-depth scale (mcd) which links sediment profiles of cores from Holes A, B, and C down to 235.41 mcd. Splicing of cores below this interval was precluded by incomplete core

recovery and incidental alignment of core gaps (Leg 184 Shipboard Scientific Party, 2000). Although the cores below 235 mcd can not be tied directly to the composite depth scale, it was possible to correlate them with each other by means of correlative features of Multi Sensor Track records (MST) and sediment color, and their depths were adjusted accordingly. This relative or floating composite depth scale is not tied to the overlying composite depth scale (Leg 184 Shipboard Scientific Party, 2000). The majority of samples below 235 mcd are from Hole A, some gaps resulting from the "floating" composite depth scale will be bridged in the future with samples from Hole B.

Results and Discussion

Oxygen isotope stratigraphy and chronology

All stable isotope data of ODP Site 1144 are given in Table 2, Appendix 2, and presented in Figure 2. Data are also available as an electronic file. The 518 m long sediment section reaches back to at least 1.03 Ma. Figure 3 shows a blow-up for the uppermost 120 m, spanning the last 135 k.y.

In general, the well known sawtooth-like appearance of the 100-k.y. climatic cycles (Prell et al., 1986) is clearly developed (Figure 4). High amplitude $\delta^{18}O$ variations are apparent throughout the entire record of Site 1144 with slightly decreasing amplitudes within the bottom 100 m. Marine oxygen Isotope Stages (MIS) 1 to 29 (Emiliani, 1955; Shackleton and Opdyke, 1973) are easily identified (Figure 2 and 4). The age model for Site 1144 was constructed by combining two independent reference records, the GISP2 ice core and the ODP Site 677 oxygen isotope records. The top 106 m of the Site 1144 $\delta^{18}O$-record were correlated to GISP2 (Grootes and Stuiver, 1997) and dated according to the GISP2 time-scale (Alley et al., 1997; Meese et al., 1997).

The oxygen isotope stages of the interval 106-504 mcd (108-1027 ka) were identified by visual correlation to the orbitally tuned $\delta^{18}O$-record of ODP Site 677 (Shackleton et al., 1990). Ages for the whole record were defined through linear interpolation between the tie points listed in Table 3.

Below 480 mcd we used two biostratigraphic datums as age tie points. The upper end of the *small Gephyrocapsa* acme zone (Gartner, 1988) at 500.66 mcd with an age of 1020 ka (Shyu, this volume) was used as age tie point to determine the position of MIS 29 (Figure 2 and 4). A major hiatus between 500.66 and 506.82 mcd is indicated by the LO of *Discoaster brouweri / triradiatus* at 506.82 mcd (Shyu, this volume). The isotope stages below the hiatus can not be identified with certainty (possibly MIS 73).

Table 3

Depth [mcd]	$\delta^{18}O$ [‰]	Age [ka]	sedimentation rate [m / ky]	Event
0.06	-2.72	90		
6.73	-1.53	11730	0.57	Top YD
10.01	-2.04	14375	1.24	IS 1
26.19	-1.17	23370	1.80	IS 2
26.89	-0.62	23810	1.59	H2
31.62	-1.55	27700	1.22	IS3
33.07	-1.56	28890	1.22	IS 4
33.57	-1.05	29290	1.25	H3
36.62	-1.62	31720	1.26	IS5
38.63	-1.57	33790	0.97	IS6
41.76	-1.70	36660	1.09	IS7
44.02	-1.76	38320	1.36	IS 8
44.52	-1.10	38770	1.11	H4
45.52	-0.14	39660	1.12	IS9
46.97	-1.72	40960	1.12	IS10
48.73	-1.77	42530	1.12	IS 11
52.9	-1.66	45140	1.60	IS 12
53.56	-1.04	45660	1.27	H5
55.06	-1.58	47090	1.05	IS 13
64.77	-2.22	56370	1.05	IS 16
66.47	-1.67	58230	0.91	IS 17
70.33	-1.53	61870	1.06	IS18
77.95	-2.13	68610	1.13	IS 19
81.21	-1.94	72880	0.76	IS 20
88.57	-2.49	83750	0.68	IS 21
95.42	-2.23	89710	1.15	IS 22
104.13	-2.50	100250	0.83	IS 23
106.81	-1.63	106360	0.44	MIS 5.4
110.05	-2.45	117400	0.29	Hiatus top

Depth [mcd]	$\delta^{18}O$ [‰]	Age [ka]	sedimentation rate [m / ky]	Event
110.3	-1.68	124780		Hiatus bot
112.05	-2.51	128500	0.47	MIS 5.53
114.55	-0.82	133310	0.52	MIS 6.2
117.23	-0.79	138010	0.57	MIS 6.3
121.81	-0.74	146040	0.57	MIS 6.4
140.05	-0.79	177990	0.57	MIS 6.6
158.75	-1.37	226970	0.38	MIS 7.4
165.76	-2.21	243780	0.42	MIS 7.5
172.16	-0.95	267940	0.26	MIS 8.4
183.92	-2.29	284380	0.72	MIS 8.5
193.61	-1.27	300810	0.59	MIS 8.6
195.49	-2.58	305000	0.45	MIS 9.1
207.4	-2.71	329030	0.50	MIS 9.3
209.16	-0.46	336980	0.22	MIS 10.2
246.33	-1.74	391000	0.69	hiatus top
247.13	-1.71	411860		hiatus bot
251.58	-0.63	420570	0.51	MIS 12.22
262.18	-0.37	439420	0.56	MIS 12.24
275.87	-0.60	462210	0.60	MIS 12.4
300.52	-2.28	500990	0.64	MIS 13
306.52	-1.21	512060	0.54	MIS 14.2
311.11	-1.51	546920	0.13	MIS 14.4
323.61	-2.25	612040	0.19	MIS 15.5
325.11	-0.76	622990	0.14	MIS 16.2
355.79	-2.25	687030	0.48	MIS 17.3
365.31	-1.08	717190	0.32	MIS 18.2
374.67	-1.79	741470	0.39	MIS 18.3
376.67	-1.22	750000	0.23	MIS 18.4
383.59	-1.84	783960	0.20	MIS 19.3
391.3	-1.16	799110	0.51	MIS 20.2
399.28	-2.16	856910	0.14	MIS 21
403.51	-0.89	872000	0.28	MIS 22
420.88	-1.89	905000	0.53	MIS 23
426.7	-0.90	912040	0.83	MIS 24
450.43	-0.81	967130	0.43	MIS 26
472.31	-1.16	1003970	0.59	MIS 28
500.66		1020000	1.77	LO small Gephyro-capsa Acme
503.76	-2.32	1028000	0.39	MIS 29.2 hiatus
506.82		1960000		LO D. brouweri /triradiatus
517.56	-2.07	1975600	0.69	MIS 73

Table 3: Names, midpoint ages, and sedimentation rates of $\delta^{18}O$ stages and events at Site 1144. YD: Younger Dryas; IS: GISP2 interstadial equivalent. Ages of last 110 kyr are based on the Meese/Sowers timescale (Meese et al. 1994); H1-6: Heinrich event analog; Ages of Marine Isotope Stages (MIS) 6-29 are based on Shackleton et al. (1990); nannofossil ages after to Shyu et al. (this volume).

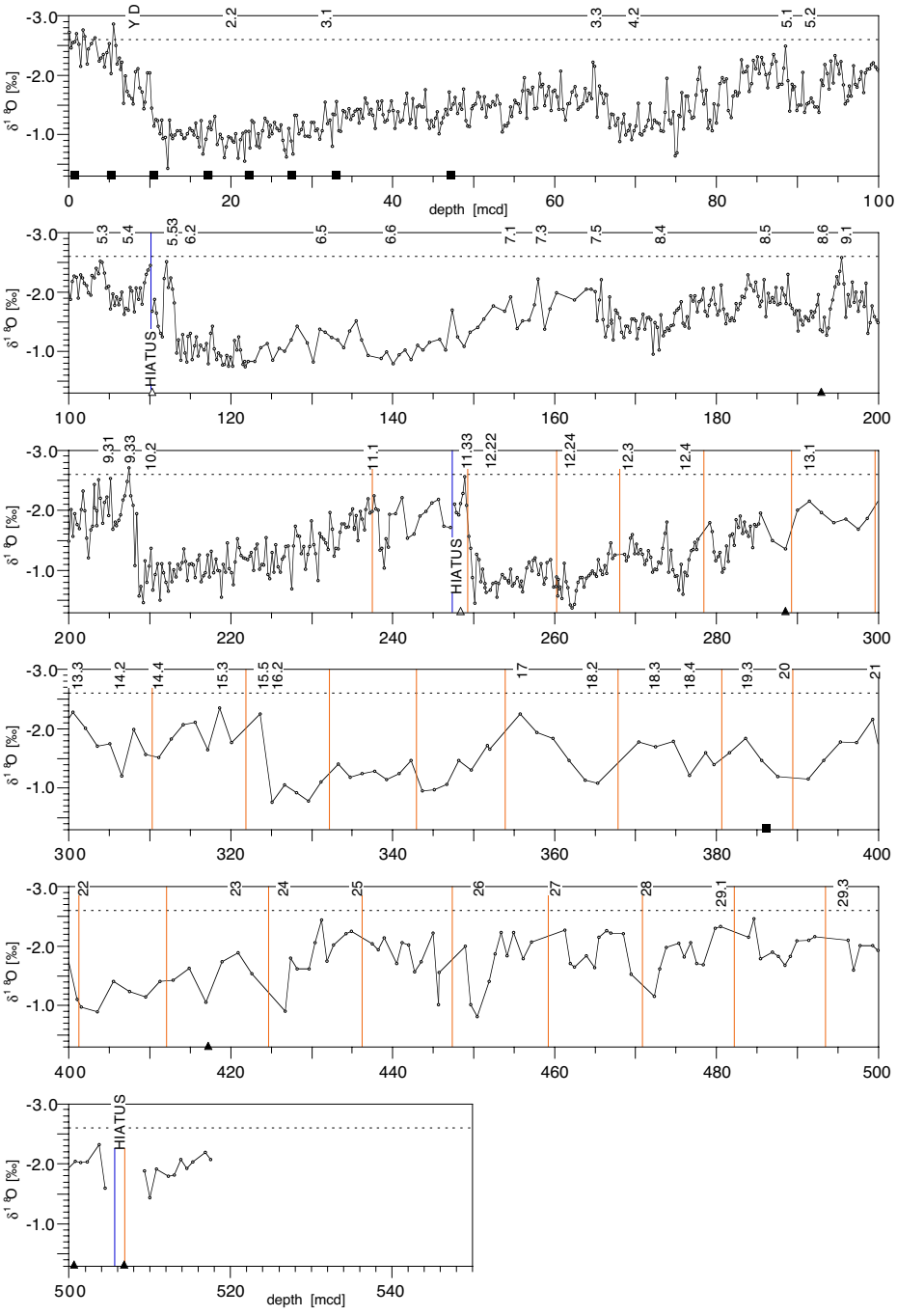

Figure 2(a). Oxygen isotope curve ($\delta^{18}O$ ratio versus PDB = PeeDee belemnite standard) of the surface-dwelling planktonic foraminifer *Globigerinoides ruber* from ODP Site 1144, plotted against core depth (meters composite depth [mcd]). The upper ~285 m of Site 1144 was sampled at irregular intervals, with an average sampling frequency of ~28 cm. Below ~285 m it is reduced to 1.5-2 m. Numbers indicate marine isotope stages and/or sub-stages. YD = Younger Dryas. Dashed line at -2.6 ‰ indicates the Holocene average $\delta^{18}O$ level. Black squares = positions of ^{14}C datings and microtektite layer, open triangles = positions of planktonic foraminifer last/first occurrence datums, filled triangles = positions of nannoplankton last/first occurrence datums. Thin vertical lines below 235 mcd indicate core breaks.

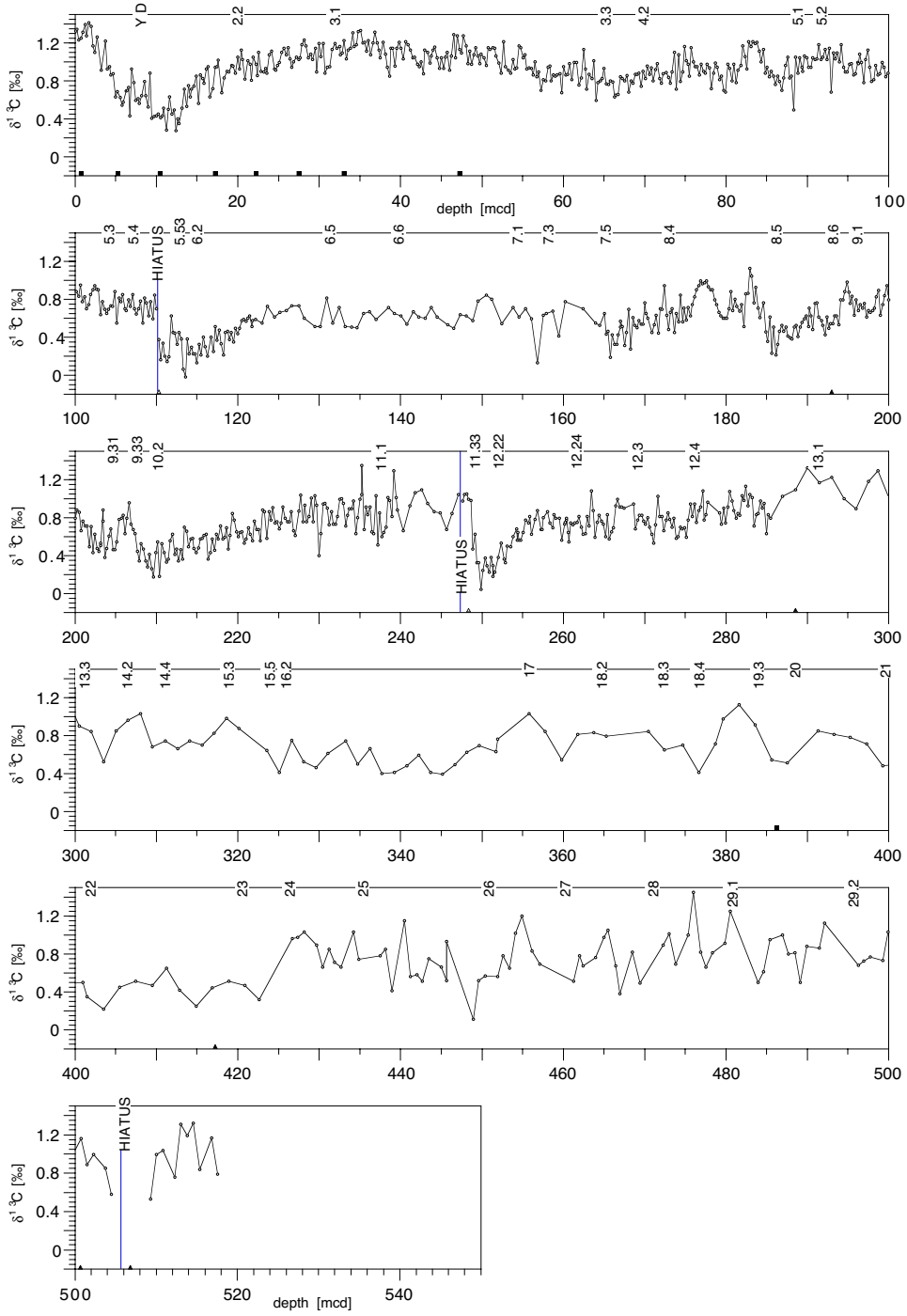

Figure 2(b). Carbon isotope curve ($\delta^{13}C$ ratio) of the surface-dwelling dwelling planktonic foraminifer *Globigerinoides ruber* from ODP Site 1144, plotted against core depth (meters composite depth [mcd]). As with the $\delta^{18}O$-curve, a high-resolution (av. ~28 cm) sampling frequency reaches down to ~285 mcd, further below sampling resolution is 1.5 to 2 m. Numbers define marine isotope stages and/or sub-stages. YD = Younger Dryas. Black squares = positions of ^{14}C datings and microtektite layer, open triangles = positions of planktonic foraminifer last/first occurrence datums, filled triangles = positions of nannoplankton last/first occurrence datums.

Further details of some marine isotope stages

Special Holocene features

The Holocene $\delta^{18}O$ record of Site 1144 displays a high-amplitude internal variability reaching 0.6-0.8 ‰ (Figure 3). The lightest values of –2.85 ‰ were measured at 5.8 mcd (near 10,000 yr BP). They probably stem from a freshwater plume in the areas close to the Pearl River due to high precipitation and run-off from China (L. Wang et al., 1999a, b, c). In general, the Holocene oxygen isotope curve is similar to the $\delta^{18}O$ record of neighboring core 17940 reported in L.Wang et al. (1999a). An early suspicion that the top 2 meters of sediment might be missing at Site 1144 (Leg 184 Shipboard Scientific Party, 2000) seems disproved by the ^{14}C age of 1700 yr (1272 ± 60 cal yr) at 0.74 mcd. This is the approximate age expected when taking into account the average Holocene sedimentation rate of around 0.5 m/k.y. at Site 1144. However, since the oxidized reddish sediment surface was not recovered, a small portion of the uppermost sediment, we estimate about 7 cm, is definitely missing.

The planktonic Holocene-to-Last Glacial Maximum (LGM) $\delta^{18}O$ shift is approximately Δ 1.8 ‰, with maximum differences of 2.4 ‰ between short-term extremes in the Holocene and LGM. The ice volume effect on the $\delta^{18}O$-record for the most recent glacial-interglacial transition (MIS 1/ 2) is estimated to be 1.2 ‰, assuming that 10 m of sea-level rise is equivalent to a 0.11 ‰ change in $\delta^{18}O$ (Labeyrie et al., 1987; Fairbanks, 1989). Thus the overall glacial-interglacial $\delta^{18}O$ change at Site 1144 records primarily the global ice volume signal, nonetheless fluctuations in local surface-water temperature and/or salinity also play an important role.

The Younger Dryas (YD) event (6.5-8.1 mcd) is recorded as a prominent isotopic shift of Δ0.7 ‰ back to more positive $\delta^{18}O$-values (Figure 3) and shows the characteristic double-peak structure known from the Greenland ice-core records (Alley et al., 1993). Prior to the YD a distinct $\delta^{18}O$ minimum near -2 ‰ marks the Bølling/Allerød warm phase (8.1-10.2

mcd). The top of Marine Isotope Stage 2 is defined by the major $\delta^{18}O$-shift of $\Delta 0.8$ ‰ toward the Bølling/Allerød level near 10.4 mcd (Termination IA).

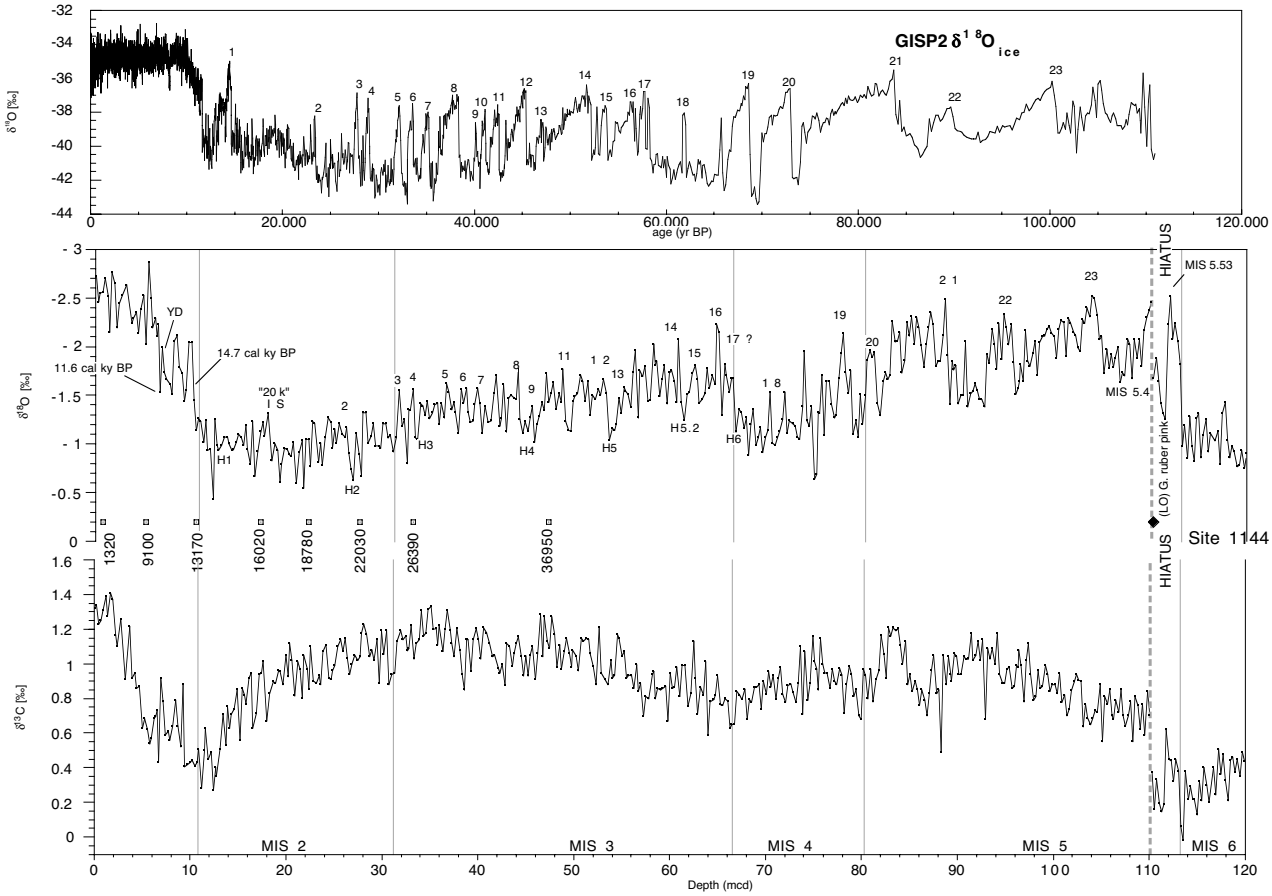

Figure 3.
Upper panel: GISP2 ice core oxygen isotope record of Grootes and Stuiver (1997) plotted against age in years BP. Numbers 1 through 23 indicate interstadials (IS).
Lower panel: ODP Site 1144 planktonic $\delta^{18}O$ (upper curve) and $\delta^{13}C$ (lower curve) ratios plotted against depth (meters composite depth [mcd]) for the upper 120 m. The thick dashed line indicates a gap in the record (Hiatus) and the thin dotted lines define boundaries between the Marine Isotope Stages (MIS) 1 to 6. Numbers (2-23) at planktonic $\delta^{18}O$ record indicate events equivalent to interstadial events defined in the GISP2 $\delta^{18}O$ ice record (upper panel). "20k"IS marks an isotopic event in the 1144 profile that is equal to an event near 20,000 years in GISP2. H1 through H6 locate possible high salinity events coeval with North Atlantic Heinrich events. YD = Younger Dryas. Position of ^{14}C-datings (reservoir corrected by -400 yr; incl. those of Shyu et al., this volume) are indicated as squares. Last Occurrence (LO) of the planktonic foraminifer *Globigerinoides ruber* (pink) is marked. Events MIS 5.4 and MIS 5.53 in the isotope record are indicated.

Detailed features in MIS 2 - 5

Marine isotope stages 2 to 5 in the Site 1144 $\delta^{18}O$ record (Figure 2a and 3) are characterized by frequent, narrow standing oscillations that reach Δ 0.7-0.85 ‰ in MIS 2 and MIS 3, up to Δ0.9 ‰ in MIS 4, and nearly Δ1.1 ‰ in late MIS 5. We interpret these $\delta^{18}O$ variations as marked shifts in monsoon intensity, which induced freshwater pulses, and correlate them with the interstadial events (IS) of the GISP2 $\delta^{18}O$ ice core record (sensu L. Wang et al, 1999a). The most prominent positive excursions in the $\delta^{18}O$ curve of the top 110 mcd of Site 1144 were correlated to North Atlantic Heinrich events, as corroborated by ^{14}C ages.

The analogs of the GISP2 interstadial (IS) events 3 to 7, 9 to 16 and 20 to 23 are well represented in the Site 1144 $\delta^{18}O$ record as prominent negative excursions. Starting from the top of MIS 2 (10.45 mcd) the first prominent negative $\delta^{18}O$ excursions at Site 1144 occur between 16.9-19.0 mcd and were termed "20k IS" because they correspond to a characteristicly similar $\delta^{18}O$ excursion near 20 ka in the GISP2 record. The $\delta^{18}O$ interval between 23.9 and 26.4 mcd was correlated to IS 2 of GISP2. It lacks the high amplitudes that appear in the ice core record but bracketing ^{14}C datings and the preceding positive $\delta^{18}O$-excursions near 26.89 mcd, which correspond to H2, support this interpretation. Similar to GISP2, the analog to IS 8 at Site 1144 is a broad interval, but lacks the typical saw-tooth pattern. The shape of the IS 17 equivalent in the Site 1144 $\delta^{18}O$ record differs from GISP2, but a drastic increase in $\delta^{18}O$ near 66 mcd, possibly the counterpart of Heinrich event 6, clearly marks the bottom of "IS 17" at the top of MIS 4 (Figure 3). Here the structure between IS 18 and 19 is richer than in GISP2. The bipartite IS 19 in GISP2 was correlated to the broad, deeply structured interval from 73.5-78.8 mcd. The Site 1144 IS equivalents 21, 22 and 23 represent marine isotope substages 5.1, 5.3.1 and 5.3.3, respectively.

The "H3" event is weak in comparison to GISP2, however, well confirmed by a ^{14}C-age of 26.8 ka at 33.07 mcd (^{14}C age range of H3: 26-26.8 ka; Sarnthein et al., 2000). Further down-

core, a positive $\delta^{18}O$ excursion corresponds to H4 (44.5 mcd), with an appropriate ^{14}C age of 36.95 ka at 47.23 mcd (Figure 3). The "H5"-equivalent at 53.6 mcd has no independent age control, but the structure of the $\delta^{18}O$ record down to "IS 14" is unequivocal and well fitting to the GISP2 curve. A distinct increase in $\delta^{18}O$ close to 61 mcd, is possibly the equivalent to Heinrich event 5.2 (van Kreveld et al., 2000; Sarnthein et al, 2000).

Downcore of marine isotope stage 5.4, which is centered around 107 mcd (108 ka) the greater part of MIS 5.5 is missing, only the very top of MIS 5. 5 and the MIS 5.4/5.5 transition are preserved (Figure 2 and 3). This major hiatus, spanning approximately 7,400 years, is deduced from the fact that the $\delta^{18}O$ values do not reach the level of -2.9 / -3.0 ‰ that we know from other cores in this region (Linsley, 1996: ODP Site 769A; L. Wang et al., 1999a: 17940; Lee et al., 1999: MD972151;) and at neighboring Site 1145 (Mc Intyre and Oppo, this volume). The hiatus is also documented in the $\delta^{13}C$ record (Figure 2 b, 3) with a sudden shift of more than Δ 0.4 ‰ at 110 mcd. Below the hiatus, the $\delta^{13}C$ record at the MIS 5 / 6 boundary shows a broad minimum similar to that observed at ODP Site 658 for late MIS 6 (Sarnthein and Tiedemann, 1990). The positive incursion in the $\delta^{18}O$ curve of Site 1144 near 110-111.5 mcd most likely represents a Younger Dryas-style climatic oscillation (event 5.52: Sarnthein and Tiedemann, 1990) and the preceding negative peak is equal to event 5.53. The transition (Termination II) from MIS 6 to MIS 5.53 near 113 mcd shows an almost instantaneous isotopic shift of 1.25 ‰ (Figure 2a and 3).

The millennial to sub-millennial scale variability in the planktonic stable isotope record at Site 1144 probably reflects changes in temperature and in particular, changes in sea surface salinity in addition to changes in global ice volume (Lambeck and Chappell, 2001). Because of the position close to the Chinese mainland and the Pearl River mouth, the $\delta^{18}O$ variability at Site 1144 most likely reflects changes in summer monsoon intensity, that is enhanced pre-

cipitation and fluvial runoff leading to negative $\delta^{18}O$ excursions. A decrease in summer monsoon intensity would result in decreased precipitation and/or temperature at Site 1144 and thus explain the maxima in planktonic $\delta^{18}O$ (high salinity "Heinrich" events) in the SCS.

Apparently, short-term changes in the Asian Monsoon system were intimately tied to high-latitude climate forcing via atmospheric signal transfer (L. Wang et al., 1999b; Kudrass et al., 2001). The question whether the sudden $\delta^{18}O$ variations in the South China Sea occur simultaneously with previously identified events in the North Atlantic (Adkins et al., 1997; Bond et al., 1997) and high latitudes (Dansgaard et al., 1993) remains unanswered (An, 2000). However, a modeling study of Mikolajewicz et al. (1997) showed that atmospheric transfer of Greenland temperature variations will result in quasi-synchronous signals across the high-latitude Northern Hemisphere.

In contrast to a scenario where the South China Sea was responding primarily to Northern Hemisphere climate changes, the other possiblity is that the tropical climate and the monsoon system was the driving force for Northern Hemispere millennial scale climate variations. Recent modeling studies of Clement and Cane (1999a, b) suggest that long-term oscillations of the El Niño-Southern Oscillation (ENSO) may be an important forcing factor for the tropical monsoon climate system, and furthermore may also have an important influence on the global climate.

Detailed features in MIS 6 - 11

Marine isotope stage 6 in the $\delta^{18}O$ record shows the characteristic features with a well developed substage 6.5 (Figure 2 and 4) and with internal amplitude variations of up to $\Delta 0.7$ ‰. However, these variations are less negative than expected when considering various other records in the South China Sea and Sulu Sea (Linsley and Dunbar, 1994; L.Wang et al., 1999a). A probable reason may be the still insufficient sampling resolution within this interval.

Accordingly, during MIS 7 the $\delta^{18}O$ values do not reach the near-Holocene level that has been observed in records elswhere from this region (Linsley and von Breymann, 1991; L. Wang et al., 1999a). Substages 7.1 and 7.3 are narrower than in the ODP Site 769 isotope record (Linsley and Dunbar, 1994), and in particular substage 7.4 (Figure 2a and 4) appears less „glacial“ than in the SPECMAP (Martinson et al., 1987) and in the ODP Site 769 isotope curves. At ODP Site 1145 (McIntyre and Oppo, this volume) substage 7.4 has similar negative values.

Highly resolved MIS 8 $\delta^{18}O$ levels are generally more negative (warmer) than in other low-latitude cores (Basssinot et al.,1994; Jian et al., 2000). Substage 8.5 at Site 1144 appears more pronounced (Δ 0.3-0.4 ‰) and warmer than at the neighboring Site 1145.

In MIS 9 the Site 1144 $\delta^{18}O$ values reach the Holocene level. A major shift of more than Δ 1.5‰ in $\delta^{18}O$ constitutes the MIS 9/10 boundary (Termination IV) at 208 mcd (Figures 2 and 4).

Oxygen isotope values in MIS 10 are at a level comparable with the LGM and display a high-frequency variability similar to MIS 2-3.

Despite the high sampling resolution, Marine Isotope Stage 11 is found incomplete, with most of the characteristically broad substage 11.3 missing (Figure 2 and 4) similar to the situation observed at the peak interglacial of MIS 5.5. Minimum isotope values of -2.6 ‰ are more positive than the values of -3.1 ‰ observed at neighbor Site 1145 (McIntyre and Oppo, this volume). Based on a detailed comparison with other planktonic high-resolution records (Berger et al., 1993 a, b; McManus et al., 1999) we assume the hiatus to be somewhere between 246.33 mcd and 247.13 mcd (Figure 2) comprising about 21,000 years. Similar to the base of the hiatus in stage 5.5, the base of this hiatus lies within a Younger Dryas-style cold episode after the short warm event 11.33 (Sarnthein and Tiedemann, 1990), which is comparable to the Bølling/Allerød warm phase at the end of the Last Glacial. The most pronounced highly resolved Marine Isotope Stage 12 shows three major cold events (12.22, 12.24 and 12.4).

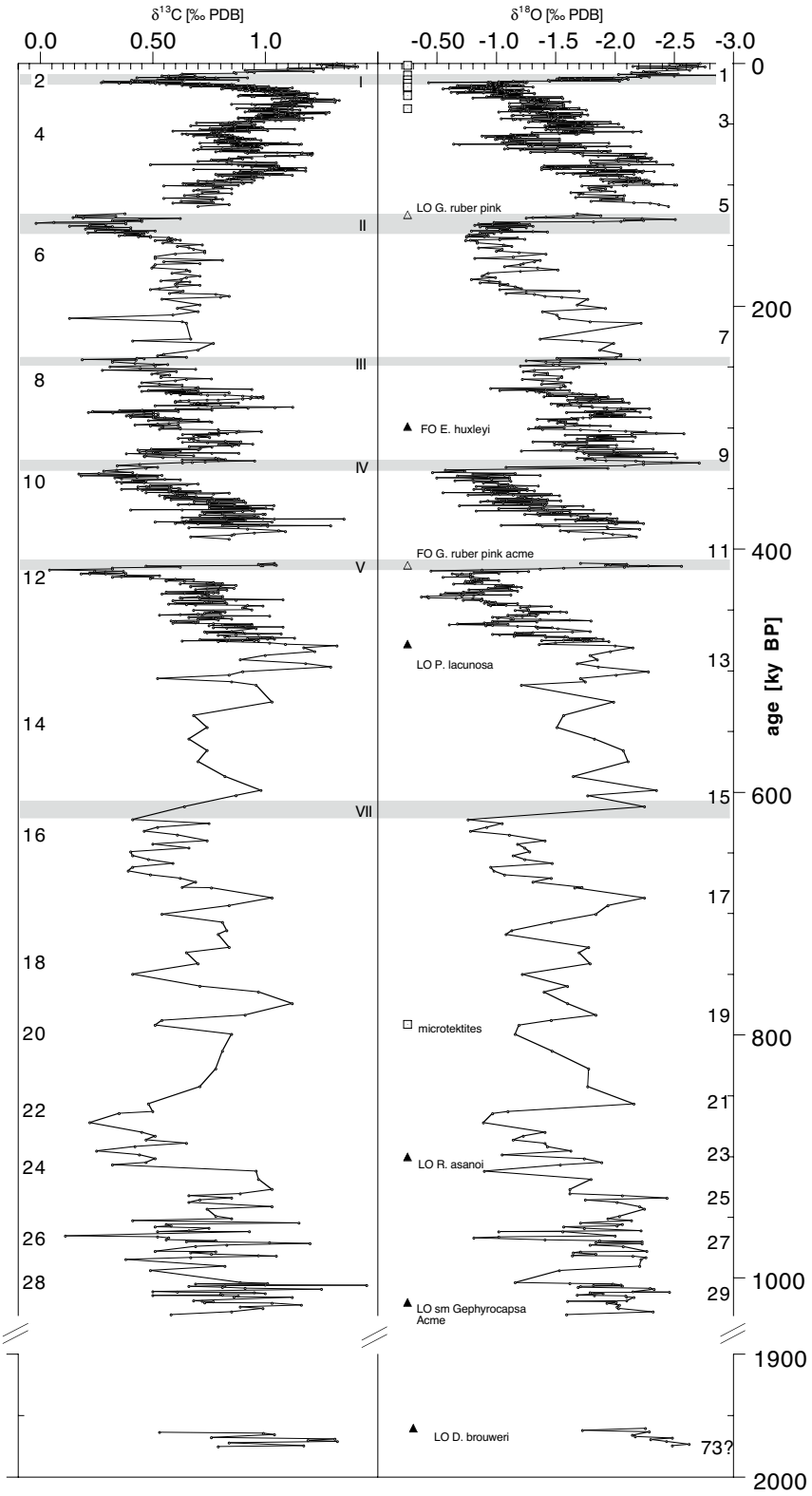

Figure 4. ODP Site 1144 oxgyen and carbon isotope curve of the planktonic foraminifer *Globigerinoides ruber* (white) versus age in kilo years (ky BP). Numbers indicate Marine Isotope Stage (MIS) stages based on a correlation with the orbitally tuned age model of Site 677 (Shackleton et al., 1990). Blanks in record = stratigraphic gaps. Note break in x-axis (// = Hiatus). Biostratigraphic First (FO) and Last (LO) Occurrence datums are marked; squares = positions of ^{14}C datings and microtektite layer, open triangles = positions of planktonic foraminifer first/last occurrence datums, filled triangles = positions of nannoplankton first/last occurrence datums, shaded vertical bars= pronounced glacial terminations (roman numerals).

Detailed features in MIS 13-29 and near to the base of the profile

Below 285 mcd (476 ka) the sampling intervals are still wide, between 1.5 and 2 m (Figure 2 and 4). Marine isotope stages 13 and 15, display the characteristic trident shape. MIS 17 precedes the wide and pronounced glacial stage 16. MIS 18 shows a pronounced substage 18.3. Stage 19 appears unusually small in comparison to Site 1145 (Mc Intyre and Oppo, this volume) or Site 677 (Shackleton et al., 1990) where the $\delta^{18}O$ values reach almost Holocene levels during MIS 19. However, a layer of Australasian microtektites (Zhao et al., this volume) represents an important age marker within the lower part of the MIS 19/20 transition.

Further downcore, isotope stages 21 through 29 are clearly identified. A major hiatus, deduced from biostratigraphy (Shyu et al., this volume), occurs near the base of MIS 29 (Figure 2a and 4) which accordingly may be incomplete. Based on two biostratigraphic ages (Table 4a) the hiatus spans almost 1 million years. Further downcore a definitive designation of isotope stages for the interval 509.3-517.9 mcd was not possible. The Last occurrence (LO) of *D. brouweri/triradiatus* (1.96 Ma) possibly indicates MIS 73 (Sarnthein and Tiedemann, 1989) at 506.82 mcd. Assuming a constant sedimentation rate of 0.73 m/ky, the bottom depth of Site 1144 (517.56 mcd) may reach to an age of 1.9615 Ma (Tables 3 and 4 a).

event	average depth (mcd)	error	age (ka)
LO G. ruber pink	110.18 ±	0.13	124.8
FO E. huxleyi [1]	192.96 ±	0.13	299
FO G. ruber pink	248.39 ±	0.25	413
LO P. lacunosa [1]	288.54 ±	0.12	478
microtectite layer [2]	386.17 ±	0.00	791
LO R. asanoi [2]	417.23 ±	0.38	900
LO sm. Gephyrocapsa Acme [1]	500.66 ±	0.38	1020
LO D. brouweri / triradiatus [1]	506.82 ±	2.04	1960

Table 4a: Biostratigraphic datums and age markers. Events in bold were used as tiepoints for the age model; [1]: Shyu et al. (this volume); [2]: Zhao et al. (this volume). These ages are derived from our $\delta^{18}O$ stratigraphic ages.

Spectral analyses

The age model for Site 1144 is based on correlating our $\delta^{18}O$ record with the GISP2 $\delta^{18}O$ ice core record from the Holocene to the middle of MIS 5. Below stage 5 it is tuned to the astronomically dated $\delta^{18}O$ record of Site 677. Accordingly, spectral analysis of the Site 1144 $\delta^{18}O$ record reveals a fourier power spectrum of the last 110 kyr (Figure 6 a) strongly resembling the GISP2 frequency spectrum, with prominent periods of near 4000, 1500 and 1000 years (Grootes and Stuiver, 1997). The spectrum of the whole $\delta^{18}O$ record at Site 1144 (Figure 6 b) is clearly dominated by typical Milankovitch- orbital frequency bands with dominant periods of 98, 41, 23 and 18 k.y.

Figure 5 a

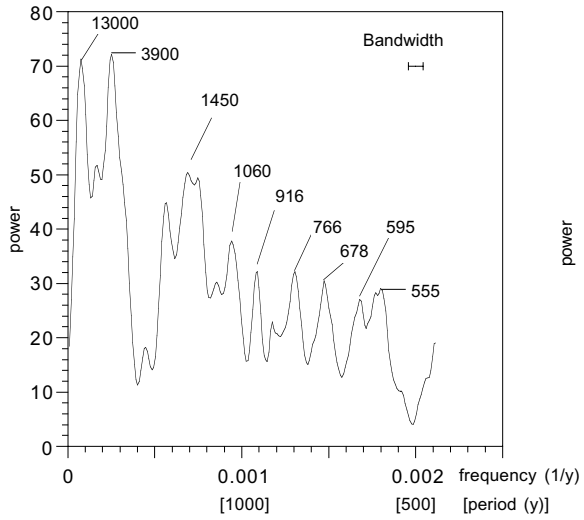

Figure 5 b

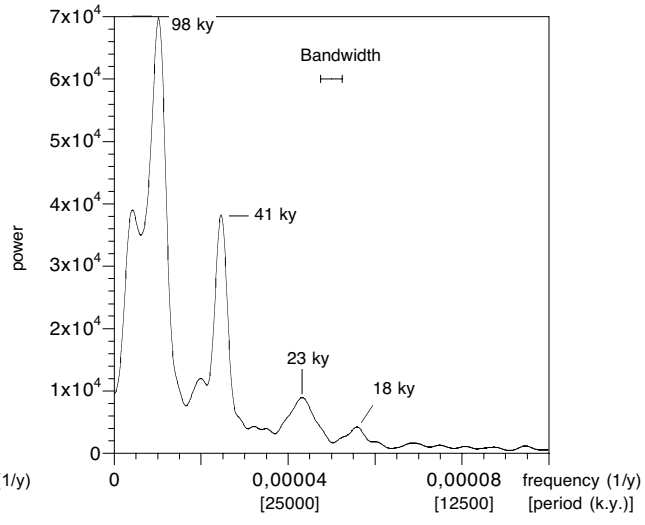

Figure 5 **(a).** Blackman-Tukey power spectrum of the $\delta^{18}O$ record for the interval 0-80 k.y. after 15 k.y. high-pass filtering. Numbers indicate periods in years. **(b).** AR-power spectrum of the non-equidistant $\delta^{18}O$ record for the interval 0-1030 k.y. Numbers indicate periods in thousand years (k.y.).

Sedimentation rates

Site 1144 is located on a thick sediment drift (Sarnthein et al., 1994; Leg 184 Shipboard Scientific Party, 2000) where changes in sedimentation rate mainly reflect variations in downslope terrestrial input and /or lateral transport by current activity. Accordingly Site 1144

is characterized by generally high sedimentation rates (Figure 5). In the bottom interval from 470-500 mcd (MIS 28 and 29), extremely high rates reaching 1.8 m/k.y.were observed. From 470 to 100 mcd (MIS 27 to 6) sedimentation rates are fairly constant near 40 cm/k.y., with only a few short intervals with lower values.

Particularly high sedimentation rates occur in the upper 100 mcd with more than 100 cm/k.y., and extremes reaching 1.8 m/k.y. In contast to the Holocene deposits in the nearby SONNE-95 core 17940, where maximum sedimentation rates of ~70 cm/k.y. occur primarily in the Preboreal (Termination IB; L. Wang et al., 1999a), the maximum sedimentation rate at Site 1144 occurs earlier, during the LGM and during Termination IA. This difference may result from the greater water depth at Site 1144 which led to an enhanced deposition at this deeper location when the sea level reached a minimum.

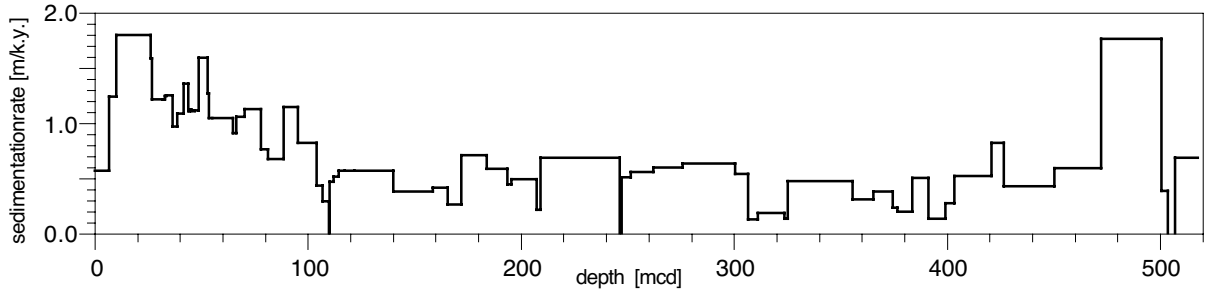

Figure 6. Sedimentation rates at Site 1144 in meters per kilo year (m/k.y.) versus meters composite depth [mcd].

Lüdmann et al. (2001), explained the differential sedimentation rates with a complex interaction between sea level stand and the location of the point of maximum sediment discharge from the Pearl River mouth. They suggest that the exposure or submergence of the Dongsha Island area, northwest of Site 1144, led to a deviation in sediment supply to the west of the island group during the LGM and to the east during the early Holocene. Site 1144, the deeper site, would have received more sediment in times of low sea level. Site 17940, ~300 m higher on the slope, would show high sedimentation rates during sea level high stands.

The small-scale differences in sedimentation rates between the two neighboring sites may also derive from a shift in the axis of the deep-water inflow of Pacific Intermediate Water. These oceanographic changes, which are probably linked to changes in the global thermohaline circulation, may have led to the stratigraphic gaps at the peak interglacial stages 5.5 and 11.3.

Carbon isotope record

The planktonic $\delta^{13}C$ record at Site 1144 (Figure 2b and 4) is consistent with neighboring records from the South China Sea and other tropical records. It shows long-term variations that roughly parallel the climatic cyclycity of the last 1 Ma, forming a ~ 420 k.y. excentricity cycle, with the lowest $\delta^{13}C$ values of less than 0.1 ‰ in Terminations II and V. Glacial-to-interglacial variations reach Δ 0.6-1.1 ‰ over the past 1.1 million years. Most of the warm stages with more negative $\delta^{18}O$ values are linked to high $\delta^{13}C$ levels, while cold stages and the deglacial intervals show minimum $\delta^{13}C$ values, except for MIS 2 and 3, and to a lesser degree MIS 6, where the carbon isotope ratios come close to interglacial levels. Extremely low $\delta^{13}C$ values and the largest $\delta^{13}C$ shifts (Δ 1.1 ‰; Figure 2b and 4) parallel glacial terminations, especially after glacial stages 2, 6, 10, 12. The $\delta^{13}C$ minima (Figure 3 and 4) are consistent with the deglacial minima found in many low-latitude planktonic records (Oppo and Fairbanks, 1989; Linsley and Dunbar, 1994) and in the neighboring core 17940 (L. Wang et al., 1999a).

The minima in $\delta^{13}C$ towards the end of the glacial maxima and early interglacial times may be a result of enhanced terrestrial nutrient input (L. Wang et al., 1999a), in particular via eolian loess, triggering higher productivity. These low $\delta^{13}C$ values may also reflect stronger winter monsoon winds that may have led to a greater mixing depth of the surface layer (Linsley and von Breymann, 1991), thereby incorporating ^{13}C depleted deep water into the

surface water masses. During Transition I the switch back to high $\delta^{13}C$ values slightly lags the maximum shift in $\delta^{18}O$. Apparently the nutrient input did not cease abruptly but continued even when the major climatic change had already occurred. Possibly, the mechanisms in nutrient influx changed from eolian dominated to fluvial. This is in concordance with L.Wang et al. (1999b) who reported a reduced **S**ea **S**urface **S**alinity (SSS) in the neighboring core 17940 during the Preboreal. This indicates a maximum in summer monsoon precipitation over China, corroborated also by granulometry data reflecting an enormous runoff event from the Pearl River (L.Wang et al., 1999a).

Improved age control of some biostratigraphic datums and other stratigraphic markers.

For the construction of the age model for Site 1144 we did not use the ages of biostratigraphic datums (Table 4) provided by Shyu et al. (this volume), except for two datums near the base of the sediment record. Instead, we employed our age model, which is correlated to the astronomically dated $\delta^{18}O$ record of ODP Site 677 (Shackleton et al., 1990), to improve the age assignment of biostratigraphic datums and the Australasian microtektite layer.

In addition, a total of 9 radiocarbon ^{14}C datings (5 datings on mixed bulk planktonic foraminifers, M.-P. Chen et al. (this volume) and 4 datings on mixed planktonic *G. ruber* and *G. sacculifer*, this study, Table 4b, c) served to better constrain the tuning-based age model for the Holocene and the Last Glacial. However, a sample at 14.97 mcd yielded an age of 20,949 ^{14}C yr, and the sample at 17.22 mcd yielded 18,999 ^{14}C yr (Table 4c). We ascribe this apparent age reversal to the differences in species composition. The upper sample consisted of a mixture of bulk planktonic foraminifers that could include deep dwelling species which have today have ^{14}C reservoir ages of 300-550 years (Southon, in press, 2001). The lower sample only contained two surface dwelling species *G. ruber* and *G. sacculifer* with lower reservoir

ages. Thus we regard the age of the lower sample as more accurate with regard to ^{14}C with a minimum (400 yr) reservoir effect.

Site, hole, core, section	interval (cm)	depth (mcd)	carbon	Corrected pMC†	Conv. ^{14}C age (yr BP)	err + (yr)	err - (yr)	$\delta^{13}C$ (‰)	calibrated age (yr BP)
1144A-2H-6	103-105	17.22	1.1 mg C	12.95 ± 0.15	16420	90	-90	1.45 ± 0.16 ‰	18999*
1144B-4H-1	126-128	22.23	0.9 mg C	9.18 ± 0.13	19180	120	-120	0.19 ± 0.12 ‰	22175*
1144B-5H-1	116-118	33.07	0.9 mg C	3.56 ± 0.11	26790	250	-240	1.24 ± 0.21 ‰	30280†
1144B-6H-3	143-145	47.23	0.7 mg C	0.96 ± 0.11	37350	960	-860	-0.38 ± 0.18 ‰	(40950)#

Table 4 b: AMS-^{14}C dates at Site 1144. For all calibrated ages a general reservoir correction of -400 yr was employed. *: age calibration with Calib 4.3 (Stuiver and Reimer, 1993). † age calibration according to Voelker (1999). # age calibration according to Voelker (1999), however, large error possible.

Site, hole, core, section	interval (cm)	deoth (mbsf)	depth (mcd)	avrg. depth (mcd)	Conv. ^{14}C age (yr BP)	error ± (yr)	calibrated age (yr BP)
1144A-1H-1	25-30	0.25	0.71	0.735	1721	60	1272*
1144A-1H-4	25-30	4.75	5.21	5.235	9487	65	10272*
1144A-2H-2	25-30	8.65	10.44	10.465	13571	75	15715*
1144A-2H-5	25-30	13.15	14.94	14.965	18115	80	20949*
1144A-4H-1	25-30	26.15	27.50	27.525	22430	110	25310†

Table 4c. AMS-^{14}C dates at Site 1144 (from Chen and Shyu, this volume). For all calibrated ages a general reservoir correction of -400 yr was employed. *: age calibration with Calib 4.3 (Stuiver and Reimer, 1993; Stuiver et al., 1998). †: age calibration according to Voelker (1999).

The last occurrence (LO) of pink *Globigerinoides ruber* at Site 1144 lies at 110.30 mcd. Since this position is directly at the base of the hiatus within stage 5.5, the true LO-position is probably younger, lying within the lost interval.

The First Occurrence (FO) of *Emiliania huxleyi* was determined at 192.82 mcd (Shyu et al., this volume), which is in the middle of MIS 8.6, with an assigned age of approximately 300 ka. Originally, the FO of *E. huxleyi* in the Mediterranean was positioned within MIS 8.4

(Vergnaud-Grazzini, 1990) and dated at 268 ka (Thierstein et al., 1977). Later Ahagon et al. (1993), located the FO datum of *E. huxleyi* in the West Pacific core RN89-PC3 at MIS 8.5, dated 285 ±3.5 ka. The age now found at Site 1144 indicates that the FO of *E. huxleyi* is not globally coeval and that *E. huxleyi* may have originated in the western Pacific and/or the South China Sea.

At 248.39 mcd, within late MIS 12 (413 ka) in the $\delta^{18}O$-curve of Site 1144, the number of *Globigerinoides ruber* (pink) abruptly increases. Previously this prominent increase has been described as FO datum (Leg 184 Shipboard Scientific Party, 2000) with an age of 400 ka (Li, 1997). However, pink pigmented *G. ruber* also occur further downcore between 261 to 273 mcd (early MIS 12; 470 ka), and in several other deeper samples, although there the coloration of specimens is very faint and mostly restricted to the juvenile chambers. A similar situation was first described by Thompson et al. (1979) from the western equatorial Pacific. Thus we conclude that the clearly recognizable increase in numbers and coloration at 248.39 mcd is not a true first occurrence of pink *G. ruber,* but is probably due to an improvement in preservation of the pigment following Thompson et al. (1979). The age assignment for the onset of *the G. ruber* pink acme zone (413 ka) however, seems to be characteristic for the West Pacific region.

Close to the MIS 12/13 transition in the $\delta^{18}O$-curve is the LO of *Pseudoemiliania lacunosa* at 288.54 mcd (Shyu et al., this volume), which dates to 478 ka. This is in accordance with cores V28-238 and -239 (Shackleton and Opdyke, 1973) where *P. lacunosa* becomes extinct in the early oxygen isotope stage 12 (Thierstein et al., 1977).

No Brunhes-Matuyama boundary (BMB) was identified at Site 1144 by the Leg 184 Shipboard Party. Since the shorebased paleomagnetic measurements that were conducted on the Site 1144 sediment profile (Solheid and Laj, this Volume) neither confirmed the shipboard results (Leg 184 Shipboard Scientific Party, 2000) nor furnished new results about paleomagnetic events, we relied on the occurrence of Australasian microtektites at 386.21 mcd (Zhao, this volume; Table 5) as the most important independent age marker near to the

BMB. Previous Ar^{40}/Ar^{39} ages of the Australasian microtektites range from, 783 ± 21 ka (Izett and Obradovich, 1992), 784 ±12 ka (Kunz et al., 1995) and 761 ± 17 ka and 816 ± 7 ka (Ya-mei et al., 2000). The microtektite layer was also reported from deep-sea sediment core 17957 from the South China Sea (Jian et al., 1999; Zhao et al., 1999) where the microtektites peak abundance occurs within the MIS 19/20 transition, 10 cm or about 11.6 k.y. prior to the B/M reversal (J. Wang et al., 2000). At Site 1144 the microtektite layer also lies within the MIS 19/20 transition and has, based on our age model, an age of 790 ka, similar to 793 ka reported by Lee and Wei (2000).

Site, hole, core, type, section, interval	Depth (mbsf)	Depth (mcd)
1144A-37X-6, (62-63 cm)	345.62	386.17
1144A-37X-6, (63-64 cm)	345.63	386.18
1144A-37X-6, (65-66 cm)	345.65	386.20
1144A-37X-6, (68-69 cm)	345.68	386.23
1144A-37X-6, (69-70 cm)	345.69	386.24
1144A-37X-6, (70-72 cm)	345.70	386.25

Table 5: Samples with microtektites at Site 1144 (Zhao et al., this volume). Samples with maximum abundance are shaded in grey.

The LO of *Reticulofenestra asanoi* occurs in the Site 1144 sediment profile at 288.54 mcd within oxygen isotope stage 22-23, which is consistent with Wei (1993), and has an assigned age of 900 ka.

Conclusions

The oxygen and carbon isotope stratigraphy at Site 1144 was obtained from largely undisturbed hemipelagic sediments from the northern continental slope of the South China Sea. The record spans the early Pleistocene to the Holocene and is interrupted by one major and two minor stratigraphic gaps. Intense hemipelagic terrigenous sediment supply, probably linked to lateral sediment advection in the nepheloid layer, formed a thick drift-type deposit with outstanding high sediment accumulation rates. Thus the sediment profile of Site 1144

provides an unprecedented time resolution of orbital-to-centennial-scale isotope oscillations over the last 1 million years.

On the basis of the Site 1144 $\delta^{18}O$ record we draw the following conclusions:

- The standard sawtooth-like character of the 100-k.y. climatic cycles during the Brunhes Chron is well developed, as early as subsequent to MIS 25.
- The $\delta^{18}O$ record of Site 1144 during the last 120 k.y. exhibits strong similarities with the Greenland climate variability which is documented in the GISP2 $\delta^{18}O$ ice core record. Similar to the Holocene and the Last Glacial, cold isotope stages 6 and 8 as well as warm stages 9 and 11 display a high-frequency variability in planktonic $\delta^{18}O$ with comparable amplitudes. Furthermore, short-term climatic reversals similar to the Younger Dryas are documented within the Terminations of cold stages at the beginning of warm MIS 11, 9 and 5.
- The $\delta^{18}O$-record indicates that larger parts of substages 5.5 and 11.3 at Site 1144 are missing. The fact that just those two events, which represent the warmest events oveer the past 500 k.y., are lost, is conspicuous. It may indicate extensive changes in ocean circulation and/or in the sedimentation regime which led to non-deposition or, more probably, to a removal of the missing sediment during and at the end of the warm phases through more vigorous contour currents.
- The planktonic carbon isotope record at Site 1144 shows that the major oscillations in $\delta^{13}C$ of the surface water parallel the general climate variations of the past 1 million years, especially a 420-k.y. excentricity cycle. The variations in $\delta^{13}C$ in part probably result from oscillations in monsoon intensity which is responsible for changes in wind stress and precipitation and thus is responsible for advection and/or influx of ^{13}C depleted carbon. In part they are a global phenomenon also seen in the North Atlantic.

Acknowledgments

We thank the Ocean Drilling Program for the possibility to participate in Leg 184 and for providing us with samples and logistical support. We especially acknowledge the ODP Core Repository in College Station for providing us with additional samples at very short notice. We thank Frank Bruhn and Pieter M. Grootes for assistance with AMS-^{14}C dating at the Leibniz Labor, Kiel. For additional ^{14}C dates and a revised biostratigraphy we thank Min-Pen Chen and Jih-Ping Shyu, Institute of Oceanography, National Taiwan University. We are much obliged for data on the microtektite layer from Quanhong Zhao, Shanghai. Special thanks to Rebecca Rendle, Geomar, Kiel, for her constructive comments and careful revision of this manuscript. Our research was generously funded by the German Science Foundation (Deutsche Forschungsgemeinschaft, DFG-grants Sa 207/38-1 "Monitor Monsun" and Sa 207/41-1 "Monsun Südchina See").

References

Adkins, J.F., Boyle, E.A., Keigwin, L., and Cortijo, E., 1997. Variability of the North Atlantic thermohaline circulation during the last interglacial period. *Nature*, 390: 154-156.

Ahagon, N., Tanaka, Y., and Ujiié, H., 1993. Florisphaera profunda, a possible nannoplankton indikator of late Quaternary changes in seawater turbidity at the northwestern margin of the Pacific. *Marine Micropaleontology*, 22: 255-273.

Alley, R.B., Meese, D.A., Shuman, C.A., Gow, A.J., Taylor, K.C., Grootes, P.M., White, J.W.C., Ram, M., Waddington, E.D., Majewski, P.A., and Zielinski, G.A., 1993. Abrupt increase in Greenland snow accumulation at the end of the Younger Dryas event. *Nature*, 362: 527-529.

Alley, R.B., Shuman, C.A., Meese, D.A., Gow, A.J., Taylor, K.C., Cuffey, K.M., Fitzpatrick, J.J., Grootes, P.M., Zielinski, G.A., Ram, M., Spinelli, G., and Elder, B., 1997. Visual-stratigraphic dating of the GISP2 ice cores: Basis, reproducibility and application. *Journal of Geophysical Research*, 102: 26,367-26,382.

An, Z., 2000. The history and variability of the East Asian paleomonsoon climate. *Quaternary Science Reviews*, 19: 171-187.

Bassinot, F.C., Labeyrie, L.D., Vincent, E., Quidelleur, X., Shackleton, N.J., and Lancelot, Y., 1994. The astronomical theory of climate and the age of the Brunhes-Matuyama magnetic reversal. *Earth and Planetary Science Letters*, 162: 91-108.

Bé, A.W.H., and Tolderlund, D.S., 1971. Distribution and ecology of living planktonic foraminifera in surface waters of the Atlantic and Pacific Oceans. *In* B.M. Funnel, and W.R. Riedel (Ed.), *Micropaleontology of the Oceans*: Cambridge (Cambridge Univeristy Press): 105-149.

Berger, W.H., Bickert, T., Schmidt, H., and Wefer, G., 1993. Quaternary oxygen isotope record of pelagic foraminifers: Site 806, Ontong Java Plateau. *In* W.H. Berger, L.W. Kroenke, L.A. Mayer, and et al (Ed.), *Proc. ODP Sci. Res. Vol. 130*: College Station (Ocean Drilling Program): 381-395.

Berger, W.H., Bickert, T., Schmidt, H., Wefer, G., and Yasuda, M., 1993. Quaternary oxygen isotope record of pelagic foraminifers: Site 805, Ontong Java Plateau. *In* W.H. Berger, L.W. Kroenke, L.A. Mayer, and et al (Ed.), *Proc. ODP Sci. Res. Vol. 130*: College Station (Ocean Drilling Program):363-379.

Berger, W.H., Diester-Haass, L., and Killingley, J.S., 1978. Upwelling off Northwest Africa; the Holocene decrease as seen in carbon isotopes and sedimentological indicators. *Oceanologica Acta*, 1: 3-7.

Berger, W.H., Yasuda, M.K., Bickert, T., Wefer, G., and Takayama, T., 1994. Quaternary time scale for the Ontong Java Plateau: Milankovitch template for Ocean Drilling Program Site 806. *Geology*, 22: 463-467.

Bond, G., Showers, W., Cheseby, M., Lotti, R., Almasi, P., de Menocal, P., Priore, P., Cullen, H., Hajdas, I., and Bonani, G., 1997. A Pervasive Millenial-Scale Cycle in North Atlantic Holocene and Glacial Climates. *Science*, 278: 1257-1266.

Clement, A., and Cane, M.A., 1999. A role for the tropical Pacific coupled ocean-atmosphere system on Milankovitch and millennial time scales. Part I: A modeling study of tropical Pacific variability. *In* P.U. Clark, R.S. Webb, and L.D. Keigwin (Ed.), *Mechanisms of global climate change at millennial time scales*: Washington DC (American Geophysical Union), Monograph 112:, 363-371.

Clement, A.C., Seager, R., and Cane, M.A., 1999. Orbital controls on the El Niño/Southern Oscillation and the tropical climate. *Paleoceanography*, 14: 441-456.

Dansgaard, W., Johnsen, S.J., Clausen, H.B., Dahl-Jensen, D., Gundestrup, N.S., Hammer, C.U., Hvidberg, C.S., Steffensen, J.P., Sveinbjörnsdottir, A.E., Jouzel, J., and Bond, G., 1993. Evidence for general instability of past climate from a 250-kyr ice-core record. *Nature*, 364: 218-220.

Emiliani, C., 1955. Pleistocene temperatures. *Journal of Geology*, 63: 538-578.

Fairbanks, R.G., 1989. A 17,000-year glacio-eustatic sea level record: influence of glacial melting rates on the Younger Dryas Event and deep-ocean circulation. *Nature*, 637-642.

Gartner, S., 1988. Paleoceanography of the Mid-Pleistocene. *Micropaleontology*, 13: 23-46.

Grootes, P.M., and Stuiver, M., 1997. Oxygen 18/16 variability in Greenland snow and ice with 10^{-3}- to 10^{5}-year resolution. *Journal of Geophysical Research*, 102: 26455-26470.

Izett, G.A., and Obradovich, J.D., 1992. Laser fusion ^{40}Ar-^{39}Ar ages of Australasian Tektite cores and flanges. *Eos Trans. AGU*, 73: 328.

Jian, Z., Wang, L., Kienast, M., Sarnthein, M., Kuhnt, W., Lin, H., and Wang, P., 1999. Benthic foraminiferal paleoceanography of the South China Sea over the last 40,000 years. *Marine Geology*, 156: 159-186.

Jian, Z., Wang, P., Chen, M.-P., Li, B., Zhao, Q., Bühring, C., Laj, C., Lin, H.-L., Pflaumann, U., Bian, Y., Wang, R., and Cheng, X., 2000. Foraminiferal responses to major Pleistocene paleoceanographic changes in the southern South China Sea. *Paleoceanography*, 15: 229-243.

Kiefer, T., Sarnthein, M., Erlenkeuser, H., Grootes, P.M., and Roberts, A., 2001. North Pacific response to millennial-scale changes in ocean circulation over the last 60 kyr. *Paleoceanography*, 16: 179-189.

Kudrass, H.R., Hofmann, A., Doose, H., Emeis, K., and Erlenkeuser, H., 2001. Modulation and amplification of climatic changes in the Northern Hemisphere by the Indian summer monsoon during the past 80 k.y. Geology, 29: 63-66.

Kunz, J., Bollinger, K., Jessberger, E.K., and Storzer, D., 1995. Ages of Australasian Tektites. *In Lunar and Planetray Science Conference XXVI*: Lunar and Planetary Institute, Houston, Texas, 809-810.

Labeyrie, L., Duplessy, J.C., and L, B.P., 1987. Variations in mode of formation and temperature of oceanic deep waters over the past 125,000 years. *Nature*, 327: 477-482.

Lambeck, K., and Chappell, J., 2001. Sea level change through the last glacial cycle. *Science*, **292**(5517): 679-686.

Lee, M.-Y., Wei, K.-Y., and Chen, Y.-G., 1999. High resolution oxygen isotope stratigraphy for the last 150,000 years in the southern South China Sea:Core MD972151. *Terrestrial, Atmospheric and Oceanic Sciences*, 10: 239-254.

Lee, M.Y., and Wei, K.Y., 2000. Australasian microtektites in the South China Sea and West Philippine Sea: implications for age, size and location of the impact crater. *Meteoritics and Planetary Science*, 35: 1151-1155.

Li, B., 1997. Paleoceanography of the Nansha Area, southern South China Sea since the last 700,000 years. (Ph. D. thesis), Academica Sinica:124 p.

Linsley, B.K., 1996. Oxygen-isotope record of sea level and climate variations in the Sulu Sea over the past 150,000 years. *Nature*, 380: 234-237.

Linsley, B.K., and Dunbar, R.B., 1994. The late Pleistocene history of surface water $\delta^{13}C$ in the Sulu Sea: Possible relationship to Pacific deepwater $\delta^{13}C$ changes. Paleoceanography, 9: 317-340.

Linsley, B.K., and von Breymann, M.T., 1991. Stable isotopic and geochemical record in the Sulu Sea during the last 750 ky: Assessment of surface water variability and paleoproductivity. *In* E.A. Silver, C. Rangin, and von Breymann (Ed.), Proc. ODP, Sci. Res., *124*: College Station (Ocean Drilling Program): 379-396.

Lüdmann, T., Wong, H.K., and Wang, P., 2001. Plio-Quaternary sedimentation processes and neotectonics of the northern continental margin of the South China Sea. Marine Geology, 172: 331-358.

Martinson, D.G., Pisias, N.G., Hays, J.D., Imbrie, J., T. C. Moore, J., and Shackleton, N.J., 1987. Age dating and the orbital theory of the Ice Ages: development of a high-resolution 0 to 300,000-Year Chronostratigraphy. *Quaternary Research*, 27: 1-29.

McManus, J.F., Oppo, D.W., and Cullen, J.L., 1999. A 0.5-million-year record of millennial-scale climate variability in the North Atlantic. *Science*, 283: 971-975.

Meese, D.A., Gow, A.J., Alley, R.B., Zielinsky, G.A., Grootes, P.M., Ram, M., Taylor, K.C., Mayewski, P.A., and Bolzan, J.F., 1997. The Greenland Ice Sheet Project 2 depth-age scale: Methods and results. *Journal of Geophysical Research*, 102: 26411-26423.

Mikolajewicz, U., Crowley, T.J., Schiller, A., and Voss, R., 1997. Modelling teleconnections between the North Atlantic and North Pacific during the Younger Dryas. *Nature*, 387: 384-387.

Oppo, D., and Fairbanks, R.G., 1989. Carbon isotope composition of tropical surface water during the past 22,000 years. *Paleoceanography*, 4: 333-351.

Prell, W.L., Imbrie, J., Martinson, D.G., Morley, J.J., Pisias, N.G., Shackleton, N.J., and Streeter, H.F., 1986. Graphic correlation of Oxygen Isotope Stratigraphy: Application to the Late Quaternary. *Paleoceanography*, 1: 137-162.

Sarnthein, M., Pflaumann, U., Wang, P.X., and Wong, H.K., 1994. Preliminary Report on Sonne-95 Cruise "Monitor Monsoon" to the South China Sea. *Berichte-Reports, Geologisch-Paläontologisches Institut der Universität Kiel*, 68: 0-225.

Sarnthein, M., Stattegger, K., Dreger, D., Erlenkeuser, H., Grootes, P., Haupt, B.J., Jung, S., Kiefer, T., Kuhnt, W., Pflaumann, U., Schäfer-Neth, C., Schulz, H., Schulz, M., Seidov, D., Simstich, J., van Kreveld, S., Vogelsang, E., Völker, A., and Weinelt, M., 2000. Fundamental modes and abrupt changes in North Atlantic circulation and climate over the last 60 ky - concepts, reconstruction and numerical modeling. *In* P. Schäfer, W. Ritzrau, M. Schlüter, and J. Thiede (Ed.), *The Northern Atlantic: A changing Environment*: Berlin (Springer), 365-410.

Sarnthein, M., and Tiedemann, R., 1989. Toward a high-resolution stable isotope stratigraphy of the last 3.4 million years: Sites 658 and 659 off northwest Africa. *In* W. Ruddiman, and M. Sarnthein (Ed.), Proc. ODP, Sci. Res., *108*: College Station (Ocean Drilling Program): 167-184.

Sarnthein, M., and Tiedemann, R., 1990. Younger Dryas-style cooling events at glacial terminations I-VI at ODP Site 658: Associated benthic $\delta^{13}C$ anomalies constrain meltwater hypothesis. *Paleoceanography*, 5: 1041-1055.

Shackleton, N.J., 1977. Tropical rainforest history and the equatorial Pacific carbonate dissolution cycles. *In* N.R. Anderson, and A. Malahoff (Ed.), *The fate of fossil fuel CO_2 in the Oceans*: New York (Plenum): 401-428.

Shackleton, N.J., Berger, A., and Peltier, W.R., 1990. An alternative astronomical calibration of the lower Pleistocene timescale based on ODP Site 677. *Trans. R . Soc. Edinburgh, Earth Sci.*, 81: 251-261.

Shackleton, N.J., and Opdyke, N.D., 1973. Oxygen isotope and paleomagnetic stratigraphy of equatorial Pacific core V28-238: Oxygen isotope temperatures and ice volumes on a 10^5 year and 10^6 year Scale. *Quaternary Research*, 3: 39-55.

Shipboard Scientific Party, 2000. Site 1144. In Wang, P., Prell, W.L., Blum, P., et al., Proc. ODP, Init. Repts., 184, 1–103 [CD-ROM]. Available from: Ocean Drilling Program, Texas A&M University, College Station TX 77845-9547, USA.

Stuiver, M., Braziunas, T.F., Grootes, P.M., and Zielinski, G.A., 1997. Is there evidence for solar forcing of climate in the GISP2 oxygen isotope record? *Quaternary Research*, 48: 259-266.

Stuiver, M., and Grootes, P.M., 2000. GISP2 oxygen isotope ratios. *Quaternary Research*, 53: 277-285.

Stuiver, M., Reimer, P.J., Bard, E., Beck, J.W., Burr, G.S., Hughen, K.A., Kromer, B., McCormack, G., Van Der Plicht, J., and Spurk, M., 1998. INTCAL98 radiocarbon age calibration, 24,000-0 cal BP. *Radiocarbon*, 40: 1041-1083.

Stuiver, M., and Reimer, P. J., 1993, Extended 14C database and revised CALIB radiocarbon calibration program, Radiocarbon 35: 215-230.

Thierstein, H.R., Geitzenauer, K.R., Molfino, B., and Shackleton, N.J., 1977. Global synchroneity of late Quaternary coccolith datum levels: validation by oxygen isotopes. *Geology*, 5: 400-404.

Thompson, P.R., Bé, A.W.H., Duplessy, J.-C., and Shackleton, N.J., 1979. Disapperarance of pink-pigmented *Globigerinoides ruber* at 120,000 yr BP in the Indian and Pacific Oceans. *Nature*, 280: 554-558.

van Kreveld, S., Sarnthein, M., Erlenkeuser, H., Grootes, P., Jung, S., Nadeau, M.J., Pflaumann, U., and Voelker, A., 2000. Potential links between surging ice sheets, circulation changes and the Dansgaard-Oeschger cycles in the Irminger Sea, 60-18 kyr. *Paleoceanography*, 15: 425-442.

Vergnaud-Grazzini, C., Saliège, J.F., Urrutiaguer, M.J., and Iannace, A., 1990. Oxygen and carbon isotope stratigraphy of ODP Hole 653A and Site 654: The Pliocene-Pleistocene glacial history recorded in the Tyrrhenian Basin (West Mediterranean). *In* K.A. Kastens, J. Mascle, C. Auroux, E. Bonatti, et al., (Ed.), Proc. ODP, Sci. Res., *107*: College Station, Texas (Ocean Drilling Program).

Voelker, A.H.L., 1999. Zur Deutung der Dansgaard-Oeschger Ereignisse in ultra-hochauflösenden Sedimentprofilen aus dem Europäischen Nordmeer. *Berichte-Reports, Inst. für Geowiss., Universität Kiel*, 9: 278.

Wang, J., Zhao, Q., Cheng, X., Wang, R., and Wang, P., 2000. Age estimation of the mid-Pleistocene microtektite event in the South China Sea: A case showing the complexity of the sea-land correlation. *Chinese Science Bulletin*, 45: 2277-2280.

Wang, L., 2000. Isotopic signals in two morphotypes of *Globigerinoides ruber* (white) from the South China Sea: implications for monsoon climate change during the last glacial cycle. *Palaeogeography, Palaeoclimatology, Palaeoecology*, 161: 381-394.

Wang, L., Sarnthein, M., Erlenkeuser, H., Grimalt, J., Grootes, P., Heilig, S., Ivanova, E., Kienast, M., Pelejero, C., and Pflaumann, U., 1999a. East Asian monsoon climate during the Late Pleistocene: high-resolution sediment records from the South China Sea. *Marine Geology*, 156: 245-284.

Wang, L., Sarnthein, M., Erlenkeuser, H., Grootes, P.M., Grimalt, J.O., Pelejero, C., and Linck, G., 1999b. Holocene variations in asian monsoon moisture: A bidecadal sediment record from the South China Sea. *Geophysical Research Letters*, 26: 2889-2892.

Wang, L., Sarnthein, M., Grootes, P.M., and Erlenkeuser, H., 1999c. Millennial reoccurrence of century-scale abrupt events of East Asian monsoon: A possible heat conveyor for the global deglaciation. *Paleoceanography*, 14: 725-731.

Wei, W., 1993. Calibration of Upper Pliocene-Lower Pleistocene nannofossil events with oxygen isotope stratigraphy. *Paleoceanography*, 8: 85-99.

Yamei, H., Potts, R., Baoyin, Y., Zhentang, G., Deino, A., Wei, W., Clark, J., Guangmao, X., and Weiwen, H., 2000. Mid-pleistocene Acheulean-like stone technology of the Bose basin, South China. *Science*, 287: 1622-1626.

Zhao, Q., Jian, Z., Li, B., Chen, X., and Wang, P., 1999. Middle Pleistocene microtektites in deep-sea sediments of the South China Sea. *Sci. China Ser. D*, 42: 531-535.

4.4: Foraminiferal responses to major Pleistocene paleoceanographic changes in the southern South China Sea (Z. Jian,P. Wang, M.-P. Chen, B. Li, Q. Zhao, C. Bühring, C. Laj, H.-L. Lin, U. Pflaumann, Y. Bian, R. Wang, X. Cheng)

PALEOCEANOGRAPHY, VOL. 15, NO. 2, PAGES 229-243, APRIL 2000

Foraminiferal responses to major Pleistocene paleoceanographic changes in the southern South China Sea

Zhimin Jian,[1,2] Pinxian Wang,[1] Min-Pen Chen,[3] Baohua Li,[4] Quanhong Zhao,[1]
Christian Bühring,[5] Carlo Laj,[6] Hui-Ling Lin,[7] Uwe Pflaumann,[5] Yunhua Bian,[1]
Rujian Wang[1] and Xinrong Cheng[1]

Abstract. A detailed age model for core 17957-2 of the southern South China Sea was developed based on $\delta^{18}O$, coarse fraction, magnetostratigraphy, and biostratigraphy for the last 1500 kyr. The $\delta^{18}O$ record has clear ~100-kyr cycles after the Mid-Pleistocene Revolution (MPR) at the entrance of marine isotopic stage (MIS) 22. Planktonic foraminifera responded to the MPR immediately, showing the increased sea surface temperature (SST) and dissolution after the MPR. Benthic foraminifera did not respond to it until the Brunhes/Matuyama boundary. Since the MPR, the depth of thermocline gradually became shallower until MISs 6-5. This major change within MISs 6-5 was also reflected in the decreased SSTs and increased productivity and Deep Water Mass. Thus two major Pleistocene paleoceanographic changes were found: One was around the MPR; the other occurred within MISs 6-5, which speculatively might be ascribed to the reorganization of surface and deep circulation, possibly induced by tectonic forces.

1. Introduction

As a marginal sea the South China Sea (SCS) has sedimentation rates higher by an order of magnitude than the Pacific, and its widespread carbonate sediments provide an ideal basis for high-resolution paleoceanographic reconstruction [*Wang et al.*, 1995]. The first cores in the world ocean used for high-resolution stratigraphy documented by accelerator mass spectrometer (AMS) ^{14}C datings were from the southern part of this basin [*Andree et al.*, 1986; *Broecker et al.*, 1988]. Since the 1980s, marine geologists in China and abroad have shown growing interest in late Quaternary paleoceanographic history of the SCS, for example, the changes in sea surface temperature (SST) [*Wang and Wang*, 1990; *Miao et al.*, 1994; *Pflaumann and Jian*, 1999], productivity [*Winn et al.*, 1992; *Thunell et al.*, 1992; *Jian et al.*, 1999], deepwater conditions [*Berger*, 1987; *Jian and Wang*, 1997], carbonate cycles [*Wang et al.*, 1986; *Thunell et al.*, 1992; *Wang et al.*, 1995], monsoon variations [*Sun and Li*, 1999; *Wang et al.*, 1999], and paleoenvironmental interactions between land and sea [*Wang and Sun*, 1995; *Wang*, 1999] during the last glacial-interglacial cycle. On the other hand, the high sedimentation rate in the SCS has hindered the Pleistocene paleoceanographic studies because no core has penetrated the last two glacial cycles. The long come from industrial exploratory wells, engineering geological drill holes and coral reef deposits, which hardly provide continuous and detailed paleoenvironmental records [e.g., *Zhang et al.*, 1996]. Therefore long-term Pleistocene paleoenvironmental records from the China coast are not yet available to be compared with those recorded in the Chinese loess [*Kukla and An*, 1989; *Liu and Ding*, 1993; *Ding et al.*, 1994], despite their primary importance in our understanding of the East Asian paleoenvironmental evolution.

The surface water masses and hydrography in the SCS are largely controlled by the seasonally reversing monsoonal wind system, which causes drift currents to change their flow direction [*Wyrtki*, 1961]. According to *Levitus and Boyer* [1994], the SST of the SCS ranges from 20° to 28.8°C during the northeast winter monsoon, with steep gradients toward the coast of China. During the southwest summer monsoon, the SST varies only from 27° to 29°C. The annual average depth of thermocline (DOT) in the SCS ranges from ~25 m in the inner shelf to ~200 m toward the western Pacific, primarily responding to the wind-driven cyclonic surface circulation (i.e., Ekman pumping). For more detailed information on the modern geographic variations of the SSTs and DOT in the SCS, see *Chen et al.* [1998] and *Pflaumann and Jian* [1999]. However, during the glacial period the SCS became a semienclosed basin connected to the western Pacific through the Bashi Strait and to the Sulu Sea through the Balabac and Mindoro Straits due to the sea level drop [*Wang et al.*, 1995]. This inevitably led to a pronounced difference in surface and deep circulation [*Wang et al.*, 1995; *Jian and Wang*, 1997] and hence altered the upper water structure and deep water conditions.

The northern part of Nansha Islands area ("Dangerous Ground"), the northern slope of the SCS deep basin, is

[1]Laboratory of Marine Geology, Tongji University, Shanghai, China.
[2]Now at Institut für Geowissenschaften, Universität Kiel, Kiel, Germany
[3]Institute of Oceanography, Taiwan University, Taipei, China.
[4]Nanjing Institute of Geology and Paleontology, Academia Sinica, Nanjing, China.
[5]Institut für Geowissenschaften, Universität Kiel, Kiel, Germany.
[6]Laboratoire des Sciences du Climat et de l' Environment, CNRS-CEA, Gif sur Yvette, France.
[7]Institute of Marine Geology, Sun Yat-Sen University, Kaohsiung, Taiwan, China.

Paper number 1999PA000431.
0883-8305/00/1999PA000431$12.00

distinguished by its very low sedimentation rate because of the limited access of terrigenous material and may provide continuous and long Pleistocene deep-sea sediment sequences [*Sarnthein et al.*, 1994; *Wang et al.*, 1995]. Moreover, this area offers a special attraction for paleoceanographers, with only slight seasonality in SST and modern annual DOT of ~175 m [*Levitus and Boyer*, 1994]. Particularly, the southern SCS is a part of the Western Pacific Warm Pool (WPWP) bounded approximately by the 28°C surface isotherm [*Yan et al.*, 1992]. Its long-term changes in upper water structure perhaps have influenced the thermodynamics role played by the WPWP. In this study we selected a long deep-sea core with good carbonate preservation from the southern SCS to establish a detailed stratigraphy at least for the last 1500 kyr through an interdisciplinary approach, including magnetostratigraphy, biostratigraphy, oxygen isotope, and coarse fraction stratigraphy. By examining paleoceanographic records from the core we were able to reveal the planktonic and benthic foraminiferal responses to major Pleistocene paleoceanographic changes, for example, the Mid-Pleistocene Revolution (MPR) near 900 ka [*Berger et al.*, 1993a], and to get insight into the changes of surface and deep circulation during the Pleistocene in the SCS.

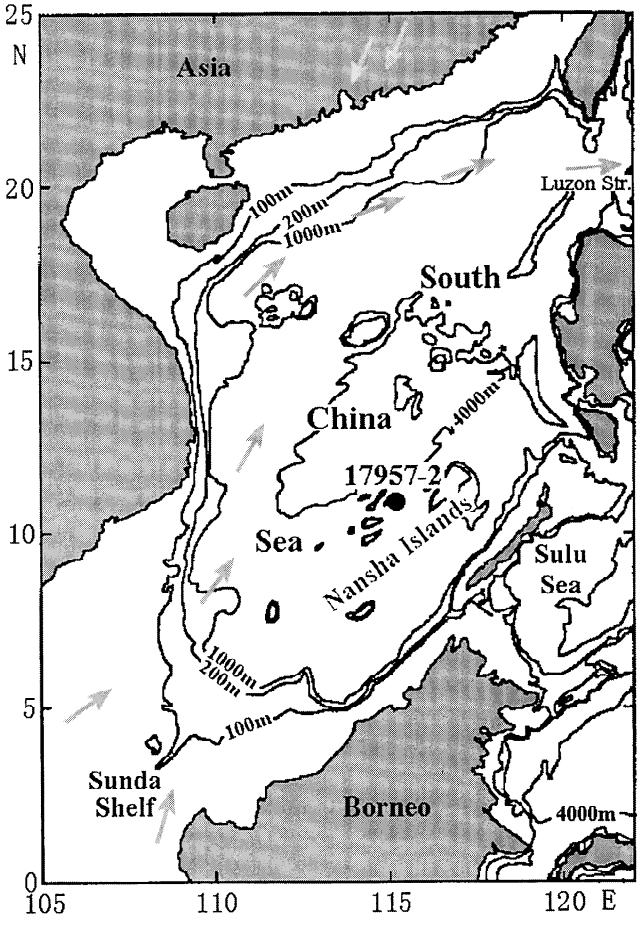

Figure 1. Location of core 17957-2 in the South China Sea. Gray arrows show modern surface currents during summer; white arrows show winter monsoon.

Table 1. Sample Information of Core 17957-2 Used in This Study

Analytical Item	Sample Interval, cm	Number of Samples
Planktonic foraminifera	5	272
Benthic foraminifera	10	136
Calcareous nannofossil	20	51
Radiolarian	10	136
Stable isotope	10	138
Coarse fraction	5	273
Carbonate	10	139
Opal	5	272

2. Material and Methods

We studied gravity core 17957-2 raised from the southern SCS, north of the Nansha Islands (10°53.9'N and 115°18.3'E; water depth 2195 m; core length 1384 cm) (Figure 1) during the SONNE-95 cruise in 1994 [*Sarnthein et al.*, 1994]. The sediment in the core consists of gray silty foraminiferal ooze free of turbiditic (or mass flow) deposition and major reworking. The core was sampled at 5-20-cm intervals, according to individual analytical item (Table 1). Three to ten cubic centimeters of wet sediment were dried and weighed for each sample while coarse fraction content was obtained through wet sieving over a 63-μm screen. Planktonic and benthic foraminifera were picked only from the size fraction ≥ 150 μm. When planktonic foraminifera were abundant, the sample was split using biseparation method to yield a subsample containing at least 300 specimens.

Planktonic and benthic foraminifera were identified and counted. Our taxonomy follows that of *Parker* [1962], *Bé* [1977], and *Kennett and Srinivasan* [1983] for planktonic foraminifera and that of *Barker* [1960] and *Loeblich and Tappen* [1988] for benthic foraminifera. On the basis of the census data the relative abundance of each species was calculated and plotted against depth to illustrate the down-core distribution patterns. We estimated the SSTs using two different planktonic foraminiferal transfer functions. The standard errors of the linear transfer function FP-12E [*Thompson*, 1981] are 2.48°C for winter SST and 1.46°C for summer SST, while those of the SIMMAX-28 formula using modern analog technique [*Pflaumann and Jian*, 1999] are 1.27° and 0.45°C, respectively. For the first time we used the thermocline depth transfer function of *Andreasen and Ravelo* [1997], which was based on the spatial distribution of 189 core top planktonic foraminifera in the tropical Pacific, to quantitatively reconstruct the changes of DOT in the SCS during the Pleistocene glacial cycles. This transfer function has a standard error of 22 m and additional 5 m of error due to insufficient counts in the core top database [*Andreasen and Ravelo*, 1997]. As for the benthic foraminifera, a *Q* mode factor analysis was carried out using the program of *Klovan and Imbrie* [1971]. Only species with relative abundance >2% in at least two samples (48 species and species groups, see Table 3) were included in the factor analysis. Carbonate dissolution/preservation was evaluated using changes in planktonic foraminiferal fragmentation, benthic foraminiferal proportion (expressed as BF/(BF+PF)%, where BF and PF are benthic and planktonic foraminiferal abundance, respectively), and the percentage of agglutinated tests in benthic foraminiferal fauna. Fragmentation is expressed as fragmentation =

$(F/8)/(F/8+W)$%, where F is the number of fragments and W is that of well-preserved planktonic foraminifera in the sample [*Le and Shackleton*, 1992]. Calcareous nannofossil and radiolarian were analyzed only for providing biostratigraphic controls in this study and will be discussed in separate papers later.

Determination of carbonate content in the sample was made at Taiwan University according to the weight loss method outlined by *Molnia* [1974]. The salt in each sample was, however, washed out by distilled water before the carbonate material was dissolved by 1 *N* hydrochloric acid. Opal content was measured at Sun Yat-Sen University in Kaohsiung following the technique of *Mortlock and Froelich* [1989] with slight modifications described by *Murray et al.* [1993], except that 0.5 *N* NaOH instead of 2 *M* Na_2CO_3 was used to extract the biogenic opal. Overall, the analytical precision of the carbonate and opal determination are better than 1.0 and 1.5%, respectively.

Oxygen and carbon stable isotope measurements were carried out on the planktonic foraminiferal species *Globigerinoides sacculifer* (wo) (without a saclike final chamber) (>150 μm) using a V. G. Micromass 602 mass spectrometer at the Institute of Earth Sciences, Academia Sinica at Taipei. The analytical precision expressed as 1σ for NBS-19 standard carbonate was 0.06‰. The average difference of duplicate foraminiferal analyses is ~0.12‰ for oxygen and 0.09‰ for carbon.

High-resolution continuous paleomagnetic measurements were performed at the Laboratoire des Sciences du Climat et de l' Environment (LSCE) of the Centre National de la Recherche Scientifique (CNRS)-Commissariat à l' Energie Atomique (CEA), France. The sediments were sampled using the 1-m-long u channel plastic container [*Tauxe et al.*, 1983; *Weeks et al.*, 1993]. The natural remnant magnetization was measured continuously with a resolution of ~3 cm using a pass-through DC-SQUID cryogenic magnetometer in a shielded room. Stepwise in-line demagnetization with an average of 8-10 steps up to 60 mT was used to retrieve the primary component of the magnetization, which was isolated after the very first steps of demagnetization.

For spectral analyses a menu-driven PC program SPECTRUM [*Schulz and Stattegger*, 1997] was used. Compared to the widely used Blackman-Turkey approach for spectral analysis, the advantage of SPECTRUM is the avoidance of any interpolation of the time series. The interpolation of unevenly spaced time series may significantly bias statistical results because the interpolated data points are no longer independent [*Schulz and Stattegger*, 1997]. In this study, we selected 1.0 and 4.0 for the highest frequency factor (HIFAC) and the oversampling factor (OFAC), respectively, for a good compromise between computing time and smoothness of a spectrum. The time series was divided into three 50% overlapping Welch-overlapped-segment-averaging (WOSA) segments which were linearly detrended.

The material used in this study is stored at the Laboratory of Marine Geology, Tongji University. The complete data discussed in this paper are available upon request.[1]

Table 2. Microfossil Datums and Magnetostratigraphic Events Adopted in This Study

Stratigraphic Events	Depth, cm	Age, Ma	Reference
Pink *Globigerinoides ruber* LAD	180	0.12	1
Pseudoemiliania lacunosa LAD	560	0.46	2
Stilostomella Extinction	690	0.62	3
Brunhes/Matuyama Boundary	795	0.78	4, 5
Top Jaramillo	967	0.99	4, 5
Base Jaramillo	1020	1.07	4, 5
Anthocyrtidium angulare LAD	1080	1.15	6, 7
Cobb Mountain	1120	1.201-1.211	4, 5

LAD is last appearance datum. (1) *Thompson et al.* [1979]; (2) *Thierstein et al.* [1977]; (3) *Schönfeld* [1996]; (4) *Shackleton et al.* [1990]; (5) *Berggren et al.* [1995]; (6) *Moore* [1995]; (7) *Shackleton et al.* [1995].

3. Results

3.1. Chronological Framework

First, a low-resolution chronological framework was developed on the basis of microfossil biostratigraphy and magnetostratigraphy for the last 1500 kyr. Four datums of calcareous and siliceous microfossils, including planktonic and benthic foraminifera, calcareous nannofossil, and radiolarian, were adopted in this study (Table 2). The Brunhes/Matuyama (B/M) magnetic polarity reversal (0.78 Ma) is clearly apparent as a change to negative inclination and a 180 swing of the declination at a depth of 795 cm. The upper Jaramillo (0.99 Ma) transition, unfortunately coinciding with the separation between two u channels, is around 967 cm. The lower Jaramillo (1.07 Ma) transition is situated at a depth of 1020 cm, again characterized by a change to negative inclination and a declination swing. The sharp swing in declination at 1120 cm might correspond to the Cobb Mountain event (between 1.201 and 1.211 Ma) (Figures 2 and 3 and Table 2).

Of particular interest is the discovery of microtektites at the depths of 780-815 cm, with conspicuous peak at the depths of 805-810 cm slightly below the B/M boundary (Figure 3) [*Zhao et al.*, 1999]. According to its chemical and physical properties, the microtektites in the core also occurred extensively in deep sediments of Australasian area [*Glass*, 1967; *Smit et al.*, 1991] and Chinese loess [*Wu et al.*, 1992]. It therefore can serve as an additional stratigraphic marker in the SCS. Time-to-depth conversions (Figure 2) were performed by assuming constant sedimentation rates between the biostratigraphic and magnetostratigraphic control points (Table 2), which shows no obvious hiatus in the core during the last 1500 kyr. The estimated average sedimentation rate for the core is ~0.93 cm/kyr.

We constructed more detailed age model primarily based on foraminiferal $\delta^{18}O$ and coarse fraction records, with constraints of biostratigraphic and magnetostratigraphic control points (Figure 3). The chronology for the isotopic age model was developed from ODP Site 677 [*Shackleton et al.*, 1990], different from those proposed by *Ruddiman et al.* [1989]. Coarse fraction stratigraphy developed in the equatorial Indian Ocean [*Bassinot et al.*, 1994]

[1] Supporting data are available on diskette or via Anonymous FTP from www.agu.org, directly APEND (username = anonymous, Password = guest). Diskette may be ordered from American Geophysical Union, 2000 Florida Avenue, N.W., Washington, DC 20009 or by phone at 800-966-2481; $15.00. Payment must accompany order.

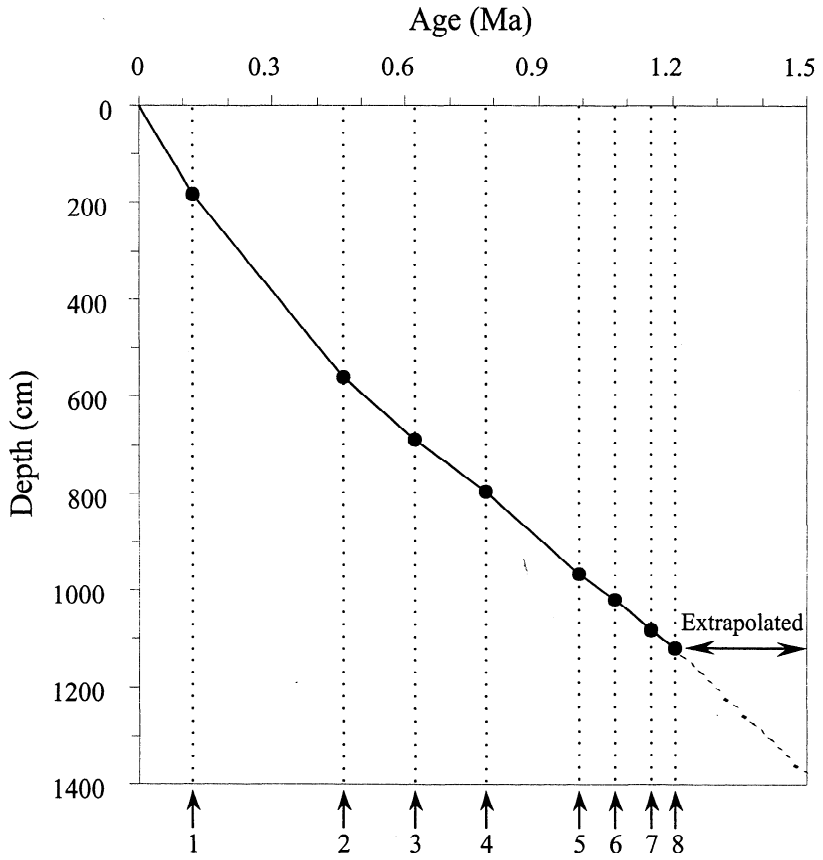

Figure 2. Age-depth plot showing sedimentation rates in core 17957-2: 1, pink *Globigerinoides ruber* last appearance datum (LAD); 2, *Pseudoemiliania lacunosa* LAD; 3, *Stilostomella* extinction; 4, Brunhes/Matuyama boundary; 5, top of Jaramillo; 6, base of Jaramillo; 7, *Anthocyrtidium angulare* LAD; 8, Cobb Mountain event.

was applied in the SCS. Major peaks (CF2~23) of the coarse fraction curve in core 17957-2 have been labeled according to their position relative to the $\delta^{18}O$ stratigraphy (Figure 3), which can be well correlated with those from ODP Site 758 in the Indian Ocean. The age of each sample was interpolated on the basis of the average sedimentation rate between the isotopic age model control points. The base of the core reaches ~1.50 Ma.

The most striking change for $\delta^{18}O$ and coarse fraction curves is the MPR at the entrance to glacial marine isotopic stage (MIS) 22 [*Berger et al.*, 1993a]. After this time, the eccentricity cycles of ~100 kyr entirely dominated. Before it, the low-amplitude obliquity cycles of 41 kyr is more important. Taking the records at face value, little or no evidence exists for a transition zone: the change is abrupt, at least on the timescale considered here (Figure 3). Thus, back to the Cobb Mountain event, the stratigraphy of this core is reliable, while a minor hiatus or extremely low sedimentation rate occurs between MISs 22 and 24 and between MISs 27 and 29 (Figure 3). Below it, however, the recognition of MIS is relatively difficult without biostratigraphy and magnetostratigraphic controls.

3.2. Variations in the Sea Surface Temperature

Variations in the relative abundance of main planktonic foraminiferal species which could be divided into shallow- and deep-dwelling species [*Bé*, 1977; *Fairbanks et al.*, 1982; *Ravelo et al.*, 1990] were examined (Figures 4 and 5). MISs 22-20 from the MPR to B/M boundary and MISs 6-5 are two important boundaries. During MISs 6-5 the abundances of tropical-subtropical species *Globigerinoides ruber* and *G. sacculifer* (wo) remarkably decreased, while those of temperate species *Neogloboquadrina dutertrei* and *Globorotalia crassaformis* reached maximum, indicating a considerable decrease in SSTs. After MISs 22-20, the abundances of shallow-dwelling species *G. ruber*, *G. sacculifer* (wo) and *Globigerina bulloides* decreased, while those of deep-dwelling species *Pulleniatina obliquiloculata*, *Globorotalia menardii*, *G. crassaformis*, and *Globorotalia inflata* remarkably increased. Nevertheless, all the species in Figures 4 and 5 except *G. inflata* have no clear consistent glacial-interglacial changes.

Planktonic foraminifera in the core are well preserved with low fragmentation (<10%; see Figure 9), and the estimated SSTs using two different techniques have very low correlation (R^2<0.01) with the fragmentation, indicating that the temperature estimates are not biased by carbonate dissolution. All planktonic foraminiferal species except pink *G. ruber* in the core can be found in surface sediments of the western pacific and SCS [*Thompson*, 1981; *Pflaumann and Jian*, 1999]. Even pink *G. ruber* took only a small part of *G. ruber* during the period of ~400-120 ka [Li, 1997]. The evolutionary changes therefore could not much influence the SST estimates during the last 1500 kyr in the SCS.

The estimated SSTs of core top from FP-12E and SIMMAX-28 are 27.2° and 27.0°C for winter, and 29.4° and 28.9°C for summer, respectively. Their differences with the present day SSTs at this site (27.03°C for winter and 28.85°C for summer [*Levitus and Boyer*, 1994]) are less than the standard errors of estimation [*Thompson*, 1981; *Pflaumann and Jian*, 1999]. The SIMMAX-28-derived winter SST ranges from 24.7° to 27.8°C, averaging 27.0°C, while the SIMMAX-28-derived summer SST changes little from 28.8° to 29.4°C with an average of 29.0°C (Figure 6a). Their amplitudes of fluctuation are much greater than the standard errors of SIMMAX-28, indicating the changes of SIMMAX-28-derived SSTs are quite reliable. As for the FP-12E-derived SSTs, the winter SST ranges from 24.5° to 27.8°C, averaging 26.4°C, while the summer SST changes little from 28.7° to 30.0°C with an average of 29.3°C (Figure 6b). The amplitude of fluctuation in the FP-12E-derived winter SST (3.3°C) is greater than the standard error of the FP-12E cold equation, implying that the changes of FP-12E-derived winter SST are really significant.

Compared to previous data in the SCS using the transfer function FP-12E [*Wang and Wang*, 1990; *Miao et al.*, 1994; *Wang et al.*, 1995], both the estimated winter and summer SSTs from FP-12E and SIMMAX-28 are slightly warmer with a narrower range of seasonality in core 17957-2. This may be explained by the fact that (1) the core is located in the tropical SCS as a part of WPWP and (2) it is far away from the influence of coastal currents. As shown in Figure 6a, the SIMMAX-28-derived winter SST changed little after the B/M boundary, except the excursions at MISs 7/8 and during MISs 6-5. However, before the boundary, it was very changeable with four distinct decreases. The average SIMMAX-28-derived winter SST before the B/M boundary is 26.7°C, lower than the average value of 27.2°C after it. However, the greatest change in the FP-12E-derived winter SST occurred at MISs 21/22, which divides the curve into two clear sections. The average FP-12E-derived winter SST was 26.6°C after MIS 21, while it was only 26.1°C before the time (Figure 6b). on the basis of the results from two different transfer functions the tropical SSTs slightly increased right after the obvious decrease in winter SST during MISs 22-20, which may correspond to the climate changes at the MPR [*Berger et al.*, 1993]. Since the B/M boundary, the winter SST changed within a range of <3°C, in agreement with those of *Climate: Long-Range Investigation, Mapping, and Prediction* (*CLIMAP*) *Project Members* [1981] in the western equatorial Pacific. This further supports that "the last 1.0 Ma was dominantly a period of lower SST in the late Neogene, except at the tropics where SST was a little higher than before and experienced only minor fluctuations in the western Pacific,"

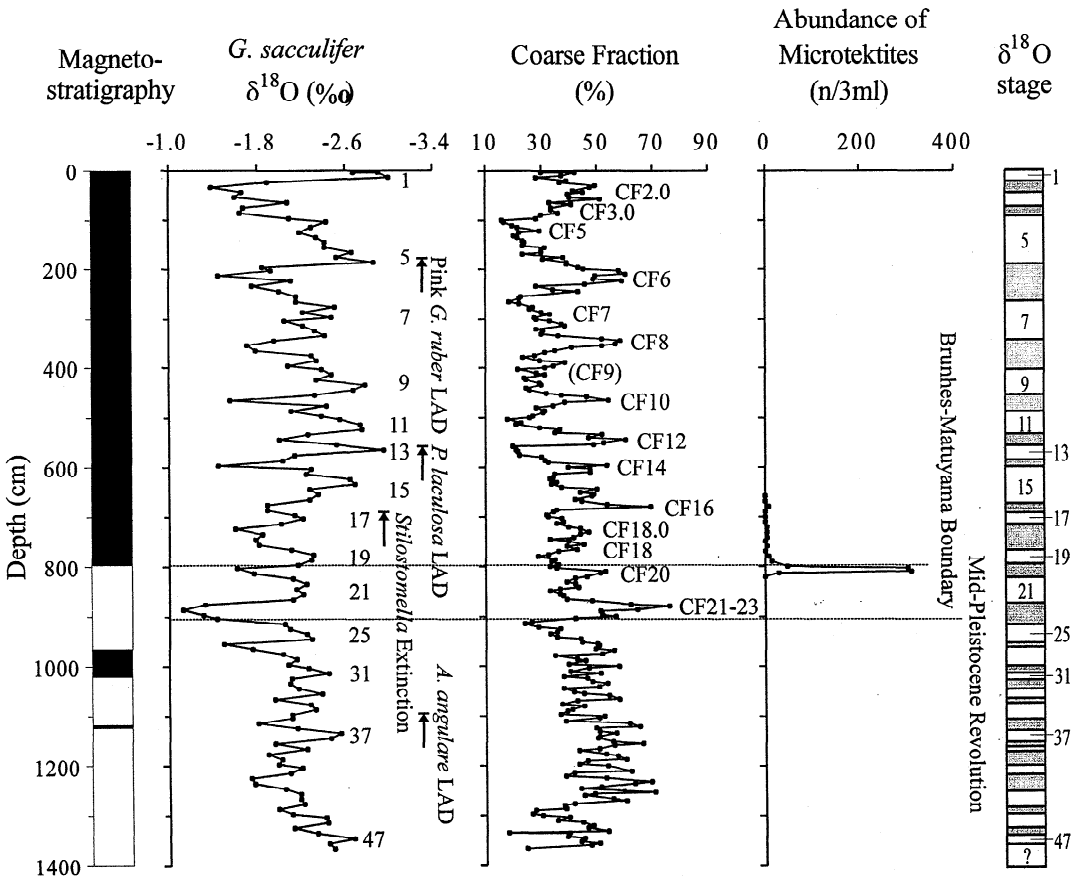

Figure 3. Magnetostratigraphic, oxygen isotopic, and coarse fraction stratigraphic framework in core 17957-2. The magnetostratigraphy is shown as a column with the usual black and white convention for normal and reverse periods, respectively. Major peaks of the coarse fraction curve (CF2~23) have been labeled according to their position relative to the $\delta^{18}O$ stratigraphy [*Bassinot et al.*, 1994]. The biostratigraphic and microtektite control points are also shown. Marine oxygen isotopic stages are indicated on the right side.

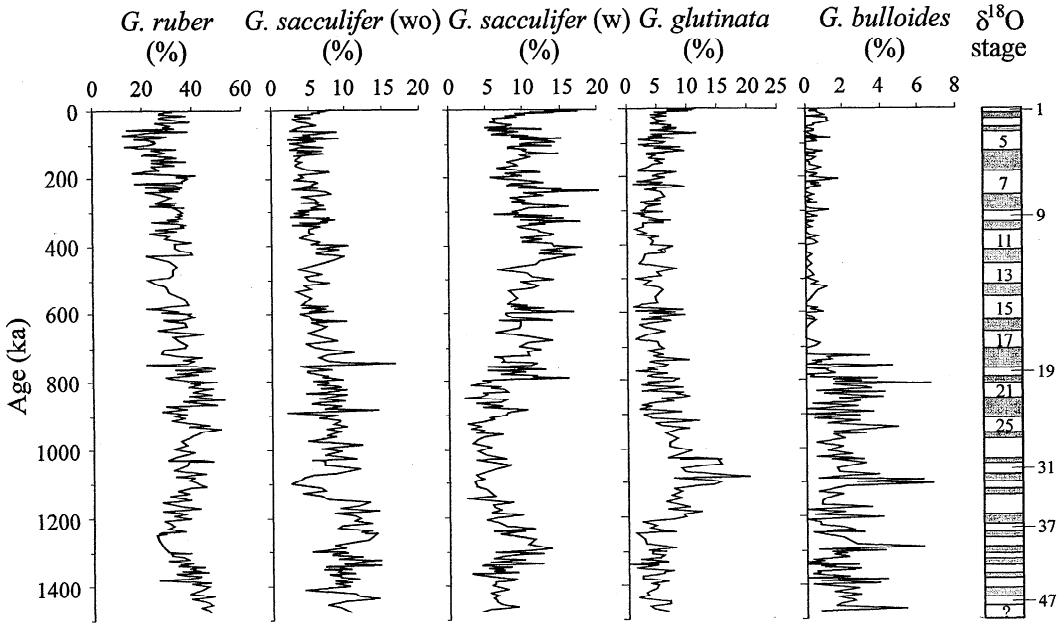

Figure 4. Variations in relative abundance of selected shallow-dwelling planktonic foraminiferal species. *G. sacculifer* (w) is *G. sacculifer* with a saclike final chamber. Marine oxygen isotopic stages are indicated on the right side.

concluded by *Wang* [1994, p. 379]. It seems that the WPWP was relatively stable during the late Pleistocene glacial cycles [*Thunell et al.*, 1994]. However, there was an obvious decrease in the winter SST during MISs 6-5, judging from the FP-12E-derived and SIMMAX-28-derived curves (Figure 6). This event made the winter SST higher during MISs 4-2 than during MIS 5, apparently conflicting with the pattern of glacial decrease and interglacial increase in SSTs revealed by previous studies in the SCS [*Wang and Wang*, 1990; *Miao et al.*, 1994; *Wang et al.*, 1995]. Therefore the SSTs here did not systematically vary with glacial-interglacial cycle.

3.3. Reconstruction of the Depth of Thermocline

Numerous tropical ocean studies suggest planktonic foraminiferal species abundance are controlled by upper water temperature and nutrient gradients [*Fairbanks and Wiebe*, 1980; *Fairbanks et al.*, 1982; *Bé et al.*, 1985; *Ravelo et al.*, 1990; *Martinetz*, 1994; *Andreasen and Ravelo*, 1997]. Some researchers have investigated the potential usefulness of very deep dwelling species *G. truncatulinoides* for reconstruction of the upper thermal structure. This species has an unusual life cycle in that it reproduces at ~600 m and from this depth, juveniles rapidly travel to the surface then slowly sink through the water column, growing by adding chambers [*Bé*, 1977; *Bé et al.*, 1985; *Hemleben et al.*, 1989]. For this reason, a higher proportion of this species may indicated a very deep thermocline and/or thick mode water thermostads [*Lohmann and Schweitzer*, 1990; *Lohmann*, 1992; *Ravelo and Fairbanks*, 1992; *Martinez*, 1994, 1997]. The percentage abundance of *G. truncatulinoides* in core 17957-2 (Figure 7) show a trend of gradual decrease during the Brunhes chronozone which indicates the scale of mixing and the DOT have gradually decreased. Especially, *G. truncatulinoides* left-coiling form, which requires a thermocline much deeper than right-coiling form, and *Globoquadrina conglomerata* (lives predominantly below 100 m as adults; [*Bé*, 1977]) abruptly increased in MIS 5 (Figure 7), indicating that the thermal structure of upper water column greatly changed during the time interval.

The average estimated DOT of Holocene (~190 m) agrees with the modern annual DOT derived from the world ocean atlas of *Levitus and Boyer* [1994] in this region. Moreover, the average communality is 0.88, indicating this transfer function technique can interpret 94% of the total variance in the observed faunal information. The estimated DOT ranges from 115 to 230 m in the core, averaging 190 m. Generally, the DOT was relatively deeper during interglacial periods than during glacial periods. The most conspicuous change for the DOT was that it changed little around 200 m before MISs 22-21, that is, before the MPR, and then it gradually decreased during the Brunhes chronozone, with an average of 180 m (Figure 7). The shallowest DOT (~115 m) occurred within MIS 6 and then became deep again after the abrupt increase of *G. truncatulinoides* left-coiling form and *G. conglomerata* in MIS 5.

Previous studies have revealed that when the DOT shoals, the mixed layer-dwelling species (*G. ruber*, *G. sacculifer*, and *Globigerinita glutinata*) decrease, while the thermocline-dwelling species (*P. obliquiloculata*, *G. menardii*, *G. inflata*, and *N. dutertrei*) increase in abundance [*Ravelo et al.*, 1990; *Ravelo and Fairbanks*, 1992]. In core 17957-2 the MPR served as a turning point for the abundances of the mixed layer- and thermocline-dwelling species. The mixed layer-dwelling species decreased in abundance since the MPR and reached minimum during MISs 6-5, while the thermocline-dwelling species changed in an opposite trend (Figure 7), corresponding to the variations of the DOT. In fact, the shallowing of the DOT since the MPR was found also in the western equatorial Pacific [*Schmidt et al.*, 1993].

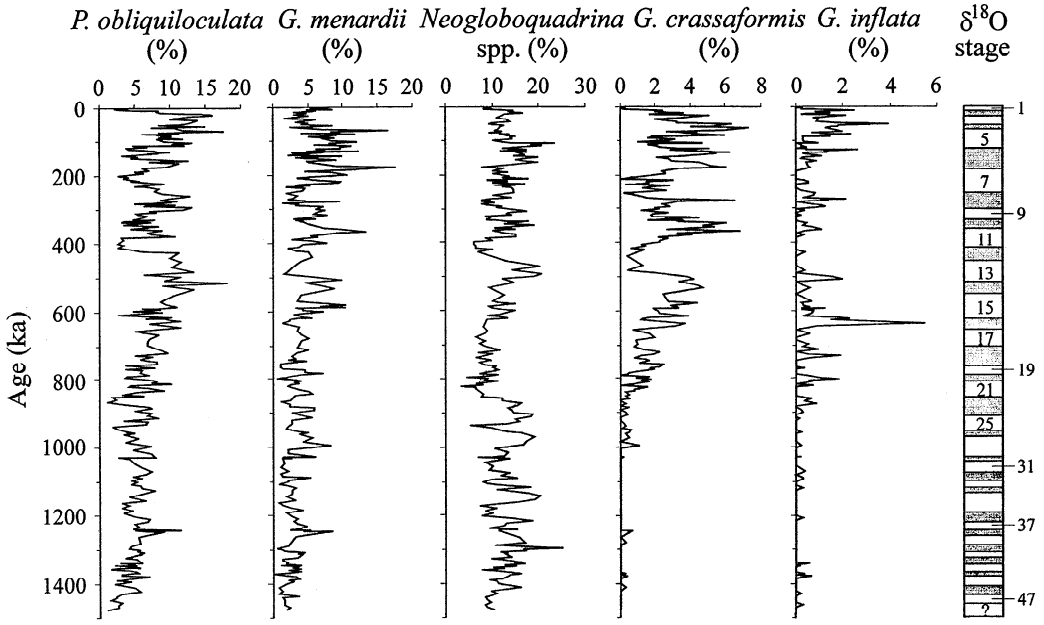

Figure 5. Variations in relative abundance of selected deep-dwelling planktonic foraminiferal species. Marine oxygen isotopic stages are indicated on the right side.

After a minimum shortly before the B/M boundary, the $\delta^{18}O$ difference between *G. sacculifer* and *P. obliquiloculata* continues to increase sharply toward the present at Ocean Drilling Program (ODP) Site 806 on the Ontong Java Plateau. Therefore the tropical DOT in this region has indeed experienced remarkable variations in the Pleistocene.

3.4. Changes of Deep Water Masses

Deep-sea benthic foraminifera has been widely used to reconstruct the late Pleistocene variations in deep water masses, carbonate dissolution, and surface productivity in the SCS for the past few years [*Miao and Thunell*, 1996; *Jian and Wang*, 1997;

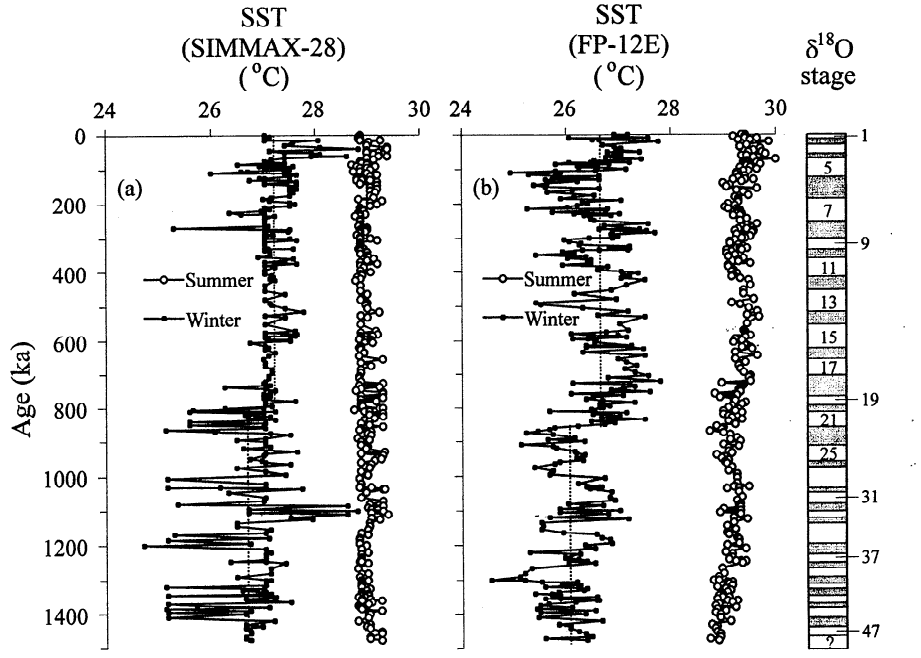

Figure 6. Down-core variations in the (a) SIMMAX-28-derived and (b) FP-12E-derived winter and summer SSTs. Dashed lines show the average winter SST: before and after the B/M boundary (Figure 6a) and before and after MIS 21 (Figure 6b). Marine oxygen isotopic stages are indicated on the right side.

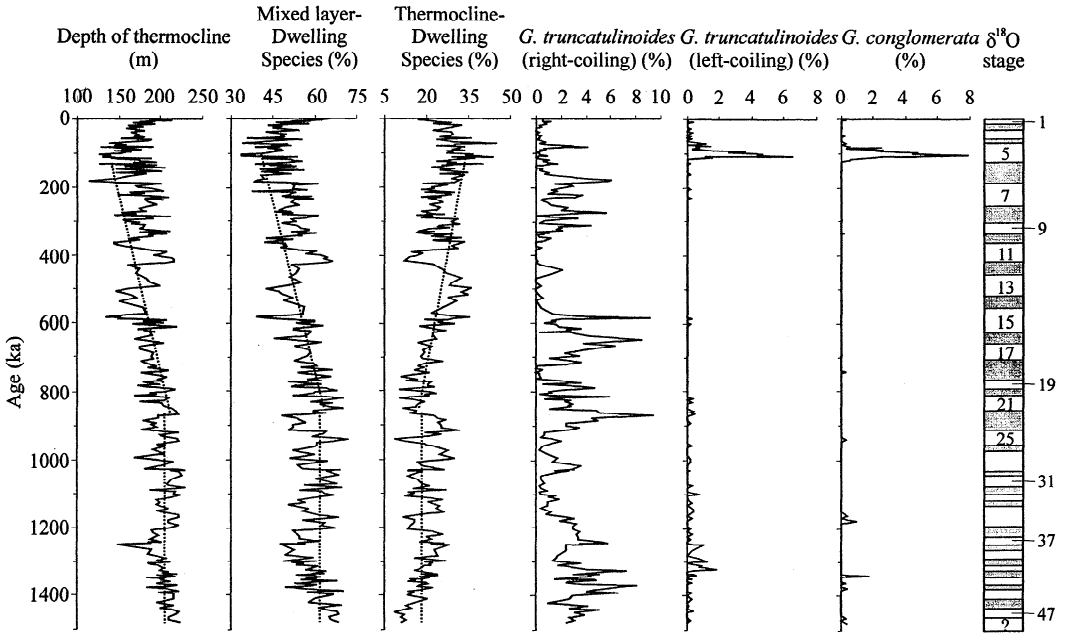

Figure 7. Long-term changes in the DOT estimated using transfer function of *Andreasen and Ravelo* [1997], relative abundances of mixed layer-dwelling species (*Globigerinoides ruber*, *Globigerinoides sacculifer*, and *Globigerinita glutinata*), thermocline-dwelling species (*Pulleniatina obliquiloculata*, *Globorotalia menardii*, *Globorotalia inflata*, and *Neogloboquadrina dutertrei*), right-coiling and left-coiling *Globorotalia truncatulinoides*, and *Globoquadrina conglomerata*. Dashed lines show the general trends of change before and after MISs 22-21. Marine oxygen isotopic stages are indicated on the right side.

Kuhnt et al., 1999]. *Jian et al.* [1999] recently claimed that deep-sea benthic foraminifera in the SCS might be divided into two major groups whose distributions are primarily controlled by the organic flux to the seafloor and the chemical/physical properties in the ambient water mass, respectively. Therefore benthic foraminiferal species and assemblages could be used to monitor the general trend of changes in deep water masses during the Pleistocene in the SCS [*Jian and Wang*, 1997].

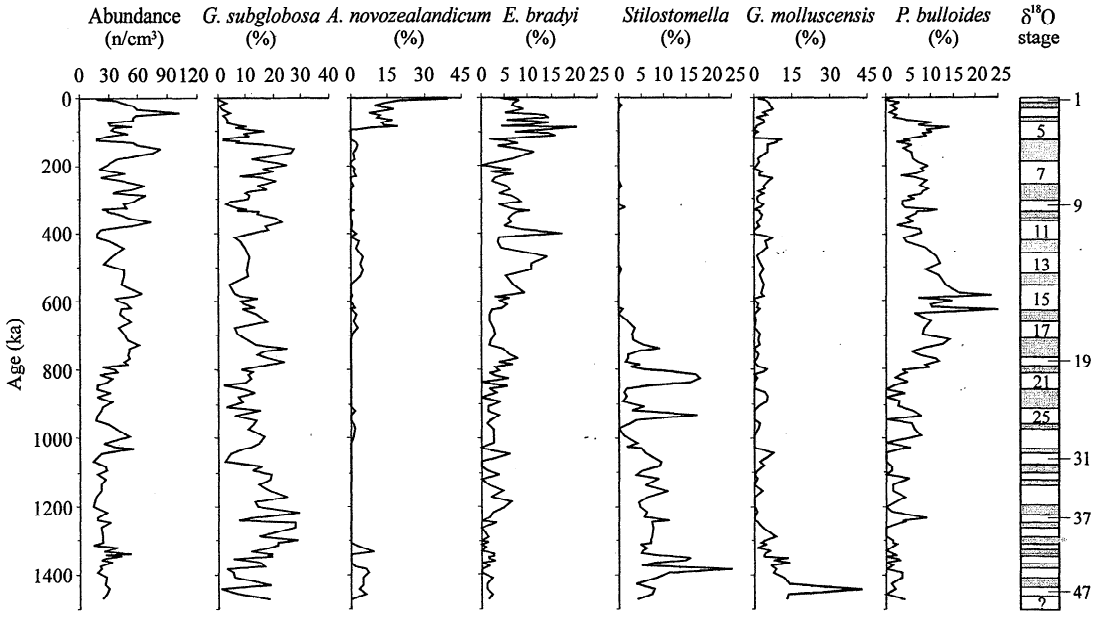

Figure 8. Variations in the abundance of benthic foraminiferal fauna and percentage abundance of main benthic foraminiferal species. Marine oxygen isotopic stages are indicated on the right side.

The abundance of benthic foraminiferal fauna (number of specimens per cubic centimeter) varies between 10 and 110 in the core, with lower values prior to the B/M boundary (Figure 8), implying a great change in deep water conditions at that time. On the basis of the down-core distribution of main benthic foraminiferal species (Figure 8), two important boundaries are found at the B/M boundary and MIS 5. At the B/M boundary, *Pullenia bulloides* increased significantly in abundance, while *Stilostomella* spp. remarkably decreased and then became extinct at the depth of 690 cm. Moreover, since MIS 5, *Globocassidulina subglobosa* obviously decreased in abundance, while *Astrononion novozealandicum* increased. We used *Q* mode factor analysis to better discriminate benthic foraminiferal assemblages. As a result, four varimax factors were obtained, which explain 78.6% of the total variance. According to the down-core variations in factor loadings of each factor (Figure 9) and the factor scores of each species or species groups (Table 3), factor 1, absolutely dominated by *G. subglobosa*, controls most part of the last 1500 kyr before MIS 5. However, factor 2, represented by the *A. novozealandicum* assemblage which is characteristic of *A. novozealandicum* and *Eggerella bradyi* (Figure 8), became more important since MIS 5. Factor 3, dominated by *Stilostomella* spp. and *Globocassidulina molluscensis*, was important before the B/M boundary, especially toward the bottom of the core, while factor 4, represented by the *P. bulloides* assemblage, controlled the period between the B/M boundary and MIS 5.

G. subglobosa is the dominant species of the modern Intermediate Water Mass (IWM) in the SCS as resolved by the same technique [*Jian and Wang*, 1997]. Because factor 1 is characterized by this species, its variations in factor loading should represent the changes of the IWM. From Figure 9 it is inferred that core 17957-2 is bathed in the Deep Water Mass (DWM) now, but it was mainly controlled by the IWM before MIS 5. The remarkable decease in factor 1 and the relative abundance of *G. subglobosa* since MIS 5 indicate that the IWM weakened, as revealed by a previous study [*Jian and Wang*, 1997]. Particularly, the IWM displays a general trend of glacial decrease and interglacial increase, which is obviously superimposed by long-term fluctuations of ~200 kyr.

Compared with those of the IWM, the changes of the DWM are much more complicated. *A. novozealandicum* is the dominant species of the modern DWM in the SCS, especially in the oligotrophic area [*Jian and Wang*, 1997]. The remarkable increase in factor 2 and the relative abundance of this species since MIS 5 indicated that the DWM abruptly strengthened at the expense of the IMW. Before that time, *P. bulloides* assemblage of factor 3 and *Stilostomella* spp. assemblage of factor 4 had successively represented the DWM instead of *A. novozealandicum* assemblage (Figure 9) because *P. bulloides* is one of the characteristic species of the modern DWM [*Jian and Wang*, 1997], while *Stilostomella* spp. is commonly found in cores with present water depths between 1500 and 3000 m [*Schönfeld*, 1996]. The faunal turnovers indicate that there were two major changes in the DWM over the last 1500 kyr. The first one occurred at the B/M boundary, slightly later than the changes in SSTs and DOT. The second one took place within MIS 5, possibly corresponding to the major changes in surface productivity (see Figure 11) and/or the thermal structure of upper water column (Figure 7) at that time.

3.5. Deep-Sea Carbonate Dissolution Fluctuations

The percentage of agglutinated tests in benthic foraminiferal fauna, BF/(BF+PF)%, and relative abundance of agglutinated *E.*

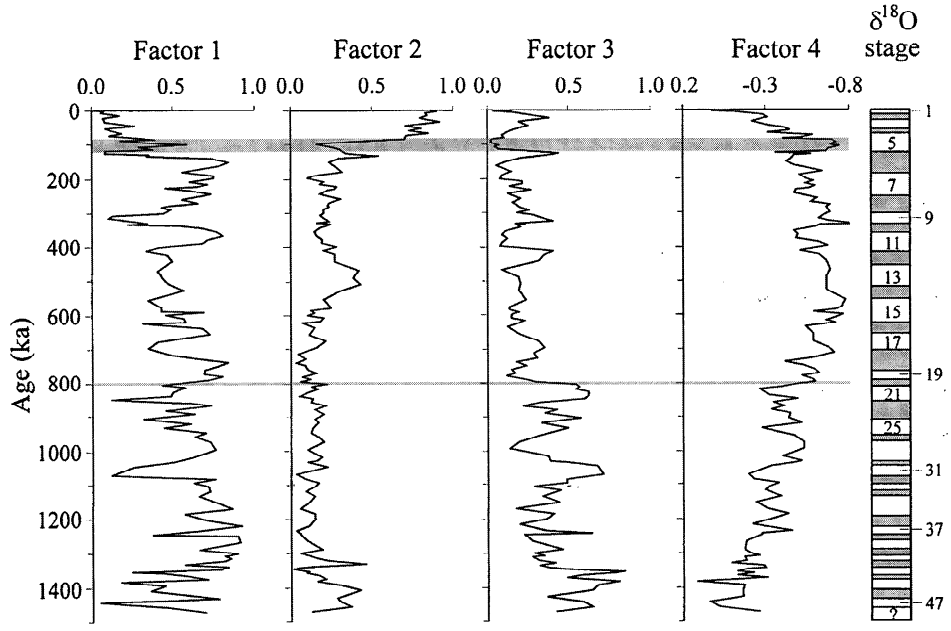

Figure 9. Results of *Q* mode factor analysis on benthic foraminifera, showing down-core variations in factor loading of the four varimax factors. The most important boundaries at the B/M boundary and MIS 5, respectively, are shaded. Marine oxygen isotopic stages are indicated on the right side.

Table 3. Matrix of Factor Scores of the Four Benthic Foraminiferal *Q* mode Varimax Factors

Species / Species Groups	Factor 1	Factor 2	Factor 3	Factor 4
Eggerella bradyi	-0.089	0.314	-0.087	-0.386
Sigmoilopsis schlumbergeri	0.010	-0.008	0.031	-0.002
Pyrgo spp.	-0.009	-0.011	0.218	-0.077
Triloculina tricarinata	-0.020	-0.012	0.198	-0.042
Quinqueloculina seminula	0.015	0.017	0.218	-0.086
Quinqueloculina venusta	-0.009	-0.008	0.039	-0.034
Quinqueloculina spp.	0.003	0.005	0.054	0.006
Lagena spp.	0.020	0.044	0.115	-0.042
Fissurina spp.	0.092	0.109	0.279	-0.203
Nodosaria spp.	0.012	-0.002	0.047	0.013
Dentalina spp.	0.050	0.022	0.131	0.042
Stilostomella spp.	0.087	-0.113	0.639	0.186
Guttulina spp.	0.006	0.039	0.020	-0.037
Bolivina pacific	-0.024	-0.020	0.074	-0.027
Pleurostomella alternans	0.051	-0.012	0.102	0.044
Bulimina alazanensis	-0.013	-0.030	-0.041	-0.244
Bulimina aculeata	-0.077	0.016	0.034	-0.144
Uvigerina peregrina	-0.003	-0.004	0.026	-0.099
Uvigerina auberiana	-0.033	0.112	0.057	-0.050
Reussella spinulosa	-0.010	0.043	0.008	0.000
Francesita advena	-0.001	0.026	0.029	-0.020
Ehrenbergina undulata	0.101	0.031	0.052	0.099
Cassidulina crassa	0.002	0.006	0.006	-0.017
Cassidulina laevigata	0.003	0.137	-0.024	-0.029
Rutherfordoides tenuis	-0.019	-0.008	0.154	0.012
Globocassidulina subglobosa	0.961	-0.032	-0.095	-0.098
Globocassidulina molluscensis	0.006	0.255	0.371	0.108
Favocassidulina favus	-0.006	-0.014	0.045	-0.119
Pullenia bulloides	-0.050	-0.056	-0.067	-0.596
Pullenia quinqueloba	-0.055	0.053	0.190	-0.171
Melonis barleeanum	0.049	0.077	0.013	-0.047
Melonis pompilioides	0.056	-0.021	-0.025	-0.075
Astrononion novozealandicum	0.019	0.798	-0.084	0.209
Elphidium spp.	-0.014	0.023	0.016	-0.008
Epistominella exigua	-0.018	-0.031	0.036	-0.095
Sphaeroidina bulloides	-0.004	0.066	0.033	-0.095
Anomalina globulosa	0.007	-0.005	0.051	-0.049
Hoeglundina elegans	-0.009	0.052	0.006	-0.003
Oridosalia umbonatus	0.055	0.132	0.116	-0.184
Gyroidina orbicularis	-0.013	0.031	-0.003	-0.060
Gyroidinoides lamarckiana	0.006	0.091	0.057	-0.262
Osangularia culter	-0.018	-0.007	0.085	-0.048
Cibicidoides robertsonianus	0.106	0.284	0.016	-0.041
Cibicidoides cf. *robertsonianus*	0.000	-0.019	0.064	-0.015
Cibicidoides wuellerstorfi	-0.028	-0.051	0.207	-0.212
Cibicidoides kullenbergi	0.015	-0.017	0.091	-0.008
Cibicides sp.	0.011	-0.016	0.022	-0.017
Cibicides okinawaensis	0.003	-0.010	0.018	-0.010

bradyi can be used to evaluate deep-sea carbonate dissolution [*Bian et al.*, 1992; *Miao and Thunell*, 1996]. Their obvious increases during the Brunhes chronozone show strengthened dissolution (Figures 8 and 10). In fact, planktonic foraminiferal fragmentation is the best indicator for deep-sea carbonate dissolution [*Le and Shackleton*, 1992; *Miao et al.*, 1994], with high values related to enhanced dissolution. In core 17957-2 the fragmentation curve is negatively well correlated with the coarse fraction and carbonate curves (Figure 10). They display a distinct glacial-interglacial pattern since the MPR. The dissolution spikes with high fragmentation and low coarse fraction and carbonate always occurred in the interglacial stage and the transition from interglacial to glacial stage, for example, MISs 5, 6/7, 8/9, 11, 12/13, 14/15, 17, 18/19, and 21. These spikes can be recognized to correspond to the dissolution events of B3, B5, B7, B9, B11, B13, B15, B17, and M1 in the equatorial Pacific, respectively [*Farrell and Prell*, 1989, 1991]. This typical "Pacific-type" carbonate cycle [*Thunell et al.*, 1992; *Wang et al.*, 1995] in the core further confirms that the SCS shared the same carbonate dissolution signals as the tropical Pacific during the Pleistocene [*Farrell and Prell*, 1989, 1991; *Yasuda et al.*, 1993].

However, the glacial-interglacial pattern of fragmentation is superimposed by a long-term oscillation with an irregular cycle length. Maxima in the fragmentation curve are found at the MPR, MISs 13-11 and MIS 5, in agreement with the changes in the percentage of agglutinated benthic foraminifera and BF/(BF+PF)% (Figure 10). This long-term oscillation of carbonate dissolution has been found in the tropical Pacific and Indian Ocean [*Vincent*, 1981; *Bassinot et al.*, 1994]. Among the three periods of enhanced dissolution, the recent one possibly corresponded to the great changes in planktonic and benthic foraminiferal fauna during MISs 6-5 (Figures 4-9). The middle one centered at ~400 ka is known as the "middle Brunhes dissolution event" [*Farrell and Prell*, 1989; *Bassinot et al.*, 1994]. The lower one at the MPR is not the most striking, though with the highest fragmentation which is not supported by other dissolution indices. Compared to those before the MPR, the average values of fragmentation, percentage of agglutinated benthic foraminifera and BF/(BF+PF)% were higher, while that of coarse fraction and carbonate were lower after the MPR (Figure 10). This implies slightly increased carbonate dissolution as a whole after the MPR in the southern SCS.

3.6. Enhanced Surface Productivity Over the Last 200 kyr

Now it is more than apparent that abundance and species composition of benthic foraminifera are primarily controlled by the organic carbon flux to the seafloor and thus, ultimately, by the surface productivity [*Herguera and Berger*, 1991; *Sarnthein and Altenbach*, 1995; *Miao and Thunell*, 1996; *Jian et al.*, 1999; *Kuhnt et al.*, 1999]. It has been found that benthic foraminifera *Bulimina aculeata* and *Uvigerina peregrina* are well associated with high surface productivity in the SCS [*Miao and Thunell*, 1996; *Jian et al.*, 1999]. Their relative abundances are generally <5% in the core (Figure 11), indicating a very low surface productivity at this site, which is consistent with the modern distribution of surface primary productivity in the SCS [*The Multidisciplinary Oceanographic Expedition Team*, 1992]. Nevertheless, the relative abundance of *B. aculeata* and *U. peregrina* generally increased during glacial periods, especially in MISs 22, 8, and 6, indicating that the productivity slightly increased at these times.

Biogenic opal is a parameter related to the surface productivity [*Herguera and Berger*, 1991; *Murray et al.*, 1993]. The percentage of opal in the core ranges from 2.7 to 28.3%, with an important boundary at ~200 ka around MISs 6/7. The average value of opal content before 200 ka is only 6.6%, while that of the last 200 kyr is as high as 15.7% (Figure 11). This enhanced surface productivity over the last 200 kyr is also confirmed by the obviously decreased abundance of *Cibicidoides wuellerstorfi* (Figure 11), an epifaunal species often associated with low surface productivity [*Sarnthein and Altenbach*, 1995; *Miao and Thunell*, 1996; *Jian et al.*, 1999].

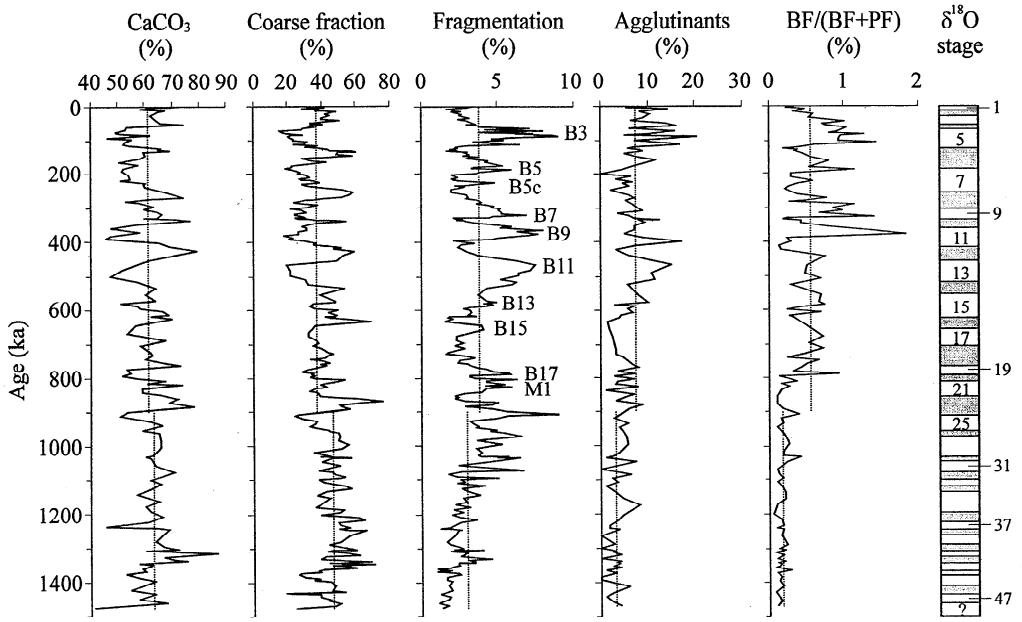

Figure 10. Deep-sea carbonate dissolution indices versus depth. B3~17 and M1 indicate major spikes of the fragmentation curve according to their corresponding dissolution events in the equatorial Pacific [*Farrell and Prell*, 1989, 1991]. Dashed lines show the average values before and after the MPR, respectively. Marine oxygen isotopic stages are indicated on the right side.

3.7. Periodic Variations in Paleoceanographic Records

Spectral analysis was used to study the variability of four paleoceanographic records ($\delta^{18}O$, *G. truncatulinoides* percent, FP-12E-derived winter SST, and IWM) for the last 1500 kyr (Figure 12). The IMW is represented by the factor loadings of benthic foraminiferal factor 1 as above discussed. After SPECTRUM has performed the analysis, some statistical parameters are displayed. Probably the most important is the reliable frequency range. Assuming that at least two full cycles are observed within each WOSA segment, the lowest reliable frequency in this study is 0.0027 1/kyr, corresponding to the period of 370 kyr. The spectral peaks with lower frequency than this limit are discarded in the study.

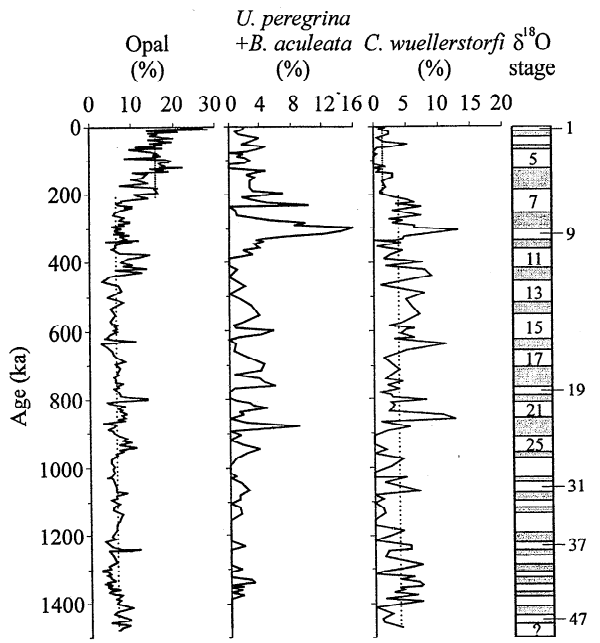

Figure 11. Down-core variations in the surface paleoproductivity indices. Dashed lines show the average values before and after 200 ka, respectively. Marine oxygen isotopic stages are indicated on the right side.

According to Figure 12a, the $\delta^{18}O$ record reveals clear eccentricity-dominated (~100 kyr) and processional (~23 kyr) signals but with weak obliquity-related (~41 kyr) response as expected. However, the obliquity response became more important for the early Pleistocene, corresponding to the climatic transformation at the MPR [*Berger et al.*, 1993a] which has been also found by previous studies on Chinese loess [*Liu and Ding*, 1993; *Ding et al.*, 1994]. An outstanding result of the spectral analyses is the existence of long-term oscillations of ~200 kyr for the records of upper water structure (e.g., *G. truncatulinoides* percent and winter SST) and deep water conditions (e.g., the IWM), with weak ~100 kyr eccentricity-related responses (Figures 12c and 12d). The obliquity-related (~46 kyr) responses for the records of upper water structure are more significant than that for the IWM record, in contrast to the spectrum of the $\delta^{18}O$ record. The ~200-kyr cyclicity has already been revealed in the *G. truncatulinoides* percent by previous study in the equatorial western Pacific [*Martinez*, 1994, 1997]. It is not confined to the upper water column but also occurred in the deep water of the SCS as shown by this study. We are not sure if the ~200-kyr cyclicity is a real cycle or not for the changes of the upper water structure and deep water conditions, and if so, its dynamics are still not clear. We suggest it possibly represents the second harmonic of the ~400 kyr period of eccentricity which became more important before the late Pleistocene ice age regime [*Clemens and Tiedemann*, 1997]. Therefore our data support eccentricity's role in the origin of low-frequency paleoceanographic oscillations in three dimensions of the WPWP.

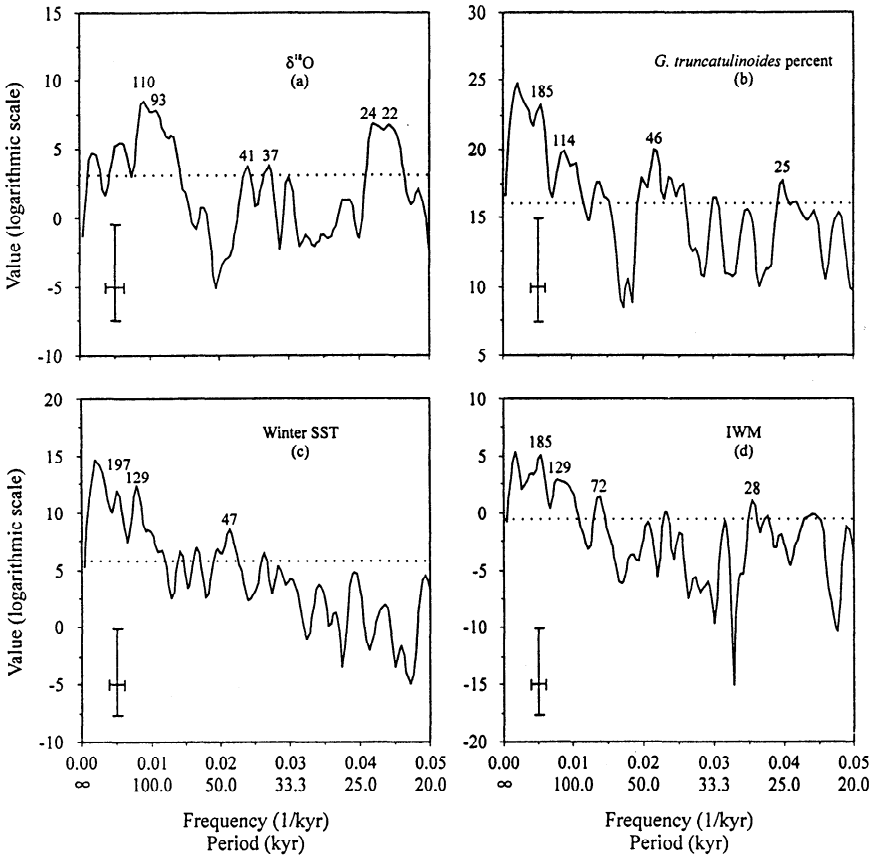

Figure 12. Spectral analysis of four paleoceanographic records: (a) $\delta^{18}O$, (b) *Globorotalia truncatulinoides* percent, (c) winter SST estimated using FP-12E transfer function, and (d) IWM for the last 1500 kyr (Settings: OFAC = 4.0; HIFAC = 1.0; number of segments is three; Welch window except Hanning window for $\delta^{18}O$. See *Schulz and Stattegger* [1997] for detailed description of these parameters). Numbers above peaks denote respective periods. Cross in lower left corner marks 6-dB bandwidth (horizontal) and 80% confidence interval (vertical). Horizontal dashed line denotes the average value of the spectrum and is a rough estimate for a white noise component in the time series. Considering only those parts of spectral peaks above this level gives an estimation of their corresponding variance contribution.

4. Discussion

Variations of the SSTs and DOT in the SCS are primarily a response to monsoonal wind-driven surface circulation [*Wyrtki*, 1961]. Core 17957-2 is located in the tropical SCS, where the foraminifera-based paleo-SST reconstruction has been a vigorous point of discussion in recent years [*Pflaumann and Jian*, 1999]. In this study, we applied two different transfer functions SIMMAX-28 and FP-12E. Both results show that the SSTs here have no consistent glacial-interglacial changes. Though there is nearly no tendency of point-by-point comparable SSTs, both results reveal (1) the slightly increased SSTs as a whole right after MISs 22-20 and (2) the obviously decreased winter SST during MISs 6-5.

Comparatively speaking, we have little knowledge about the variation of modern DOT in the SCS. Being a part of the WPWP, the southern SCS has other effects on its variation in the DOT except the East Asian monsoonal wind system. For example, the variations in the magnitude of the trade winds and associated equatorial currents may affect regional SCS circulation [*Wyrtki*, 1961]. Especially, during the Pleistocene glacial periods the SCS changed its configuration into a semienclosed basin due to the exposed shelf [*Wang et al.*, 1995]. This caused the outflow of subsurface water from the SCS into the Indian Ocean [*Wyrtki*, 1961] to be unlikely and altered the upper water structure of the southern SCS. The DOT there indeed experienced significant variations over the last 1500 kyr. Since the MPR, the DOT gradually became shallower until MISs 6-5 and then deepened afterward, as also confirmed by the changes in very deep dwelling species *G. truncatulinoides*. The shallowest DOT in MIS 6 can be used to evoke an upwelling enhancing the surface productivity.

It is interesting that the two major changes in deep water masses of the southern SCS were almost synchronous with those in surface water masses but generally with a potential lag in response. For example, planktonic foraminiferal fauna responded to the MPR immediately, while benthic foraminiferal fauna did not change until the B/M boundary. As for the paleoceanographic changes within MISs 6-5, the winter SSTs, DOT, and surface productivity greatly changed since MIS 6, while the deep water masses changed since MIS 5. Therefore both the surface and deep circulation in the southern SCS had experienced significant variations over the last 1500 kyr.

A variety of interpretations have been suggested to explain the striking paleoceanographic changes at the MPR, such as changes in North Atlantic Deep Water production [*Farrell and Prell*, 1991], increase of marine-based ice sheets, uplift of highlands from erosion, and tectonic forces [*Ruddiman and Raymo*, 1988; *Berger*

et al., 1993b]. The great changes within MISs 6-5, however, are addressed for the first time in the deep-sea areas of the western Pacific. The present study has no intention of drawing any conclusion on the nature of the two major Pleistocene paleoceanographic changes at the MPR and MISs 6-5 but only proposes possible links between paleoceanography and tectonics to interpret why the planktonic and benthic foraminiferal records show great changes at these times.

Despite the considerable dispute about timing and mechanism of the uplift of the Tibetan Plateau it is generally believed that the uplift has played a key role in adjusting Asian and Northern Hemispheric atmospheric circulation [*Kutzbach et al.*, 1989; *Molnar and England*, 1990; *Li*, 1991; *Harrison et al.*, 1991]. On the basis of the geological records of Tibetan Plateau and adjacent regions the uplift of the Plateau intensified since 3.6 Ma with three successive stages: 3.6-1.7 Ma, 1.1-0.6 Ma, and around 0.15 Ma [*Li*, 1991; *Li and Fang*, 1998]. The tectonic episode around 0.8 Ma was the most remarkable within the second stage when the plateau was uplifted to 3000-3500 m and entered into the cryosphere [*Shi and Zheng*, 1996; *Li and Fang*, 1998]. This episode coincided with the climatic transformation at the MPR revealed in the Chinese loess [*Liu and Ding*, 1993; *Ding et al.*, 1994] and deep-sea sediments in the western equatorial Pacific [*Berger et al.*, 1993a] and the SCS (see above). The tectonic event around 0.15 Ma resulted in the cutting through of the Long Yang Gorge [*Li*, 1991], which eventually brought about the entire Yellow River flowing eastward into the sea [*Wu et al.*, 1998]. This tremendous geomorphological change coincided with the onset of the extensive late Pleistocene marine transgression in East China [*Wang et al.*, 1985; *Yang et al.*, 1996], suggesting that the China offshore subsided at that time. Because the accelerating uplift of Tibetan Plateau has been suggested to be responsible for both the late Cenozoic global cooling and the intensification of Asian monsoon [e.g., *Ruddiman and Kutzbach*, 1989], we speculated it might be the tectonic events in China around 1.1-0.6 Ma and 0.15 Ma that caused important evolutionary changes in the East Asian monsoon. These major changes, furthermore, led to the reorganization of surface and deep circulation in the SCS, which were reflected by a series of paleoceanographic changes recorded in planktonic and benthic foraminifera.

However, the relationships between tectonics, climate, and paleoceanography are complex and highly nonlinear. It is likely that the middle and late Pleistocene major paleoceanographic changes in the SCS shall remain a mystery yet for some time, and the questions regarding their natures require a broad attack using many different signals from various environments [*Imbrie et al.*, 1989; *Berger et al.*, 1993a]. Fortunately, for possible further work on it, ~5500 m sediment from the northern and southern slopes of the SCS, which have been recovered by JOIDES Resolution in 1999 during ODP Leg 184 [*Prell et al.*, 1998], can be studied. We believe it will make a substantial contribution to understanding links between uplift of the Tibetan Plateau and major Pleistocene paleoceanographic changes in the SCS.

5. Conclusions

1. Core 17957-2 from the southern SCS provides nearly continuous paleoceanographic records of the last 1500 kyr on the basis of $\delta^{18}O$ curve of *G. sacculifer* and coarse fraction stratigraphy, as well as magnetostratigraphy and microfossil (including planktonic and benthic foraminifera, nannofossil, and radiolarian) biostratigraphy. Two major Pleistocene paleoceanographic changes were found: One was the MPR at the entrance of MIS 22 (near 900 ka); the other occurred within MISs 6-5 (centered at 130 ka).

2. Using planktonic foraminiferal transfer functions, we found that the SST rose, while the DOT shoaled after the MPR in the southern SCS. Since the MPR, the DOT gradually became shallower until MISs 6-5 and then deepened afterward, as confirmed by the changes in very deep dwelling species *G. truncatulinoides*. Particularly, the relative abundance of *G. truncatulinoides* left-coiling form and *G. conglomerata* abruptly increased within MIS 5 while the winter SSTs obviously decreased.

3. The IWM and carbonate dissolution display a pattern of glacial decrease and interglacial increase. The dissolution spikes in the southern SCS can be well correlated with the dissolution events in the equatorial Pacific, indicating that the SCS shares the same carbonate dissolution signals as the tropical Pacific. There were two major changes in the DWM, at the B/M boundary and MIS 5 respectively, reflected by three successive deep-sea benthic foraminiferal assemblages. Judging from the results of benthic foraminiferal factor analysis and down-core distributions of characteristic species, the influence of the DWM gradually increased during the Brunhes chronozone and remarkably strengthened since MIS 5, while that of the IWM decreased at the same time. In addition, the variations in the biogenic opal content and relative abundance of *Uvigerina* plus *Bulimina* and *C. wuellerstorfi* reveal that the surface productivity was greatly enhanced over the last 200 kyr.

4. Generally, benthic foraminifera lagged behind planktonic foraminifera in their response to the two major Pleistocene paleoceanographic changes. For example, planktonic foraminiferal fauna responded to the MPR immediately, while benthic foraminiferal fauna did not changed until the Brunhes/Matuyama boundary. As for the major paleoceanographic changes within MISs 6-5, the winter SSTs, DOT, and surface paleoproductivity greatly changed since MIS 6 (near 200 ka), while the deep water masses changed since MIS 5. We speculated that the two major Pleistocene paleoceanographic changes might be related to the reorganization of surface and deep circulation in the SCS possibly induced by tectonic forces (e.g., the intensified uplift of Tibetan Plateau).

5. The oxygen isotope record for ice mass fluctuations has clear ~100 kyr eccentricity-dominated signals after the MPR, but with significant precession- and obliquity-related response before the MPR. The upper water structure (e.g., SST and *G. truncatulinoides* percent) and deep water conditions (e.g., the IWM) display long-term oscillations of ~200 kyr (perhaps representing the second harmonic of the ~400 kyr period of eccentricity) for the last 1500 kyr. Our data support eccentricity's role in the origin of low-frequency paleoceanographic oscillations in three dimensions of the WPWP.

Acknowledgements. We would like to thank the crew and scientists aboard the *R/V SONNE* for assistance during Cruise 95; M. Sarnthein and S. Clemens for helpful discussion; D. Budziak for help in the spectral analysis; and W. Huang for assistance in preparation of the manuscript. T. Barrows and D. Andreasen reviewed the manuscript and their comments, suggestions, and constructive criticisms greatly improved the manuscript. This work was funded by the National Natural Science Foundation of China (grants 49999560 and 49776290), the Trans-Century Training Program Foundation for the Talents by the Ministry of Education of China, and the Alexander von Humboldt Foundation of Germany.

References

Andreasen, D. J., and A. C. Ravelo, Tropical Pacific Ocean thermocline depth reconstructions for the Last Glacial Maximum, *Paleoceanography, 12(3)*, 395-413, 1997.

Andree, M., et al., AMS radiocarbon dates on foraminifera from deep sea sediments, *Radiocarbon, 28(2A)*, 424-428, 1986.

Barker, R. W., Taxonomic notes on the species figured by H.B. Brady in his report on the foraminifera dredged by H.M.S. "Challenger" during the years 1873-1876, *Spec. Publ. Soc. Econ. Paleontol. Mineral., 9*, 1-238, 1960.

Bassinot, F. C., L. Beaufort, E. Vincent, L. D. Labeyrie, F. Rostek, P. J. Müller, X. Quideleur, and Y. Lancelot, Coarse fraction fluctuations in pelagic carbonate sediments from the tropical Indian Ocean: A 1500-kyr record of carbonate dissolution, *Paleoceanography, 9(4)*, 579-600, 1994.

Bé, A. W. H., An ecological, zoogeographic and taxonomic review of recent planktonic foraminifera, in *Oceanic Micropaleontology, vol. 1*, edited by A. T. S. Ramsay, pp. 1-100, Academic, San Diego, Calif., 1977.

Bé, A. W. H., J. K. B. Bishop, M. S. Sverdlove, and W. D. Gardner, Standing stock, vertical distribution and flux of planktonic foraminifera in the Panama Basin, *Mar. Micropaleontol., 9*, 307-333, 1985.

Berger, W. H., Ocean ventilation during the last 12,000 years: Hypothesis of counterpoint deep water production, *Mar. Geol., 78*, 1-10, 1987.

Berger, W. H., T. Bickert, H. Schmidt, and G. Wefer, Quaternary oxygen isotope record of pelagic foraminifers: Site 806, Ontong Java Plateau, *Proc. Ocean Drill. Program Sci. Results, 130*, 381-396, 1993a.

Berger, W. H., T. Bickert, E. Jansen, G. Wefer, and M. Yasuda, The central mystery of the Quaternary ice age, *Oceanus, 36(4)*, 53-56, 1993b.

Berggren, W. A., D. V. Kent, C. C. Swisher III, and M. P. Aubry, A Revised Cenozoic geochronology and chronostratigraphy, in *Geochronology, Time Scales and Global Stratigraphic Correlation*, edited by W. A. Berggren, et al., *Spec. Publ. Soc. Econ. Paleontol. Mineral., 54*, 129-212, 1995.

Bian, Y., P. Wang, and L. Zheng, Deep-water dissolution cycles of late Quaternary planktonic foraminifera in the South China Sea (in Chinese, with English abstract), in *Contributions to Late Quaternary Paleoceanography of the South China Sea*, edited by Z. Ye and P. Wang, pp. 261-273, Qingdao Ocean Uni. Press, Qingdao, China, 1992.

Broecker, W. S., M. Andree, M. Klass, G. Bonani, W. Wolfli, and H. Oeschger, New evidence from the South China Sea for an abrupt termination of the last glacial period, *Nature, 333*, 156-158, 1988.

Chen, M.-T., H.-W. Ho, T.-D. Lai, L. Zheng, Q. Miao, K.-S. Shea, M.-P. Chen, P. Wang, K.-Y. Wei, and C.-Y. Huang, Recent planktonic foraminifers and their relationships to surface ocean hydrography of the South China Sea, *Mar. Geol., 146*, 173-190, 1998.

Clemens, S., and R. Tiedemann, Eccentricity forcing of Pliocene-Early Pleistocene climate revealed in a marine oxygen-isotope record, *Nature, 385*, 801-804, 1997.

Climate: Long-Range Investigation, Mapping, and Prediction (CLIMAP) Project Members, Seasonal reconstructions of the Earth's surface at the last glacial maximum, *Geol. Soc. Am. Map Chart Ser., MC-36*, 1-18, 1981.

Ding, Z. L., Z. W. Yu, N. W. Rutter, and T. S. Liu, Towards an orbital time scale for Chinese loess deposits, *Quat. Sci. Rev., 13*, 39-70, 1994.

Fairbanks, R. G., and P. H. Wiebe, Foraminifera and chlorophyll maximum: Vertical distribution, seasonal succession, and paleoceanographic significance, *Science, 209*, 1524-1526, 1980.

Fairbanks, R. G., M. Sverdlove, R. Free, P. H. Wiebe, and A. W. H. Bé, Vertical distribution and isotopic fractionation of living planktonic foraminifera from the Panama Basin, *Nature, 298*, 841-844, 1982.

Farrell, J. W., and W. Prell, Climate change and $CaCO_3$ preservation: An 800,000 year bathymetric reconstruction from the central equatorial Pacific Ocean, *Paleoceanography, 4*, 447-466, 1989.

Farrell, J. W., and W. Prell, Pacific $CaCO_3$ preservation and $\delta^{18}O$ since 4 Ma: Paleoceanographic and paleoclimatic implications, *Paleoceanography, 6*, 485-498, 1991.

Glass, B., Microtektites in deep-sea sediments, *Nature, 214*, 373-374, 1967.

Harrison, T. M., P. Copeland, W. S. F. Kidd, and A. Yin, Raising Tibet, *Science, 255*, 1663-1670, 1991.

Herguera, J. C., and W. Berger, Paleoproductivity from benthic foraminifera abundance: Glacial to postglacial change in the west-equatorial Pacific, *Geology, 19*, 1173-1176, 1991.

Hemleben, G., M. Splinder, and O. R. Anderson, *Modern Planktonic Foraminifera*, 363 pp., Springer-Verlag, New York, 1989.

Imbrie, J., A. McIntyre, and A. Mix, Oceanic response to orbital forcing in the late Quaternary: Observational and experimental strategies, in *Climate and Geo-Sciences*, edited by A. Berger, S. Schneider, and J. C. Duplessy, pp. 121-164, Kluwer Acad., Norwell, Mass., 1989.

Jian, Z., and L. Wang, Late Quaternary benthic foraminifera and deep-water paleoceanography in the South China Sea, *Mar. Micropaleontol., 32*, 127-154, 1997.

Jian, Z., L. Wang, M. Kienast, M. Sarnthein, W. Kuhnt, H.-L. Lin, and P. Wang, Benthic foraminiferal paleoceanography of the South China Sea over the last 40,000 years, *Mar. Geol., 156(1-4)*, 159-186, 1999.

Kennett, J. P., and M. S. Srinivasan, *Neogene Planktonic Foraminifera, A Phylogenetic Atlas*, 265 pp., Hutchinson Ross, Stroudsburg, 1983.

Klovan, J. E., and J. Imbrie, An algorithm and FORTRAN IV program for large scale Q-mode factor analysis, *J. Int. Assoc. Math. Geol., 3*, 61-78, 1971.

Kuhnt, W., S. Hess, and Z. Jian, Quantitative composition of benthic foraminiferal assemblages as a proxy indicator for organic carbon flux rates in the South China Sea, *Mar. Geol., 156(1-4)*, 123-157, 1999.

Kukla, G. J., and Z. An, Loess stratigraphy in central China, *Palaeogeogr. Palaeoclimatol. Palaeoecol., 72*, 203-225, 1989.

Kutzbach, J. E., P. J. Guetter, W. F. Ruddiman, and W. L. Prell, Sensitivity of climate to late Cenozoic uplift in Southern Asia and the American West: Numerical experiments, *J. Geophys. Res., 94(D15)*, 18,393-18,407, 1989.

Le, J., and N. J. Shackleton, Carbonate dissolution fluctuations in the western equatorial Pacific during the late Quaternary, *Paleoceanography, 7(1)*, 21-42, 1992.

Levitus, S., and T. P. Boyer, *World Ocean Atlas 1994, vol. 4, Temperature, NOAA Atlas NESDIS 4*, 117 pp., Nati. Oceanic and Atmos. Admin., Silver Spring, Ma., 1994.

Li, B., Paleoceanography of the Nansha Area, southern South China Sea since the last 700,000 years (in Chinese, with English abstract), Ph.D. thesis, 96 pp., Nanjing Inst. of Geol. and Paleontol., Acad. Sinica, Nanjing, China, 1997.

Li, J., The environmental effects of the uplift of the Qinghai-Xizang Plateau, *Quat. Sci. Rev., 10*, 479-483, 1991.

Li, J., and X. Fang, Studies on the uplift and environmental change of the Qinghai-Xizang Plateau (in Chinese), *Chin. Sci. Bull., 43(15)*, 1569-1574, 1998.

Liu, T., and Z. Ding, Stepwise coupling of monsoon circulations to global ice volume variations during the late Cenozoic, *Global Planet. Change, 7(1-3)*, 119-130, 1993.

Loeblich, A. R., Jr., and H. Tappan, *Foraminiferal Genera and Their Classification*, 868 pp., Van Nostrand Reihhold, New York, 1988.

Lohmann, G. P., Increasing seasonal upwelling in the subtropical South Atlantic over the past 700,000 yrs: Evidence from deep-living planktonic foraminifera, *Mar. Micropaleontol., 19*, 1-12, 1992.

Lohmann, G. P., and P. N. Schweitzer, *Globorotalia truncatulinoides* growth and chemistry as probes of the past thermocline, 1, Shell size, *Paleoceanography, 5(1)*, 55-75, 1990.

Martinez, J. I., Late Pleistocene paleoceanography of the Tasman Sea: Implications for the dynamics of the warm pool in the western Pacific, *Palaeogeogr. Palaeoclimatol. Palaeoecol., 112*, 19-62, 1994.

Martinez, J. I., Decreasing influence of Subantarctic Mode Water north of the Tasman Front over the past 150 kyr, *Palaeogeogr. Palaeoclimatol. Palaeoecol., 131*, 355-364, 1997.

Miao, Q., and R. C. Thunell, Late Pleistocene-Holocene distribution of deep-sea benthic foraminifera in the South China Sea and Sulu Sea: Paleoceanographic implications, *J. Foraminiferal Res. 26(1)*, 9-23, 1996.

Miao, Q., R. C. Thunell, and D. M. Anderson, Glacial-Holocene paleoceanography of the western equatorial Pacific Ocean: Carbonate dissolution and sea surface temperature in the South China and Sulu Seas, *Paleoceanography, 9(1)*, 69-90, 1994.

Molnar, P., and P. England, Late Cenozoic uplift of mountain ranges and global climate change: Chicken or egg?, *Nature, 346*, 29-34, 1990.

Molnia, B. F., A rapid and accurate method for the analysis of calcium carbonate in small samples, *J. Sediment. Petrol., 44*, 589-590, 1974.

Moore, T. C., Radiolarian stratigraphy, Leg 138, *Proc. Ocean Drill. Program Sci. Results, 138*, 191-232, 1995.

Mortlock, R. A., and P. N. Froelich, A simple method for the rapid determination of biogenic opal in pelagic marine sediments, *Deep Sea Res., Part A, 36*, 1415-1426, 1989.

Murray, D. W., J. W. Farrell, and V. Mckenna, Biogenic sedimentation at Site 847, eastern equatorial Pacific Ocean during the past 3 m.y., *Proc. Ocean Drill. Program Sci. Results, 138*, 429-460, 1993.

Parker, F. L., Planktonic foraminiferal species in Pacific sediments, *Micropaleontology, 8*, 219-254, 1962.

Pflaumann, W., and Z. Jian, Modern distribution patterns of planktonic foraminifera in the South China Sea and west Pacific: A new transfer

technique to estimate regional sea-surface temperatures, *Mar. Geol., 156(1-4)*, 41-83, 1999.

Prell, W., P. Wang, and P. Blum, Ocean Drilling Program Leg 184 scientific prospectus, *Ocean Drill. Program Sci. Prospectus, 83*, 1-71, 1998.

Ravelo, A. C., and R. G. Fairbanks, Oxygen isotopic composition of multiple species of planktonic foraminifera: Recorders of the modern photic zone temperature gradient, *Paleoceanography, 7(6)*, 815-831, 1992.

Ravelo, A. C., R. G. Fairbanks, and S. G. H. Philander, Reconstructing tropical Atlantic hydrography using planktonic foraminifera and an ocean model, *Paleoceanography*, 5(3), 409-431, 1990.

Ruddiman, W. F., and J. E. Kutzbach, Forcing of Late Cenozoic Northern Hemisphere climate by plateau uplift in Southern Asia and the American West, *J. Geophys. Res., 94*, 18,409-18,427, 1989.

Ruddiman, W. F., and M. E. Raymo, Northern Hemisphere climatic regimes during the past 3 Ma: Possible tectonic connections, *Philos. Trans. R. Soc. London, Ser. B, 318*, 411-430, 1988.

Ruddiman, W. F., M. E. Raymo, D. G. Martinson, B. M. Clement, and J. Backman, Pleistocene evolution: Northern Hemisphere ice sheets and North Atlantic Ocean, *Paleoceanography, 4*, 353-412, 1989.

Sarnthein, M., and A. V. Altenbach, Late Quaternary changes in surface water and deep water masses of the Nordic Seas and north-eastern North Atlantic: A review, *Geol. Rundsch, 84*, 89-107, 1995.

Sarnthein, M., U. Pflaumann, P. Wang, and H.-K. Wong (Eds.), *Preliminary Report on Sonne-95 Cruise "Monitor Monsoon" to the South China Sea, Ber. Rep. 68*, 225 pp., Geol.-Paläont. Inst. Univ. Kiel, Kiel, Germany, 1994.

Schmidt, H., W. H. Berger, T. Bickert, and G. Wefer, Quaternary carbon isotope record of pelagic foraminifers: Site 806, Ontong Java Plateau, *Proc. Ocean Drill. Program Sci. Results, 130*, 397-409, 1993.

Schönfeld, J., The "Stilostomella Extinction", Structure and dynamics of the last turnover in deep-sea benthic foraminiferal assemblages, in *Microfossils and Oceanic Environments*, edited by A. Mogurlevsky and R. Whatly, pp. 27-37, Uni. of Wales, Aberystwth Press, Aberystwth, 1996.

Schulz, M., and K. Stattegger, Spectrum: Spectral analysis of unevenly spaced paleoclimatic time series, *Comput. Geosci., 23(9)*, 929-945, 1997.

Shackleton, N. J., A. Berger, and W. R. Peltier, An alternative astronomical calibration of the lower Pleistocene time scale based on ODP Site 677, *Trans. R. Soc. Edinburgh Earth Sci., 81*, 251-261, 1990.

Shackleton, N. J., J. G. Baldauf, J.-A. Flores, M. Iwai, T. C. Moore Jr., I. Raffi, and E. Vincent, Biostratigraphic summary for Leg 138, *Proc. Ocean Drill. Program Sci. Results, 138*, 517-536, 1995.

Shi, Y., and B. Zheng, Timing and height of the Qinghai-Xizang Plateau uplifting into the cryosphere and its impact on the surrounding area (in Chinese), in *Formation, Environmental Evolution and Ecological System of Tibetan Plateau, Annuals (1995)*, edited by Qingzang Programme Comm., pp. 136-146, Sci. Press, Beijing, 1996.

Smit, J, A. J. M. van Eijden, and S. R. Troelstra, Analysis of the Australasian microtektite event, the Toba Lake event, and the Cretaceous/Paleogene boundary, eastern Indian Ocean, *Proc. Ocean Drill. Program Sci. Results, 121*, 489-503, 1991.

Sun, X., and X. Li, A pollen record of the last 37 ka in deep sea core 17940 from the northern slope of the South China Sea, *Mar. Geol., 156(1-4)*, 227-244, 1999.

Tauxe, L., J. L. LaBreque, R. Dodson, M. Fuller, and J. Dematteo, "U"-channel – A new technique for paleomagnetic analysis of hydraulic piston cores, *Eos Trans. AGU, 64 (18)*, 219, 1983.

The Multidisciplinary Oceanographic Expedition Team of Chinese Academy of Sciences to the Nansha Islands, *Quaternary Coral Reef Geology of Yongshu Reef, Nansha Islands* (in Chinese, with English abstract), 264 pp., China Ocean Press, Beijing, 1992.

Thierstein, H. R., K. R. Geitzenauer, B. Molfino, and N. J. Shackleton, Global synchroneity of late Quaternary coccolith datum levels: Validation by oxygen isotopes, *Geology, 5*, 400-404, 1977.

Thompson, P. R., Planktonic foraminifera in the western North Pacific during the past 150,000 years: Comparison of modern and fossil assemblages, *Palaeogeogr. Palaeoclimatol. Palaeoecol., 35*, 241-279, 1981.

Thompson, P. R., A. W. H. Bé, J.–C. Duplessy, and N. J. Shackleton, Disappearance of pink-pigmented *Globigerinoides ruber* at 120,000 yr B.P. in the Indian and Pacific Oceans, *Nature, 280*, 554-558, 1979.

Thunell, R. C., Q. Miao, S. E. Calvert, and T. F. Pedersen, Glacial-Holocene biogenic sedimentation patterns in the South China Sea: Productivity variations and surface water *p*CO2, *Paleoceanography, 7(2)*, 143-162, 1992.

Thunell, R. C., D. Anderson, D. Gellar, and Q. Miao, Sea-surface temperature estimates for the tropical Western Pacific during the last glaciation and their implications for the Pacific Warm Pool, *Quat. Res., 41*, 255-264, 1994.

Vincent, E., Carbonate stratigraphy of Hess Rise, Central North Pacific and paleoceanographic implications, *Initial Rep. Deep Sea Drill. Proj., 62*, 571-606, 1981.

Wang, L., Sea surface temperature history of the low latitude western Pacific during the last 5.3 million years, *Palaeogeogr. Palaeoclimatol. Palaeoecol., 108(3/4)*, 379-436, 1994.

Wang, L., and P. Wang, Late Quaternary paleoceanography of the South China Sea: Glacial-interglacial contrasts in enclosed basin, *Paleoceanography, 5(1)*, 77-90, 1990.

Wang, L., M. Sarnthein, H. Erlenkeuser, J. Grimalt, P. Grootes, S. Heilig, E. Ivanova, M. Kienast, C. Pelejero, and U. Pflaumann, East Asian monsoon climate during the Late Pleistocene: High-resolution sediment records from the South China Sea, *Mar. Geol., 156(1-4)*, 245-284, 1999.

Wang, P., Response of West Pacific marginal seas to glacial cycles: Paleoceanographic and sedimentological features, *Mar. Geol., 156(1-4)*, 5-39, 1999.

Wang, P., and X. Sun, Last Glacial Maximum in China: Comparison between land and sea, *Catena, 23*, 341-353, 1995.

Wang, P., Q. Min, Y. Bian, and X. Cheng, On micropaleontology and stratigraphy of Quaternary marine transgressions in East China, in *Marine Micropaleontology of China*, edited by P. Wang, pp. 265-264, China Ocean Press, Beijing, 1985.

Wang, P., Q. Min, Y. Bian, and W. Feng, Planktonic foraminifera in the continental slope of the northern South China Sea during the last 130,000 years and their paleoceanographic implications, *Dizhi Xuebao*, 60, 1-11, 1986.

Wang, P., L. Wang, Y. Bian, and Z. Jian, Late Quaternary paleoceanography of the South China Sea: Surface circulation and carbonate cycles, *Mar. Geol., 127*, 145-165, 1995.

Weeks, R., C. Laj, L. Endignoux, M. Fuller, A. Roberts, R. Manganne, E. Blanchard, and W. Goree, Improvements in long-core measurements technique: Applications in paleomagnetism and paleoceanography, *Geophys. J. Int., 114*, 651-662, 1993.

Winn, K., L. Zheng, H. Erlenkeuser, and P. Stoffers, Oxygen/carbon isotopes and paleo-productivity in the South China Sea during the past 110,000 years, in *Marine Geology and Geophysics of the South China Sea*, edited by X. Jin, H.R. Kudrass, and G. Pautot, pp. 154-166, China Ocean Press, Beijing, 1992.

Wu, X., F. Jiang, S. Wang, and B. Xue, On the problem of the Yellow River cutting the Sanmen Gorge and flowing eastward into the sea (in Chinese), *Quat. Sci. Beijing, 2*, 188, 1998.

Wu, X., H. Xu, J. Deng, W. Yin, Z. Zen, H. Zheng, and Z. Ouyang, Records of two astrogeologic events in the loess strata, Lantian, Shaanxi, China, *Chin. Sci. Bull., 37(11)*, 946-950, 1992.

Wyrtki, K., *Physical oceanography of the Southeast Asian waters, scientific results of marine investigations of the South China Sea and the Gulf of Thailand 1959-1961, NAGA Rep. 2*, 195pp., Scripps Inst. Oceanogr., La Jolla, Calif., 1961.

Yan, X., C. Ho, Q. Zheng, and V. Klemas, Temperature and size variabilities of the western Pacific warm pool, *Science, 258*, 1643-1645, 1992.

Yang, Z., H. Lin, B. Tang, and W. Xue, Correlation of Quaternary event stratigraphy of shelf areas in the Asia—Pacific region, in *Research of Marine Geology and Mineral Resources*, edited by Inst. of Mar. Geol., MGMR, pp. 68-82, Qingdao Ocean Univ. Press, Qingdao, China, 1996.

Yasuda, M., W. H. Berger, G. Wu, S. Burke, and H. Schmidt, Foraminifera preservation record for the last million years: Site 805, Ontong Java Plateau. *Proc. Ocean Drill. Program Sci. Results, 130*, 491-508, 1993.

Zhang, M., A. Chivas, X. Wang, J. Liu, S. Li, and B. Liu, A study diagenesis of reef succession in Well Xichen-1, Xisha Islands, in *Research of Marine Geology and Mineral Resources*, edited by Inst. of Mar. Geol., MGMR, pp. 130-148, Qingdao Ocean Univ. Press, Qingdao, China, 1996.

Zhao, Q., Z. Jian, B. Li, X. Cheng, and P. Wang, Middle Pleistocene microtektites in deep-sediments of the South China Sea, *Sci. China Ser. D, 42(5)*, 531-535, 1999.

Y. Bian, X. Cheng, P. Wang, R. Wang, and Q. Zhao, Laboratory of Marine Geology, Tongji University, Shanghai 200092, China.

C. Bühring, Z. Jian, and U. Pflauman, Institut für Geowissenschaften, Universität Kiel, D-24118 Kiel, Germany. (zj@zaphod.gpi.uni-kiel.de)

M.-P. Chen, Institute of Oceanography, Taiwan University, Taipei, China.

C. Laj, Laboratoire des Sciences du Climat et de l' Environment, CNRS-CEA, 91198 Gif sur Yvette, France.

B. Li, Nanjing Institute of Geology and Paleo-ntology, Academia Sinica, Nanjing 210008, China.

H.-L. Lin, Institute of Marine Geology, Sun Yat-Sen University, Kaohsiung, Taiwan 804, China.

(Received July 30, 1999;
revised December 21, 1999;
accepted January 5, 2000.)

Supplement to 4.4: Magnetostratigraphy of core 17957-2

Introduction

Gravity core 17957-2 from the southern center of the South China Sea (10°53.9' N and 115°18.3E, 2195 m water depth, 1384 cm core length) was used for detailed studies on foraminiferal responses to paleoceanographic changes during the Pleistocene (see Results Chapter 4.4). The chronostratigraphic framework for this site is largely based the magnetostratigraphy presented here.

Sampling and methods

To measure the magnetic properties of the sediment of core 17957-2, the archive halves from 0 to 1384 cm core depth were subsampled continuously using 1 meter long u-channels (Tauxe et al., 1983; Weeks et al., 1993). The magnetic measurements were performed at the Laboratoire des Sciences du Climat et de l'Environnement (**LSCE**), CEA-CNRS, Gif-sur-Yvette, France.

Standard u-channels are up to 1.5 m in length with a 2 x 2 cm square cross section, with three fixed long sides and a clip-on lid constituting the fourth side. The u-channels were pushed into the soft sediment, and the base of the u-channel was subsequently cut free using nylon-coated stainless steel wire so that the sediment filled u-channel could be removed from the core section. The base was then sealed with the lid and the ends closed with plastic caps.

The low field volume magnetic susceptibility (k_{lf}) core 17957-2 (Figure 1) was measured in high-resolution on the u-channels using a Bartington sensing coil with 4 cm diameter. The u-channels were kept steady and the sensing coil was moved continuously along them at a rate that was consistent with the sensitivity range used (Weeks, 1993; Kissel et al., 1998). Measurements were made every 1 cm which resulted in a resolution of ~ 3 cm.

Natural **R**emanent **M**agnetization (NRM) was measured in 1-cm-steps, resulting in a resolution of about 3 cm, with a pass-through DC-SQUID cryogenic magnetometer in the shiel-

ded room of the LSCE. Stepwise in-line alternating field (AF) demagnetization with an average of 8-10 steps from 0 mT up to 60 mT was used to retrieve the primary component of the magnetization, which was isolated after the very first steps of demagnetization.

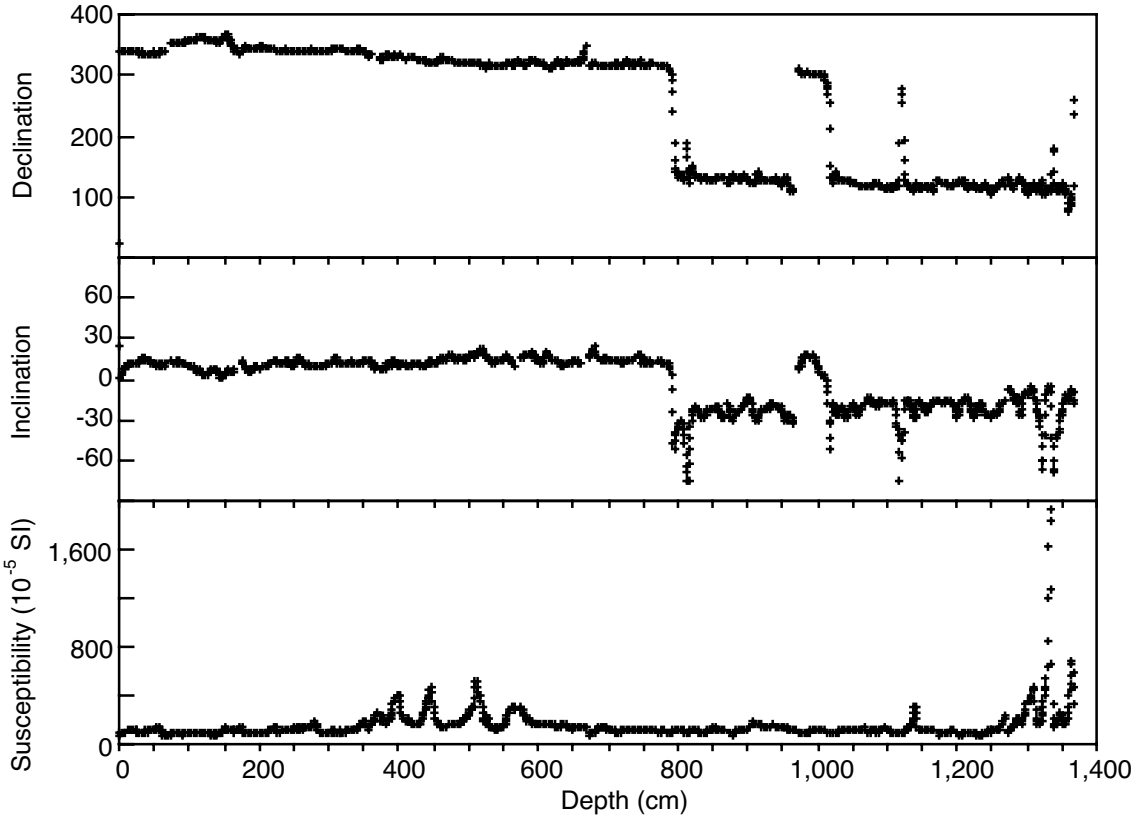

Figure 1: Variations in low field volume magnetic suceptibility, inclination and declination of core 17957-2. High susceptibilities are caused by volcanic ash layers (Sarnthein et al., 1994). Records of inclination and declination show normal polarity from 0 to 800 cm, below magnetic polarity is reversed with short-term returns to normal.

Anhysteretic **R**emanent **M**agnetization (ARM) was produced in-line along the u-channel axis, that is perpendicular to the bedding plane, using a 50 μT bias field parallel to the AF field. ARM was demagnetized with steps of 0, 10, 20, 25, 30, 40, 50, 60 mT (Figure 2).

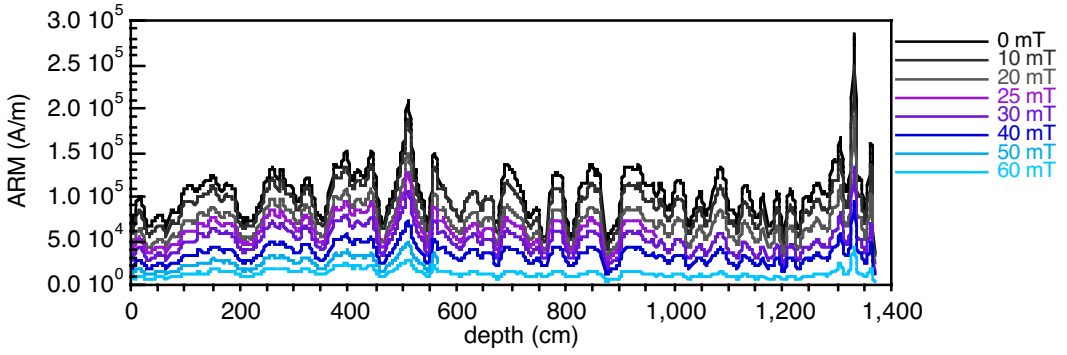

Figure 2: Relative variations of ARM at stepwise demagnetization levels.

Magnetic results

The magnetic measurements performed on this core yielded clear magnetic polarity changes with sharply defined boundaries that can be used as stratigraphic age markers .

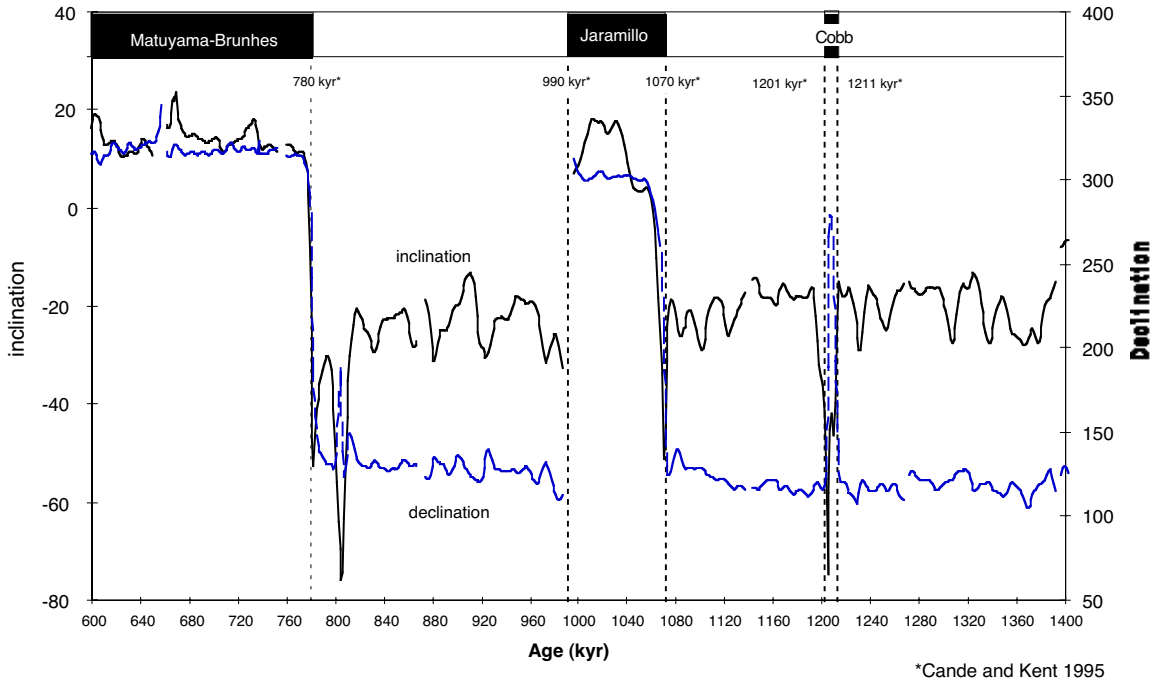

Figure 3: Paleomagnetic events in the inclination and declination records of core 17957-2. Teh end of the Brunhes normal period lies at 780 cm. A fluctuation in both records near 800 cm is situated within a horizon where Australasian microtectites were found (Zhao et al., 1999).

Because the core was not azimuthally oriented, the declinations were adjusted so that the mean declination for the Brunhes period was zero. The Brunhes-Matuyama boundary (0.78 Ma) is clear and apparent as a change to negative inclination and a 180° swing of the declination at a depth of 785 cm (Figure 3). The upper Jaramillo (0.990 Ma) transition unfortunately coincides with the separation between two u-channels, the lower Jaramillo (1.070 Ma) transition is situated at a depth of 1020 cm, again characterized by a change to negative inclination and a declination swing. The sharp swing in declination at 1120 cm might correspond to the Cobb event (between 1.201 and 1.211 Ma). The ages for the paleomagnetic events are from Berggren et al. (1995) and Cande and Kent (1995) The resulting age/depth graph is shown in Figure 4.

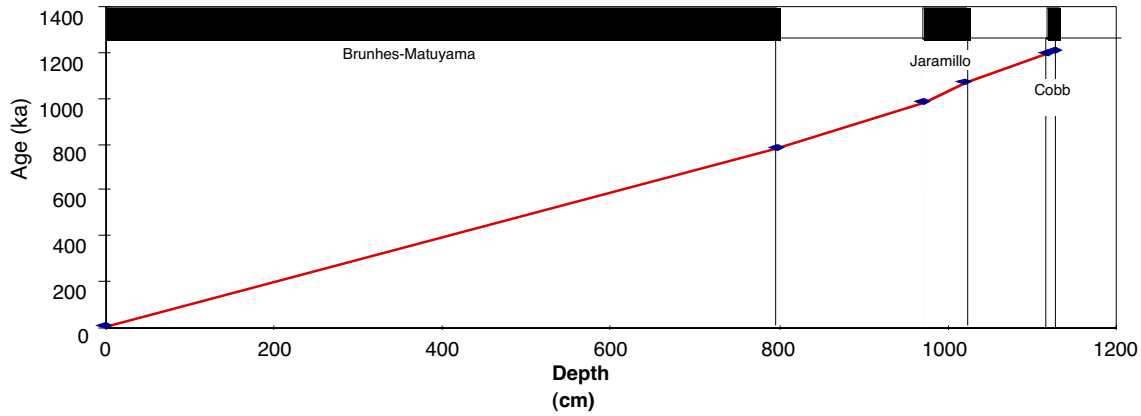

Figure 4: Age / depth diagram of core 17957-2 according to the magnetostratigraphy, assuming constant sedimentation rates.

The large oscillations in the inclination at the bottom of the core (Figure 1 and 3) coincide with the presence of ash layers, also revealed by corresponding peaks in magnetic susceptibility (Figure 1). Therefore these inclination changes have no geomagnetic meaning. The corresponding magnetostratigraphy is shown as a column with the usual black and white convention for normal and reverse periods respectively (Figures 3 and 4).

A spectral analysis of the susceptibility record and NRM intensities was carried out using the age model deduced from the magnetic events (Figure 3) assuming constant sedimentation rates between tie points.

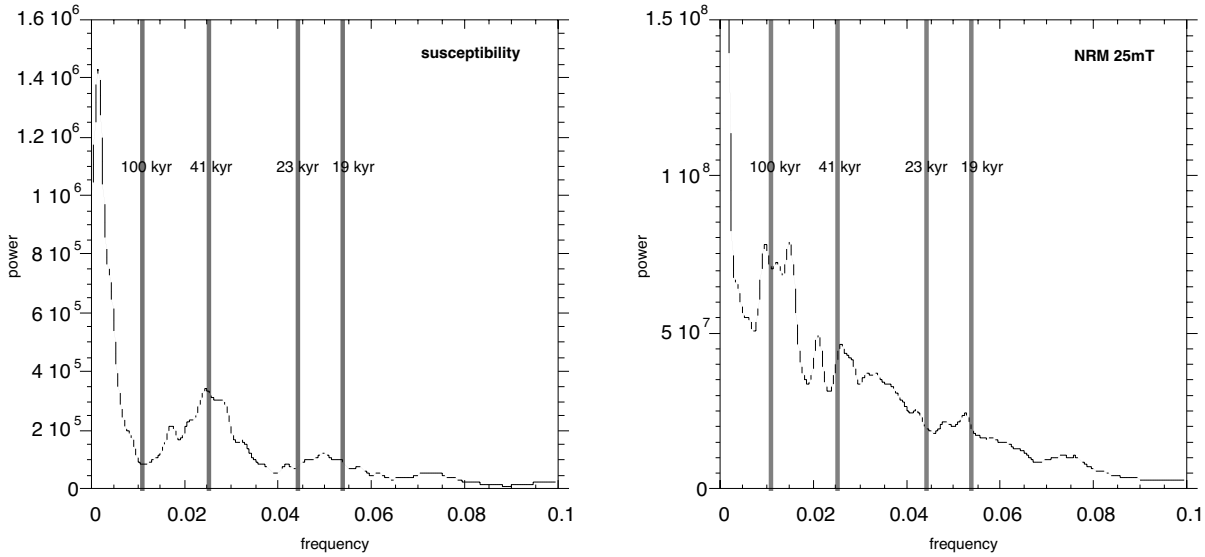

Figure 5: Power spectra of suceptibility and NRM signals (at 80% confidence level). Milankovitch-periods are indicated

Blackman-Tukey powerspectra (Figure 5) indicate a periodic component of 41 k.y. in the susceptibility record and a prevalent 100 k.y. period in the NRM record. The periodicity in suceptibility might correspond to some residual influence of lithologic variability and possibly indicates climatically controlled changes in the amount/nature of the magnetic mineral (Mazaud et al., 1999). Whether this is true for the 100 k.y. period in NRM intensity has yet to be verified, however it seems unlikely that it represents a periodicity in the geomagnetic field.

References

Berggren, W.A., Kent, D.V., Swisher, C.C., and Aubry, M.-P., 1995. A revised cenozoic geochronology and chronostratigraphy. *In* W.A. Breggren, D.V. Kent, M.-P. Aubry, and J. Hardenbol (Ed.), *Geochronology, Times Scales and Global Stratigraphic correlation*: Spec. Publ. - Soc. Econ. Plaeont. Mineral (Soc. Sediment. Geol.). 54:, 129-212.

Cande, S.C., and Kent, D.V., 1995. Revised calibration of the geomagnetic polarity time scale for the late Cretaceous and Cenozoic. *Journal of geophysical Research*, 100: 6093-6095.

Kissel, C., Laj, C., Mazaud, A., and Dokken, T., 1998. Magnetic anisotropy and environmental changes in two sedimentary cores from the Norwegian Sea and the North Atlantic. *Earth and Planetary Science Letters*, 164: 617-626.

Mazaud, A., and Channell, J.E.T., 1999. The top Olduvai polarity transition at ODP Site 983 (Iceland Basin). *Earth and Planetary Science Letters*, 166: 1-13.

Sarnthein, M., Pflaumann, U., Wang, P.X., and Wong, H.K., 1994. Preliminary Report on Sonne-95 Cruise "Monitor Monsoon" to the South China Sea. *Berichte-Reports, Geologisch-Paläontologisches Institut der Universität Kiel*, 68: 0-225.

Tauxe, L., LaBreque, J.L., Dodson, R., Fuller, M., and Dematteo, J., 1983. "U"-channel – a new technique for paleomagnetic analysis of hydraulic piston cores. *EOS, Trans. AGU*, 64: 219.

Weeks, R., Laj, C., Endignoux, L., Fuller, M., Roberts, A., Manganne, R., Blanchard, E., and Goree, W., 1993. Improvements in long-core measurements technique: applications in paleomagnetism and paleoceanography. *Geophys. J. Int*, 114: 651-662.

Zhao, Q., Jian, Z., Li, B., Chen, X., and Wang, P., 1999. Middle Pleistocene microtektites in deep-sea sediments of the South China Sea. *Sci. China Ser. D*, 42: 531-535.

5.: Conclusions

5. Conclusions

The results of the present study of East Asian Monsoon variability on orbital- to sub-decadal time scales from sediments of the South China Sea can be summarized as follows:

- The sediment profile of Sonne-95 core 17940 documents the fluvial runoff of the Pearl River both as a $\delta^{18}O$-freshwater signal in planktonic foraminifers and by variations in the color records of siliciclastic sediment discharge. The sediment color reflects variations in sediment composition and thus indicates changes in East Asian Monsoon intensity.
- Ultrahigh-resolution sediment color analyses revealed an unexpected but significant record of high-frequency climate variability, despite bioturbational mixing. Various independent spectral techniques identified a number of significant millennial-to-decadal-scale periodicities.
- Both the $\delta^{18}O$-freshwater signal and the blue record of fluvial clay discharge show that the Holocene long-term monsoon variations are dominated by a ~950-year periodicity. However, no DO-style cyclicity of ~1500 years was found. A similar 950-year periodicity in the GISP2 ice core record clearly leads, and thus probably controls, the low-latitude monsoon variations by several 100 years. The mechanism for the 950-year periodicity and its global signal transfer are unknown.
- A number of "common" solar cyclicities (200-year Suess cycle, 80-105year Gleissberg cycle, 20/24 year Hale cycle and its multiple near 44 years, 11-yr Schwabe cycle) form a substantial portion of decadal- to centennial-scale monsoon variability as documented at Site 17940. A broad spectrum of significant subdecadal frequencies documents the response of the east Asian Monsoon to the ENSO signal.

- The planktonic $\delta^{18}O$ record of Site 1144 during the last 120 k.y. exhibits marked similarities with the Greenland climate variability which is documented in the GISP2 $\delta^{18}O$ ice core record. Likewise the older isotope stages display a high-frequency variability in planktonic $\delta^{18}O$. Furthermore, short-term climatic reversals similar to the Younger Dryas are documented within the Terminations of cold stages at the beginning of MIS 11, 9 and 5.
- The variability in $\delta^{18}O$ reflects sea surface salinity changes induced by changes in precipitation and thus serves as sensitive indicator for East Asian Monsoon variability.
- The $\delta^{18}O$-record indicates that the larger parts of substages 5.5 and 11.3 at Site 1144 are missing. This suggests extensive changes in ocean circulation and/or in the sedi-

mentation regime which led to non-deposition or, more probably, to a removal of the missing sediment at the end of the warm phases through contour currents.

- The planktonic carbon isotope record at Site 1144 shows that the major oscillations in $\delta^{13}C$ of the surface water parallel the general climate variations of the past 1 million years. The variations in $\delta^{13}C$ probably result from oscillations in monsoon intensity which drives wind stress and precipitation and thus is responsible for advection and/or influx of ^{13}C depleted carbon.

- Rhyolithic ash layers in two cores from the southern South China Sea were geochemically identified as ashfalls from the youngest Toba eruption. The ash layers were deposited at the oxygen isotope stage 4-5 boundary at ca. 74 000 ka, matching the date of the Youngest Toba eruption on Sumatra.
- The occurence of abundant Toba ash in the South China Sea extends the previously known ash-fall zone significantly to the East and implies a larger volume of erupted Toba ash. Furthermore, it allows the reconstruction of paleo-wind directions which indicate an eruption during summer.

- The magnetostratigraphy of SONNE core 17957-2 from the central southern South China Sea shows a clear Brunhes/Matuyama magnetic polarity reversal, the Jaramillo magnetic interval and possibly the Cobb Mountain polarity event.
- Frequency analyses of magnetic parameters reveal strong 100 k.y. and 41 k.y. cycles, possibly reflecting climatically controlled changes in the amount or nature of the magnetic minerals.

6. Acknowledgments

The completion of this thesis was only possible due to the continued support of many people to whom I will be eternally grateful to.

First of all I would like to express my special thanks to Herrn Professor Dr. Michael Sarnthein, who initiated this project and gave me the opportunity to carry out the research for this dissertation. I am furthermore indebted to him for his continuous encouragements, new ideas, support and, above all for his invaluable scientific input and advice.

I am specially thankful to Michael Schulz for his great efforts in introducing me to the "frequency domain", for his sometimes desperately needed advice and software, and for his patience.

For the numerous discussions, helpful ideas and for carrying out the isotope measurements I owe special thanks to Helmut Erlenkeuser and the crew at the Leibniz Labor for doing a great job. For the careful supervision of microprobe analyses I want to thank Dietrich Ackermann and Barbara Mader, with a special thank you to Susanne Fretzdorff for important technical support and suggestions. I thank Frank Bruhn and Pieter M. Grootes for assistance with the AMS-^{14}C dating at the Leibniz Labor.

To Carlo Laj, Alain Mazaud and Catherine Kissel from Gif-sur-Yvette I am greatly indebted for their expertise, their guidance into the depths of cryogenic SQUIDS, and for their hospitality.

I am very grateful to many other people who have given me ideas and provided constructive criticism or moral support, especially to my friends and colleagues Mara Weinelt, Thorsten Kiefer, Hiroshi Kawamura, Stephan Steinke, Johannes Simstich, Antje Voelker and Sybille Grandel. *Muchas gracias* to my room mate TOM Papenfuss, for inspiring suggestions and

good humour. Matthias Haeckel I thank for his help and expertise in computers and software, and for his cheerful way of looking at things in life.
Karin Kißling I thank for her technical help and delicioous provisions. Heike Wegner, Nadine Wittig, Ringo Kloß, Waleid Hassan and Utami Kadarwati I thank for their valuable help and laboratory assistance.
For the possibility to take part in the SONNE 115 cruise to the South China Sea I thank Karl Stattegger and Wolfgang Kuhnt. I am grateful to the Ocean Drilling Program to let me participate in Leg 184 and for providing me with samples and logistical support.
This study was supported by the "Graduiertenkolleg Dynamik Globaler Kreisläufe im System Erde" and by grants from the Deutsche Forschungsgemeinschaft (DFG) "Monitor Monsun"(Sa 207/38-1) and "ODP Site 1144 Monsun Südchina See" (Sa 207/41-1).

In rememberance of my late colleague Luejiang Wang I am indebted to him for his devoted efforts at the start of this project and for his experience.

I especially thank Rebecca Rendle for her constructive comments and careful revision of this manuscript, for her emotional support and patience during these long and often hard times. Finally, I thank my parents Christa und Manfred Bühring for their continued moral and financial support throughout my studies. Without their constant encouragements none of this would have been possible.

Appendix

Appendix 1:

Results of CAMEBAX electron-beam micro-probe analyses of ash particles from core 17961-1 (781.0-783.5 cm core depth) and core 17962-4 (1075.5-1079.0 cm core depth) from the South China Sea.

Label	Core	SiO_2	Al_2O_3	TiO_2	FeO	MnO	MgO	CaO	Na_2O	K_2O	total (%)
61-P7 1b	17961-2	75.86	12.17	0.09	0.86	0.07	0.05	0.83	2.61	5.07	97.60
61-P7 1c	17961-2	75.99	12.19	0.07	0.91	0.09	0.07	0.81	2.79	4.76	97.66
61-P7 1d	17961-2	76.44	12.40	0.07	0.86	0.07	0.06	0.80	3.05	4.74	98.48
61-P7 1e	17961-2	76.99	12.55	0.02	0.98	0.11	0.06	0.85	3.04	4.63	99.23
61-P7 1f	17961-2	76.87	12.43	0.07	0.83	0.06	0.06	0.81	2.95	4.68	98.76
61-P7 2a	17961-2	76.28	12.13	0.05	0.76	0.09	0.04	0.70	2.77	4.96	97.78
61-P7 2b	17961-2	76.31	11.92	0.05	0.82	0.10	0.06	0.65	2.82	4.87	97.58
61-P7 2c	17961-2	75.97	12.14	0.03	0.78	0.03	0.03	0.68	2.98	4.61	97.25
61-P7 3a	17961-2	75.54	12.19	0.07	0.76	0.03	0.07	0.78	2.62	4.90	96.94
61-P7 3b	17961-2	75.63	12.07	0.04	0.69	0.07	0.07	0.77	2.55	5.04	96.93
61-P7 3c	17961-2	75.92	12.20	0.06	0.94	0.06	0.06	0.80	2.83	4.66	97.52
61-P7 3d	17961-2	75.99	12.15	0.07	0.93	0.09	0.07	0.82	2.81	4.66	97.58
61-P7 4a	17961-2	75.99	11.99	0.05	0.76	0.07	0.05	0.69	2.77	4.67	97.04
61-P7 4b	17961-2	76.05	12.16	0.04	0.73	0.09	0.05	0.74	2.72	4.62	97.21
61-P7 4c	17961-2	76.10	12.04	0.07	0.85	0.04	0.06	0.79	2.78	4.62	97.35
61-P7 5a	17961-2	76.44	12.03	0.04	0.93	0.05	0.05	0.67	2.91	4.62	97.75
61-P7 5b	17961-2	75.91	12.09	0.02	0.86	0.12	0.05	0.65	2.91	4.52	97.12
61-P7 5c	17961-2	76.08	12.02	0.06	0.78	0.06	0.03	0.69	2.89	4.48	97.08
61-P7 6a	17961-2	75.95	12.05	0.04	0.80	0.09	0.03	0.67	2.81	4.71	97.15
61-P7 6b	17961-2	75.99	12.12	0.05	0.85	0.10	0.05	0.66	2.93	4.62	97.39
61-P7 6c	17961-2	76.21	12.11	0.02	0.89	0.07	0.07	0.69	2.89	4.57	97.52
61-P7 7a	17961-2	76.90	12.24	0.05	0.82	0.10	0.04	0.84	2.83	5.03	98.85
61-P7 7b	17961-2	76.74	12.19	0.03	0.93	0.06	0.06	0.75	2.87	5.03	98.66
61-P7 7c	17961-2	77.03	12.26	0.08	0.94	0.06	0.06	0.74	2.93	4.94	99.04
61-P7 8a	17961-2	76.29	12.17	0.06	0.76	0.09	0.05	0.77	2.80	4.69	97.70
61-P7 8b	17961-2	75.95	12.13	0.00	0.88	0.01	0.06	0.75	2.79	4.75	97.31
61-P7 8c	17961-2	76.13	12.00	0.06	0.91	0.11	0.05	0.76	2.79	4.76	97.57
61-P7 9a	17961-2	75.50	12.14	0.02	0.85	0.05	0.06	0.78	2.68	4.89	96.98
61-P7 9b	17961-2	75.96	12.18	0.05	0.84	0.02	0.06	0.79	2.80	4.81	97.51
61-P7 9c	17961-2	75.66	12.20	0.05	0.87	0.08	0.06	0.84	2.70	4.79	97.25
61-P7 10a	17961-2	76.49	12.23	0.05	0.79	0.08	0.05	0.75	2.80	4.73	97.97
61-P7 10b	17961-2	76.65	12.28	0.05	0.88	0.06	0.05	0.74	2.78	4.69	98.17
61-P7 10c	17961-2	76.04	12.07	0.05	0.82	0.02	0.07	0.80	2.74	4.73	97.32
61-P6A 2a	17961-2	76.14	12.09	0.04	0.77	0.08	0.05	0.61	2.78	4.67	97.23
61-P6A 2b	17961-2	75.86	11.93	0.05	0.69	0.10	0.05	0.65	2.79	4.63	96.74
61-P6A 2c	17961-2	75.95	11.95	0.04	0.76	0.08	0.03	0.65	2.72	4.67	96.86
61-P6A 3a	17961-2	75.88	12.13	0.06	0.79	0.05	0.04	0.68	2.69	4.83	97.16
61-P6A 3b	17961-2	75.76	12.06	0.05	0.74	0.12	0.05	0.65	2.74	4.80	96.96
61-P6A 3c	17961-2	75.19	12.02	0.03	0.87	0.08	0.04	0.62	2.70	4.88	96.42
61-P6A 5a	17961-2	76.29	12.02	0.04	0.72	0.08	0.04	0.70	2.79	4.84	97.54
61-P6A 5b	17961-2	76.22	12.07	0.06	0.83	0.07	0.06	0.68	2.73	4.82	97.53
61-P6A 5c	17961-2	76.03	12.04	0.04	0.81	0.10	0.03	0.66	2.78	4.84	97.33
61-P6A 6a	17961-2	76.08	12.18	0.09	0.90	0.07	0.08	0.79	2.66	4.86	97.71
61-P6A 6b	17961-2	75.87	12.13	0.01	0.79	0.07	0.06	0.78	2.73	4.61	97.05
61-P6A 6c	17961-2	75.72	12.11	0.05	0.84	0.06	0.04	0.75	2.78	4.58	96.94
61-P6A 7a	17961-2	75.61	11.93	0.05	0.76	0.11	0.04	0.68	2.73	4.74	96.65
61-P6A 7b	17961-2	75.90	12.07	0.01	0.74	0.06	0.05	0.66	2.99	4.43	96.91
61-P6A 7c	17961-2	76.16	12.08	0.05	0.85	0.12	0.05	0.66	2.83	4.48	97.28
61-P6A 7d	17961-2	76.14	12.15	0.08	0.74	0.11	0.05	0.70	2.99	4.56	97.52
61-P7 17a	17961-2	75.75	12.10	0.06	0.93	0.06	0.06	0.77	2.82	4.74	97.28
61-P7 17b	17961-2	75.84	12.08	0.06	0.88	0.08	0.04	0.77	2.77	4.70	97.23
61-P7 17c	17961-2	75.55	12.01	0.05	0.83	0.03	0.04	0.73	2.74	4.75	96.73
61-P7 18a	17961-2	76.37	12.11	0.02	0.90	0.06	0.07	0.75	2.93	4.61	97.81
61-P7 18b	17961-2	75.79	12.15	0.05	0.85	0.04	0.06	0.75	2.83	4.62	97.15
61-P7 18c	17961-2	75.23	12.13	0.05	0.91	0.15	0.05	0.70	2.74	4.65	96.61

Appendix 1: Microprobe analyses of Toba Ash

Label	Core	SiO_2	Al_2O_3	TiO_2	FeO	MnO	MgO	CaO	Na_2O	K_2O	total (%)
61-P7 19a	17961-2	75.21	11.91	0.06	0.81	0.07	0.06	0.83	2.59	4.83	96.37
61-P7 19b	17961-2	74.85	12.08	0.07	0.85	0.10	0.06	0.74	2.74	4.63	96.13
61-P7 19c	17961-2	75.31	12.01	0.03	0.85	0.09	0.05	0.82	2.84	4.58	96.58
61-P7 19d	17961-2	75.37	11.97	0.08	0.88	0.05	0.06	0.79	2.72	4.55	96.46
61-P7 20a	17961-2	75.22	12.16	0.05	0.86	0.06	0.07	0.85	2.62	4.67	96.56
61-P7 20b	17961-2	75.12	12.13	0.05	0.91	0.06	0.07	0.80	2.75	4.64	96.53
61-P7 20c	17961-2	75.61	12.21	0.06	0.85	0.06	0.07	0.82	2.83	4.73	97.24
61-P7 21a	17961-2	75.57	12.12	0.07	0.92	0.12	0.05	0.82	2.65	4.76	97.08
61-P7 21b	17961-2	75.66	12.14	0.09	0.87	0.02	0.05	0.81	2.88	4.64	97.16
61-P7 21c	17961-2	76.25	12.23	0.07	0.91	0.08	0.06	0.82	2.73	4.76	97.91
62-P8 1a	17962-4	74.82	12.12	0.03	0.87	0.12	0.05	0.82	2.61	4.61	96.06
62-P8 1b	17962-4	74.42	12.09	0.06	0.83	0.10	0.04	0.72	2.66	4.53	95.46
62-P8 2a	17962-4	76.57	12.29	0.03	0.89	0.06	0.06	0.78	2.75	4.72	98.16
62-P8 2b	17962-4	77.63	12.47	0.04	0.79	0.02	0.06	0.80	3.01	4.70	99.52
62-P8 2c	17962-4	76.97	12.38	0.06	0.82	0.02	0.05	0.80	2.84	4.73	98.68
62-P8 3a	17962-4	75.94	12.28	0.06	0.79	0.07	0.05	0.82	2.80	4.62	97.43
62-P8 3b	17962-4	75.79	12.11	0.06	0.82	0.07	0.05	0.78	2.75	4.70	97.11
62-P8 3c	17962-4	75.95	12.22	0.04	0.79	0.01	0.06	0.85	2.74	4.73	97.40
62-P8 4a	17962-4	75.77	12.18	0.05	0.86	0.05	0.04	0.71	2.72	4.97	97.34
62-P8 4b	17962-4	75.87	12.28	0.02	0.79	0.02	0.04	0.75	2.66	4.73	97.16
62-P8 4c	17962-4	76.38	12.20	0.05	0.77	0.07	0.05	0.72	2.83	4.73	97.78
62-P8 5a	17962-4	76.76	12.31	0.05	0.82	0.03	0.05	0.75	2.93	4.61	98.30
62-P8 5b	17962-4	76.91	12.42	0.05	0.77	0.07	0.05	0.73	2.99	4.65	98.64
62-P8 5c	17962-4	76.44	12.34	0.04	0.81	0.08	0.06	0.74	2.99	4.68	98.16
62-P8 2.2a	17962-4	75.43	11.82	0.06	0.77	0.10	0.07	0.75	1.99	4.52	95.50
62-P8 2.2b	17962-4	75.04	11.78	0.06	0.84	0.08	0.04	0.72	2.06	4.55	95.16
62-P8 3.2a	17962-4	75.19	11.95	0.07	0.75	0.15	0.06	0.78	2.52	4.64	96.13
62-P8 3.2b	17962-4	75.63	11.95	0.11	0.90	0.03	0.04	0.76	2.09	4.85	96.37
62-P8 3.2c	17962-4	75.50	12.09	0.02	0.88	0.07	0.04	0.77	2.45	4.83	96.66
62-P8 3.2d	17962-4	75.76	11.93	0.03	0.85	0.00	0.05	0.75	2.42	4.97	96.76
62-P8 4.2a	17962-4	76.58	12.22	0.07	0.83	0.03	0.07	0.71	2.91	4.79	98.20
62-P8 4.2c	17962-4	77.10	12.26	0.03	0.83	0.06	0.05	0.77	2.61	4.75	98.46
62-P8 4.2b	17962-4	77.03	12.10	0.05	0.72	0.03	0.05	0.76	2.80	4.81	98.36
62-P8 4.2d	17962-4	76.35	12.12	0.06	0.80	0.15	0.06	0.78	2.78	4.83	97.93
62-P8 5.2a	17962-4	76.07	12.13	0.06	0.75	0.05	0.04	0.65	2.75	4.90	97.40
62-P8 5.2b	17962-4	76.21	12.26	0.06	0.70	0.09	0.05	0.69	2.92	4.85	97.82
62-P8 5.2c	17962-4	76.74	12.37	0.04	0.97	0.08	0.05	0.68	2.91	4.80	98.63
62-P8 6a	17962-4	76.94	12.43	0.03	0.82	0.08	0.05	0.79	2.77	4.84	98.75
62-P8 6b	17962-4	75.72	12.39	0.06	0.82	0.08	0.07	0.75	2.75	4.88	97.54
62-P8 8a	17962-4	73.24	11.97	0.05	0.75	0.10	0.04	0.70	2.65	5.09	94.59
62-P8 8b	17962-4	72.94	11.98	0.04	0.68	0.12	0.04	0.70	2.64	5.01	94.14
62-P8 9a	17962-4	75.37	12.11	0.08	0.79	0.04	0.05	0.67	2.77	4.70	96.57
62-P8 9b	17962-4	75.52	12.05	0.05	0.80	0.09	0.05	0.64	2.73	4.65	96.56
62-P8 9c	17962-4	75.69	12.15	0.05	0.81	0.08	0.06	0.70	2.66	4.58	96.77
62-P8 10a	17962-4	75.50	12.06	0.06	0.75	0.08	0.05	0.79	2.59	5.08	96.96
62-P8 10b	17962-4	76.46	12.28	0.06	0.89	0.05	0.08	0.76	2.81	4.76	98.14
62-P8 10c	17962-4	76.47	12.42	0.03	0.78	0.05	0.08	0.82	2.94	4.78	98.38
62-P8 10d	17962-4	76.35	12.37	0.10	0.90	0.06	0.08	0.77	2.81	4.84	98.27
62-P8 11a	17962-4	77.76	12.58	0.08	0.90	0.04	0.07	0.91	3.02	4.79	100.15
62-P8 11b	17962-4	76.40	12.39	0.05	0.92	0.07	0.04	0.86	2.90	4.81	98.45
62-P8 11c	17962-4	76.86	12.36	0.09	0.78	0.09	0.06	0.85	2.79	4.73	98.62
62-P8 12a	17962-4	76.91	12.30	0.03	0.81	0.08	0.04	0.72	2.86	4.74	98.49
62-P8 12b	17962-4	76.68	12.26	0.07	0.81	0.03	0.04	0.77	2.87	4.63	98.16
62-P8 12c	17962-4	76.30	12.07	0.06	0.83	0.06	0.04	0.73	2.55	4.56	97.20

Appendix 1: Microprobe analyses of Toba Ash

Label	Core	SiO_2	Al_2O_3	TiO_2	FeO	MnO	MgO	CaO	Na_2O	K_2O	total (%)
62-P8 12d	17962-4	75.20	12.06	0.06	0.88	0.05	0.06	0.77	2.72	4.56	96.37
62-P8 13a	17962-4	75.75	12.18	0.06	0.75	0.08	0.08	0.80	2.66	4.74	97.09
62-P8 13b	17962-4	75.80	12.13	0.02	0.86	0.05	0.07	0.82	2.58	4.82	97.15
62-P8 13c	17962-4	75.93	12.26	0.06	0.92	0.08	0.06	0.84	2.79	4.67	97.61
62-P8 14a	17962-4	75.23	12.00	0.04	0.77	0.05	0.05	0.73	2.58	4.57	96.02
62-P8 14b	17962-4	75.61	12.05	0.04	0.76	0.00	0.06	0.75	2.55	4.65	96.48
62-P8 14c	17962-4	75.38	12.05	0.06	0.89	0.02	0.04	0.74	2.50	4.63	96.30
62-P8 16a	17962-4	75.16	11.86	0.04	0.82	0.06	0.06	0.69	2.77	4.36	95.83
62-P8 16b	17962-4	75.34	11.92	0.07	0.73	0.08	0.07	0.63	2.81	4.39	96.04
62-P8 16c	17962-4	75.77	12.00	0.05	0.89	0.08	0.04	0.67	3.04	4.36	96.91
62-P8 16d	17962-4	75.91	12.12	0.05	0.90	0.10	0.07	0.66	3.08	4.43	97.32

Appendix 2:

Stable isotope analyses of G. ruber (white) (250-315 μm), from ODP Site 1144, South China Sea

Leg	Site, Hole, Core, Section	Interval (cm)	Depth (mbsf)	Depth (mcd)	$\delta^{18}O$ G.ruber	$\delta^{13}C$ G.ruber	Age (ka)
184	1144C-1H-1	6-8	0.06	0.06	-2.72	1.32	0.09
184	1144C-1H-1	26-28	0.26	0.26	-2.46	1.34	0.44
184	1144C-1H-1	48-50	0.48	0.48	-2.55	1.23	0.83
184	1144C-1H-1	73-75	0.73	0.73	-2.56	1.25	1.28
184	1144C-1H-1	96-98	0.96	0.96	-2.70	1.31	1.68
184	1144C-1H-1	126-128	1.26	1.26	-2.52	1.39	2.22
184	1144C-1H-1	143-145	1.43	1.43	-2.15	1.28	2.52
184	1144C-1H-2	23-25	1.73	1.73	-2.76	1.41	3.05
184	1144C-1H-2	48-50	1.98	1.98	-2.65	1.37	3.50
184	1144C-1H-2	73-75	2.23	2.23	-2.19	1.17	3.94
184	1144C-1H-2	93-95	2.43	2.43	-2.44	1.10	4.29
184	1144C-1H-2	125-127	2.75	2.75	-2.53	1.26	4.86
184	1144C-1H-3	23-25	3.23	3.23	-2.63	0.91	5.71
184	1144C-1H-3	73-75	3.73	3.73	-2.24	1.22	6.60
184	1144C-1H-3	96-98	3.96	3.96	-2.29	0.92	7.01
184	1144C-1H-3	125-127	4.25	4.25	-2.35	0.95	7.52
184	1144C-1H-3	143-145	4.43	4.43	-2.14	0.86	7.84
184	1144C-1H-4	18-20	4.68	4.68	-2.38	0.87	8.29
184	1144C-1H-4	48-50	4.98	4.98	-2.53	0.63	8.82
184	1144C-1H-4	73-75	5.23	5.23	-2.03	0.69	9.26
184	1144C-1H-4	103-105	5.53	5.53	-2.86	0.62	9.80
184	1144C-1H-4	126-128	5.76	5.76	-2.50	0.54	10.21
184	1144C-1H-4	143-145	5.93	5.93	-2.19	0.57	10.51
184	1144C-1H-5	26-28	6.26	6.26	-2.29	0.69	11.09
184	1144B-2H-2	143-145	3.03	6.41	-2.10	0.70	11.36
184	1144B-2H-3	6-8	3.16	6.54	-2.22	0.73	11.58
184	1144C-1H-5	73-75	6.73	6.73	-1.53	0.43	11.73
184	1144C-1H-5	96-98	6.96	6.96	-1.99	0.92	11.93
184	1144B-2H-3	73-75	3.83	7.21	-1.73	0.78	12.14
184	1144C-1H-5	143-145	7.43	7.43	-1.66	0.59	12.33
184	1144B-2H-3	128-130	4.38	7.76	-1.61	0.61	12.61
184	1144B-2H-3	143-145	4.53	7.91	-1.51	0.56	12.73
184	1144B-2H-4	23-25	4.83	8.21	-2.06	0.64	12.99
184	1144B-2H-4	53-55	5.13	8.51	-2.11	0.79	13.24
184	1144B-2H-4	73-75	5.33	8.71	-1.79	0.64	13.41
184	1144B-2H-4	103-105	5.63	9.01	-1.72	0.52	13.66
184	1144B-2H-4	126-128	5.86	9.24	-1.44	0.88	13.86
184	1144B-2H-4	143-145	6.03	9.41	-1.55	0.41	14.00
184	1144B-2H-5	23-25	6.33	9.71	-2.04	0.42	14.26
184	1144B-2H-5	53-55	6.63	10.01	-2.04	0.43	14.50
184	1144B-2H-5	73-75	6.83	10.21	-1.45	0.45	14.63
184	1144A-2H-2	33-35	8.73	10.52	-1.14	0.41	14.81
184	1144A-2H-2	53-55	8.93	10.72	-1.26	0.43	14.93
184	1144A-2H-2	73-75	9.13	10.92	-1.23	0.51	15.04
184	1144A-2H-2	103-105	9.43	11.22	-1.02	0.28	15.22
184	1144A-2H-2	128-130	9.68	11.47	-1.24	0.50	15.37
184	1144A-2H-2	143-145	9.83	11.62	-0.93	0.63	15.46
184	1144A-2H-3	23-25	10.13	11.92	-0.95	0.45	15.63
184	1144A-2H-3	53-55	10.43	12.22	-0.43	0.49	15.81
184	1144A-2H-3	73-75	10.63	12.42	-1.25	0.27	15.93
184	1144A-2H-3	93-95	10.83	12.62	-0.99	0.40	16.04
184	1144A-2H-3	113-115	11.03	12.77	-0.93	0.35	16.13
184	1144A-2H-3	143-145	11.33	13.12	-0.99	0.51	16.34
184	1144A-2H-4	23-25	11.63	13.42	-1.07	0.71	16.51
184	1144A-2H-4	53-55	11.93	13.72	-1.07	0.53	16.69

Appendix 2: Stable isotope data of ODP Site 1144

Leg	Site, Hole, Core, Section	Interval (cm)	Depth (mbsf)	Depth (mcd)	$\delta^{18}O$ G.ruber	$\delta^{13}C$ G.ruber	Age (ka)
184	1144A-2H-4	73-75	12.13	13.92	-1.00	0.75	16.81
184	1144A-2H-4	96-98	12.37	14.16	-0.93	0.63	16.95
184	1144A-2H-4	111-113	12.52	14.31	-0.94	0.71	17.04
184	1144A-2H-4	143-145	12.83	14.62	-1.02	0.74	17.22
184	1144A-2H-5	23-25	13.13	14.92	-1.10	0.85	17.39
184	1144A-2H-5	53-55	13.43	15.22	-1.06	0.56	17.57
184	1144A-2H-5	73-75	13.63	15.42	-0.99	0.86	17.69
184	1144A-2H-5	96-98	13.87	15.66	-1.19	0.82	17.83
184	1144A-2H-5	116-118	14.07	15.86	-0.95	0.77	17.95
184	1144A-2H-5	143-145	14.33	16.12	-0.79	0.92	18.10
184	1144A-2H-6	16-18	14.57	16.36	-1.23	0.95	18.24
184	1144A-2H-6	36-38	14.77	16.56	-0.67	0.63	18.36
184	1144A-2H-6	73-75	15.13	16.92	-0.92	0.72	18.57
184	1144A-2H-6	103-105	15.43	17.22	-1.12	0.94	18.75
184	1144A-2H-6	126-128	15.67	17.46	-1.22	0.95	18.89
184	1144A-2H-6	143-145	15.83	17.62	-1.08	1.02	18.98
184	1144A-2H-7	33-35	16.23	18.02	-1.31	0.67	19.21
184	1144A-3H-1	36-38	16.77	18.34	-0.83	0.83	19.38
184	1144A-3H-1	73-75	17.13	18.70	-1.00	0.90	19.56
184	1144A-3H-1	96-98	17.37	18.94	-0.93	0.89	19.68
184	1144A-3H-1	126-128	17.67	19.24	-0.61	0.96	19.84
184	1144A-3H-1	143-145	17.83	19.40	-0.79	0.96	19.92
184	1144A-3H-2	23-25	18.13	19.70	-0.96	0.88	20.07
184	1144A-3H-2	53-55	18.43	20.00	-0.94	1.05	20.22
184	1144A-3H-2	73-75	18.63	20.20	-0.89	0.93	20.32
184	1144A-3H-2	93-95	18.83	20.40	-0.87	1.12	20.42
184	1144A-3H-2	111-113	19.02	20.59	-1.02	1.02	20.52
184	1144A-3H-2	143-145	19.33	20.90	-0.60	0.82	20.68
184	1144A-3H-3	23-25	19.63	21.20	-0.91	1.01	20.83
184	1144A-3H-3	53-55	19.93	21.50	-1.03	0.97	20.98
184	1144B-4H-1	73-75	19.83	21.69	-0.55	0.81	21.08
184	1144B-4H-1	93-95	20.03	21.89	-1.05	1.05	21.18
184	1144B-4H-1	126-128	20.37	22.23	-1.05	0.97	21.36
184	1144B-4H-1	143-145	20.53	22.39	-0.77	0.86	21.44
184	1144B-4H-2	11-13	20.72	22.58	-1.23	1.10	21.53
184	1144B-4H-2	36-38	21.27	22.84	-1.21	0.90	21.67
184	1144B-4H-2	73-75	21.33	23.19	-0.81	0.89	21.84
184	1144B-4H-2	96-98	21.57	23.43	-1.01	0.93	21.97
184	1144B-4H-2	111-113	21.72	23.58	-0.78	0.88	22.04
184	1144B-4H-2	143-145	22.03	23.89	-1.06	1.07	22.20
184	1144B-4H-3	23-25	22.32	24.19	-1.27	1.11	22.35
184	1144B-4H-3	53-55	22.63	24.49	-1.22	0.92	22.50
184	1144B-4H-3	73-75	22.83	24.69	-0.96	0.91	22.61
184	1144B-4H-3	93-95	23.03	24.89	-1.15	0.96	22.71
184	1144B-4H-3	111-113	23.22	25.08	-1.01	0.99	22.80
184	1144B-4H-3	143-145	23.53	25.39	-1.21	1.10	22.96
184	1144B-4H-4	23-25	23.83	25.69	-1.10	1.14	23.11
184	1144B-4H-4	53-55	24.13	25.99	-1.07	1.07	23.27
184	1144B-4H-4	73-75	24.33	26.19	-1.17	1.15	23.37
184	1144B-4H-4	93-95	24.53	26.39	-0.90	1.03	23.47
184	1144B-4H-4	116-118	24.77	26.63	-0.74	0.94	23.62
184	1144B-4H-4	143-145	25.03	26.89	-0.62	1.00	23.81
184	1144B-4H-5	23-25	25.33	27.19	-1.11	1.05	24.05
184	1144B-4H-5	53-55	25.63	27.49	-0.89	1.02	24.30
184	1144B-4H-5	73-75	25.83	27.69	-0.67	1.04	24.46
184	1144B-4H-5	93-95	26.03	27.89	-1.32	1.18	24.63

Appendix 2: Stable isotope data of ODP Site 1144

Leg	Site, Hole, Core, Section	Interval (cm)	Depth (mbsf)	Depth (mcd)	$\delta^{18}O$ G.ruber	$\delta^{13}C$ G.ruber	Age (ka)
184	1144B-4H-5	116-118	26.27	28.13	-1.32	1.23	24.83
184	1144B-4H-5	143-145	26.53	28.39	-1.01	1.17	25.04
184	1144B-4H-6	23-25	26.83	28.69	-1.08	1.04	25.29
184	1144B-4H-6	46-48	27.07	28.93	-1.21	1.08	25.48
184	1144B-4H-6	73-75	27.33	29.19	-0.98	1.02	25.70
184	1144A-4H-2	73-75	28.17	29.52	-0.98	1.14	25.97
184	1144A-4H-2	91-93	28.36	29.71	-0.96	0.89	26.13
184	1144A-4H-2	116-118	28.61	29.96	-1.21	1.19	26.33
184	1144A-4H-2	143-145	28.87	30.22	-1.21	1.06	26.55
184	1144A-4H-3	21-23	29.16	30.51	-1.06	1.19	26.78
184	1144A-4H-3	41-43	29.36	30.71	-1.09	0.88	26.95
184	1144A-4H-3	73-75	29.67	31.02	-0.92	0.94	27.20
184	1144A-4H-3	103-105	29.97	31.32	-1.06	0.95	27.45
184	1144A-4H-3	133-135	30.27	31.62	-1.55	1.13	27.70
184	1144A-4H-4	16-18	30.61	31.96	-1.18	1.19	27.98
184	1144A-4H-4	41-43	30.86	32.21	-1.25	1.14	28.18
184	1144A-4H-4	73-75	31.17	32.52	-0.80	1.16	28.44
184	1144B-5H-1	73-75	29.33	32.63	-1.35	1.08	28.53
184	1144B-5H-1	91-93	29.52	32.82	-1.34	1.09	28.69
184	1144B-5H-1	116-118	29.77	33.07	-1.56	1.22	28.89
184	1144B-5H-1	143-145	30.03	33.33	-1.06	1.03	29.10
184	1144B-5H-2	16-18	30.26	33.57	-1.05	1.12	29.29
184	1144B-5H-2	46-48	30.57	33.87	-1.41	1.14	29.53
184	1144B-5H-2	73-75	30.83	34.13	-1.39	1.31	29.74
184	1144B-5H-2	91-93	31.02	34.32	-1.29	1.16	29.89
184	1144B-5H-2	116-118	31.27	34.57	-1.44	1.18	30.09
184	1144B-5H-2	143-145	31.53	34.83	-1.26	1.32	30.29
184	1144B-5H-3	21-23	31.82	35.12	-1.32	1.33	30.53
184	1144B-5H-3	45-47	32.05	35.35	-1.40	1.20	30.71
184	1144B-5H-3	73-75	32.33	35.63	-1.42	1.21	30.93
184	1144B-5H-3	91-93	32.52	35.82	-1.20	1.11	31.08
184	1144B-5H-3	111-113	32.72	36.02	-1.42	1.22	31.24
184	1144B-5H-3	143-145	33.03	36.33	-1.27	1.07	31.49
184	1144B-5H-4	21-23	33.32	36.62	-1.62	1.20	31.72
184	1144B-5H-4	41-43	33.52	36.82	-1.53	1.31	31.88
184	1144B-5H-4	73-75	33.83	37.13	-1.35	1.20	32.13
184	1144B-5H-4	91-93	34.02	37.32	-1.43	1.12	32.28
184	1144B-5H-4	113-115	34.22	37.52	-1.32	1.04	32.46
184	1144B-5H-4	143-145	34.53	37.83	-1.11	1.21	32.81
184	1144B-5H-5	21-23	34.82	38.12	-1.56	1.08	33.17
184	1144B-5H-5	46-48	35.07	38.37	-1.42	0.94	33.47
184	1144B-5H-5	73-75	35.33	38.63	-1.57	0.85	33.79
184	1144B-5H-5	91-93	35.52	38.82	-1.33	1.14	34.02
184	1144B-5H-5	111-113	35.72	39.02	-1.22	1.14	34.26
184	1144B-5H-5	143-145	36.03	39.33	-1.24	0.96	34.64
184	1144B-5H-6	11-13	36.22	39.52	-1.40	1.14	34.87
184	1144A-5H-2	143-145	38.33	39.82	-1.57	1.21	35.20
184	1144A-5H-3	16-18	38.57	40.06	-1.41	1.14	35.41
184	1144A-5H-3	41-43	38.82	40.31	-1.11	1.03	35.59
184	1144A-5H-3	73-75	39.13	40.62	-1.39	1.21	35.82
184	1144A-5H-3	103-105	39.43	40.92	-1.22	1.18	36.04
184	1144A-5H-3	133-135	39.73	41.22	-1.24	1.12	36.26
184	1144A-5H-4	11-13	40.02	41.51	-1.52	1.04	36.47
184	1144A-5H-4	36-38	40.27	41.76	-1.70	1.05	36.66
184	1144A-5H-4	73-75	40.63	42.12	-1.18	0.98	36.92
184	1144A-5H-4	91-93	40.82	42.31	-1.26	0.95	37.06

Appendix 2: Stable isotope data of ODP Site 1144

Leg	Site, Hole, Core, Section	Interval (cm)	Depth (mbsf)	Depth (mcd)	$\delta^{18}O$ G.ruber	$\delta^{13}C$ G.ruber	Age (ka)
184	1144A-5H-4	111-113	41.02	42.51	-1.61	1.00	37.21
184	1144A-5H-4	143-145	41.33	42.82	-1.12	0.88	37.44
184	1144A-5H-5	11-13	41.52	43.01	-1.47	1.12	37.58
184	1144A-5H-5	41-43	41.82	43.31	-1.50	1.10	37.80
184	1144A-5H-5	73-75	42.13	43.62	-1.47	0.99	38.03
184	1144A-5H-5	91-93	42.32	43.81	-1.46	1.06	38.17
184	1144B-6H-1	121-123	39.32	44.02	-1.76	1.12	38.33
184	1144B-6H-1	143-145	39.53	44.23	-1.25	1.16	38.51
184	1144B-6H-2	21-23	39.82	44.52	-1.11	1.04	38.77
184	1144B-6H-2	46-48	40.07	44.77	-1.23	0.93	38.99
184	1144B-6H-2	73-75	40.33	45.03	-1.13	1.05	39.22
184	1144B-6H-2	96-98	40.57	45.27	-1.27	0.93	39.44
184	1144B-6H-2	121-123	40.82	45.52	-1.39	1.05	39.66
184	1144B-6H-2	143-145	41.03	45.73	-1.02	1.10	39.85
184	1144B-6H-3	21-23	41.32	46.02	-1.20	0.91	40.11
184	1144B-6H-3	41-43	41.52	46.22	-1.28	1.06	40.29
184	1144B-6H-3	73-75	41.83	46.53	-1.43	1.29	40.57
184	1144B-6H-3	96-98	42.07	46.77	-1.34	1.04	40.78
184	1144B-6H-3	116-118	42.27	46.97	-1.72	1.27	40.96
184	1144B-6H-3	143-145	42.53	47.23	-1.43	1.13	41.19
184	1144B-6H-4	16-18	42.77	47.47	-1.52	1.09	41.41
184	1144B-6H-4	41-43	43.02	47.72	-1.63	1.27	41.63
184	1144B-6H-4	73-75	43.33	48.03	-1.36	1.17	41.91
184	1144B-6H-4	96-98	43.57	48.27	-1.52	0.98	42.12
184	1144B-6H-4	121-123	43.82	48.52	-1.43	1.11	42.35
184	1144B-6H-4	143-145	44.03	48.73	-1.77	0.97	42.53
184	1144B-6H-5	21-23	44.32	49.02	-1.23	1.07	42.72
184	1144B-6H-5	46-48	44.57	49.27	-1.14	1.15	42.87
184	1144B-6H-5	73-75	44.83	49.53	-1.13	1.06	43.03
184	1144B-6H-5	96-98	45.07	49.77	-1.44	0.98	43.18
184	1144B-6H-5	111-113	45.22	49.92	-1.49	1.08	43.28
184	1144B-6H-5	143-145	45.53	50.23	-1.52	1.05	43.47
184	1144B-6H-6	21-23	45.82	50.52	-1.71	0.96	43.65
184	1144B-6H-6	46-48	46.07	50.77	-1.64	1.15	43.81
184	1144B-6H-6	73-75	46.33	51.03	-1.44	1.13	43.97
184	1144B-6H-6	103-105	46.63	51.33	-1.64	1.15	44.16
184	1144B-6H-6	126-128	48.87	51.57	-1.30	1.14	44.31
184	1144A-6H-3	41-43	48.32	51.75	-1.50	1.06	44.42
184	1144A-6H-3	73-75	48.63	52.06	-1.46	0.99	44.62
184	1144A-6H-3	103-105	48.93	52.36	-1.56	0.88	44.80
184	1144A-6H-3	133-135	49.23	52.66	-1.50	1.21	44.99
184	1144A-6H-4	6-8	49.47	52.90	-1.66	0.95	45.14
184	1144A-6H-4	41-43	49.82	53.25	-1.52	0.91	45.39
184	1144A-6H-4	73-75	50.13	53.56	-1.04	0.88	45.66
184	1144A-6H-4	103-105	50.43	53.86	-1.16	1.02	45.94
184	1144A-6H-4	121-123	50.62	54.05	-1.14	0.92	46.12
184	1144A-6H-4	143-145	50.83	54.26	-1.20	0.94	46.33
184	1144A-6H-5	21-23	51.12	54.55	-1.47	1.17	46.60
184	1144A-6H-5	41-43	51.32	54.75	-1.31	1.15	46.79
184	1144A-6H-5	73-75	51.63	55.06	-1.58	1.05	47.09
184	1144A-6H-5	91-93	51.82	55.25	-1.54	1.07	47.27
184	1144A-6H-5	116-118	52.07	55.50	-1.51	0.92	47.51
184	1144A-6H-5	143-145	52.33	55.76	-1.37	0.94	47.76
184	1144A-6H-6	21-23	52.62	56.05	-1.74	0.93	48.04
184	1144A-6H-6	46-48	52.87	56.30	-1.96	0.86	48.27
184	1144A-6H-6	73-75	53.13	56.56	-1.27	1.00	48.52

Appendix 2: Stable isotope data of ODP Site 1144

Leg	Site, Hole, Core, Section	Interval (cm)	Depth (mbsf)	Depth (mcd)	$\delta^{18}O$ G.ruber	$\delta^{13}C$ G.ruber	Age (ka)
184	1144A-6H-6	91-93	53.32	56.75	-1.75	0.84	48.70
184	1144A-6H-6	116-118	53.57	57.00	-1.69	0.89	48.94
184	1144A-6H-6	143-145	53.83	57.26	-1.80	0.70	49.19
184	1144A-6H-7	21-23	54.12	57.55	-1.44	0.81	49.47
184	1144C-6H-2	21-23	53.42	57.82	-1.45	0.80	49.73
184	1144C-6H-2	56-58	53.77	58.17	-2.03	0.94	50.06
184	1144C-6H-2	73-75	53.93	58.33	-1.81	0.96	50.21
184	1144C-6H-2	91-93	54.12	58.52	-1.85	0.80	50.40
184	1144C-6H-2	116-118	54.37	58.77	-1.49	0.86	50.63
184	1144C-6H-2	143-145	54.63	59.03	-1.66	0.85	50.88
184	1144C-6H-3	16-18	54.87	59.27	-1.81	0.86	51.11
184	1144C-6H-3	46-48	55.17	59.57	-1.41	0.87	51.40
184	1144C-6H-3	73-75	55.43	59.83	-1.73	0.67	51.65
184	1144C-6H-3	96-98	55.67	60.07	-1.75	0.95	51.88
184	1144C-6H-3	121-123	55.92	60.32	-1.64	0.86	52.12
184	1144C-6H-3	143-145	56.13	60.53	-1.43	0.87	52.32
184	1144C-6H-4	16-18	56.37	60.77	-2.07	0.98	52.55
184	1144C-6H-4	48-50	56.68	61.07	-1.43	0.81	52.83
184	1144C-6H-4	73-75	56.93	61.33	-1.24	0.99	53.08
184	1144C-6H-4	103-105	57.23	61.63	-1.51	0.99	53.37
184	1144A-7H-2	73-75	56.63	61.89	-1.53	0.76	53.62
184	1144A-7H-2	103-105	56.93	62.19	-1.72	0.83	53.90
184	1144A-7H-3	3-5	57.25	62.51	-1.81	1.13	54.21
184	1144A-7H-3	21-23	57.44	62.70	-1.66	0.92	54.39
184	1144A-7H-3	41-43	57.65	62.91	-1.42	0.71	54.59
184	1144A-7H-3	73-75	57.95	63.21	-1.46	0.87	54.88
184	1144A-7H-3	103-105	58.25	63.51	-1.52	0.82	55.16
184	1144A-7H-3	126-128	58.49	63.75	-1.78	1.01	55.39
184	1144A-7H-4	16-18	58.76	64.02	-1.57	0.59	55.65
184	1144A-7H-4	41-43	59.01	64.27	-1.70	0.78	55.89
184	1144A-7H-4	73-75	59.32	64.58	-1.61	0.80	56.19
184	1144A-7H-4	91-93	59.51	64.77	-2.22	0.82	56.37
184	1144A-7H-4	111-113	59.71	64.97	-2.15	0.93	56.57
184	1144A-7H-4	143-145	60.02	65.28	-1.30	0.77	56.91
184	1144A-7H-5	21-23	60.31	65.57	-1.82	0.76	57.23
184	1144A-7H-5	41-43	60.51	65.77	-1.70	0.80	57.45
184	1144A-7H-5	73-75	60.82	66.08	-1.53	0.79	57.80
184	1144A-7H-5	91-93	61.01	66.27	-1.68	0.63	58.02
184	1144A-7H-5	111-113	61.21	66.47	-1.67	0.65	58.23
184	1144A-7H-5	143-145	61.52	66.78	-1.12	0.66	58.53
184	1144A-7H-6	16-18	61.76	67.02	-1.35	0.84	58.76
184	1144A-7H-6	41-43	62.01	67.27	-1.33	0.82	58.99
184	1144A-7H-6	73-75	62.32	67.58	-1.16	0.80	59.28
184	1144B-8H-3	3-5	60.13	67.82	-1.27	0.86	59.51
184	1144B-8H-3	28-30	60.38	68.07	-0.88	0.68	59.74
184	1144B-8H-3	53-55	60.63	68.32	-1.20	0.80	59.98
184	1144B-8H-3	78-80	60.88	68.57	-1.35	0.78	60.21
184	1144B-8H-3	104-106	61.14	68.83	-0.99	0.87	60.46
184	1144B-8H-3	128-130	61.38	69.07	-1.06	0.87	60.68
184	1144B-8H-4	3-5	61.63	69.32	-1.17	0.88	60.92
184	1144B-8H-4	28-30	61.88	69.57	-0.91	0.74	61.16
184	1144B-8H-4	53-55	62.13	69.82	-1.07	0.90	61.39
184	1144B-8H-4	78-80	62.38	70.07	-1.14	0.83	61.63
184	1144B-8H-4	104-106	62.64	70.33	-1.53	0.96	61.88
184	1144B-8H-4	128-130	62.88	70.57	-1.01	0.87	62.13
184	1144B-8H-5	3-5	63.13	70.82	-0.99	0.94	62.40

Appendix 2: Stable isotope data of ODP Site 1144

Leg	Site, Hole, Core, Section	Interval (cm)	Depth (mbsf)	Depth (mcd)	$\delta^{18}O$ G.ruber	$\delta^{13}C$ G.ruber	Age (ka)
184	1144B-8H-5	28-30	63.38	71.07	-1.06	0.80	62.67
184	1144B-8H-5	53-55	63.63	71.32	-1.13	0.92	62.94
184	1144B-8H-5	78-80	63.88	71.57	-1.25	0.98	63.21
184	1144B-8H-5	104-106	64.14	71.83	-1.53	0.83	63.49
184	1144B-8H-5	128-130	64.38	72.07	-1.11	0.78	63.75
184	1144B-8H-6	3-5	64.63	72.32	-1.24	0.88	64.02
184	1144C-7H-4	28-30	65.98	72.65	-1.21	0.89	64.38
184	1144C-7H-4	53-55	66.23	72.90	-1.18	0.84	64.65
184	1144C-7H-4	78-80	66.48	73.15	-1.07	0.78	64.92
184	1144C-7H-4	104-106	66.74	73.41	-1.05	0.89	65.21
184	1144C-7H-4	128-130	66.98	73.65	-1.38	1.10	65.47
184	1144C-7H-5	3-5	67.23	73.90	-1.95	0.71	65.72
184	1144C-7H-5	28-30	67.48	74.15	-1.24	1.07	65.91
184	1144C-7H-5	53-55	67.73	74.40	-1.18	0.79	66.09
184	1144C-7H-5	78-80	67.98	74.65	-1.39	0.89	66.26
184	1144C-7H-5	104-106	68.24	74.91	-0.64	1.16	66.45
184	1144C-7H-5	128-130	68.48	75.15	-0.69	1.01	66.62
184	1144C-7H-6	3-5	68.68	75.35	-1.32	0.97	66.76
184	1144B-9H-2	104-106	67.85	75.47	-1.31	0.85	66.84
184	1144B-9H-2	128-130	68.09	75.71	-1.71	1.15	67.01
184	1144B-9H-3	3-5	68.34	75.96	-1.09	1.00	67.19
184	1144B-9H-3	28-30	68.59	76.21	-1.65	0.95	67.36
184	1144B-9H-3	53-55	68.84	76.46	-1.65	0.95	67.54
184	1144B-9H-3	78-80	69.09	76.71	-1.40	0.86	67.71
184	1144B-9H-3	104-106	69.35	76.97	-1.27	0.97	67.90
184	1144B-9H-3	128-130	69.59	77.21	-1.30	0.90	68.06
184	1144B-9H-4	3-5	69.84	77.46	-1.67	0.88	68.24
184	1144B-9H-4	28-30	70.09	77.71	-1.93	0.98	68.42
184	1144B-9H-4	53-55	70.34	77.96	-2.13	0.94	68.62
184	1144B-9H-4	78-80	70.59	78.21	-1.74	0.72	68.92
184	1144B-9H-4	104-106	70.85	78.47	-1.52	0.88	69.27
184	1144B-9H-4	128-130	71.09	78.71	-1.75	0.99	69.58
184	1144B-9H-5	3-5	71.34	78.96	-1.10	0.94	69.91
184	1144B-9H-5	28-30	71.59	79.21	-1.24	0.81	70.24
184	1144B-9H-5	53-55	71.84	79.46	-1.07	0.85	70.57
184	1144B-9H-5	78-80	72.09	79.71	-1.51	0.70	70.90
184	1144B-9H-5	104-106	72.35	79.97	-1.20	0.68	71.25
184	1144B-9H-5	128-130	72.59	80.21	-1.50	0.97	71.57
184	1144B-9H-6	3-5	72.84	80.46	-1.86	0.93	71.90
184	1144B-9H-6	28-30	73.09	80.71	-1.96	0.80	72.23
184	1144B-9H-6	53-55	73.34	80.96	-1.89	0.97	72.56
184	1144B-9H-6	78-80	73.59	81.21	-1.94	0.78	72.85
184	1144B-9H-6	104-106	73.85	81.47	-1.41	0.91	73.08
184	1144A-9H-2	53-55	75.43	81.82	-1.29	0.96	73.34
184	1144A-9H-2	78-80	75.68	82.07	-1.65	1.17	73.53
184	1144A-9H-2	104-106	75.94	82.33	-1.73	1.06	73.72
184	1144A-9H-2	128-130	76.18	82.57	-1.66	0.92	73.90
184	1144A-9H-3	3-5	76.43	82.82	-1.71	1.21	74.09
184	1144A-9H-3	28-30	76.68	83.07	-2.26	1.16	74.34
184	1144A-9H-3	53-55	76.93	83.32	-2.05	1.21	74.71
184	1144A-9H-3	78-80	77.18	83.57	-2.06	1.19	75.14
184	1144A-9H-3	104-106	77.44	83.83	-2.15	1.21	75.59
184	1144A-9H-3	128-130	77.68	84.07	-1.73	1.11	76.00
184	1144A-9H-4	3-5	77.93	84.32	-1.86	1.00	76.43
184	1144A-9H-4	28-30	78.18	84.57	-2.25	1.13	76.86
184	1144A-9H-4	53-55	78.43	84.82	-2.11	0.88	77.29

Appendix 2: Stable isotope data of ODP Site 1144

Leg	Site, Hole, Core, Section	Interval (cm)	Depth (mbsf)	Depth (mcd)	$\delta^{18}O$ G.ruber	$\delta^{13}C$ G.ruber	Age (ka)
184	1144A-9H-4	78-80	78.68	85.07	-2.31	0.94	77.72
184	1144A-9H-4	104-106	78.94	85.33	-2.03	0.84	78.17
184	1144A-9H-4	128-130	79.18	85.57	-2.30	0.90	78.59
184	1144A-9H-5	3-5	79.43	85.82	-2.19	0.85	79.02
184	1144A-9H-5	28-30	79.68	86.07	-2.01	0.76	79.45
184	1144A-9H-5	53-55	79.93	86.32	-1.79	0.85	79.88
184	1144A-9H-5	78-80	80.18	86.57	-2.03	0.79	80.31
184	1144A-9H-5	104-106	80.44	86.83	-2.19	0.70	80.76
184	1144A-9H-5	128-130	80.68	87.07	-2.35	0.83	81.17
184	1144A-9H-6	3-5	80.93	87.32	-2.23	0.96	81.60
184	1144A-9H-6	28-30	81.18	87.57	-1.80	1.05	82.03
184	1144A-9H-6	53-55	81.43	87.82	-1.85	0.83	82.46
184	1144A-9H-6	78-80	81.68	88.07	-1.85	0.85	82.89
184	1144A-9H-6	104-106	81.94	88.33	-2.12	0.49	83.34
184	1144A-9H-6	128-130	82.18	88.57	-2.49	1.05	83.73
184	1144A-9H-7	3-5	82.43	88.82	-1.91	0.88	83.97
184	1144A-9H-7	28-30	82.68	89.07	-1.40	1.04	84.19
184	1144A-9H-7	53-55	82.93	89.32	-1.85	0.94	84.40
184	1144C-9H-1	53-55	80.73	89.42	-1.76	0.90	84.49
184	1144C-9H-1	78-80	80.98	89.67	-1.81	1.06	84.71
184	1144C-9H-1	104-106	81.24	89.93	-1.41	1.04	84.93
184	1144C-9H-1	128-130	81.48	90.17	-1.50	0.94	85.14
184	1144C-9H-2	3-5	81.73	90.42	-1.50	0.94	85.36
184	1144C-9H-2	28-30	81.98	90.67	-2.05	1.04	85.58
184	1144C-9H-2	53-55	82.23	90.92	-1.38	1.03	85.79
184	1144C-9H-2	78-80	82.48	91.17	-1.52	1.03	86.01
184	1144C-9H-2	104-106	82.74	91.43	-1.54	1.18	86.24
184	1144C-9H-2	128-130	82.98	91.67	-1.62	1.02	86.44
184	1144C-9H-3	3-5	83.23	91.92	-1.55	1.05	86.66
184	1144C-9H-3	28-30	83.48	92.17	-1.46	1.13	86.88
184	1144C-9H-3	53-55	83.73	92.42	-1.46	1.02	87.10
184	1144C-9H-3	78-80	83.98	92.67	-1.38	1.14	87.31
184	1144C-9H-3	104-106	84.24	92.93	-1.92	0.68	87.54
184	1144C-9H-3	128-130	84.48	93.17	-1.83	1.09	87.75
184	1144C-9H-4	3-5	84.73	93.42	-2.18	1.03	87.96
184	1144C-9H-4	28-30	84.98	93.67	-2.03	1.09	88.18
184	1144C-9H-4	53-55	85.23	93.92	-1.77	1.00	88.40
184	1144C-9H-4	78-80	85.48	94.17	-2.24	1.18	88.61
184	1144C-9H-4	104-106	85.74	94.43	-1.87	0.94	88.84
184	1144C-9H-4	128-130	85.98	94.67	-2.33	0.89	89.05
184	1144C-9H-5	3-5	86.23	94.92	-2.19	0.89	89.27
184	1144C-9H-5	28-30	86.48	95.17	-2.02	0.97	89.48
184	1144C-9H-5	53-55	86.73	95.42	-2.23	0.98	89.72
184	1144C-9H-5	78-80	86.98	95.67	-1.84	0.86	90.00
184	1144C-9H-5	104-106	87.24	95.93	-1.51	0.87	90.32
184	1144C-9H-5	128-130	87.48	96.17	-1.57	0.99	90.61
184	1144C-9H-6	3-5	87.62	96.31	-1.65	0.98	90.78
184	1144B-11H-1	128-130	86.88	96.41	-1.82	1.08	90.90
184	1144B-11H-2	3-5	87.13	96.66	-1.65	0.99	91.20
184	1144B-11H-2	28-30	87.38	96.91	-2.16	0.78	91.51
184	1144B-11H-2	53-55	87.63	97.16	-1.85	1.02	91.81
184	1144B-11H-2	78-80	87.88	97.41	-1.80	1.12	92.11
184	1144B-11H-2	104-106	88.14	97.67	-1.93	0.94	92.43
184	1144B-11H-2	128-130	88.38	97.91	-2.06	0.79	92.72
184	1144B-11H-3	3-5	88.63	98.16	-1.71	0.81	93.02
184	1144B-11H-3	28-30	88.88	98.41	-2.04	0.96	93.33

Appendix 2: Stable isotope data of ODP Site 1144

Leg	Site, Hole, Core, Section	Interval (cm)	Depth (mbsf)	Depth (mcd)	$\delta^{18}O$ G.ruber	$\delta^{13}C$ G.ruber	Age (ka)
184	1144B-11H-3	53-55	89.13	98.66	-2.10	0.86	93.63
184	1144B-11H-3	78-80	89.38	98.91	-2.11	0.87	93.93
184	1144B-11H-3	104-106	89.64	99.17	-2.18	0.99	94.25
184	1144B-11H-3	128-130	89.88	99.41	-2.21	0.94	94.54
184	1144B-11H-4	3-5	90.13	99.66	-2.14	0.84	94.84
184	1144B-11H-4	28-30	90.38	99.91	-2.10	0.88	95.15
184	1144B-11H-4	53-55	90.63	100.16	-1.88	0.88	95.45
184	1144B-11H-4	78-80	90.88	100.41	-2.18	0.83	95.75
184	1144B-11H-4	104-106	91.14	100.67	-2.27	0.95	96.07
184	1144B-11H-4	128-130	91.38	100.91	-2.25	0.78	96.36
184	1144B-11H-5	3-5	91.63	101.16	-1.90	0.82	96.66
184	1144B-11H-5	28-30	91.88	101.41	-2.29	0.70	96.96
184	1144B-11H-5	53-55	92.13	101.66	-2.24	0.74	97.27
184	1144B-11H-5	78-80	92.38	101.91	-2.15	0.85	97.57
184	1144B-11H-5	104-106	92.64	102.17	-2.11	0.90	97.89
184	1144B-11H-5	128-130	92.88	102.41	-1.99	0.94	98.18
184	1144B-11H-6	3-5	93.13	102.66	-1.95	0.91	98.48
184	1144C-10H-4	3-5	94.23	102.88	-2.28	0.90	98.75
184	1144C-10H-4	28-30	94.48	103.13	-2.24	0.64	99.05
184	1144C-10H-4	53-55	94.73	103.38	-2.40	0.77	99.35
184	1144C-10H-4	78-80	94.98	103.63	-2.31	0.69	99.66
184	1144C-10H-4	104-106	95.24	103.89	-2.52	0.65	99.97
184	1144C-10H-4	128-130	95.48	104.13	-2.50	0.69	100.25
184	1144C-10H-5	3-5	95.73	104.38	-2.32	0.73	100.41
184	1144C-10H-5	28-30	95.98	104.63	-2.07	0.72	100.55
184	1144C-10H-5	53-55	96.23	104.88	-2.10	0.88	100.69
184	1144C-10H-5	78-80	96.48	105.13	-1.72	0.55	100.92
184	1144C-10H-5	104-106	96.74	105.39	-1.97	0.81	101.69
184	1144C-10H-5	128-130	96.98	105.63	-1.78	0.77	102.48
184	1144C-10H-6	3-5	97.23	105.88	-1.92	0.85	103.30
184	1144C-10H-6	28-30	97.48	106.13	-1.79	0.70	104.12
184	1144B-12H-1	53-55	95.63	106.30	-1.88	0.68	104.68
184	1144B-12H-1	78-80	95.88	106.55	-2.00	0.79	105.50
184	1144B-12H-1	104-106	96.14	106.81	-1.63	0.72	106.36
184	1144B-12H-1	128-130	96.38	107.05	-1.73	0.85	107.14
184	1144B-12H-2	3-5	96.63	107.30	-1.70	0.70	107.97
184	1144B-12H-2	28-30	96.88	107.55	-2.08	0.64	108.79
184	1144B-12H-2	53-55	97.13	107.80	-2.02	0.70	109.61
184	1144B-12H-2	78-80	97.38	108.05	-1.67	0.78	110.43
184	1144B-12H-2	104-106	97.64	108.31	-2.07	0.55	111.28
184	1144B-12H-2	128-130	97.88	108.55	-1.88	0.81	112.07
184	1144B-12H-3	3-5	98.13	108.80	-2.07	0.76	112.89
184	1144B-12H-3	28-30	98.38	109.05	-1.80	0.63	113.72
184	1144B-12H-3	53-55	98.63	109.30	-2.16	0.77	114.54
184	1144B-12H-3	78-80	98.88	109.55	-2.30	0.59	115.36
184	1144B-12H-3	104-106	99.14	109.81	-2.37	0.84	116.22
184	1144B-12H-3	128-130	99.38	110.05	-2.45	0.70	117.67
184	1144B-12H-4	3-5	99.63	110.30	-1.68	0.38	123.76
184	1144B-12H-4	28-30	99.88	110.55	-1.88	0.16	125.47
184	1144B-12H-4	53-55	100.13	110.80	-1.65	0.34	126.00
184	1144B-12H-4	78-80	100.38	111.05	-1.42	0.20	126.50
184	1144B-12H-4	104-106	100.64	111.31	-1.31	0.15	127.02
184	1144B-12H-4	128-130	100.88	111.55	-1.25	0.19	127.50
184	1144B-12H-5	3-5	101.13	111.80	-2.23	0.62	128.00
184	1144B-12H-5	28-30	101.38	112.05	-2.51	0.45	128.50

Appendix 2: Stable isotope data of ODP Site 1144

Leg	Site, Hole, Core, Section	Interval (cm)	Depth (mbsf)	Depth (mcd)	$\delta^{18}O$ G.ruber	$\delta^{13}C$ G.ruber	Age (ka)
184	1144B-12H-5	53-55	101.63	112.30	-2.08	0.44	129.00
184	1144B-12H-5	78-80	101.88	112.55	-2.24	0.32	129.50
184	1144B-12H-5	104-106	102.14	112.81	-2.05	0.45	130.02
184	1144B-12H-5	128-130	102.38	113.05	-1.82	0.38	130.50
184	1144B-12H-6	3-5	102.63	113.30	-0.98	0.06	131.00
184	1144B-12H-6	28-30	102.88	113.55	-1.19	-0.02	131.50
184	1144B-12H-6	53-55	103.13	113.80	-0.85	0.38	131.98
184	1144B-12H-6	78-80	103.38	114.05	-1.28	0.22	132.44
184	1144B-12H-6	104-106	103.64	114.31	-0.97	0.29	132.89
184	1144B-12H-6	128-130	103.88	114.55	-0.82	0.22	133.31
184	1144A-12H-1	104-106	102.94	114.74	-1.26	0.22	133.65
184	1144A-12H-1	128-130	103.18	114.98	-1.31	0.13	134.07
184	1144A-12H-2	3-5	103.43	115.23	-0.86	0.32	134.51
184	1144A-12H-2	28-30	103.68	115.48	-1.09	0.21	134.94
184	1144A-12H-2	53-55	103.93	115.73	-1.25	0.40	135.38
184	1144A-12H-2	78-80	104.18	115.98	-0.92	0.30	135.82
184	1144A-12H-2	104-106	104.44	116.24	-1.11	0.20	136.28
184	1144A-12H-3	3-5	104.93	116.73	-1.03	0.40	137.13
184	1144A-12H-3	28-30	105.18	116.98	-1.13	0.25	137.57
184	1144A-12H-3	53-55	105.43	117.23	-0.79	0.51	138.01
184	1144A-12H-3	78-80	105.68	117.48	-1.31	0.37	138.45
184	1144A-12H-3	104-106	105.94	117.74	-1.43	0.48	138.90
184	1144A-12H-3	128-130	106.18	117.98	-1.04	0.33	139.33
184	1144A-12H-4	3-5	106.43	118.23	-0.86	0.21	139.76
184	1144A-12H-4	28-30	106.68	118.48	-0.98	0.45	140.20
184	1144A-12H-4	53-55	106.93	118.73	-0.92	0.46	140.64
184	1144A-12H-4	78-80	107.18	118.98	-0.77	0.38	141.08
184	1144A-12H-4	101-103	107.41	119.21	-0.78	0.45	141.48
184	1144A-12H-4	128-130	107.68	119.48	-0.93	0.35	141.95
184	1144A-12H-5	3-5	107.93	119.73	-0.75	0.49	142.39
184	1144A-12H-5	28-30	108.18	119.98	-0.90	0.44	142.83
184	1144A-12H-5	53-55	108.43	120.23	-0.75	0.49	143.27
184	1144A-12H-5	78-80	108.68	120.48	-1.18	0.57	143.71
184	1144A-12H-5	104-106	108.94	120.74	-1.03	0.59	144.16
184	1144A-12H-5	128-130	109.18	120.98	-1.24	0.57	144.58
184	1144A-12H-6	3-5	109.43	121.23	-1.03	0.60	145.02
184	1144A-12H-6	28-30	109.68	121.48	-0.78	0.62	145.46
184	1144A-12H-6	53-55	109.93	121.73	-0.83	0.51	145.90
184	1144A-12H-7	3-5	110.01	121.81	-0.74	0.57	146.04
184	1144B-13H-2	142-144	107.52	122.17	-0.84	0.59	146.67
184	1144B-13H-3	73-75	108.33	122.98	-0.84	0.55	148.09
184	1144B-13H-3	142-144	109.02	123.67	-1.06	0.72	149.30
184	1144B-13H-4	73-75	109.83	124.48	-1.13	0.61	150.72
184	1144B-13H-4	142-144	110.52	125.17	-0.85	0.66	151.93
184	1144B-13H-5	73-75	111.33	125.98	-1.05	0.68	153.34
184	1144B-13H-5	142-144	112.02	126.67	-1.00	0.73	154.55
184	1144B-13H-6	73-75	112.83	127.48	-1.19	0.73	155.97
184	1144B-13H-6	142-144	113.52	128.17	-1.42	0.60	157.18
184	1144B-14H-1	73-75	114.83	129.47	-1.14	0.51	159.46
184	1144B-14H-1	142-144	115.52	130.16	-0.82	0.51	160.67
184	1144B-14H-2	73-75	116.33	130.97	-1.37	0.81	162.09
184	1144B-14H-2	142-144	117.02	131.66	-1.32	0.55	163.30
184	1144B-14H-3	73-75	117.83	132.47	-1.23	0.71	164.72
184	1144B-14H-3	142-144	118.52	133.16	-1.20	0.51	165.93
184	1144B-14H-4	73-75	119.33	133.97	-1.07	0.51	167.35
184	1144B-14H-4	142-144	120.02	134.66	-1.35	0.50	168.56

Appendix 2: Stable isotope data of ODP Site 1144

Leg	Site, Hole, Core, Section	Interval (cm)	Depth (mbsf)	Depth (mcd)	$\delta^{18}O$ G.ruber	$\delta^{13}C$ G.ruber	Age (ka)
184	1144B-14H-5	73-75	120.83	135.47	-1.52	0.65	169.97
184	1144B-14H-5	142-144	121.52	136.16	-1.20	0.67	171.18
184	1144B-14H-6	73-75	122.33	136.97	-0.93	0.59	172.60
184	1144B-15H-1	73-75	124.33	138.55	-0.88	0.71	175.37
184	1144B-15H-1	143-145	125.03	139.25	-0.99	0.65	176.60
184	1144B-15H-2	73-75	125.83	140.05	-0.79	0.63	177.97
184	1144B-15H-2	143-145	126.53	140.75	-0.94	0.54	178.91
184	1144B-15H-3	73-75	127.33	141.55	-1.03	0.67	179.94
184	1144B-15H-3	143-145	128.03	142.25	-0.86	0.61	180.84
184	1144B-15H-4	73-75	128.83	143.05	-1.10	0.60	181.88
184	1144B-15H-4	143-145	129.53	143.75	-1.03	0.71	182.78
184	1144B-15H-5	73-75	130.31	144.53	-1.16	0.61	183.79
184	1144A-15H-3	73-75	134.18	145.84	-1.21	0.53	185.48
184	1144A-15H-3	143-145	134.88	146.54	-1.03	0.49	186.39
184	1144A-15H-4	73-75	135.68	147.34	-1.70	0.64	187.42
184	1144A-15H-4	143-145	136.38	148.04	-1.25	0.62	188.33
184	1144A-15H-5	73-75	137.18	148.84	-1.08	0.58	189.36
184	1144A-15H-5	143-145	137.88	149.54	-1.32	0.78	190.27
184	1144A-15H-7	73-75	138.86	150.52	-1.41	0.84	191.53
184	1144A-15H-7	143-145	139.56	151.22	-1.55	0.80	192.44
184	1144A-16H-1	73-75	140.63	152.43	-1.77	0.54	194.17
184	1144A-16H-2	73-75	142.05	153.85	-1.68	0.71	199.15
184	1144A-16H-2	143-145	142.75	154.55	-1.92	0.61	201.68
184	1144A-16H-3	73-75	143.55	155.35	-1.39	0.70	204.58
184	1144A-16H-3	143-145	144.25	156.05	-1.51	0.59	207.12
184	1144A-16H-4	73-75	145.05	156.85	-1.53	0.13	210.01
184	1144A-16H-4	143-145	145.75	157.55	-1.79	0.63	212.55
184	1144B-17H-2	143-145	144.63	157.95	-2.22	0.65	214.09
184	1144B-17H-3	73-75	145.43	158.75	-1.37	0.67	226.94
184	1144B-17H-3	143-145	146.13	159.45	-1.72	0.41	228.68
184	1144B-17H-4	73-75	146.93	160.25	-1.99	0.77	230.59
184	1144B-17H-5	143-145	149.13	162.45	-1.87	0.70	235.86
184	1144B-17H-6	143-145	150.63	163.95	-2.05	0.55	239.45
184	1144A-17H-3	3-5	152.39	164.51	-2.05	0.52	240.79
184	1144A-17H-3	56-58	152.92	165.04	-2.01	0.65	242.06
184	1144A-17H-3	78-80	153.14	165.26	-1.51	0.43	242.58
184	1144A-17H-3	104-106	153.40	165.52	-1.87	0.46	243.21
184	1144A-17H-3	128-130	153.64	165.76	-2.21	0.19	243.78
184	1144A-17H-4	3-5	153.90	166.02	-1.54	0.43	244.40
184	1144A-17H-4	28-30	154.15	166.27	-1.25	0.32	245.05
184	1144A-17H-4	56-58	154.43	166.55	-1.42	0.32	246.09
184	1144A-17H-4	78-80	154.65	166.77	-1.92	0.42	246.95
184	1144A-17H-4	104-106	154.91	167.03	-1.53	0.51	247.97
184	1144A-17H-4	104-106	154.91	167.03	-1.48	0.57	247.97
184	1144A-17H-4	128-130	155.15	167.27	-1.20	0.51	248.91
184	1144A-17H-5	3-5	155.42	167.54	-1.70	0.31	249.96
184	1144A-17H-5	28-30	155.67	167.79	-1.65	0.45	250.94
184	1144A-17H-5	56-58	155.95	168.07	-1.57	0.69	252.03
184	1144A-17H-5	78-80	156.17	168.29	-1.32	0.28	252.89
184	1144A-17H-5	104-106	156.43	168.55	-1.23	0.61	253.90
184	1144A-17H-5	128-130	156.67	168.79	-1.43	0.52	254.84
184	1144A-17H-6	3-5	156.92	169.04	-1.43	0.50	255.82
184	1144A-17H-6	28-30	157.17	169.29	-1.32	0.58	256.79
184	1144A-17H-6	56-58	157.45	169.57	-1.55	0.54	257.89
184	1144A-17H-6	78-80	157.67	169.79	-1.55	0.54	258.75
184	1144A-17H-6	104-106	157.93	170.05	-1.52	0.76	259.76

Appendix 2: Stable isotope data of ODP Site 1144

Leg	Site, Hole, Core, Section	Interval (cm)	Depth (mbsf)	Depth (mcd)	$\delta^{18}O$ G.ruber	$\delta^{13}C$ G.ruber	Age (ka)
184	1144B-18H-3	104-106	155.33	170.17	-1.22	0.65	260.23
184	1144B-18H-3	128-130	155.57	170.41	-1.39	0.60	261.17
184	1144B-18H-4	28-30	156.07	170.91	-1.63	0.45	263.12
184	1144B-18H-4	56-58	156.35	171.19	-1.38	0.53	264.21
184	1144B-18H-4	78-80	156.57	171.41	-1.57	0.63	265.07
184	1144B-18H-4	104-106	156.83	171.67	-1.58	0.44	266.09
184	1144B-18H-4	128-130	157.07	171.91	-1.54	0.70	267.02
184	1144B-18H-5	3-5	157.32	172.16	-0.95	0.69	267.86
184	1144B-18H-5	28-30	157.57	172.41	-1.49	0.94	268.34
184	1144B-18H-5	56-58	157.85	172.69	-1.41	0.63	268.74
184	1144B-18H-5	78-80	158.07	172.91	-1.03	0.48	269.05
184	1144B-18H-5	104-106	158.33	173.17	-1.62	0.66	269.41
184	1144B-18H-5	128-130	158.57	173.41	-1.26	0.70	269.74
184	1144B-18H-6	3-5	158.82	173.66	-1.33	0.45	270.09
184	1144B-18H-6	28-30	159.07	173.91	-1.40	0.65	270.44
184	1144B-18H-6	56-58	159.35	174.19	-1.36	0.56	270.83
184	1144B-18H-6	78-80	159.57	174.41	-1.43	0.84	271.13
184	1144B-18H-6	104-106	159.83	174.67	-1.45	0.56	271.50
184	1144A-18H-2	28-30	160.68	174.85	-1.65	0.70	271.75
184	1144A-18H-2	56-58	160.96	175.13	-1.70	0.58	272.14
184	1144A-18H-2	78-80	161.18	175.35	-1.73	0.71	272.44
184	1144A-18H-2	104-106	161.44	175.61	-1.84	0.62	272.81
184	1144A-18H-2	128-130	161.68	175.85	-1.48	0.74	273.14
184	1144A-18H-3	5-7	161.95	176.12	-1.43	0.82	273.52
184	1144A-18H-3	28-30	162.18	176.35	-1.59	0.90	273.84
184	1144A-18H-3	56-58	162.46	176.63	-1.40	0.94	274.23
184	1144A-18H-3	78-80	162.68	176.85	-1.94	0.99	274.53
184	1144A-18H-3	104-106	162.94	177.11	-1.85	0.96	274.89
184	1144A-18H-3	128-130	163.18	177.35	-1.94	0.97	275.23
184	1144A-18H-4	3-5	163.43	177.60	-1.67	0.99	275.58
184	1144A-18H-4	28-30	163.68	177.85	-1.84	0.93	275.93
184	1144A-18H-4	56-58	163.96	178.13	-1.87	0.90	276.32
184	1144A-18H-4	78-80	164.18	178.35	-2.06	0.90	276.62
184	1144A-18H-4	104-106	164.44	178.61	-1.68	0.79	276.98
184	1144A-18H-4	128-130	164.68	178.85	-1.60	0.74	277.32
184	1144A-18H-5	3-5	164.93	179.10	-1.78	0.66	277.67
184	1144A-18H-5	28-30	165.18	179.35	-1.87	0.62	278.01
184	1144A-18H-5	56-58	165.46	179.63	-2.07	0.60	278.40
184	1144A-18H-5	78-80	165.68	179.85	-1.80	0.60	278.71
184	1144A-18H-5	104-106	165.94	180.11	-1.62	0.60	279.07
184	1144A-18H-5	129-131	166.19	180.36	-1.69	0.70	279.42
184	1144A-18H-6	3-5	166.43	180.60	-2.12	0.88	279.76
184	1144A-18H-6	28-30	166.68	180.85	-1.72	0.68	280.10
184	1144A-18H-6	56-58	166.96	181.13	-1.46	0.80	280.49
184	1144A-18H-6	78-80	167.18	181.35	-1.63	0.72	280.80
184	1144B-19H-3	78-80	165.38	181.67	-1.52	0.67	281.25
184	1144B-19H-3	104-106	165.64	181.93	-1.57	0.74	281.61
184	1144B-19H-3	128-130	165.88	182.17	-1.52	0.51	281.94
184	1144B-19H-4	3-5	166.13	182.42	-1.80	0.85	282.29
184	1144B-19H-4	28-30	166.38	182.67	-1.70	0.86	282.64
184	1144B-19H-4	56-58	166.66	182.95	-1.81	1.12	283.03
184	1144B-19H-4	78-80	166.88	183.17	-1.93	1.04	283.33
184	1144B-19H-4	104-106	167.14	183.43	-1.91	0.76	283.70
184	1144B-19H-4	128-130	167.38	183.67	-2.05	0.92	284.03
184	1144B-19H-5	3-5	167.63	183.92	-2.29	0.70	284.38
184	1144B-19H-5	28-30	167.88	184.17	-2.12	0.60	284.73

Appendix 2: Stable isotope data of ODP Site 1144

Leg	Site, Hole, Core, Section	Interval (cm)	Depth (mbsf)	Depth (mcd)	$\delta^{18}O$ G.ruber	$\delta^{13}C$ G.ruber	Age (ka)
184	1144C-18H-3	128-130	168.65	184.61	-2.02	0.76	285.34
184	1144C-18H-4	3-5	168.90	184.86	-2.17	0.45	285.69
184	1144C-18H-4	28-30	169.15	185.11	-1.93	0.35	286.04
184	1144C-18H-4	56-58	169.43	185.39	-1.75	0.61	286.43
184	1144C-18H-4	78-80	169.65	185.61	-1.85	0.23	286.73
184	1144C-18H-4	104-106	169.91	185.87	-2.21	0.50	287.10
184	1144C-18H-4	128-130	170.15	186.11	-1.59	0.21	287.43
184	1144C-18H-5	3-5	170.40	186.36	-1.98	0.32	287.78
184	1144C-18H-5	28-30	170.65	186.61	-1.83	0.46	288.13
184	1144C-18H-5	56-58	170.93	186.89	-1.91	0.52	288.52
184	1144C-18H-5	78-80	171.15	187.11	-1.83	0.46	288.82
184	1144C-18H-5	104-106	171.41	187.37	-2.08	0.50	289.18
184	1144C-18H-5	128-130	171.65	187.61	-1.79	0.41	289.52
184	1144C-18H-6	3-5	171.90	187.86	-1.81	0.39	289.87
184	1144C-18H-6	28-30	172.15	188.11	-2.07	0.38	290.21
184	1144C-18H-6	56-58	172.43	188.39	-1.95	0.50	290.60
184	1144C-18H-6	78-80	172.65	188.61	-1.81	0.52	290.91
184	1144C-18H-6	104-106	172.91	188.87	-2.30	0.40	291.27
184	1144C-18H-6	128-130	173.15	189.11	-1.79	0.50	291.61
184	1144C-18H-7	3-5	173.40	189.36	-1.73	0.55	291.96
184	1144C-18H-7	28-30	173.65	189.61	-1.63	0.59	292.30
184	1144C-18H-7	56-58	173.93	189.89	-1.69	0.62	292.69
184	1144C-18H-7	78-80	174.15	190.11	-1.35	0.51	293.03
184	1144B-20H-3	56-58	174.66	190.21	-1.69	0.70	293.24
184	1144B-20H-3	78-80	174.88	190.43	-1.53	0.62	293.71
184	1144B-20H-3	104-106	175.14	190.69	-1.44	0.48	294.29
184	1144B-20H-3	128-130	175.38	190.93	-1.59	0.75	294.83
184	1144B-20H-4	3-5	175.63	191.18	-1.56	0.76	295.39
184	1144B-20H-4	28-30	175.88	191.43	-1.52	0.61	295.94
184	1144B-20H-4	56-58	176.16	191.71	-1.68	0.57	296.57
184	1144B-20H-4	78-80	176.38	191.93	-1.58	0.52	297.06
184	1144B-20H-4	104-106	176.64	192.19	-1.66	0.42	297.64
184	1144B-20H-4	128-130	176.88	192.43	-1.79	0.61	298.17
184	1144B-20H-5	3-5	177.05	192.60	-1.96	0.49	298.55
184	1144B-20H-5	28-30	177.30	192.85	-1.37	0.54	299.11
184	1144B-20H-5	56-58	177.58	193.13	-1.33	0.54	299.74
184	1144B-20H-5	78-80	177.80	193.35	-1.57	0.62	300.23
184	1144B-20H-5	104-106	178.06	193.61	-1.27	0.62	300.81
184	1144B-20H-5	128-130	178.30	193.85	-1.39	0.53	301.34
184	1144B-20H-6	3-5	178.55	194.10	-1.71	0.79	301.90
184	1144B-20H-6	28-30	178.80	194.35	-1.87	0.79	302.46
184	1144B-20H-6	56-58	179.08	194.63	-2.09	0.88	303.08
184	1144B-20H-6	78-80	179.30	194.85	-2.26	0.98	303.57
184	1144B-20H-6	104-106	179.56	195.11	-2.14	0.87	304.15
184	1144A-20H-1	56-58	178.46	195.27	-2.35	0.75	304.51
184	1144A-20H-1	78-80	178.68	195.49	-2.58	0.83	305.00
184	1144A-20H-1	104-106	178.94	195.75	-2.14	0.63	305.52
184	1144A-20H-1	128-130	179.18	195.99	-1.58	0.79	306.01
184	1144A-20H-2	3-5	179.43	196.24	-1.96	0.68	306.51
184	1144A-20H-2	28-30	179.68	196.49	-1.77	0.74	307.02
184	1144A-20H-2	56-58	179.96	196.77	-2.17	0.70	307.58
184	1144A-20H-2	78-80	180.18	196.99	-1.83	0.75	308.02
184	1144A-20H-2	104-106	180.44	197.25	-2.00	0.61	308.55
184	1144A-20H-2	128-130	180.68	197.49	-1.68	0.68	309.03
184	1144A-20H-3	3-5	180.93	197.74	-1.85	0.66	309.53
184	1144A-20H-3	28-30	181.18	197.99	-2.00	0.68	310.04

Appendix 2: Stable isotope data of ODP Site 1144

Leg	Site, Hole, Core, Section	Interval (cm)	Depth (mbsf)	Depth (mcd)	$\delta^{18}O$ G.ruber	$\delta^{13}C$ G.ruber	Age (ka)
184	1144A-20H-3	56-58	181.46	198.27	-1.76	0.70	310.60
184	1144A-20H-3	78-80	181.68	198.49	-2.15	0.82	311.05
184	1144A-20H-3	104-106	181.94	198.75	-1.31	0.89	311.57
184	1144A-20H-3	128-130	182.18	198.99	-1.49	0.63	312.05
184	1144A-20H-4	3-5	182.43	199.24	-1.77	0.74	312.56
184	1144A-20H-4	28-30	182.68	199.49	-1.59	0.83	313.06
184	1144A-20H-4	56-58	182.96	199.77	-1.53	0.94	313.63
184	1144A-20H-4	78-80	183.18	199.99	-1.49	0.79	314.07
184	1144A-20H-4	104-106	183.44	200.25	-2.01	0.88	314.59
184	1144A-20H-4	128-130	183.68	200.49	-1.56	0.85	315.08
184	1144A-20H-5	3-5	183.93	200.74	-1.94	0.66	315.58
184	1144A-20H-5	28-30	184.18	200.99	-1.76	0.76	316.08
184	1144A-20H-5	56-58	184.46	201.27	-1.69	0.71	316.65
184	1144A-20H-5	78-80	184.68	201.49	-2.01	0.71	317.09
184	1144A-20H-5	104-106	184.94	201.75	-2.32	0.49	317.62
184	1144A-20H-5	128-130	185.18	201.99	-1.99	0.70	318.10
184	1144A-20H-6	3-5	185.36	202.17	-1.54	0.43	318.46
184	1144A-20H-6	28-30	185.61	202.42	-1.21	0.62	318.97
184	1144A-20H-6	56-58	185.89	202.70	-1.67	0.47	319.53
184	1144A-20H-6	78-80	186.11	202.92	-1.73	0.44	319.97
184	1144A-20H-6	104-106	186.37	203.18	-2.43	0.53	320.50
184	1144C-20H-2	104-106	186.11	203.18	-2.04	0.50	320.50
184	1144C-20H-2	128-130	186.35	203.42	-1.99	0.88	320.98
184	1144A-20H-6	128-130	186.61	203.42	-1.74	0.76	320.98
184	1144C-20H-3	3-5	186.60	203.67	-2.51	0.38	321.48
184	1144C-20H-3	28-30	186.85	203.92	-2.20	0.47	321.99
184	1144C-20H-3	56-58	187.13	204.20	-1.78	0.60	322.55
184	1144C-20H-3	78-80	187.35	204.42	-2.13	0.68	323.00
184	1144C-20H-3	104-106	187.61	204.68	-2.22	0.46	323.52
184	1144C-20H-3	128-130	187.85	204.92	-1.92	0.46	324.00
184	1144C-20H-4	3-5	188.08	205.15	-2.53	0.54	324.47
184	1144C-20H-4	28-30	188.33	205.40	-1.68	0.78	324.97
184	1144C-20H-4	56-58	188.61	205.68	-1.81	0.79	325.53
184	1144C-20H-4	78-80	188.83	205.90	-1.75	0.82	325.98
184	1144C-20H-4	104-106	189.09	206.16	-1.83	0.63	326.50
184	1144C-20H-4	128-130	189.33	206.40	-1.93	0.79	326.99
184	1144C-20H-5	3-5	189.58	206.65	-2.18	0.95	327.49
184	1144C-20H-5	28-30	189.83	206.90	-2.24	0.73	327.99
184	1144C-20H-5	56-58	190.11	207.18	-2.48	0.67	328.56
184	1144C-20H-5	78-80	190.33	207.40	-2.71	0.63	329.07
184	1144C-20H-5	104-106	190.59	207.66	-2.24	0.44	330.18
184	1144C-20H-5	128-130	190.83	207.90	-2.08	0.34	331.27
184	1144C-20H-6	3-5	191.08	208.15	-1.08	0.52	332.41
184	1144C-20H-6	28-30	191.33	208.40	-1.94	0.47	333.55
184	1144C-20H-6	56-58	191.61	208.68	-0.57	0.34	334.82
184	1144C-20H-6	78-80	191.83	208.90	-0.73	0.28	335.82
184	1144C-20H-6	104-106	192.09	209.16	-0.46	0.41	336.87
184	1144C-20H-6	128-130	192.33	209.40	-1.16	0.26	337.52
184	1144C-20H-7	3-5	192.58	209.65	-0.80	0.17	338.07
184	1144C-20H-7	28-30	192.83	209.90	-1.07	0.43	338.61
184	1144C-20H-7	56-58	193.11	210.18	-1.37	0.54	339.22
184	1144C-20H-7	78-80	193.33	210.40	-0.67	0.18	339.70
184	1144C-20H-7	104-106	193.59	210.66	-0.93	0.52	340.26
184	1144B-22H-1	78-80	190.88	210.96	-1.11	0.43	340.91
184	1144B-22H-1	104-106	191.14	211.22	-0.50	0.33	341.48
184	1144B-22H-1	128-130	191.38	211.46	-1.11	0.36	342.00

Appendix 2: Stable isotope data of ODP Site 1144

Leg	Site, Hole, Core, Section	Interval (cm)	Depth (mbsf)	Depth (mcd)	$\delta^{18}O$ G.ruber	$\delta^{13}C$ G.ruber	Age (ka)
184	1144B-22H-2	3-5	191.63	211.71	-0.96	0.55	342.54
184	1144B-22H-2	28-30	191.88	211.96	-0.80	0.62	343.09
184	1144B-22H-2	56-58	192.16	212.24	-0.65	0.41	343.70
184	1144B-22H-2	78-80	192.38	212.46	-1.12	0.47	344.17
184	1144B-22H-2	104-106	192.64	212.72	-0.81	0.34	344.74
184	1144B-22H-2	128-130	192.88	212.96	-1.01	0.46	345.26
184	1144B-22H-3	3-5	193.13	213.21	-0.89	0.36	345.80
184	1144B-22H-3	28-30	193.38	213.46	-1.10	0.70	346.35
184	1144B-22H-3	56-58	193.66	213.74	-1.02	0.65	346.96
184	1144B-22H-3	78-80	193.88	213.96	-1.13	0.49	347.44
184	1144B-22H-3	104-106	194.14	214.22	-1.35	0.57	347.95
184	1144B-22H-3	128-130	194.38	214.46	-1.15	0.58	348.29
184	1144B-22H-4	3-5	194.54	214.62	-0.83	0.47	348.48
184	1144B-22H-4	28-30	194.79	214.87	-1.10	0.43	348.78
184	1144B-22H-4	56-58	195.07	215.15	-1.11	0.48	349.12
184	1144B-22H-4	78-80	195.29	215.37	-1.09	0.57	349.38
184	1144B-22H-4	104-106	195.55	215.63	-0.88	0.58	349.70
184	1144B-22H-4	128-130	195.79	215.87	-1.17	0.61	349.99
184	1144B-22H-5	3-5	196.04	216.12	-1.26	0.62	350.29
184	1144B-22H-5	28-30	196.29	216.37	-0.81	0.36	350.59
184	1144B-22H-5	56-58	196.57	216.65	-0.91	0.43	350.92
184	1144B-22H-5	78-80	196.79	216.87	-0.96	0.57	351.19
184	1144B-22H-5	104-106	197.05	217.13	-1.26	0.45	351.50
184	1144B-22H-5	128-130	197.29	217.37	-0.89	0.62	351.79
184	1144B-22H-6	3-5	197.54	217.62	-1.32	0.57	352.09
184	1144B-22H-6	28-30	197.79	217.87	-0.96	0.71	352.39
184	1144B-22H-6	56-58	198.07	218.15	-1.19	0.57	352.73
184	1144B-22H-6	78-80	198.29	218.37	-1.00	0.59	352.99
184	1144B-22H-6	104-106	198.55	218.63	-0.99	0.69	353.31
184	1144A-22H-3	3-5	199.93	218.80	-0.55	0.47	353.51
184	1144A-22H-3	28-30	200.18	219.05	-1.10	0.61	353.81
184	1144A-22H-3	56-58	200.46	219.33	-0.97	0.84	354.15
184	1144A-22H-3	78-80	200.68	219.55	-1.46	0.77	354.41
184	1144A-22H-3	104-106	200.94	219.81	-1.03	0.65	354.73
184	1144A-22H-3	128-130	201.18	220.05	-0.96	0.60	355.01
184	1144A-22H-4	3-5	201.43	220.30	-0.76	0.64	355.31
184	1144A-22H-4	28-30	201.68	220.55	-1.14	0.65	355.62
184	1144A-22H-4	56-58	201.96	220.83	-1.53	0.53	355.95
184	1144A-22H-4	78-80	202.18	221.05	-1.38	0.57	356.22
184	1144A-22H-4	104-106	202.44	221.31	-1.25	0.69	356.53
184	1144A-22H-4	128-130	202.68	221.55	-1.21	0.62	356.82
184	1144A-22H-5	3-5	202.93	221.80	-1.20	0.55	357.12
184	1144A-22H-5	28-30	203.18	222.05	-1.18	0.76	357.42
184	1144A-22H-5	56-58	203.46	222.33	-1.24	0.67	357.76
184	1144A-22H-5	78-80	203.68	222.55	-1.30	0.67	358.02
184	1144A-22H-5	104-106	203.94	222.81	-1.00	0.55	358.33
184	1144A-22H-5	128-130	204.18	223.05	-1.35	0.88	358.62
184	1144A-22H-6	3-5	204.43	223.30	-1.43	0.86	358.92
184	1144A-22H-6	28-30	204.68	223.55	-1.02	0.58	359.22
184	1144A-22H-6	56-58	204.96	223.83	-1.10	0.86	359.56
184	1144A-22H-6	78-80	205.18	224.05	-1.09	0.77	359.83
184	1144B-23X-4	28-30	204.38	224.32	-1.55	0.90	360.15
184	1144B-23X-4	56-58	204.66	224.60	-0.93	0.74	360.49
184	1144B-23X-4	78-80	204.88	224.82	-0.87	0.75	360.75
184	1144B-23X-4	104-106	205.14	225.08	-1.30	0.68	361.07
184	1144B-23X-4	128-130	205.38	225.32	-0.98	0.74	361.35

Appendix 2: Stable isotope data of ODP Site 1144

Leg	Site, Hole, Core, Section	Interval (cm)	Depth (mbsf)	Depth (mcd)	$\delta^{18}O$ G.ruber	$\delta^{13}C$ G.ruber	Age (ka)
184	1144B-23X-5	3-5	205.63	225.57	-1.43	0.91	361.65
184	1144B-23X-5	28-30	205.88	225.82	-1.06	0.79	361.96
184	1144B-23X-5	56-58	206.16	226.10	-0.98	0.75	362.29
184	1144B-23X-5	78-80	206.38	226.32	-1.19	0.75	362.56
184	1144B-23X-5	104-106	206.64	226.58	-1.23	0.86	362.87
184	1144B-23X-5	128-130	206.88	226.82	-1.39	0.66	363.16
184	1144B-23X-6	3-5	207.13	227.07	-1.41	0.61	363.46
184	1144A-23H-2	56-58	208.20	227.52	-0.69	0.86	364.02
184	1144A-23H-2	78-80	208.42	227.74	-1.41	1.04	364.32
184	1144A-23H-2	104-106	208.68	228.00	-1.73	0.75	364.69
184	1144A-23H-2	128-130	208.92	228.24	-1.58	0.93	365.03
184	1144A-23H-3	3-5	209.17	228.49	-1.56	0.75	365.39
184	1144A-23H-3	28-30	209.42	228.74	-1.28	0.81	365.75
184	1144A-23H-3	56-58	209.70	229.02	-1.39	1.00	366.15
184	1144A-23H-3	78-80	209.92	229.24	-1.02	0.75	366.47
184	1144A-23H-3	104-106	210.18	229.50	-1.27	1.03	366.84
184	1144A-23H-3	128-130	210.42	229.74	-1.40	0.93	367.19
184	1144A-23H-4	3-5	210.67	229.99	-1.82	0.40	367.55
184	1144A-23H-4	28-30	210.92	230.24	-1.43	0.63	367.90
184	1144A-23H-4	56-58	211.20	230.52	-1.28	0.94	368.31
184	1144A-23H-4	78-80	211.42	230.74	-0.83	0.95	368.62
184	1144A-23H-4	104-106	211.68	231.00	-1.62	0.90	369.00
184	1144A-23H-4	128-130	211.92	231.24	-1.55	0.72	369.34
184	1144A-23H-5	3-5	212.17	231.49	-1.51	0.86	369.70
184	1144A-23H-5	28-30	212.42	231.74	-1.46	0.73	370.06
184	1144A-23H-5	56-58	212.70	232.02	-1.35	0.73	370.46
184	1144A-23H-5	78-80	212.92	232.24	-1.96	0.81	370.78
184	1144A-23H-5	104-106	213.18	232.50	-1.68	0.99	371.15
184	1144A-23H-5	128-130	213.42	232.74	-1.24	1.00	371.49
184	1144A-23H-6	3-5	213.67	232.99	-1.37	0.95	371.85
184	1144A-23H-6	28-30	213.92	233.24	-1.36	0.71	372.21
184	1144A-23H-6	56-58	214.20	233.52	-1.63	0.82	372.61
184	1144A-23H-6	78-80	214.42	233.74	-1.77	0.89	372.93
184	1144A-23H-6	104-106	214.68	234.00	-1.77	0.89	373.30
184	1144A-23H-6	128-130	214.92	234.24	-1.71	0.97	373.65
184	1144A-23H-7	3-5	215.17	234.49	-1.72	0.63	374.01
184	1144A-23H-7	28-30	215.42	234.74	-1.93	0.80	374.36
184	1144A-23H-7	56-58	215.70	235.02	-2.02	0.99	374.77
184	1144A-23H-7	78-80	215.92	235.24	-1.68	1.04	375.08
184	1144B-24X-4	15-17	213.85	235.25	-1.71	1.35	375.10
184	1144B-24X-4	40-42	214.10	235.50	-1.91	0.67	375.45
184	1144B-24X-4	65-67	214.35	235.75	-1.50	0.91	375.81
184	1144B-24X-4	90-92	214.60	236.00	-1.98	0.83	376.17
184	1144B-24X-4	115-117	214.85	236.25	-1.85	0.91	376.53
184	1144B-24X-4	140-142	215.10	236.50	-1.67	0.65	376.89
184	1144B-24X-5	10-12	215.30	236.70	-2.01	0.63	377.18
184	1144B-24X-5	35-37	215.55	236.95	-2.19	1.03	377.54
184	1144B-24X-5	60-62	215.80	237.20	-1.95	0.51	377.89
184	1144B-24X-5	85-87	216.05	237.45	-1.98	0.85	378.25
184	1144B-24X-5	110-112	216.30	237.70	-2.24	0.60	378.61
184	1144B-24X-5	135-137	216.55	237.95	-2.02	0.64	378.97
184	1144B-24X-6	10-12	216.80	238.20	-2.00	0.70	379.33
184	1144B-24X-6	35-37	217.05	238.45	-1.34	1.01	379.69
184	1144B-24X-6	60-62	217.30	238.70	-1.37	0.98	380.05
184	1144B-24X-6	85-87	217.55	238.95	-1.04	0.81	380.41
184	1144B-24X0	11-13	217.80	239.20	-1.53	1.29	380.77

Appendix 2: Stable isotope data of ODP Site 1144

Leg	Site, Hole, Core, Section	Interval (cm)	Depth (mbsf)	Depth (mcd)	$\delta^{18}O$ G.ruber	$\delta^{13}C$ G.ruber	Age (ka)
184	1144B-24X0	36-38	218.05	239.45	-1.39	1.01	381.12
184	1144A-24H-1	73-75	216.63	239.63	-1.93	0.88	381.38
184	1144A-24H-1	143-145	217.33	240.33	-1.94	0.66	382.39
184	1144A-24H-2	73-75	218.13	241.13	-2.21	0.92	383.54
184	1144A-24H-2	143-145	218.83	241.83	-1.54	1.06	384.54
184	1144A-24H-3	73-75	219.63	242.63	-1.61	1.09	385.69
184	1144A-24H-3	143-145	220.33	243.33	-1.90	0.95	386.69
184	1144A-24H-4	73-75	221.13	244.13	-1.98	0.86	387.84
184	1144A-24H-4	143-145	221.83	244.83	-2.12	0.85	388.85
184	1144A-24H-5	73-75	222.63	245.63	-2.18	0.67	390.00
184	1144A-24H-5	143-145	223.33	246.33	-1.74	0.84	391.77
184	1144A-24H-6	73-75	224.13	247.13	-1.71	1.04	411.35
184	1144B-25X-2	5-7	220.35	247.64	-2.10	0.97	412.57
184	1144B-25X-2	30-32	220.60	247.89	-1.96	1.04	412.86
184	1144B-25X-2	55-57	220.85	248.14	-1.92	1.05	413.15
184	1144B-25X-2	80-82	221.10	248.39	-2.11	0.99	413.43
184	1144B-25X-2	105-107	221.35	248.64	-2.28	0.98	413.72
184	1144B-25X-2	130-132	221.60	248.89	-2.56	0.47	414.11
184	1144B-25X-3	5-7	221.85	249.14	-2.08	0.62	414.80
184	1144B-25X-3	30-32	222.10	249.39	-1.57	0.32	415.60
184	1144B-25X-3	55-57	222.35	249.64	-1.37	0.32	416.40
184	1144B-25X-3	80-82	222.60	249.89	-0.88	0.04	417.20
184	1144B-25X-3	105-107	222.85	250.14	-0.45	0.24	417.97
184	1144B-25X-3	130-132	223.10	250.39	-1.27	0.37	418.45
184	1144B-25X-4	5-7	223.35	250.64	-1.18	0.29	418.89
184	1144B-25X-4	30-32	223.60	250.89	-0.81	0.22	419.34
184	1144B-25X-4	55-57	223.85	251.14	-1.02	0.38	419.78
184	1144A-25H-1	7-9	225.47	251.38	-0.78	0.29	420.21
184	1144B-25X-4	79-81	224.09	251.38	-0.71	0.18	420.21
184	1144A-25H-1	27-29	225.67	251.58	-0.63	0.22	420.57
184	1144A-25H-1	73-75	226.13	252.04	-0.67	0.38	421.38
184	1144A-25H-1	104-106	226.44	252.35	-0.78	0.53	421.94
184	1144A-25H-1	143-145	226.83	252.74	-0.80	0.36	422.63
184	1144A-25H-2	7-9	226.97	252.88	-0.55	0.32	422.88
184	1144A-25H-2	27-29	227.17	253.08	-0.78	0.50	423.24
184	1144A-25H-2	73-75	227.63	253.54	-0.93	0.49	424.06
184	1144A-25H-2	104-106	227.94	253.85	-0.87	0.60	424.61
184	1144A-25H-2	143-145	228.33	254.24	-0.82	0.68	425.30
184	1144A-25H-3	1-3	228.41	254.32	-0.79	0.56	425.45
184	1144A-25H-3	7-9	228.47	254.38	-0.83	0.64	425.55
184	1144A-25H-3	27-29	228.67	254.58	-1.02	0.56	425.91
184	1144A-25H-3	51-53	228.91	254.82	-0.74	0.56	426.34
184	1144A-25H-3	73-75	229.13	255.04	-0.78	0.64	426.73
184	1144A-25H-3	104-106	229.44	255.35	-0.88	0.77	427.28
184	1144A-25H-3	143-145	229.83	255.74	-0.73	0.74	427.98
184	1144A-25H-4	7-9	229.97	255.88	-0.82	0.81	428.22
184	1144A-25H-4	27-29	230.17	256.08	-0.64	0.62	428.58
184	1144A-25H-4	73-75	230.63	256.54	-1.04	0.78	429.40
184	1144A-25H-4	104-106	230.94	256.85	-1.14	0.87	429.95
184	1144A-25H-4	143-145	231.33	257.24	-0.99	0.67	430.65
184	1144A-25H-5	7-9	231.47	257.38	-1.17	0.67	430.90
184	1144A-25H-5	27-29	231.67	257.58	-1.21	0.80	431.25
184	1144A-25H-5	73-75	232.13	258.04	-0.93	0.86	432.07
184	1144A-25H-5	104-106	232.44	258.35	-1.11	0.74	432.62
184	1144A-25H-5	143-145	232.83	258.74	-0.77	0.69	433.32

Appendix 2: Stable isotope data of ODP Site 1144

Leg	Site, Hole, Core, Section	Interval (cm)	Depth (mbsf)	Depth (mcd)	$\delta^{18}O$ G.ruber	$\delta^{13}C$ G.ruber	Age (ka)
184	1144A-25H-6	7-9	232.97	258.88	-0.87	0.83	433.57
184	1144A-25H-6	27-29	233.17	259.08	-1.13	0.79	433.92
184	1144A-25H-6	73-75	233.63	259.54	-1.18	0.79	434.74
184	1144A-25H-6	104-106	233.94	259.85	-0.72	0.56	435.30
184	1144A-26X-1	3-5	234.93	260.18	-0.73	0.73	435.88
184	1144A-25H-6	143-145	234.33	260.24	-0.89	0.75	435.99
184	1144A-25H-7	7-9	234.47	260.38	-0.57	0.77	436.24
184	1144A-26X-1	28-30	235.18	260.43	-0.85	0.79	436.33
184	1144A-25H-7	27-29	234.67	260.58	-0.69	0.64	436.60
184	1144A-26X-1	53-55	235.43	260.68	-0.72	0.54	436.77
184	1144A-26X-1	78-80	235.68	260.93	-0.53	0.74	437.22
184	1144A-26X-1	104-106	235.94	261.19	-1.12	0.72	437.68
184	1144A-26X-1	128-130	236.18	261.43	-0.81	0.74	438.11
184	1144A-26X-2	3-5	236.43	261.68	-0.71	0.75	438.56
184	1144A-26X-2	28-30	236.68	261.93	-0.42	0.81	439.00
184	1144A-26X-2	53-55	236.93	262.18	-0.37	0.70	439.42
184	1144A-26X-2	78-80	237.18	262.43	-0.43	0.62	439.83
184	1144A-26X-2	104-106	237.44	262.69	-0.66	0.63	440.27
184	1144A-26X-2	128-130	237.68	262.93	-0.80	0.81	440.67
184	1144A-26X-3	3-5	237.93	263.18	-0.88	0.71	441.08
184	1144A-26X-3	28-30	238.18	263.43	-0.88	1.08	441.50
184	1144A-26X-3	53-55	238.43	263.68	-0.72	0.87	441.91
184	1144A-26X-3	78-80	238.68	263.93	-0.87	0.59	442.33
184	1144A-26X-3	104-106	238.94	264.19	-0.91	0.75	442.76
184	1144A-26X-3	128-130	239.18	264.43	-0.94	0.82	443.16
184	1144A-26X-4	3-5	239.43	264.68	-0.99	0.76	443.58
184	1144A-26X-4	28-30	239.68	264.93	-0.94	0.73	444.00
184	1144A-26X-4	53-55	239.93	265.18	-0.90	0.60	444.41
184	1144A-26X-4	78-80	240.18	265.43	-1.18	0.83	444.83
184	1144A-26X-4	104-106	240.44	265.69	-1.00	0.57	445.26
184	1144A-26X-4	128-130	240.68	265.93	-0.93	0.65	445.66
184	1144A-26X-5	3-5	240.93	266.18	-1.08	0.69	446.08
184	1144A-26X-5	28-30	241.18	266.43	-0.95	0.92	446.49
184	1144A-26X-5	53-55	241.43	266.68	-1.28	0.99	446.91
184	1144A-26X-5	78-80	241.68	266.93	-1.46	0.91	447.33
184	1144A-26X-5	104-106	241.94	267.19	-1.20	0.91	447.76
184	1144A-26X-5	128-130	242.18	267.43	-1.26	0.90	448.16
184	1144A-27X-1	3-5	241.33	268.62	-1.27	0.94	450.14
184	1144A-27X-1	28-30	241.58	268.87	-1.16	0.68	450.56
184	1144A-27X-1	53-55	241.83	269.12	-1.23	0.77	450.97
184	1144A-27X-1	78-80	242.08	269.37	-1.54	0.82	451.39
184	1144A-27X-1	104-106	242.34	269.63	-1.59	0.82	451.82
184	1144A-27X-1	128-130	242.58	269.87	-1.28	0.76	452.22
184	1144A-27X-2	3-5	242.83	270.12	-1.44	0.73	452.64
184	1144A-27X-2	28-30	243.08	270.37	-1.28	0.80	453.05
184	1144A-27X-2	53-55	243.33	270.62	-1.35	0.70	453.47
184	1144A-27X-2	78-80	243.58	270.87	-1.27	0.62	453.89
184	1144A-27X-2	104-106	243.84	271.13	-1.10	0.53	454.32
184	1144A-27X-2	128-130	244.08	271.37	-1.17	0.72	454.72
184	1144A-27X-3	3-5	244.33	271.62	-1.33	1.02	455.13
184	1144A-27X-3	28-30	244.58	271.87	-1.22	0.81	455.55
184	1144A-27X-3	53-55	244.83	272.12	-0.97	0.81	455.97
184	1144A-27X-3	78-80	245.08	272.37	-1.02	0.66	456.38
184	1144A-27X-3	104-106	245.34	272.63	-1.01	0.77	456.82
184	1144A-27X-3	128-130	245.58	272.87	-1.14	0.85	457.22
184	1144A-27X-4	3-5	245.83	273.12	-1.12	0.78	457.63

Appendix 2: Stable isotope data of ODP Site 1144

Leg	Site, Hole, Core, Section	Interval (cm)	Depth (mbsf)	Depth (mcd)	$\delta^{18}O$ G.ruber	$\delta^{13}C$ G.ruber	Age (ka)
184	1144A-27X-4	28-30	246.08	273.37	-1.37	0.70	458.05
184	1144A-27X-4	53-55	246.33	273.62	-1.62	0.79	458.47
184	1144A-27X-4	78-80	246.58	273.87	-1.80	0.58	458.88
184	1144A-27X-4	104-106	246.84	274.13	-0.97	0.60	459.31
184	1144A-27X-4	128-130	247.08	274.37	-1.34	0.70	459.71
184	1144A-27X-5	3-5	247.33	274.62	-1.01	0.68	460.13
184	1144A-27X-5	28-30	247.58	274.87	-0.90	0.69	460.55
184	1144A-27X-5	53-55	247.83	275.12	-0.91	0.59	460.96
184	1144A-27X-5	78-80	248.08	275.37	-0.67	0.77	461.38
184	1144A-27X-5	104-106	248.34	275.63	-1.10	0.94	461.81
184	1144A-27X-5	128-130	248.58	275.87	-0.60	0.81	462.21
184	1144A-27X-6	3-5	248.83	276.12	-0.97	0.94	462.63
184	1144A-27X-6	28-30	249.08	276.37	-0.91	0.75	463.04
184	1144A-27X-6	53-55	249.33	276.62	-1.18	0.87	463.46
184	1144A-27X-6	78-80	249.58	276.87	-1.33	0.91	463.88
184	1144A-27X-6	104-106	249.84	277.13	-1.35	1.08	464.31
184	1144A-27X-7	3-5	250.03	277.32	-1.47	0.77	464.63
184	1144A-27X-7	28-30	250.28	277.57	-1.35	0.83	465.04
184	1144A-27X0	3-5	250.43	277.72	-1.52	0.96	465.29
184	1144A-28X-1	3-5	250.93	279.20	-1.79	0.85	467.76
184	1144A-28X-1	28-30	251.18	279.45	-1.64	0.73	468.17
184	1144A-28X-1	55-57	251.45	279.72	-1.31	0.90	468.62
184	1144A-28X-1	78-80	251.68	279.95	-1.16	0.74	469.01
184	1144A-28X-1	104-106	251.94	280.21	-1.23	0.91	469.44
184	1144A-28X-1	128-130	252.18	280.45	-1.30	1.07	469.84
184	1144A-28X-2	3-5	252.43	280.70	-0.97	0.97	470.25
184	1144A-28X-2	28-30	252.68	280.95	-1.03	0.87	470.67
184	1144A-28X-2	55-57	252.95	281.22	-1.41	0.79	471.12
184	1144A-28X-2	78-80	253.18	281.45	-1.15	0.84	471.50
184	1144A-28X-2	104-106	253.44	281.71	-1.58	0.82	471.94
184	1144A-28X-2	128-130	253.68	281.95	-1.60	1.03	472.34
184	1144A-28X-3	3-5	253.93	282.20	-1.42	0.98	472.75
184	1144A-28X-3	28-30	254.18	282.45	-1.84	1.13	473.17
184	1144A-28X-3	55-57	254.45	282.72	-1.71	0.92	473.62
184	1144A-28X-3	78-80	254.68	282.95	-1.90	1.04	473.95
184	1144A-28X-3	104-106	254.94	283.21	-1.62	1.01	474.21
184	1144A-28X-3	128-130	255.18	283.45	-1.80	0.71	474.41
184	1144A-28X-4	3-5	255.43	283.70	-1.65	0.83	474.62
184	1144A-28X-4	28-30	255.68	283.95	-1.57	0.84	474.82
184	1144A-28X-4	55-57	255.95	284.22	-1.73	0.97	475.04
184	1144A-28X-4	78-80	256.18	284.45	-1.38	0.90	475.23
184	1144A-28X-4	104-106	256.44	284.71	-1.76	0.95	475.44
184	1144A-28X-4	128-130	256.68	284.95	-1.74	0.63	475.64
184	1144A-28X-5	3-5	256.93	285.20	-1.77	0.83	475.84
184	1144A-28X-5	28-30	257.18	285.45	-1.95	0.79	476.05
184	1144A-28X-6	28-30	258.68	286.95	-1.50	1.02	477.28
184	1144A-28X0	28-30	260.28	288.55	-1.36	1.09	478.59
184	1144A-29X-1	104-106	261.54	289.99	-2.00	1.32	479.77
184	1144A-29X-2	104-106	263.04	291.49	-2.15	1.17	481.08
184	1144A-29X-3	104-106	264.54	292.99	-1.96	1.22	484.32
184	1144A-29X-4	104-106	266.04	294.49	-1.79	1.00	487.65
184	1144A-29X-5	104-106	267.54	295.99	-1.85	0.89	490.97
184	1144A-29X-6	104-106	269.04	297.49	-1.68	1.18	494.29
184	1144A-29X0	28-30	270.20	298.65	-1.86	1.29	496.86
184	1144A-30X-1	3-5	270.13	300.52	-2.28	0.90	500.97
184	1144A-30X-2	3-5	271.63	302.02	-2.01	0.84	503.75

Appendix 2: Stable isotope data of ODP Site 1144

Leg	Site, Hole, Core, Section	Interval (cm)	Depth (mbsf)	Depth (mcd)	$\delta^{18}O$ G.ruber	$\delta^{13}C$ G.ruber	Age (ka)
184	1144A-30X-3	3-5	273.13	303.52	-1.71	0.52	506.50
184	1144A-30X-4	3-5	274.63	305.02	-1.75	0.85	509.25
184	1144A-30X-5	3-5	276.13	306.52	-1.21	0.96	512.14
184	1144A-30X-6	3-5	277.63	308.02	-1.99	1.03	525.98
184	1144A-30X-7	3-5	279.13	309.52	-1.57	0.68	536.96
184	1144A-31X-1	28-30	279.98	311.11	-1.51	0.74	546.92
184	1144A-31X-2	28-30	281.48	312.61	-1.83	0.66	556.28
184	1144A-31X-3	28-30	282.98	314.11	-2.07	0.74	565.64
184	1144A-31X-4	28-30	284.48	315.61	-2.11	0.70	575.06
184	1144A-31X-5	28-30	285.98	317.11	-1.65	0.82	587.00
184	1144A-31X-6	28-30	287.48	318.61	-2.35	0.98	598.60
184	1144A-31X-7	28-30	288.98	320.11	-1.77	0.87	602.90
184	1144A-32X-2	3-5	290.83	323.61	-2.25	0.64	612.09
184	1144A-32X-3	3-5	292.33	325.11	-0.76	0.41	622.87
184	1144A-32X-4	3-5	293.83	326.61	-1.05	0.75	626.13
184	1144A-32X-5	3-5	295.33	328.11	-0.92	0.52	629.26
184	1144A-32X-6	3-5	296.83	329.61	-0.78	0.46	632.39
184	1144A-32X-7	3-5	298.33	331.11	-1.11	0.61	635.52
184	1144A-33X-1	3-5	299.03	333.25	-1.41	0.74	639.98
184	1144A-33X-2	3-5	300.53	334.75	-1.18	0.50	643.11
184	1144A-33X-3	3-5	302.03	336.25	-1.24	0.66	646.24
184	1144A-33X-4	3-5	303.53	337.75	-1.28	0.40	649.37
184	1144A-33X-5	3-5	305.03	339.25	-1.14	0.41	652.50
184	1144A-33X-6	3-5	306.53	340.75	-1.24	0.48	655.63
184	1144A-33X-7	3-5	308.03	342.25	-1.47	0.59	658.76
184	1144A-34X-2	3-5	310.13	343.67	-0.95	0.41	661.72
184	1144A-34X-3	3-5	311.63	345.17	-0.98	0.39	664.85
184	1144A-34X-4	3-5	313.13	346.67	-1.07	0.49	667.98
184	1144A-34X-5	3-5	314.63	348.17	-1.46	0.62	671.10
184	1144A-34X-6	3-5	316.13	349.67	-1.31	0.69	674.23
184	1144A-34X0	3-5	318.17	351.71	-1.72	0.63	678.49
184	1144A-34X0	28-30	318.42	351.96	-1.66	0.76	679.01
184	1144A-35X-1	5-7	318.25	355.79	-2.25	1.03	687.05
184	1144A-35X-2	53-55	320.23	357.77	-1.94	0.84	693.70
184	1144A-35X-3	104-106	322.24	359.78	-1.84	0.54	700.50
184	1144A-35X-5	5-7	324.25	361.79	-1.46	0.81	707.30
184	1144A-35X-6	53-55	326.23	363.77	-1.13	0.83	713.95
184	1144A-35X0	5-7	327.77	365.31	-1.08	0.79	717.19
184	1144A-36X-1	5-7	327.95	370.44	-1.78	0.84	727.83
184	1144A-36X-2	56-58	329.96	372.45	-1.70	0.65	732.17
184	1144A-36X-3	128-130	332.18	374.67	-1.79	0.70	741.47
184	1144A-36X-5	28-30	334.18	376.67	-1.22	0.41	750.02
184	1144A-36X-6	78-80	336.18	378.67	-1.60	0.71	759.83
184	1144A-36X-7	28-30	337.18	379.67	-1.40	0.97	764.74
184	1144A-37X-3	53-55	341.03	381.58	-1.60	1.12	774.12
184	1144A-37X-4	104-106	343.04	383.59	-1.84	0.91	783.79
184	1144A-37X-6	5-7	345.05	385.60	-1.46	0.54	788.06
184	1144A-37X0	5-7	347.00	387.55	-1.19	0.51	792.00
184	1144A-38X-1	5-7	347.15	391.30	-1.16	0.85	799.34
184	1144A-38X-2	53-55	349.13	393.28	-1.47	0.81	813.39
184	1144A-38X-3	104-106	351.14	395.29	-1.78	0.78	828.00
184	1144A-38X-5	5-7	353.15	397.30	-1.77	0.71	842.61
184	1144A-38X-6	53-55	355.13	399.28	-2.16	0.48	856.85
184	1144A-38X0	28-30	356.84	400.99	-1.10	0.50	863.06
184	1144A-39X-1	7-9	356.77	401.52	-0.97	0.35	864.94
184	1144A-39X-2	56-58	358.76	403.51	-0.89	0.22	872.01

Appendix 2: Stable isotope data of ODP Site 1144

Leg	Site, Hole, Core, Section	Interval (cm)	Depth (mbsf)	Depth (mcd)	$\delta^{18}O$ G.ruber	$\delta^{13}C$ G.ruber	Age (ka)
184	1144A-39X-3	106-108	360.76	405.51	-1.41	0.45	879.95
184	1144A-39X-5	1-3	362.71	407.46	-1.23	0.51	883.17
184	1144A-39X-6	55-57	364.75	409.50	-1.14	0.47	886.49
184	1144A-39X0	26-28	366.48	411.23	-1.41	0.65	889.30
184	1144A-40X-1	3-5	366.43	412.88	-1.43	0.42	891.99
184	1144A-40X-2	53-55	368.43	414.88	-1.63	0.25	895.24
184	1144A-40X-3	104-106	370.44	416.89	-1.05	0.44	898.51
184	1144A-40X-5	3-5	372.43	418.88	-1.74	0.51	901.75
184	1144A-40X-6	53-55	374.43	420.88	-1.89	0.47	904.98
184	1144A-40X0	28-30	376.17	422.62	-1.54	0.32	907.09
184	1144A-41X-1	73-75	376.73	426.70	-0.90	0.96	912.07
184	1144A-41X-1	143-145	377.43	427.40	-1.80	0.97	918.84
184	1144A-41X-2	73-75	378.23	428.20	-1.62	1.03	926.86
184	1144A-41X-3	73-75	379.73	429.70	-1.62	0.89	930.61
184	1144A-41X-3	143-145	380.43	430.40	-2.06	0.66	932.30
184	1144A-41X-4	73-75	381.23	431.20	-2.44	0.85	934.23
184	1144A-41X-4	143-145	381.93	431.90	-1.75	0.71	935.91
184	1144A-41X-5	73-75	382.73	432.70	-2.02	0.66	937.84
184	1144A-41X-6	73-75	384.23	434.20	-2.21	1.03	941.46
184	1144A-41X-6	143-145	384.93	434.90	-2.25	0.74	943.15
184	1144A-42X-1	73-75	386.33	437.49	-2.04	0.78	949.39
184	1144A-42X-1	143-145	387.03	438.19	-1.94	0.85	951.08
184	1144A-42X-2	73-75	387.83	438.99	-2.14	0.41	952.93
184	1144A-42X-3	73-75	389.33	440.49	-1.71	1.15	955.02
184	1144A-42X-3	143-145	390.03	441.19	-2.06	0.56	955.96
184	1144A-42X-4	73-75	390.83	441.99	-2.02	0.58	957.04
184	1144A-42X-4	143-145	391.53	442.69	-1.57	0.51	957.98
184	1144A-42X-5	73-75	392.33	443.49	-1.74	0.75	959.05
184	1144A-42X-6	73-75	393.83	444.99	-2.22	0.66	961.06
184	1144B-43X-4	36-38	393.36	445.64	-1.02	0.52	961.93
184	1144A-42X-6	143-145	394.53	445.69	-1.56	0.93	961.99
184	1144A-43X-1	73-75	395.93	448.93	-2.00	0.11	965.51
184	1144A-43X-1	143-145	396.63	449.63	-1.02	0.52	966.27
184	1144A-43X-2	73-75	397.43	450.43	-0.81	0.57	967.13
184	1144A-43X-3	73-75	398.93	451.93	-1.41	0.56	968.75
184	1144A-43X-3	143-145	399.63	452.63	-1.87	0.78	969.51
184	1144A-43X-4	73-75	400.43	453.43	-2.23	0.65	970.38
184	1144A-43X-4	143-145	401.13	454.13	-1.84	1.02	971.13
184	1144A-43X-5	73-75	401.93	454.93	-2.23	1.20	972.00
184	1144A-43X-6	43-45	403.13	456.13	-1.79	0.83	973.15
184	1144A-43X-6	143-145	404.13	457.13	-2.07	0.69	974.10
184	1144A-44X-1	73-75	405.53	461.27	-2.27	0.51	978.04
184	1144A-44X-1	143-145	406.23	461.97	-1.71	0.78	978.71
184	1144A-44X-2	43-45	406.73	462.47	-1.65	0.67	979.18
184	1144A-44X-3	43-45	408.23	463.97	-1.84	0.76	980.62
184	1144A-44X-3	143-145	409.23	464.97	-1.64	0.97	981.59
184	1144A-44X-4	43-45	409.73	465.47	-2.15	1.05	982.07
184	1144A-44X-4	143-145	410.73	466.47	-2.26	0.67	983.21
184	1144A-44X-5	43-45	411.23	466.97	-2.22	0.38	984.84
184	1144A-44X-6	43-45	412.73	468.47	-2.21	0.82	990.21
184	1144A-44X-6	143-145	413.73	469.47	-1.53	0.49	993.79
184	1144A-45X-1	73-75	415.13	472.31	-1.16	0.89	1003.90
184	1144A-45X-1	143-145	415.83	473.01	-1.62	1.01	1004.40
184	1144A-45X-2	73-75	416.63	473.81	-1.98	0.69	1004.90
184	1144A-45X-3	73-75	418.14	475.32	-2.05	1.00	1005.80
184	1144A-45X-3	143-145	418.84	476.02	-1.82	1.45	1006.30

Appendix 2: Stable isotope data of ODP Site 1144

Leg	Site, Hole, Core, Section	Interval (cm)	Depth (mbsf)	Depth (mcd)	$\delta^{18}O$ G.ruber	$\delta^{13}C$ G.ruber	Age (ka)
184	1144A-45X-4	73-75	419.66	476.84	-2.06	0.82	1006.80
184	1144A-45X-4	143-145	420.36	477.54	-1.71	0.66	1007.20
184	1144A-45X-5	73-75	421.16	478.34	-1.69	0.81	1007.70
184	1144A-45X-6	73-75	422.66	479.84	-2.30	0.91	1008.60
184	1144A-45X-6	143-145	423.36	480.54	-2.33	1.25	1009.10
184	1144A-46X-1	73-75	424.73	483.94	-2.15	0.50	1011.20
184	1144A-46X-1	143-145	425.43	484.64	-2.46	0.61	1011.60
184	1144A-46X-2	73-75	426.23	485.44	-1.79	0.95	1012.10
184	1144A-46X-3	73-75	427.73	486.94	-1.90	1.00	1013.00
184	1144A-46X-3	143-145	428.43	487.64	-1.83	0.80	1013.40
184	1144A-46X-4	73-75	429.23	488.44	-1.68	0.81	1013.90
184	1144A-46X-4	143-145	429.93	489.14	-1.83	0.50	1014.30
184	1144A-46X-5	73-75	430.73	489.94	-2.09	0.88	1014.80
184	1144A-46X-6	73-75	432.23	491.44	-2.10	0.86	1015.80
184	1144A-46X-6	143-145	432.93	492.14	-2.16	1.12	1016.20
184	1144A-47X-1	73-75	434.33	496.26	-2.10	0.68	1018.70
184	1144A-47X-1	143-145	435.03	496.96	-1.60	0.72	1019.20
184	1144A-47X-2	73-75	435.83	497.76	-2.01	0.77	1019.70
184	1144A-47X-3	73-75	437.33	499.26	-2.01	0.73	1020.60
184	1144A-47X-3	143-145	438.03	499.96	-1.93	1.03	1021.00
184	1144A-47X-4	73-75	438.83	500.76	-2.04	1.16	1022.50
184	1144A-47X-4	143-145	439.53	501.46	-2.02	0.89	1023.80
184	1144A-47X-5	73-75	440.33	502.26	-2.03	0.99	1025.20
184	1144A-47X-6	73-75	441.83	503.76	-2.32	0.85	1028.00
184	1144A-47X-6	143-145	442.53	504.46	-1.59	0.58	1030.40
184	1144A-48X-1	73-75	443.93	509.33	-1.88	0.53	1963.60
184	1144A-48X-1	143-145	444.63	510.03	-1.44	0.99	1964.60
184	1144A-48X-2	73-75	445.43	510.83	-1.91	1.04	1965.80
184	1144A-48X-3	73-75	446.94	512.34	-1.79	0.76	1968.00
184	1144A-48X-3	143-145	447.64	513.04	-1.81	1.31	1969.00
184	1144A-48X-4	73-75	448.46	513.86	-2.07	1.19	1970.20
184	1144A-48X-4	143-145	449.16	514.56	-1.92	1.32	1971.20
184	1144A-48X-5	73-75	449.96	515.36	-2.03	0.84	1972.40
184	1144A-48X-6	73-75	451.46	516.86	-2.19	1.17	1974.60
184	1144A-48X-6	143-145	452.16	517.56	-2.07	0.79	1975.60